A PETROLOGICAL MODEL FOR EMPLACEMENT OF THE ULTRAMAFIC

NI-CU-PGE ALPHA COMPLEX, EASTERN ALASKA RANGE
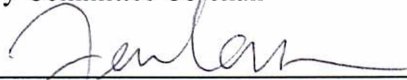
By

Lauren Lande

RECOMMENDED:
_____
Dr. Rainer Newberry
Advisory Committee Co-chair

_____
Dr. Jessica Larsen
Advisory Committee Co-chair

_____
Evan Twelker, CPG

_____
Dr. Mary Keskinen

_____
Dr. Paul McCarthy
Chair, Department of Geosciences

APPROVED:
_____
Dr. Paul Layer
Dean, College of Natural Science and Mathematics

_____
Dr. John Eichelberger
Dean of the Graduate School

_____
27 July 2016
Date

A PETROLOGICAL MODEL FOR EMPLACEMENT OF THE ULTRAMAFIC

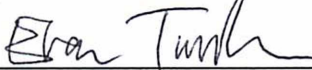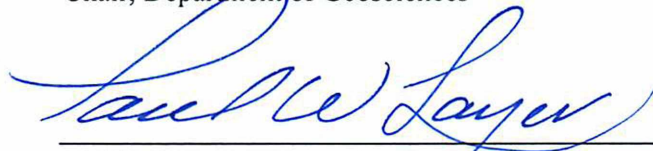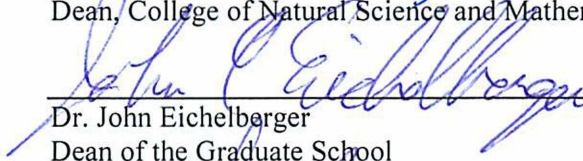NI-CU-PGE ALPHA COMPLEX, EASTERN ALASKA RANGE

By

Lauren L. Lande, B.S.

A Thesis Submitted in Partial Fulfillment of the Requirements

for the Degree of

Master of Science

in

Geology

University of Alaska Fairbanks

August 2016

APPROVED:

Rainer Newberry, Committee Co-Chair
Jessica Larsen, Committee Co-Chair
Evan Twelker, Committee Member
Mary Keskinen, Committee Member
Paul McCarthy, Chair
    Department of Geosciences
Paul Layer, Dean
    College of Natural Science and Mathematics
John Eichelberger, *Dean of the Graduate School*

Abstract

The Alpha complex, also known as the Fish Lake complex, is a mineralized Ni-Cu-PGE (platinum group element) mafic-ultramafic intrusive complex located within the Wrangellia terrane in the Eastern Alaska Range. The complex, a 30-km long, 3-km wide, sill-form body, consists of alternating layers of dunite, wehrlite, and clinopyroxenite. Previous industry-led exploration has yet to converge on a geological model for the complex that adequately explains multiple aspects of the observed mineralization and crystallization patterns. Due to poor exposure and a lack of chilled margins, it is not immediately clear whether this is a single body or a multi-sill complex.

I found that the complex consists of numerous individual sills ranging from 30-200 m thick. These can be identified based on the forsterite (Fo) component of olivine. Sills have primitive margins with high Fo contents in olivine that grade inwards to evolved cores with lower Fo olivine. Some of the sills have distinctly wehrlitic centers that were identifiable in the field. High Fo contents in olivine (up to Fo 87) and high Cr/(Cr+Al) in spinel (0.46-0.96) suggest a primitive basaltic parental magma. Individual zones in the complex contain clinopyroxene with a range of TiO_2 values; these TiO_2 values reflect the associated melt and can be used to differentiate between different magma series. Clinopyroxene compositions suggest three different magmatic compositions: a low-TiO_2 magma in the upper unit, an intermediate magma in the basal unit, and a high-TiO_2 magma in the central unit.

Ultramafic sills in the upper unit contain the most primitive olivine with a range in MgO contents (Fo 87-83) and clinopyroxene with low-TiO_2 values (<0.4 wt.%). The central ultramafic sill has the most evolved olivine (Fo 84-79) compositions and clinopyroxene with high-TiO_2 values (up to 0.9 wt.%). The theoretical wt.% TiO_2 and Mg number ($Mg/(Mg+Fe^{2+})$) of the parental melts were calculated from clinopyroxene compositions and they suggest that the low-TiO_2 sills are similar to the Lower Nikolai basalt, and the high-TiO_2 sills are similar to the high-TiO_2 Upper Nikolai basalt.

Intermediate TiO_2 compositions in clinopyroxene and disequilibrium compositions in olivine in the basal sills indicate an origin from magmatic mixing. One sample has a bimodal olivine phenocryst assemblage, with one group averaging Fo 80.5 and the other group averaging Fo 82.5. This sample is nearby another sample with high-MgO olivine (Fo 86). These compositions may record multiple magmatic inputs from mixing of the Lower Nikolai magma series with the Upper Nikolai magma series.

PGE ratios record two distinct Pt versus Pd trends: a low Pd:Pt trend and a high Pd:Pt trend. Elevated Pd in the Upper Nikolai basalt and low Pd in the Lower Nikolai basalt suggest high Pd in the central sill is related to crystallization from the Upper Nikolai basalt. When exploring for sills with high PGE content, high-TiO_2 contents in clinopyroxene may be a good indicator of whether or not a sill has the potential to host elevated PGE mineralization.

Table of Contents

List of Figures

List of Tables

List of Appendices

Acknowledgements

Chapter 1 Introduction and Methods

1.1. Introduction

The Nikolai basalts erupted in the Late Triassic near the equator, forming an enormous oceanic plateau. Initial submarine extrusion of basalt was followed by subaerial extrusion and accompanied by emplacement of gabbroic dikes and mafic-ultramafic intrusions at depth (Nokleberg et al., 1985). Magmatic sulfide deposits hosted in the mafic-ultramafic complexes that fed the extrusive portions of large igneous provinces (LIP) contain some of the most economically significant resources of Ni, Cu, and platinum group elements (PGE) worldwide (Schmidt and Rogers, 2007). The Alpha complex is one such ultramafic feeder system to the Wrangellia LIP and thus represents an attractive target for mineral exploration.
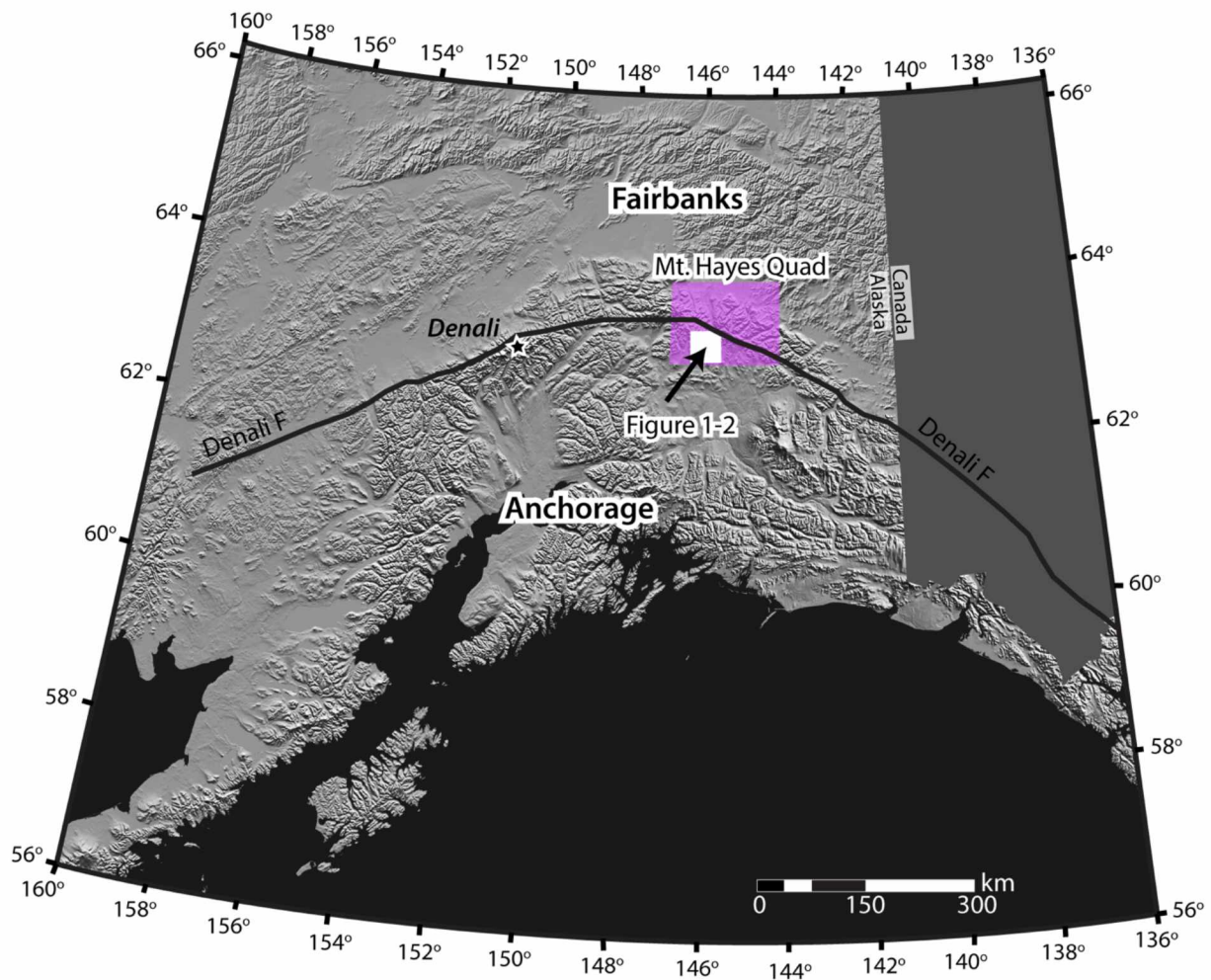
Figure 1-1. Shaded relief image showing the location of the Alpha complex and other major mafic-ultramafic complexes in the Eastern Alaska Range within the Mt. Hayes quadrangle.

The Alpha complex is one of five mafic-ultramafic complexes located within the Mt. Hayes quadrangle (Figure 1-1), about 400 km north of Anchorage. The mafic-ultramafic intrusions contain variably mineralized layers of dunite, wehrlite, and clinopyroxenite. The property (Figure 1-2) has been the focus of exploration for its Ni-Cu-PGE potential for over sixty years. However, the petrology and metallogeny of the Alpha complex remains poorly understood.

There are three competing petrological hypotheses to consider for the Alpha complex. The first is that the complex is a single differentiated mafic-ultramafic intrusion, similar to the Bushveld Igneous Complex in South Africa. This type of intrusion develops repetitive layers during cooling that grade upwards from dunite to gabbro. Another possibility is that it is a series of thin sills emplaced closely on top of one another and later intruded by gabbro, similar to the Pechanga deposits of Russia. Sills would have primitive margins (dunite, high forsterite olivine) that would grade inwards to more evolved compositions (wehrlite, lower forsterite olivine) as the cumulate magma cooled. The last possibility is that the complex is similar to the Quill Creek complex (Wellgreen deposit) in the Yukon. This model is for a single large intrusion that was fed from a continuously replenishing source. This would have resulted in the formation of a single intrusion with a quenched gabbroic margin and a primitive (dunitic) core.

The purpose of this research is to approach the problem from a systematic perspective looking at compositional changes observed in the mineralogy of the ultramafic rocks in order to better understand the petrological subdivisions of the complex. Another important goal of this research is to interpret the history of Ni-Cu-PGE mineralization. Copper, nickel, and platinum group elements preferentially partition into the sulfide phase within a magma, thus the history and timing of sulfide saturation is extremely important in understanding the metallogenesis of the complex. Examining the evolution of sulfide and chalcophile elements throughout the crystallization process and determining where the melt became sulfide saturated and what triggered sulfide saturation will help to determine the economic potential of the Alpha complex. The final product of this research will identify the most suitable geological model and which areas within the complex have the highest potential for economic grade mineralization. This is critical to the exploration strategy and could potentially lead to discoveries of more highly mineralized zones in the complex.
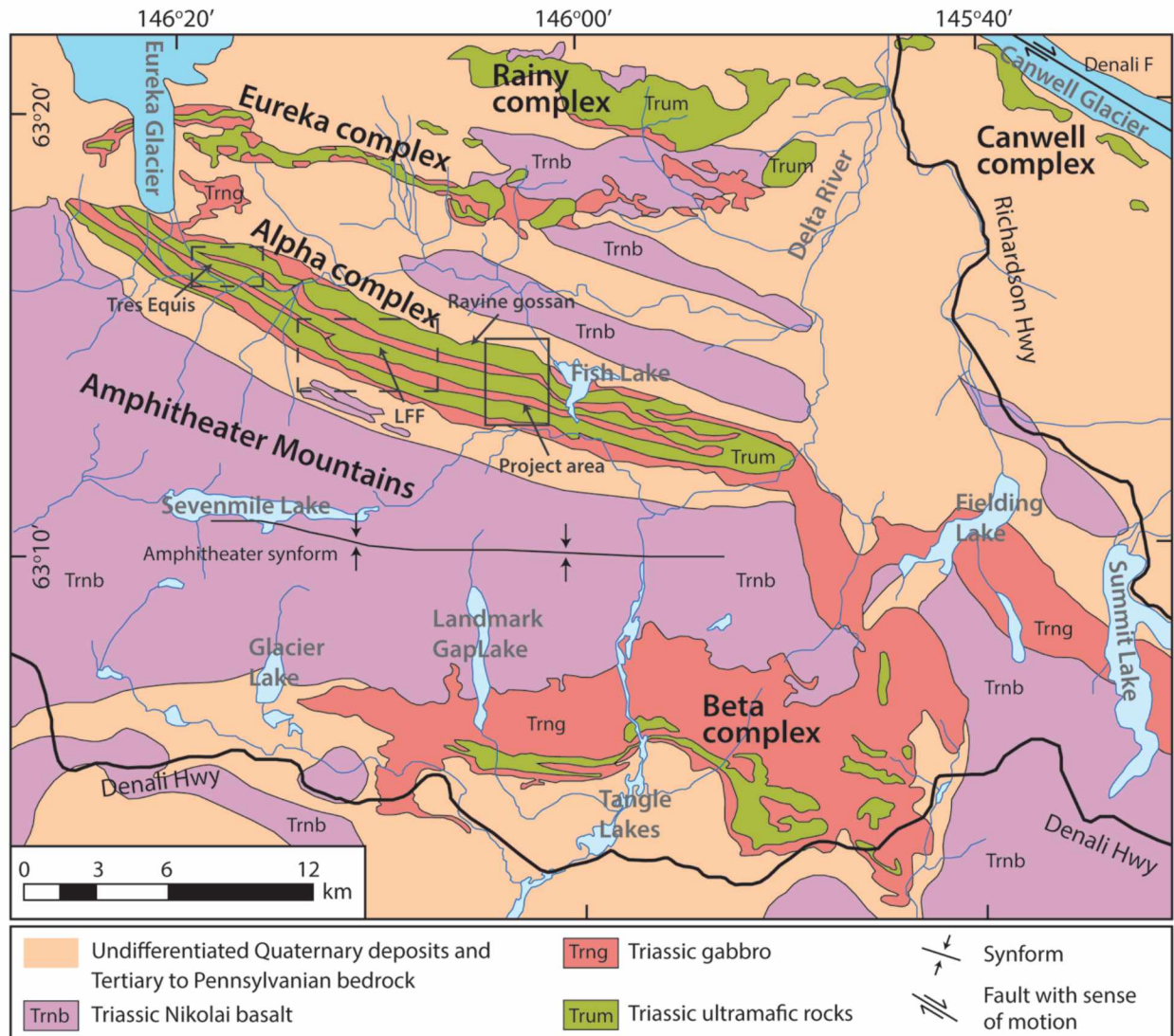
Figure 1-2. A simplified geologic map of the Alpha complex and surrounding property based on mapping by the American Copper and Nickel Company (ACNC), the Geological Survey of Canada, and Nevada Star Resource Corp. (modified from Schmidt and Rogers, 2007). Three of the more highly mineralized prospects within the Alpha complex are labeled. The Alpha and Beta complexes make up the Amphitheater synform.

1.2. Geologic setting

1.2.1. Regional geology

Wrangellia is one of the largest accreted terranes of western North America and can be traced discontinuously from southern Alaska to as far south as eastern Oregon over a distance of 2000 km (Hulbert and Stone, 2006). Wrangellia formed in an oceanic plateau flood basalt setting with a relatively short-lived extrusive event in the late Triassic. Geochronological and fossil evidence demonstrates that the onset of Triassic magmatism began around 230 Ma and was complete by 223 Ma (Schmidt and

Rogers, 2007). Paleomagnetic evidence suggests that the Wrangellia flood basalts were extruded at low latitude (<20°) in the Pacific Ocean such that Wrangellia was situated near the paleoequator in the Triassic (Jones et al., 1977; Schmidt and Rogers, 2007). Wrangellia subsequently migrated northward and was accreted on to the continental margin (Figure 1-3) in the mid- to late- Mesozoic (Nokleberg et al., 1985).
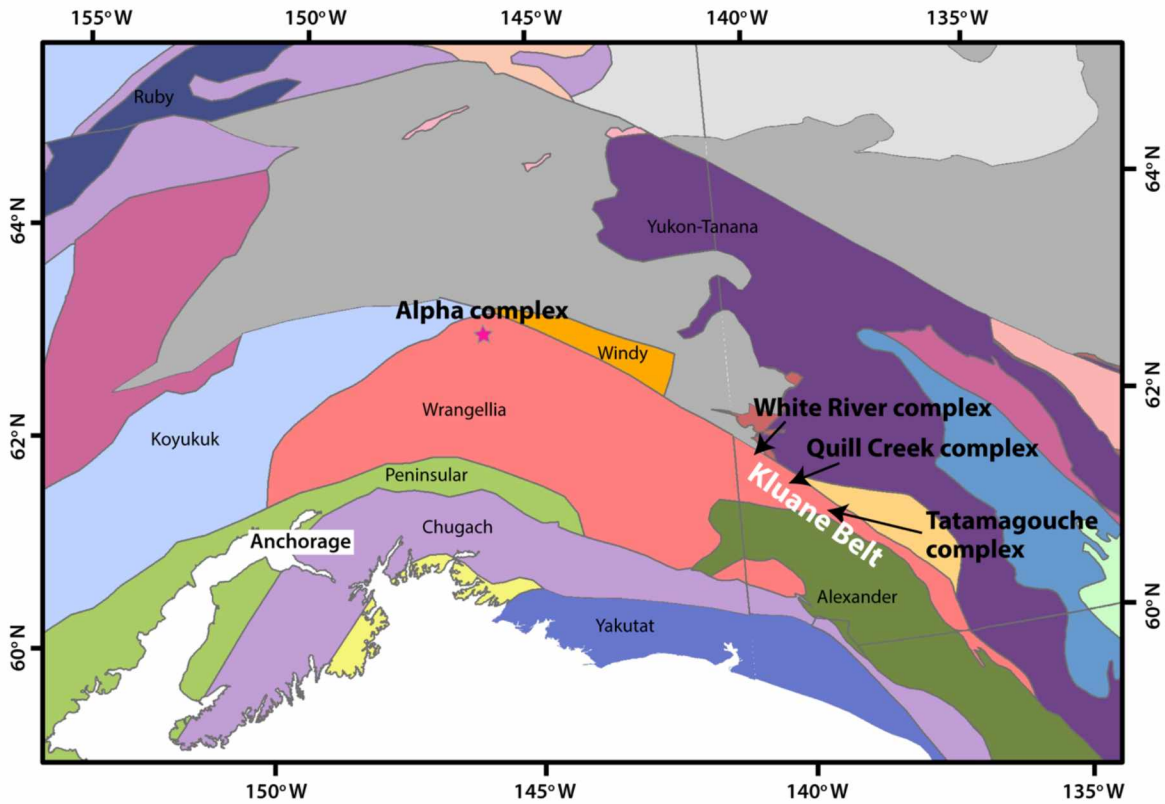
Figure 1-3. Terrane map illustrating distribution of Wrangellia and the lateral confines of Triassic ultramafic-mafic bodies extending from northern British Columbia to east-central Alaska (modified from Colpron and Nelson, 2011).

The Nikolai Group basalts are the most distinctive feature of Wrangellia (Greene et al., 2008). The Amphitheater Mountains (Figure 1-2), just south of the Alpha complex, contain one of the most complete sections of a large igneous province (LIP) worldwide. The Nikolai basalts in this region are exposed in an almost continuous section of basal gabbroic sills and submarine-to-subaerial basalts (Glen et al., 2011). The majority of the flood basalts were deposited subaerially (~3.5-4 km); however, in some areas there are pillowed and volcaniclastic basalts in the lower part of the stratigraphy, suggesting deposition under subaqueous conditions (Greene et al., 2008). The Nikolai volcanic and intrusive rocks overlie and intrude Pennsylvanian age volcanic and sedimentary rocks. Late Triassic platform carbonate

4

rocks cap the basalts. The mafic-ultramafic intrusions, which occur throughout the terrane, are thought to represent the underlying feeder systems to the Nikolai basalts (Figure 1-4; Hulbert, 1997).
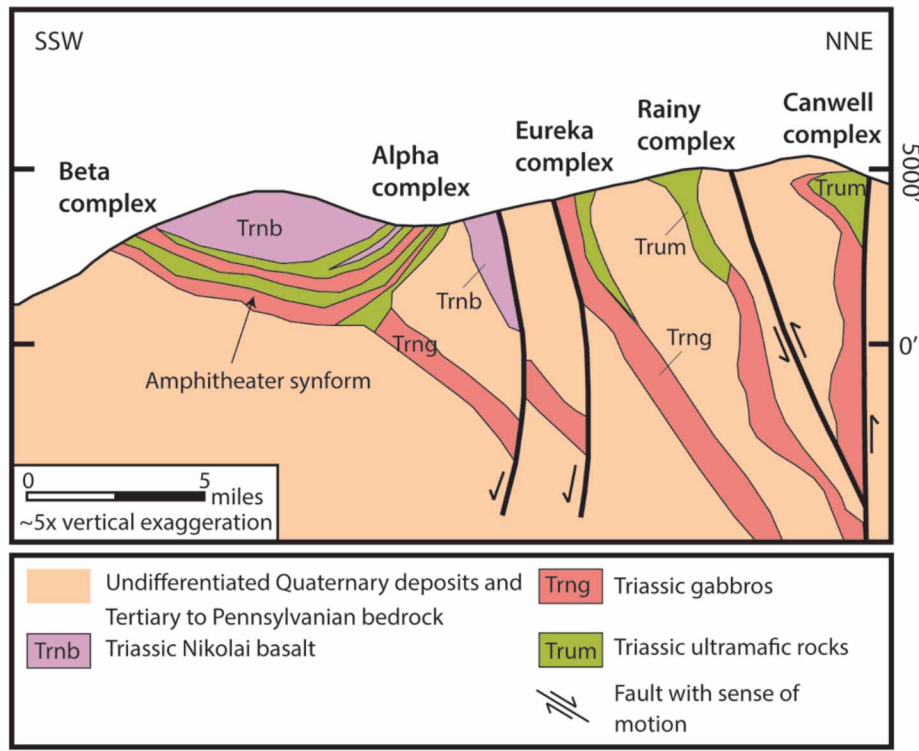
Figure 1-4. Schematic cross section facing northwest illustrating possible structural relationships between mafic-ultramafic complexes in the region (modified from Schmidt and Rogers, 2007).

The intrusive complexes of Wrangellia are compositionally tholeiitic to picritic and are sill-like in form (Hulbert, 1997). Hulbert (1997) proposed that the Mt. Hayes quadrangle, in which the Alpha complex resides, represents the main center of the Wrangellia Triassic magmatic system in Alaska. Primitive, ultramafic intrusions and olivine-rich volcanic rocks were derived from the hotter, axial portion of the mantle plume, whereas tholeiitic melts were derived from more distal areas near the plume edge (Hulbert and Stone, 2006). Metallogenic models for both the nickel deposits of Noril'sk, Russia and the Kluane Range deposits suggest that many large basaltic igneous provinces have potential for Ni-Cu-PGE mineralization related to the emplacement and evolution of their feeder systems (Schmidt and Rogers, 2007). Thus, more accurate characterization of the Alpha complex may have important implications for assessment of the mineralization potential of the complex.

The Alpha complex is located along strike to the belt of Triassic age mafic-ultramafic intrusions known in the Yukon as the "Kluane Mafic-Ultramafic Belt" (Figure 1-3; Hulbert, 1997). This belt extends along the northern margin of Wrangellia and can be traced for over 600 km from east-central Alaska to

British Columbia. It is composed of large, lithologically zoned, tholeiitic intrusions. The intrusions that have been studied in the eastern portion of the Kluane Belt (e.g., Quill Creek complex) are sill-like in form and have well developed internal zonation that consists of a thin gabbroic margin that envelops the intrusion and layers that become progressively more mafic towards the core. This zoning gives rise to layers of mela-gabbro/olivine mela-gabbro, clinopyroxenite, olivine clinopyroxenite, wehrlite, and dunite at the core (Hulbert and Stone, 2006). In the Yukon, volatile, sulfur, and Ba-rich Permian strata provided the source of magma contamination that initiated sulfide immiscibility within magma chambers. The most highly concentrated areas of mineralization are found where sulfide-bearing magma flowed over irregularities at the base of intrusions and formed areas of concentrated sulfide mineralization. Economic concentrations of Ni, Cu, Co, and PGE in the Yukon occur in the basal gabbro, in the underlying sediments, or in the contact between them (Hulbert, 1997).

1.2.2. Wrangellia stratigraphy

Rocks of the Wrangellia terrane range from late Paleozoic to late Mesozoic and were deposited in a range of settings from island arc to continental margin (Schmidt and Rogers, 2007). In the study area, Permian to Triassic age fine-grained argillite and shale (Tangle Formation) underlie the Nikolai basalt in the Amphitheater Mountains (Figure 1-5, left). Gabbroic sills, interpreted as feeders to the Nikolai basalts, variably intrude these. In contrast, the type section in the Wrangell Mountains (Figure 1-5, right) contains a greater abundance of Pennsylvanian to Permian volcaniclastic and volcanic rocks (Glen et al., 2011).

Late Triassic to Early Jurassic shallow- (Chitistone Limestone) to deep-water (Nizina Limestone) limestone and shale (McCarthy and Lubbe Creek Formations) disconformably overlie the Nikolai Formation (Figure 1-5; Schmidt and Rogers, 2007). Middle Jurassic plutons intrude southwest of the study area. Some of the sills and basalts of the Amphitheater Nikolai sequence yield plagioclase $^{40}Ar/^{39}Ar$ ages of 160-169 Ma, which suggests thermal resetting by these plutons (Glen et al., 2011).
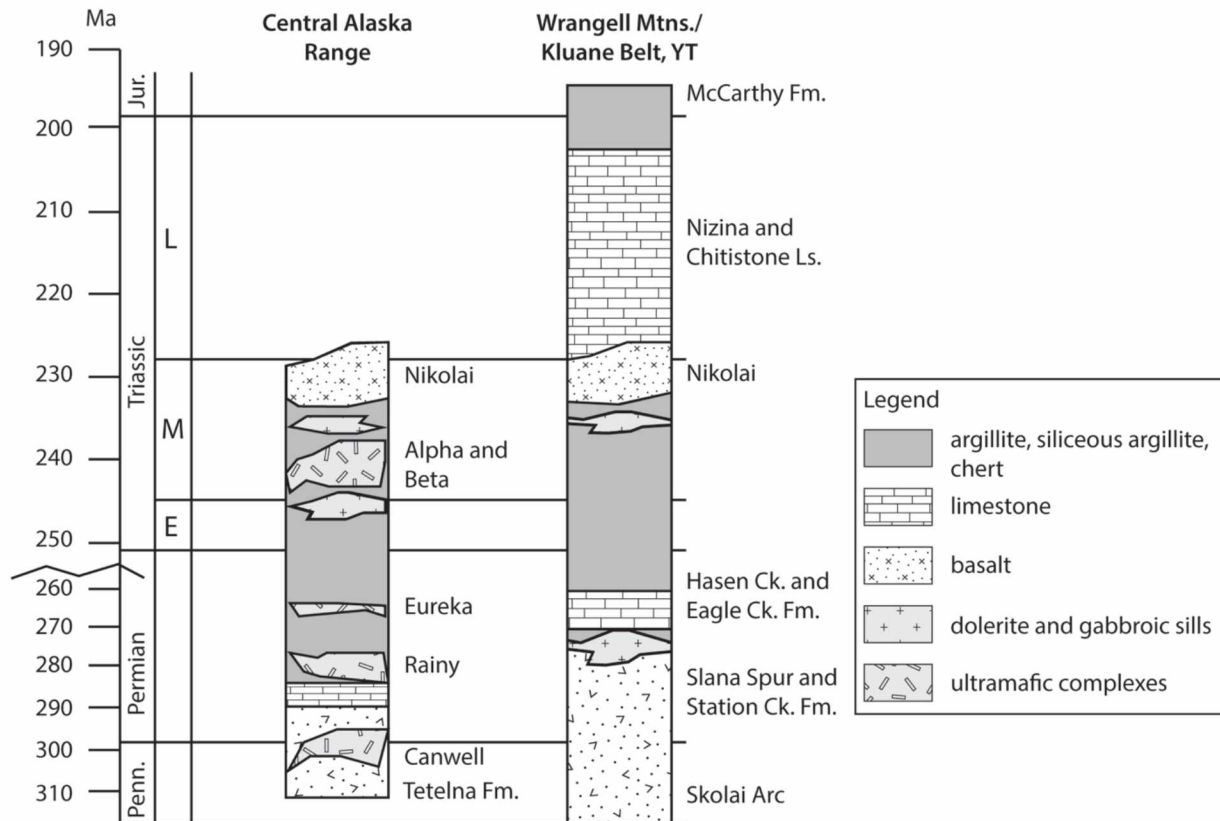
Figure 1-5. Generalized stratigraphic column for Carboniferous to Triassic rocks of the Wrangellia terrane for different physiographic regions (modified from Schmidt and Rogers, 2007).

1.2.3. Nikolai Greenstone

The Triassic Nikolai Greenstone is well exposed across southern Alaska. The Nikolai basalts are comprised of two distinct lava types, which record a change in the source of magmas that constructed the Wrangellia oceanic plateau. The lower stratigraphy is composed of low-titanium basalt (0.4-1.2 wt.% TiO_2) and the upper part of the volcanic stratigraphy is comprised of high-titanium basalt (1.6-2.4 wt.% TiO_2; Greene et al., 2008). These sequences formed during a single, short-lived phase of volcanism lasting <5 Ma (Schmidt and Rogers, 2007).

The Lower Nikolai basalt (Trn1) makes up the lowest ~ 400 m of the volcanic stratigraphy in the Alaska Range (Greene et al., 2008). This basalt is light rare earth element (LREE) -depleted, low-Ti, and has pronounced negative high field strength element (HFSE) anomalies and Hf isotopic compositions that are displaced well above the ocean island basalt (OIB) mantle array ($\Delta\varepsilon_{Hf}$ = +4 to +8). Trn1 has a range in MgO of 6.4 to 12.0 wt.% and in SiO_2 of 46.7 to 52.2 wt.% (Greene et al., 2008). Greene et al. (2008) suggest that pre-existing arc lithosphere was involved in the formation of the early, low-Ti basalts based

7

on the radiogenic Hf and HFSE-depleted signature. The displacement above the OIB array indicates involvement of a depleted component (mantle or crust), distinct from depleted MORB mantle.

The Upper Nikolai basalt (Trn2) makes up the upper ~ 3 km of the volcanic stratigraphy. This basalt is LREE-enriched and high-Ti with uniform OIB-type Pacific mantle isotopic compositions. Trn2 has a much more limited range in MgO (5.7-7.9 wt.%) and SiO_2 (49.2-52.1 wt.%) compared to Trn1 (Greene et al., 2008). The high-Ti basalt was deposited subaerially and makes up the majority of the stratigraphy of the oceanic plateau. Greene et al. (2008) proposed a deep plume as the source of the Upper Nikolai basalt. The initial Hf and Nd isotopic compositions indicate a uniform plume-type Pacific mantle source, derived from a depleted mantle source distinct from the source of MORB and with compositional similarities to that of ocean islands and plateaus in the Pacific Ocean. High Ti/Yb ratios for the high-Ti basalts indicate residual garnet from melting at high pressure within the OIB melting array (Greene et al., 2008).

In contrast, Taylor et al. (2008) proposed decompressional melting of mantle due to intra- or back-arc rifting as a source for the Nikolai basalt. Their conclusions are supported by geochemical modeling conducted by Wypych et al. (2015b). Wypych et al. proposed that enriched MORB was the source for the Upper Nikolai group and that deep mantle partial melts mixed with Skolai Arc were necessary to derive the Lower Nikolai group. They suggest that geochemical scatter (observed in both major and trace element compositions) in the Lower Nikolai basalts indicates the composition was produced by mixing of mantle with heterogeneous Skolai Arc. They also suggest that the homogenous geochemical behavior of the Upper Nikolai basalt could have been solely produced from the homogenous upper mantle. While either the deep plume source or decompressional melting models can be supported by their geochemical data, they propose that the back-arc/intra-arc spreading and decompressional melting model is more plausible, as the geographic extent of the Nikolai basalts follows the Skolai arc.

Picrites occur in several areas in the lower stratigraphy, overlying Paleozoic arc rocks. The majority of picrites have high-MgO and high-TiO_2 compositions and are LREE-enriched, similar to the high-Ti basalt (Greene et al., 2008). Two samples identified by Greene et al. (2008) and Wypych et al. (2015a) have high-MgO and low-TiO_2. This suggests there may be picrites associated with both the low-Ti and high-Ti Nikolai basalts.

1.2.4. Post-Triassic tectonic evolution and deformation of Wrangellia

Wrangellia initially formed in an island-arc setting during the late Paleozoic. During the late Mesozoic, Wrangellia migrated northwest toward the continental margin of North America. As Wrangellia approached North America, Cretaceous flysch sediments and andesitic flows and breccia were deposited. Generation of the andesitic flows and breccias likely occurred within a short-lived island-arc

8

environment. Local continentally derived cobbles within conglomerate of the flysch may indicate that Wrangellia was nearing the continental margin of North America during the Late Jurassic.

With closure of the ocean basin, Wrangellia was obducted onto the accretionary margin of North America along the Broxson Gulch thrust during the Middle Cretaceous. The collision of Wrangellia with North America and the resulting obduction, and deformation led to low-grade, greenschist facies metamorphism of the Nikolai basalts and weak penetrative deformation of Wrangellia (Nokleberg et al., 1985).

During the early tertiary, the Denali fault, which is an ancient subduction zone, was re-activated as a ridge-arc dextral transform fault (Richter and Jones, 1970). The Wrangellia and Maclaren terranes were dispersed and migrated northward along the continental margin. Local volcanism resulted in extrusion of middle Tertiary volcanic rocks. During this migration, strike slip movement took place along the Broxson Gulch thrust. In the middle to late Tertiary, the Maclaren and Wrangellia terranes began to move around the oroclinal bend in the Denali fault. This resulted in folding of the Broxson Gulch thrust and formation of the Amphitheater syncline (Nokleberg et al., 1985).

1.3. Alpha complex

1.3.1. Existing hypotheses on the geology of the Alpha complex

The Alpha complex is a 30-km long, 3-km wide, sill-form body emplaced in the Eastern Alaska Range, north of the Amphitheater Mountains. The complex is moderately well exposed in some areas along the northern margin and within its interior but exposure along the southern margin is poor. Early mapping characterized the complex as having four layered magmatic cycles that grade upward from dunite to wehrlite to minor clinopyroxenite and then to mafic lithologies like leucogabbro and norite (Schmidt and Rogers, 2007). Mineral layering dips to the south. Pure Nickel Inc. conducted reconnaissance mapping during the 2009 exploration season and identified subparallel layers of wehrlite surrounded by dunite country rock and crosscut by gabbro (Figure 1-6). The complex is intruded into Paleozoic sediments and overlain by the Nikolai Greenstone.

The Alpha complex and Beta complex (also known as the Tangle complex) were intruded at approximately the same stratigraphic level below the base of the Nikolai basalts and may be connected at depth (Figure 1-4; Schmidt and Rogers, 2007). Geophysical data demonstrated that the Alpha and Beta complexes underlie an area greater than 800 km^2 and that there may be a feeder system at depth below the synform (Schmidt and Rogers, 2007; Schmidt et al., 2002).

9
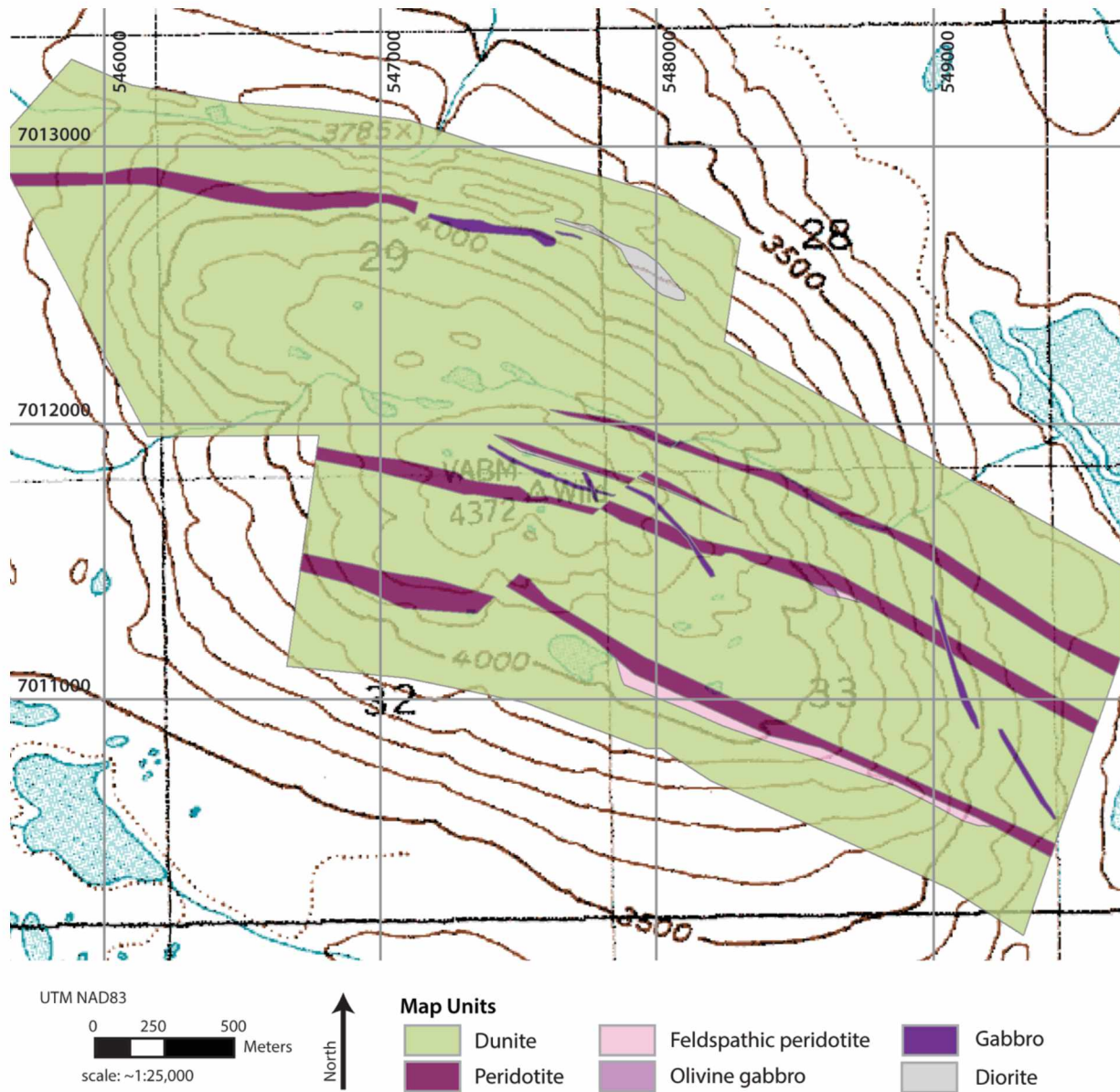
Figure 1-6. 1:25,000 scale geologic map of the central section of the Alpha complex (Pure Nickel Inc., unpublished data).

Geophysical modeling by Glen et al. (2011) estimated the volume of the Nikolai basalts to be on the order of 1000 km^3 and the ultramafic rocks on the order of 2000 km^3. Geophysical modeling also shows that the Alpha complex is connected to the Beta complex to the south at depth, forming the Amphitheater synform (Figure 1-7). Their modeling demonstrates that the Amphitheater synform gradually thickens and plunges westward, and extends to depths below 5 km. This suggests the entire magmatic feeder system to the Nikolai basalt is larger and more extensive than previously known. The

ultramafic material at depth forms a funnel like structure that they interpret to be the upper portion of a chamber that fed magma to the Nikolai basalts and to the Nikolai-related intrusions.

Glen et al. (2011) also suggested the crustal structure of the Amphitheater Mountains is a sag basin. Other authors have explained the structure as a syncline that formed after deposition due to regional deformation (e.g., Nokleberg et al., 1985; Schmidt and Rogers, 2007). The sag basin model is a structural downwarp, that could have formed from emplacement of the Nikolai basalts on the surface. This could form structurally, from faulting along the basin, or by deflation as the magma chamber emptied and collapsed under the weight of the overlying basalts (Figure 1-7). Geophysical modeling favors the sag basin model. Magnetic gradients suggest the volume of the gabbroic sills varies substantially and increases towards the center of the synform. However, the alignment of the axis of the synform is parallel to folding in the Beta complex. This suggests the synform may have been steepened later by Cretaceous to Tertiary deformation (Glen et al., 2011).
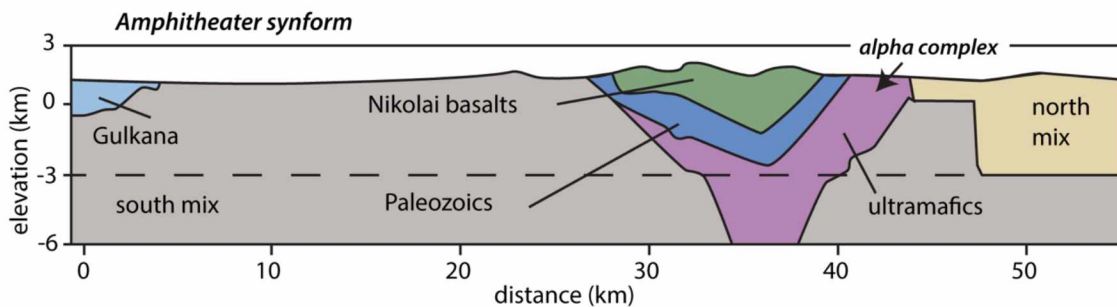
Figure 1-7. Geophysical model based on a 3-D potential field model demonstrating the potential presence of a deep magmatic feeder system (modified from Glen et al., 2011).

1.3.2. Mineralization of the Alpha complex

The Alpha complex has been found to be weakly to moderately mineralized with Cu-Ni-PGE-enriched sulfides. The Eureka zone (Figure 1-8) is potentially the most important source of ore in the Alpha complex, containing a large volume of low-grade, disseminated mineralization. Drilling and mapping indicate the zone extends over a minimum strike length of 15 km. Drilling encountered intersections ranging up to 320 m thick (Figure 1-8). A nickel deportment study conducted in 2014 by SGS Minerals Services concluded that 75.3% of the nickel in the composite sample occurs in potentially recoverable phases of Ni-Fe sulfides and Ni-Fe alloys. Only 20% of the total nickel occurs in unrecoverable silicate minerals. The remaining nickel occurs in Fe-sulfides, Fe-alloys, chromite, and sulfide alteration minerals (Pure Nickel Inc., 2014). The most highly mineralized drill hole, PNI-12-063, intercepted a 90-meter interval that averaged approximately 270 ppb Pt+Pd (maximum 549 ppb), 1500 ppm Cu (maximum 3071 ppm) and 2300 ppm Ni (maximum 3742 ppm; Figure 1-8). The zone of

anomalous metal concentrations is present in three different lithological units. Sulfides in this zone appear to be primary magmatic sulfides.

The Tres Equis prospect (XXX prospect; Figure 1-2), located on the western end of the Alpha complex, has been described as magmatic sulfide in the past but it has many of the characteristics of hydrothermal, remobilized sulfide. The sulfide showings have very high Pd to Pt ratios (>15:1), and very little Os, Ru, Rh, or Ir. However, it also exhibits high Ni to Cu ratios. The best mineralization at the surface assayed 6.68% Ni, 1.02% Cu, 0.42% Co, 88 ppb Pt and 1400 ppb Pd (Pure Nickel Inc., unpublished data).
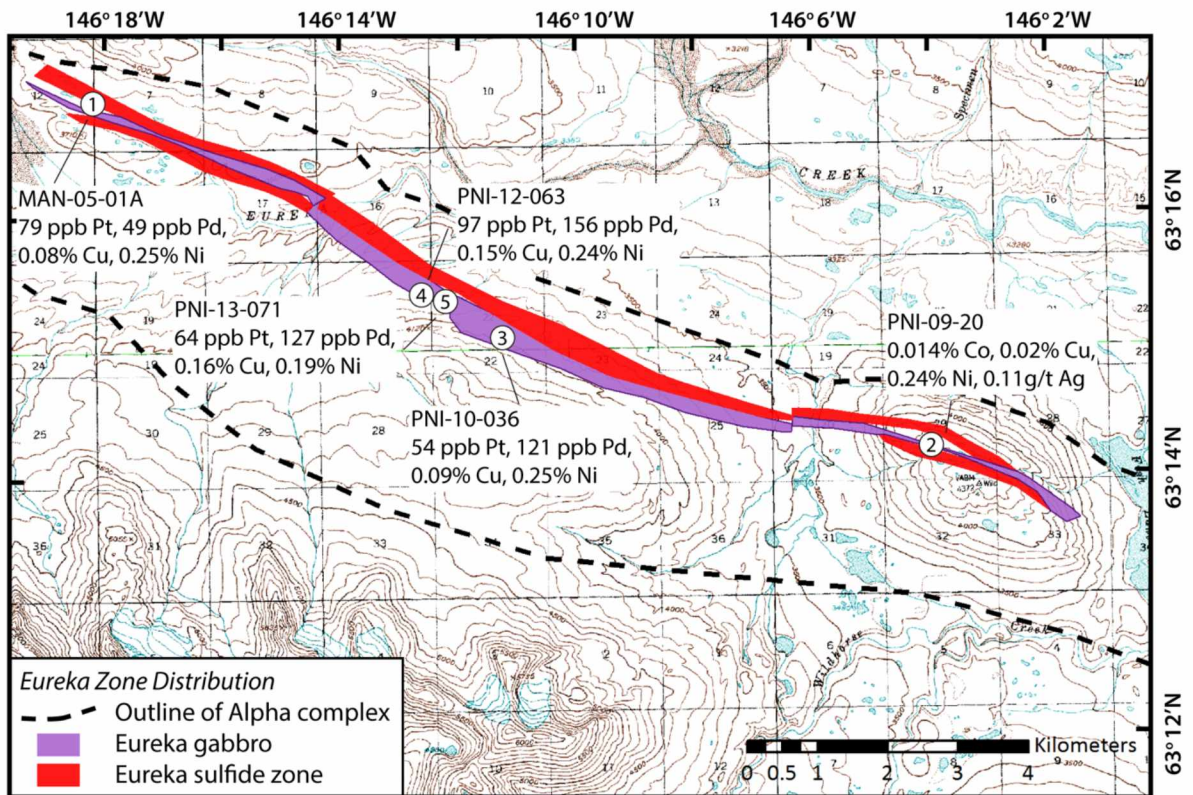
Figure 1-8. Map showing the location of the Eureka zone (in red and purple) and a few of the more highly mineralized drilling intercepts (modified from Pure Nickel Inc., 2013).

Truly magmatic sulfides contain pyrrhotite ($Fe_{1-x}S$), pentlandite with Fe equal to Ni, and chalcopyrite. The PGE mineralization will have Pt greater than Pd and significant Os, Ir, Ru, and Rh. Fractionation processes can lower the Pt/Pd values if Pt is preferentially incorporated into olivine or chromite (Cawthorn et al., 2005). Conversely, hydrothermal deposits should have high Cu to Ni ratios and Pd much greater than Pt, with small amounts of Ir, Os, Ru, and Rh. This reflects the relative solubility of these elements under hydrothermal conditions, where Ir, Os, Ru, and Rh are especially immobile.

1.3.3. Formation processes of magmatic Ni-Cu-PGE deposits

It is important to understand the processes that lead to the formation of economic Ni-Cu-PGE deposits when attempting to evaluate whether or not the Alpha complex has the potential to have produced an economic deposit. Magmatic Ni-Cu-PGE sulfide deposits have been broadly classified into two major groupings; sulfide rich systems (>10% sulfide) valuable for their Ni and Cu concentrations, and sulfide poor systems (<5% sulfide), which are primarily valuable for their PGE content (Naldrett, 2010). Examples of Ni-Cu deposits include those associated with komatiitic magmatism (e.g., Raglan and Thompson belts), deposits related to flood basaltic magmatism (e.g., Noril'sk, Russia), and the more unusual Sudbury class, whose mineralization was developed from the melt produced by meteoric impact. The flood basalt and the Sudbury classes alone account for over 50% of all known Ni resources (Naldrett, 2010). The sulfur-poor, PGE-rich class of deposits are characterized according to their petrology and morphology. They are divided on the basis of parental magma compositions and on the basis of morphology (stratiform, strata bound, or discordant) and whether the PGE show a sulfide, magnetite, or chromite association. Seventy-five percent of the worlds PGE resources come from just three intrusions, the Bushveld, the Great Dyke, and the Stillwater, though several other smaller deposits occur throughout the world. All of these intrusions were crystallized from two magma types, a high SiO_2, MgO, and Cr_2O_3 and low Al_2O_3 magma that was emplaced early and a later, Al_2O_3 rich, tholeiitic-type magma. The highest PGE concentrations in these deposits occur at levels in the intrusions for which trace element compositions suggest variable degrees of magma mixing (Naldrett, 2011).

Ultramafic complexes that host magmatic ore deposits form through the fractional crystallization of mafic to ultramafic magmas. These magmas form in especially hot parts of the mantle and rise toward the crust because their density is less than that of the surrounding mantle rocks. Subsequently, they may rise to the surface to erupt as lava flows or they may crystallize as intrusive bodies when they reach density discontinuities in the crust. Most of the time, the consequent rocks are composed of silicate minerals with minor amounts of oxides and sulfides. However, in some cases, minor differences in the composition of the parental magma, the degree of partial melting in the mantle, and the composition of the assimilated crustal rocks can result in the development of economic concentrations of ore metals. Thus, understanding the factors that disrupt the normal formation of an uneconomic intrusive magmatic body is vital to understanding the origins of magmatic ore deposits.

For a magmatic ore deposit to form, a high degree of partial melting of the precious metals enriched-lower mantle has to occur in order to get primary enrichment of nickel, copper, and platinum group elements (PGE) in the silicate magma (Barnes and Lightfoot, 2005). As a portion of the mantle melts, chalcophile elements enter the melt at different rates. Ni will become concentrated in the magma first, through progressive melting of olivine. Once the melt has a large enough volume to dissolve all of

the sulfide present, Pt, Pd, and Cu will reach their maximum concentrations (Naldrett, 2010). As the mass of magma increases with melting, these metals become progressively diluted without the addition of sulfide. Subsequently, if a magma is released from the mantle after only a modest degree of melting, it will be poor in PGE and contain only modest amounts of Ni and Cu. Magmas released after all of the mantle sulfide has been incorporated will be rich in PGE and Cu, and those released at advanced stages of melting will be enriched in Ni (Naldrett, 2010).

This magma must then be transported to the surface quickly enough before Ni is removed from the magma by olivine crystallization. External sulfur must be incorporated into a melt during emplacement in the crust through either assimilation of crustal rocks or S-rich country rocks, in order for the melt to become sulfur saturated and segregate out an immiscible sulfide liquid. The solubility of sulfide in mafic-ultramafic magmas increases with increasing temperature and f_{S2} and decreases with increasing pressure and f_{O2} (Naldrett, 2011). Thus, during ascent from the mantle, the decrease in pressure increases the ability of the magma to dissolve sulfur. Ascent through 55 km will more than double the ability of a typical basaltic melt to dissolve sulfur from around 1,000 ppm S at 64-km depth to 2,300 ppm S at 9-km (Mavrogenes and O'Neill, 1999). This means that even a melt that was sulfur saturated on leaving its mantle source will be far from saturated near the surface. The form of external sulfur that is incorporated into the magma will also affect the system. The solubility of S as sulfate may be as much as ten times greater than the solubility of S as sulfide (Arndt et al., 2005).

During cooling, silicates in the magma will crystallize first, increasing the concentration of sulfur in the melt until it reaches the saturation level. The sulfide liquid will then settle through the less dense silicate magma and crystallize at the base of the intrusion. If a given magma is too undersaturated in sulfide or doesn't incorporate sufficient external sulfur, it won't reach sulfide saturation until much of the magma has crystallized, resulting in only small amounts of disseminated sulfide. If PGE abundances in the magma are too low, or if the magma interacts with too large of a sulfide melt, PGEs will be too diluted and the deposit will not be of economic grade (Arndt et al., 2005). Metals partition strongly into sulfide liquid, thus the ore composition can be highly influenced not only by the composition of the primary magma, but also by metals present in rocks that are incorporated into the melt at later stages.

The abundance of PGE in magmas depends primarily on the nature and abundance of phases that retain these elements (sulfides, oxides, alloys) in the melting residue. Platinum group elements are very chalcophile and extremely siderophile. Sulfide-silicate partition coefficients for the chalcophile elements decrease with increasing f_{O2}/f_{S2}. Copper partition coefficients are lower than those for PGE but it is still mainly hosted in sulfides. Nickel is both chalcophile and lithophile so it is partitioned between sulfides and olivine (Arndt et al., 2005). Thus, exsolution of a magmatic sulfide should cause depletion of Ni in the silicate melt by metal partitioning into the sulfide liquid. The olivine crystallizing from such a melt

should have a lower Ni content than olivine that crystallized from a sulfide free melt. Ni concentrations in olivine should also decrease as the magma becomes more evolved. Depletion of chalcophile elements within particular magmatic subdivisions in an ultramafic complex can indicate episodes of sulfide formation and may be a useful tool for exploration of metal-rich massive sulfide.

In summary, multiple factors play a role in the formation of economic magmatic deposits. If sulfide saturation occurs at too deep of a level, Cu, Ni, and PGE will not be extracted with the melt. If olivine crystallization happens too early, Ni will be tied up in the silicates and won't be extracted by the sulfide melt. If sulfide and olivine are both undersaturated until high levels of emplacement, the sulfide melt can interact with the silicate melt and metals will partition into the sulfide, forming an economic deposit. Analyzing Ni depletion in olivine, as well as PGE compositions, within the Alpha complex will reveal whether or not sulfide saturation occurred before or after olivine crystallization and whether or not it had the potential to form economic grade mineralization.

1.3.4. Potential deposit models

In early years of exploration at the Alpha complex, the primary focus of exploration was massive sulfide mineralization. The deposit model conceived by exploration was of other large deposits, where massive Ni-rich sulfide accumulated at the base of, or in feeders to, large mafic-ultramafic intrusions. The original model envisioned by geologists was for a classic differentiated mafic-ultramafic intrusion (e.g., Bushveld igneous complex), which develops repetitive layers during cooling that grade upwards from dunite to gabbro (Figure 1-9A). This results in parallel layers of ultramafic and mafic rocks.

One of the essential features of this type of model is that the host bodies are generally large, intrusive bodies into which magma flowed through "feeder" dikes. Mapping conducted in 2009 by Pure Nickel Inc. suggests that this large, differentiated magma chamber model may not be the correct interpretation of the morphology of the complex. Rankin (2005) proposed a different interpretation for emplacement. He considered the complex to represent multiple ultramafic sills emplaced in wet sedimentary rocks at high crustal levels, and subsequently intruded by later gabbro. Sills would have a primitive margin (dunite, high forsterite) and would grade inwards to more evolved compositions (wehrlite, lower forsterite; Figure 1-9B). He suggested that the individual ultramafic bodies were on the order of 10 to 250 m in thickness.

This is similar to the model for the deposits of Pechanga, on the Kola Peninsula of Russia. At Pechanga, ferropicritic magmas were emplaced as a swarm of sills, which intruded, and fed, comagmatic volcanic flows (Eckstrand and Hulbert, 2007). More than 226 discrete mafic-ultramafic intrusions have been identified at Pechanga, and 25 of these contain economic mineralization. The sills are 10 to 250 m thick and have strike lengths of 100 m to 6.5 km.
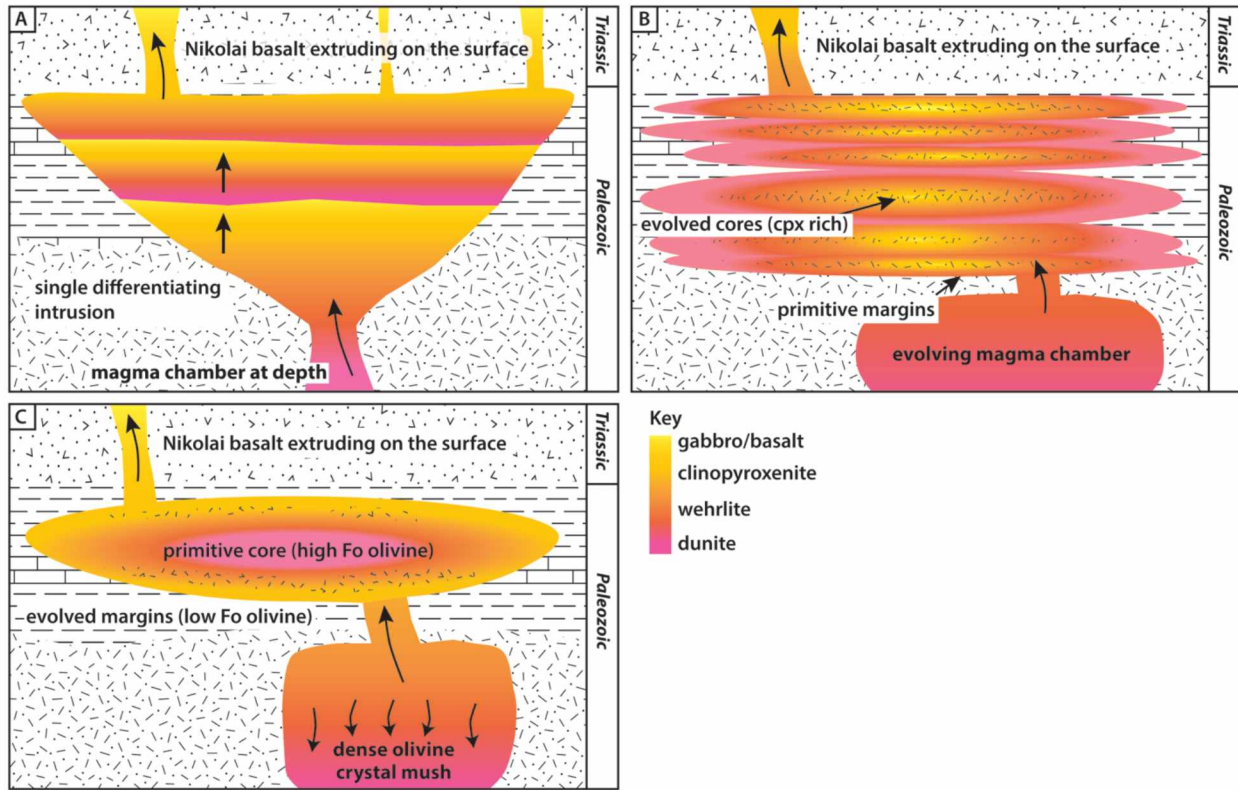
Figure 1-9. Schematic diagrams of the three potential models for emplacement of the Alpha complex: A) a differentiated mafic ultramafic intrusion, B) a multi-sill complex, and C) a single intrusion fed from a replenishing source.

A third possibility is that the Alpha complex is similar to the Quill Creek complex (Wellgreen) in the Yukon. The Quill Creek complex is interpreted to be a single large intrusion that was fed from a continuously replenishing source. The intrusion has an evolved (gabbroic) margin and a primitive (dunitic) core (Hulbert and Stone, 2006). A continuously replenishing magma source from a deep magma chamber is essential to forming this type of complex. As the deep magma chamber was evolving, dense olivine crystal mush would settle to the bottom of the chamber and the more evolved (less dense) magma would rise to the top of the chamber. The first thing to intrude into the crust would be the evolved magma from the top of the chamber so that the margin of the sill would be more evolved. As magma was continuously intruded through the sill, the last melt to intrude would be primitive olivine from the base of the magma chamber. Thus, early melt forms a chilled gabbroic margin and layers become progressively more primitive towards the center of the intrusion (Figure 1-9C). If an immiscible sulfide liquid formed, this would settle through the less dense silicate melt and crystallize at the base of the intrusion.

The Alpha complex thus represents an attractive target for magmatic Ni-Cu-PGE exploration. However, designing an appropriate exploration strategy requires a better understanding of the

16

morphology of the complex. The principal questions that need to be answered here are whether the processes of sulfide saturation, immiscibility, and metal partitioning occurred with enough efficiency to produce a large volume of metal-enriched sulfide melt, and if so, where that sulfide melt was subsequently deposited.

1.4. Exploration history

The region surrounding the Alpha complex (Figure 1-2) has been of interest to geologists since the early twentieth century when early placer gold miners were panning Broxson Gulch and Rainy Creek. Prospecting discovered a number of copper showings; however, no substantial work was conducted until the early 1960's when Newmont trenched the Emerick and Canwell Ni-Cu-PGE showings. The State of Alaska Department of Natural Resources conducted general prospecting and mapping of the area, as well as an airborne magnetic survey between 1963 and 1977. J.H. Stout and others of the Alaska Division of Geological and Geophysical Surveys (DGGS) completed geologic mapping of the region at a 1:63,360 scale in 1976. In 1978 and 1979, W.J. Nokleberg and others of the U.S. Geological Survey (USGS) remapped the geology of the area at a scale of 1: 63,360 and reduced this mapping to a 1: 250,000 scale. USGS followed up with an Alaska Mineral Resources Assessment Program (AMRAP) geologic study of the Mt. Hayes quadrangle that took place between 1980 and 1983.

Interest in the property peaked again in 1989, when Cominco Alaska Exploration acquired the property. Between 1991 and 2004, the property was explored by an additional five companies: North East Mining Ltd., Falconbridge Exploration USA, American Copper and Nickel Company/Inco, Nevada Star Resource Corp., and Anglo American Exploration (USA) Inc. Work conducted during this period included lithogeochemical sampling and prospecting, airborne magnetics/EM surveys, UTEM ground geophysics, borehole pulse EM, further geological mapping, and diamond core drilling. Drill core intervals yielded grades as high as 17.5 ppm Pt, 15.5 ppm Pd, 15.3 ppm Au, 15.36% Ni and 7.9% Cu.

Pure Nickel Inc. acquired the property in 2005. To date, Pure Nickel Inc. has drilled over 50 diamond drill holes, collected over a thousand soil samples, and conducted hundreds of kilometers of geophysical surveys. Partnered with ITOCHU Corporation of Japan from 2008-2013, approximately US$23.5 million was spent on exploration. Microprobe data is available for various samples of olivine, chromite, clinopyroxene, orthopyroxene, and amphibole spread out over the 30 km length of the complex. While there is a fairly large data set with which to work, the various analyses from across the field area do not reach the scale we need to comprehensively understand the petrogenesis of the complex.

Dr. Rainer Newberry, working with DGGS, completed a traverse through the central section of the complex in 2013 located just west of Fish Lake. No mapping was conducted but outcrops were located and identified and samples were collected from different lithologies to initiate this study.

1.5. Objectives

The main goals of this study are to evaluate the emplacement, crystallization, and mineralization history of the Alpha complex. The principal objectives that will be pursued to accomplish these goals will be to characterize the igneous layering in the intrusion in terms of the ultramafic sequence, sulfide mineralization, cryptic mineral variations, and changes in the bulk geochemistry. Specific questions to be addressed in this study include:

- How many stages of magma emplacement were involved in the formation of the Alpha complex? Is this one large intrusion or multiple small intrusions?
- To what extent did fractional crystallization produce the observed cumulate stratigraphy and cryptic mineral variation?
- What was the composition of the parental magma(s) of the Alpha complex?
- What was the history of sulfide saturation during the emplacement and crystallization of the complex?

Previous observations regarding the igneous stratigraphy of the Alpha complex do not adequately explain many aspects of the mineralization and crystallization patterns observed in the study area. Detailed analysis of the mineralogical variations within the ultramafic rocks and of the crosscutting relationships between the two gabbro series and the ultramafic layering will help to determine the timing of emplacement and origination of the ultramafic rocks.

1.6. Methods

I have used several methods of study to accomplish the goals and objectives listed above. I conducted field mapping of the igneous layering in the Alpha complex to study the ultramafic stratigraphy macroscopically. I conducted petrographic studies in transmitted light in order to discern changes in mineralogy, textures, and alteration across the complex. I conducted WDS electron microprobe analyses to measure minor and trace elements in olivine, clinopyroxene, and spinel in order to characterize cryptic changes in the silicate mineralogy. I utilized whole rock XRF analyses to evaluate the geochemical evolution of the magma during crystallization. Finally, geochemical data for chalcophile elements and sulfur allowed for evaluation of the history of sulfide saturation and mineralization in the complex.

1.6.1. Detailed field mapping

Detailed mapping of the Alpha complex was completed at a 1:10,000 scale over a six-day period in August 2015. Rock stations were taken where changes in lithology occurred and contacts and faults were mapped in detail whenever possible. Samples were also collected at 10 m intervals cutting perpendicular to the ultramafic layering in sections of the complex that had abundant outcrop. Stations were recorded in the field using a Juno T41 C Trimble handheld computer that was loaded with ESRI's ArcGIS® mobile version 10.3.1. The GPS location in the WGS84 UTM coordinate system of each station was recorded along with lithologic attributes (modal mineralogy, mineral habits, grain size, and magnetic susceptibility) and other features of interest in a rock station layer. Structural attributes (igneous layering, foliation and geological contacts) were collected in a separate structure station layer. A total of 103 stations were collected in order to obtain the most detailed understanding of the petrological subdivisions present in the complex.

Field data were compiled using ESRI's ArcGIS® version 10.3.1. Rock stations and structure stations were loaded into a map project assigned to a WGS84 UTM base. Map units and contacts were interpreted from rock stations and structure data and compiled into polygon and line layers, respectively. Units were assigned for each polygon and colors added to signify each map unit.

1.6.2. Petrographic study

A total of 101 thin sections were described using transmitted and reflected light for this study. Of the 101 thin sections, 14 were collected from 5 drill holes and the rest were collected during field mapping. The features described in the study include bulk rock texture, grain size, mineral habit, mineral mode, and alteration. Modal percentages of minerals were visually estimated and normalized and modal rock types were determined using the IUGS ultramafic classification scheme.

1.6.3. Mineral chemical analysis

I utilized three different sample sets for this study. Dr. Newberry collected a set of 21 samples in the summer of 2013 along a north-south transect across the Alpha complex for early sample analysis. These samples were made into polished thin sections in 2014. An additional 14 samples were selected from drill core and made into polished thin sections in 2014. Sixty-six supplementary samples were collected in the summer of 2015 during field mapping and made into polished thin sections.

Prior to carbon coating, all thin sections were ultrasonically cleaned to remove any residual compounds. I used a carbon coat of 250-300 Å thickness on all specimens. Quantitative routines were developed for analysis of olivine, clinopyroxene, and chromite using a wavelength-dispersive spectrometer on a JEOL JXA-8530F electron microprobe in the Advanced Instruments Laboratory at the

University of Alaska Fairbanks and natural mineral standards. Estimated error for each element analyzed for a given mineral are given in Table 1-1.

Table 1-1. Estimated error for electron microprobe analyses in wt.%.

Mineral	SiO$_2$	Al$_2$O$_3$	FeO	MnO	MgO	CaO	Na$_2$O	NiO	TiO$_2$	Cr$_2$O$_3$
Olivine	±0.08		±0.05	±0.005	±0.1			±0.0035		
Clinopyroxene	±0.5	±0.015	±0.045	±0.015	±0.1	±0.04	±0.02		±0.01	
Spinel		±0.15	±0.1	±0.05	±0.08				±0.01	±0.2

Olivine

Major (Fe, Mg, Si) and minor (Ni, Mn) elements were measured using five different spectrometers. Olivine has a very high melting temperature of about 1200 to 1900 degrees C at atmospheric pressure, thus sample degradation under the determined analytical conditions was not problematic for this routine. A higher voltage gives a greater yield of x-rays, so a beam current of 25 nA at 20 KeV and a diameter of 10 microns was applied. Three to four olivine grains were selected from each thin section. Each grain was analyzed at least six times: three times on the core and three times at the rim. Ni was measured on spectrometers one and two using the LIFL crystal. Mn and Fe were both measured on spectrometer three using the LIFL crystal. Mg and Si were measured on spectrometers four and five, respectively, using the PETL crystal. The analytical precision of microprobe analyses improves with increased counting time, so elements requiring the highest level of precision were given longer count times. For Ni, Mg and Si, count times of 60 seconds on peak and 20 seconds on background were applied. A peak count time of 15 seconds was applied to Fe with the background measured for 6 seconds. Mn had peak and background count times of 40 and 10 seconds, respectively.

Four different compositions of olivine standards were available for use and five standard analyses were made on each of the reference standards. The fayalite standard was used as a reference standard for analysis of Fe and Mn. Olivine with a published composition of 0.29 wt.% Ni was used as the reference standard for analysis of Ni. A different olivine standard was used for Mg and Si. PHA bias scans were performed on stainless steel for Ni and on the respective standards for Fe, Mg, Mn, and Si in order to account for changes in their peak heights. Wavelength scans were performed on all of the standards in order to check for the presence of any interfering elements.

Clinopyroxene

Nine elements were measured in clinopyroxene: Mg, Mn, Cr, Na, Al, Ca, Si, Fe, and Ti. An accelerating beam of 20 keV was used with a beam current of 25 nA and a diameter of 5 microns. Three to four grains were chosen in a given thin section and roughly eight or more analyses were made on each

grain depending on the size of the grain. All clinopyroxene in the Alpha complex exhibits some amount of orthopyroxene exsolution. Exsolution lamellae were avoided when choosing spots for analysis. Fe and Mn were analyzed on spectrometer one using the LIFL crystal. Ca and Ti were measured on spectrometer two using the PETL crystal. Cr was analyzed on spectrometer three using the LIFL crystal. Si and Al were measured on spectrometer four using the TAPL crystal. Na and Mg were analyzed on spectrometer 5 using the TAPL crystal. Fe and Mg were analyzed for 50 seconds on peak and for 30 seconds on background. Cr was analyzed for 75 seconds on peak and 50 seconds on background. Ca and Ti were analyzed for 30 seconds on peak and 20 and 24 seconds on background, respectively. Si was analyzed on peak for 40 seconds and for 30 seconds on background. Al was analyzed on peak for 20 seconds, Na was analyzed on peak for 10 seconds, and Mn was analyzed for 15 seconds on peak. Al, Na, and Mn were all analyzed on background for 10 seconds.

Multiple clinopyroxene standards were available for use. Five standard analyses were made on each of the reference standards. The augite standard (204) was used as a reference standard for analysis of Al, Fe, Si, Ca, and Ti. Omphacite (226) was used for analysis of Na. Hypersthene (220) was used for Cr, Mn, and Mg. A second augite standard was used as a secondary standard. PHA bias scans were performed on the respective standards in order to account for changes in their peak heights. Wavelength scans were performed on all of the standards in order to check for the presence of any interfering elements.

Chromite

Major (Fe, Cr) and minor (Mg, Mn, Al, Ti) elements were measured using five different spectrometers. An accelerating beam of 15 keV was used to reach the excitation energy of Fe with a beam current of 20 nA and a diameter of 3 microns. Five to ten chromite grains were selected from each thin section. Each grain was analyzed two to five times near the core of the grain. The rims were avoided because they are more likely to have been altered at sub-solidus conditions. Fe and Mn were measured on spectrometer one using the LIFL crystal. Cr and Ti were measured on spectrometers two and three, respectively, using the PETL crystal. Mg and Al were measured on spectrometers four and five using the TAPL crystal. For Cr, Ti, Mg and Al, count times of 50 seconds on peak and 40 seconds on background were applied. A peak count time of 30 seconds was applied to Fe with the background measured for 20 seconds. Mn had peak and background count times of 15 and 10 seconds, respectively. The relative amounts of Fe_2O_3 and FeO were determined using stoichiometry and charge balance.

I employed five standards: two different chromite standards, one spinel, one magnetite, and one ilmenite. Five standard analyses were made on each of the reference standards. The chromite standard was used as a reference standard for analysis of Cr. Magnetite was used for analysis of Fe, ilmenite was used for Ti and Mn, and spinel was used for Mg and Al. The remaining chromite standard was used as a

secondary standard. PHA bias scans were performed on the respective standards in order to account for changes in their peak heights. Wavelength scans were performed on all of the standards in order to check for the presence of any interfering elements.

Elemental maps were also made for some grains to examine intra-grain compositional variations. Maps were made for Fe (spec 1), Cr (spec 2), Ti (spec 3), Mg (spec 4), and Al (spec 5), to account for each spectrometer. Beam conditions of 20 keV and 20 nA were used in stage scan mode. A pixel size of 0.5 x 0.5 microns and a dwell time of 30 ms were used in order to get the appropriate level of definition in the map images.

1.6.4. Whole rock XRF analysis

Ninety-six samples collected in the field were chosen for whole rock XRF analysis. Samples were cut into approximately 37 mm diameter circular slabs. These were polished on an Ameritool polishing wheel at 60, 180, and 280 grit for 2 minutes each. Samples were then analyzed using a PANalytical Axios XRF unit for a variety of major and trace elements (SiO_2, Al_2O_3, FeO, MnO, MgO, CaO, Na_2O, K_2O, TiO_2, P_2O_5, BaO, S, Cr, Cu, Ga, Nb, Ni, Pb, Rb, Sr, V, Y, Zn, and Zr). The analysis routine utilized international press pellet standards as well as rock slab standards from the DGGS (9 samples) that had been commercially analyzed by 4 acid digestion, ICP-MS, and XRF. Beta and line overlap coefficients in the routine were calculated using SuperQ as appropriate.

1.6.5. Major-Trace-REE-PGE analyses

ALS Minerals prepared and analyzed REE, PGE, and major and trace elements for 19 samples of different lithologies within the complex, including 5 composite rock samples (15LL201-205). The composite samples were created by combining three to five different samples from a single unit within the complex. These samples then represent the average values for the area from which they were taken.

Rock samples were processed by ALS Minerals using their PREP-31 package. The samples were crushed to better than 70 percent passing 2 mm, and a 250 g split was pulverized to better than 85 percent passing 75 microns. Prior to crushing, samples for whole-rock analysis were trimmed by DGGS staff to remove weathering, and cut surfaces were sanded to remove any saw metal.

Samples were analyzed for a variety of suites of major and trace elements depending on the sample type. In addition to ALS Minerals' accredited (ISO/IEC 17025–2005) internal quality-control program, DGGS monitored analysis quality with one standard reference material per batch of 20 analyses.

For whole-rock geochemistry samples, major and minor oxides were analyzed by lithium metaborate fusion digestion and ICP-AES (ALS Minerals method ME-ICP06). Trace elements, including rare-earth elements, were determined using lithium metaborate fusion digestion and ICP-MS (ALS

Minerals method ME-MS81). Ag, Cd, Co, Cu, Li, Mo, Ni, Pb, Sc, and Zn were determined by four-acid digestion and ICP-AES (ALS Minerals method ME-4ACD81); and As, Bi, Hg, In, Re, Sb, Se, Te, and Tl were determined by aqua regia digestion followed by ICP-MS (ALS Minerals method ME-MS42). Total C and S were analyzed by LECO furnace (ALS Minerals methods C-IR07 and S-IR08, respectively).

Chapter 2 Results

2.1. Geology and major element compositions

The following results were garnered from field mapping and petrographic study. The map units will be described in the following section on the basis of the petrographic study and XRF analysis.

Previous bedrock mapping by Pure Nickel Inc. interpreted the Alpha complex to have five subparallel layers of wehrlite surrounded by dunite with crosscutting gabbroic dikes (Figure 1-6). Field mapping was undertaken to determine how accurately this map describes the geology and as the basis for detailed sampling. My map (Figure 2-1) shows four major subparallel layers of wehrlite striking roughly east west. The three major mafic and ultramafic lithologies identified in the field were dunite, wehrlite, and gabbro. I identified multiple gabbroic dikes, which crosscut the mineral layering in some areas at moderate angles and variably display chilled margins. XRF analyses show that the margins of these dikes are more mafic and that both the high-Ti and low-Ti varieties of gabbro are present (see ahead, section 2.1.2.5.). XRF analyses of the ultramafic samples identified an elongate body in the north-central portion of the complex that is different than the other ultramafic rocks by having higher Al_2O_3 contents (Figure 2-1; Figure 3-3). Rocks in this body also contain visible, but very altered, plagioclase (see ahead, section 2.1.2.1.). I mapped serpentinization as intense, moderate, or weak, based in part on increase of magnetic susceptibility with increasing serpentinization. In general, serpentinization increases to the north, with proximity to the N-bounding fault (Figure 2-1). Mineral layering dips to the south: the northern edge of the complex is the base of the body (Figure 2-2) and the southern edge constitutes the top.
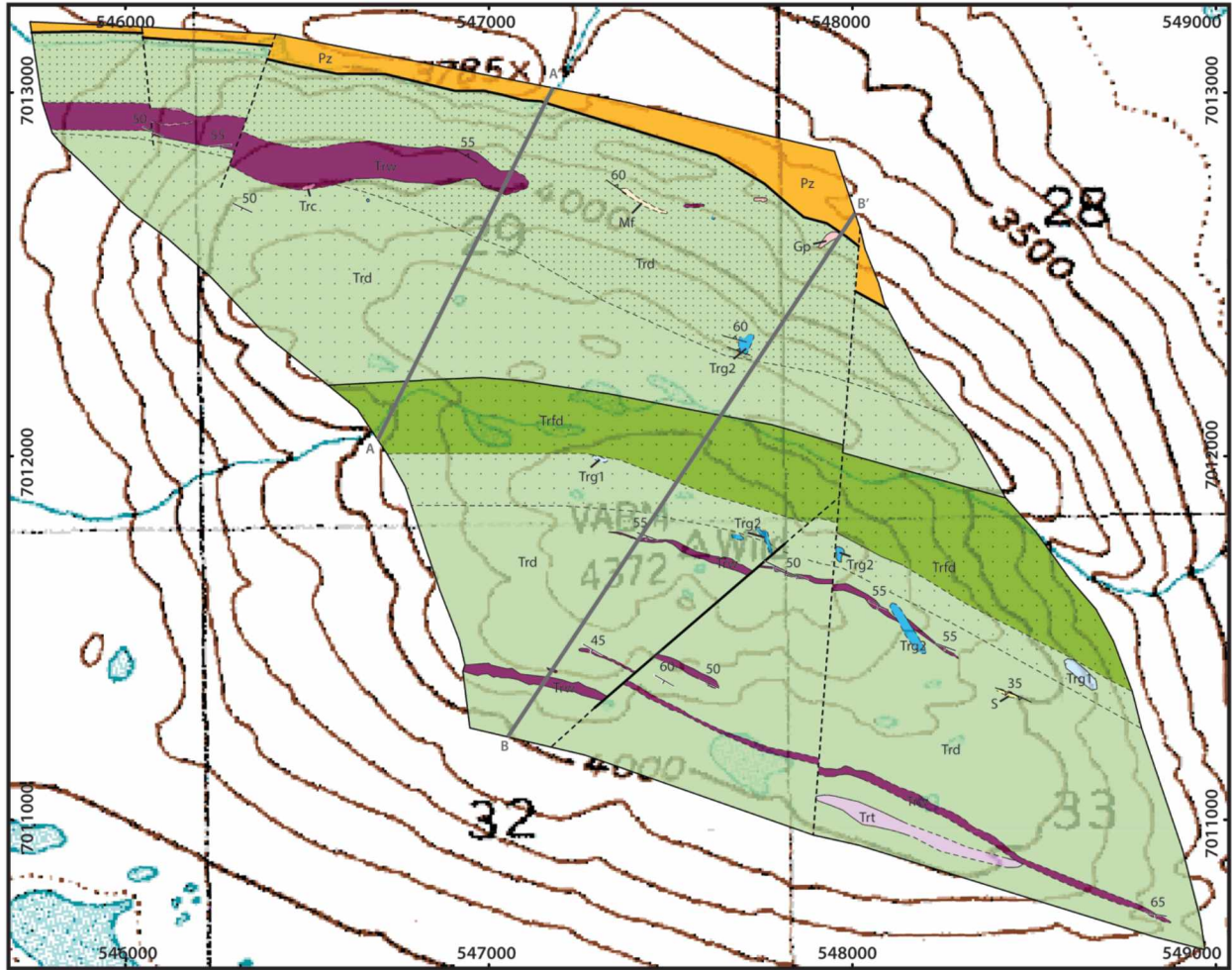
GEOLOGIC MAP OF THE ALPHA COMPLEX

Map Units

Gp	Granodiorite porphyry
Mf	Metafelsite
S	Schist

Triassic Nikolai gabbro

Trg2	High-TiO$_2$ gabbro
Trg1	Low-TiO$_2$ gabbro

Triassic ultramafic rocks

Trt	Troctolite
Trc	Clinopyroxenite
Trg	Wehrlite
Trfd	Feldspathic dunite
Trd	Dunite

Paleozoic rocks

Pz	Paleozoic undivided

Alteration

	Variably serpentinized dunite
	Serpentinite

Map Symbols

Geologic contact
Inferred contact
Igneous mineral layering (40)
Foliation (56)
Fault
Inferred fault
Cross section line

North

0   125   250   500   Meters

Figure 2-1. Bedrock geologic map of the central portion of the Alpha complex.

26
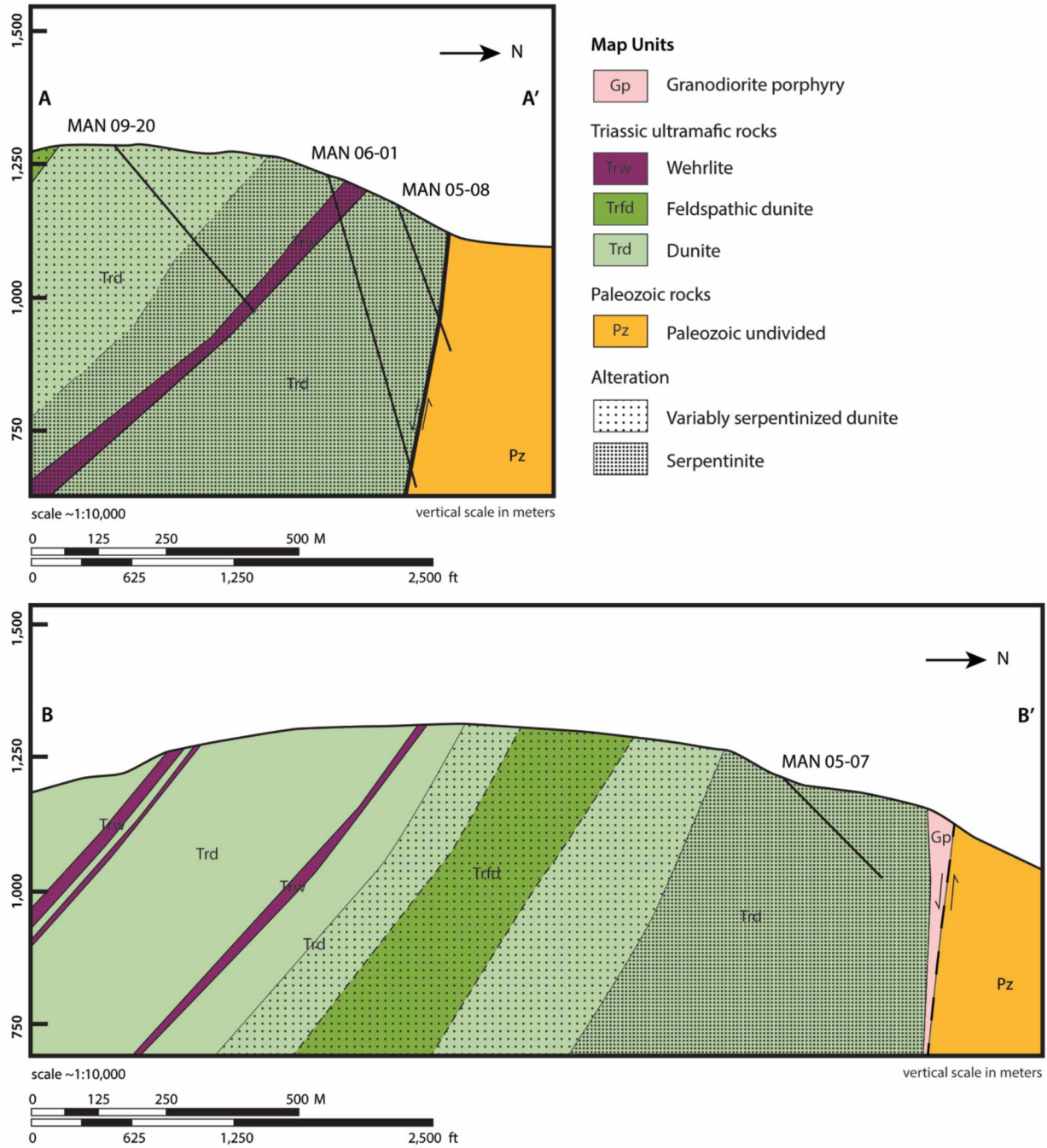
Figure 2-2. Cross sections A-A' (above) and B-B' (below) showing the contact relationships between the ultramafic layering (and their degree of serpentinization) and the Paleozoic rocks at the base of the complex. Two drill holes define the orientation of the basal fault.

27

2.1.1. Geologic overview from field observations

2.1.1.1. Dunite

Dunite in the complex is medium grained (1-5 mm), non-foliated, with less than 10% pyroxene. Dunite is best exposed in the north central and in the southern part of the complex but smaller outcrops are scattered throughout the map area. Outcrops of dunite range from small outcroppings a few centimeters high to larger, continuous outcroppings 2-3 meters high. Contacts between the dunite and wehrlite are generally sharp (Figure 2-3C,D) and can be traced for up to 500 m in some areas.

At the northern edge of the complex, dunite has been fully serpentinized and there are no remnant olivine grains. Magnetic susceptibilities are high, ranging from 50-100 x 10^{-3} SI [Système International], due to the presence of magnetite produced during serpentinization. In the central portion of the complex there is some serpentinization of the dunite, but olivine grains are visible. Magnetic susceptibilities in this area are 10-70 x 10^{-3} SI. In the southern portion of the complex the dunite is fresh and exhibits almost no alteration. This dunite has magnetic susceptibilities of less than 5 x 10^{-3} SI.

2.1.1.2. Wehrlite

Wehrlite is a medium to coarse grained (0.5-30 mm), non-foliated rock, with clinopyroxene oikocrysts up to 3 cm in diameter (Figure 2-3A). Wehrlite contains 10-80% clinopyroxene. The unit is best exposed near the northwest and south edges of the complex (Figure 2-1). Wehrlite is always surrounded by dunite or serpentinite. Wehrlite layers in the upper (southern) portion of the complex are approximately 10-30 m thick, with 0.3-1 cm clinopyroxene oikocrysts (Figure 2-3A). The wehrlite layer in the lower (northern) part of the complex is up to 115 m thick and contains 1-3 cm clinopyroxene oikocrysts. The largest outcrops occur as 3-4 m high ledges on the hillside and as discrete outcrops on flatter ground. Smaller outcrops are typically 50 cm high.
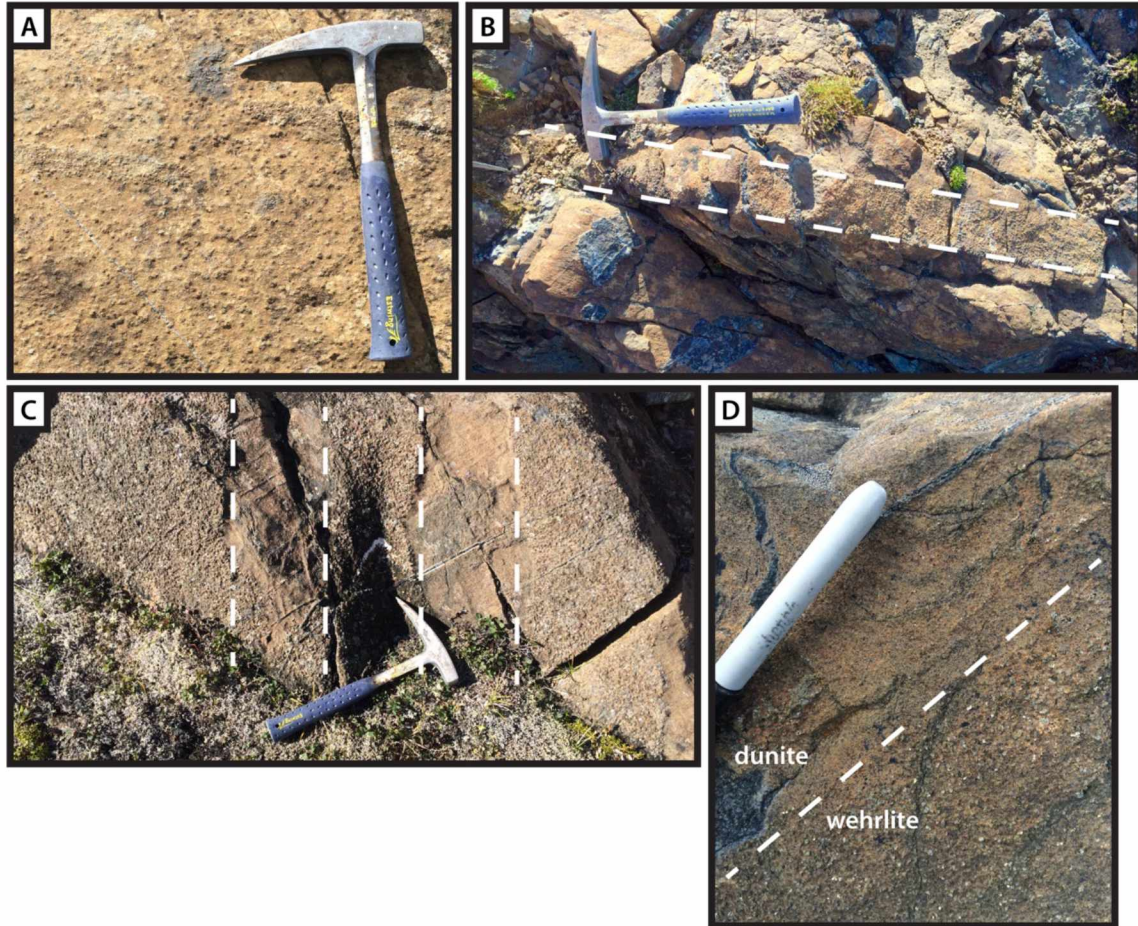
Figure 2-3. Outcrop photos of: A) wehrlite with visible clinopyroxene oikocrysts; B) a clinopyroxenite band surrounded by wehrlite; C) alternating layers of wehrlite and dunite; and D) a sharp contact between wehrlite and dunite.

2.1.1.3. Clinopyroxenite

Clinopyroxenite is a medium to coarse grained (1-12 mm) and non-foliated rock with greater than 90% clinopyroxene. Clinopyroxenite layers variably occur within and along the edges of the wehrlite layers. In the upper portion clinopyroxenite layers are generally less than 10 cm thick and can be traced along strike for only a few meters (Figure 2-3B). The largest clinopyroxenite layer I found, within the thick wehrlite layer at the base of the complex (Figure 2-1), is approximately 10 m wide and 40 m long. Clinopyroxenite layers have sharp contacts with wehrlite where contacts are visible. Mineral layering can be measured from these contacts, with a consistent strike of 110-120° and dip of 45-55°.

2.1.1.4. Troctolite

The southern part of the complex contains a troctolite layer: medium to coarse grained (1-25 mm) and non-foliated with visible clinopyroxene and plagioclase oikocrysts. The largest oikocrysts are ~1 cm

across. The troctolite forms a single layer about 600 m long and 40 m wide (Figure 2-1). It contacts a wehrlite layer along the eastern edge; the western edge of the intrusion is surrounded by dunite and abutted by a fault. The largest outcrop is on the eastern edge as a 3-4 m high ledge on the side of a steep hill. The western edge is comprised of small, scattered outcrops. Disseminated sulfide grains were visible in outcrop.

2.1.1.5. Gabbro

Gabbroic dikes across the complex are fine to medium grained (0.5-4 mm) and usually non-foliated; there was only one foliated outcrop. The non-foliated gabbro occurs in small, two meter or less high outcrops. In at least one outcrop, the gabbro clearly cuts across ultramafic layering. One foliated gabbro outcrop (surrounded by serpentinite) occurs in the basal portion of the complex. This outcrop is over 6 m high and has identifiable leucocratic and melanocratic gabbroic phases. The foliation dips to the north at 30-55° and strikes 285-290°.

2.1.1.6. Schist

Cordierite biotite schist was identified in one outcrop and in another area along strike as subcrop. Schist is fine to medium grained (0.25-2 mm) with cordierite porphyroblasts up to 2 mm in diameter. Schistosity strikes 110-115° and dips south at 30-35°.

2.1.1.7. Granodiorite porphyry

Granodiorite porphyry was identified in two small outcrops in the northeast corner of the map area, near the contact with Paleozoic rocks. The porphyry is composed of approximately 85% aphanitic groundmass and 15% phenocrysts. Phenocrysts are medium to coarse grained (1-4 mm) euhedral plagioclase and biotite.

2.1.1.8. Structural relationships

The contact between the serpentinite at the base of the complex and Paleozoic rocks is a steeply dipping (~80° S) fault (Figure 2-1, Figure 2-2, Figure 2-4). The original intrusive base of the complex is not exposed either on the surface or in drill core (Figure 2-2). Given its geometry, it must have normal displacement. The granodiorite porphyry body is present close to the inferred fault, and might have intruded along the fault (Figure 2-2, below).

Four faults with apparent strike-slip displacement cut through the complex; they strike approximately perpendicular to mineral layering. Two small faults cut the basal wehrlite layer. The other two faults are present near the eastern margin of the map area (Figure 2-1). Based in part on aeromagnetic

data, the easternmost fault cuts the fault contact with Paleozoic rocks in the north and can be traced continuously to the south edge.
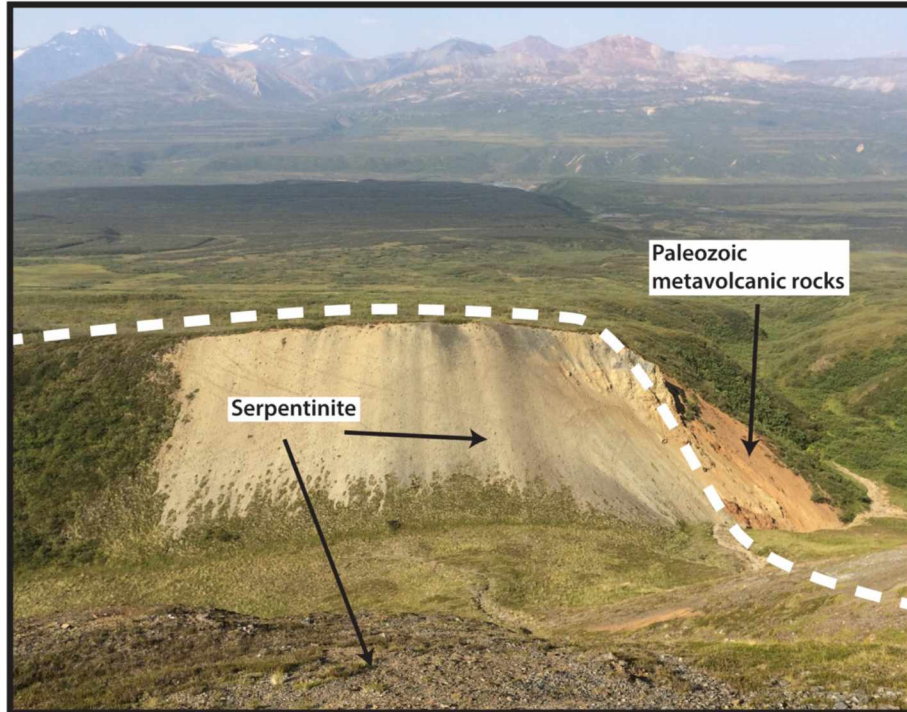
Figure 2-4. Field photo of the contact between the serpentinite and the Paleozoic rocks at the base of the Alpha complex.

2.1.2. Lithostratigraphy determined from petrography of field samples and XRF analysis

XRF analysis of field samples helped to identify geochemical variations between ultramafic and mafic rocks that weren't apparent in the field. Three ultramafic units were determined based on major element composition, petrography, and field characteristics. The three major identifiable units are the upper ultramafic unit, the central feldspathic unit, and the basal ultramafic unit (Figure 2-5). The basal ultramafic unit is composed of a basal wehrlite and a basal dunite layer. Major and some trace element compositions are given in Appendices A and B. Petrographic descriptions of thin sections and sample locations are given in Appendix D.
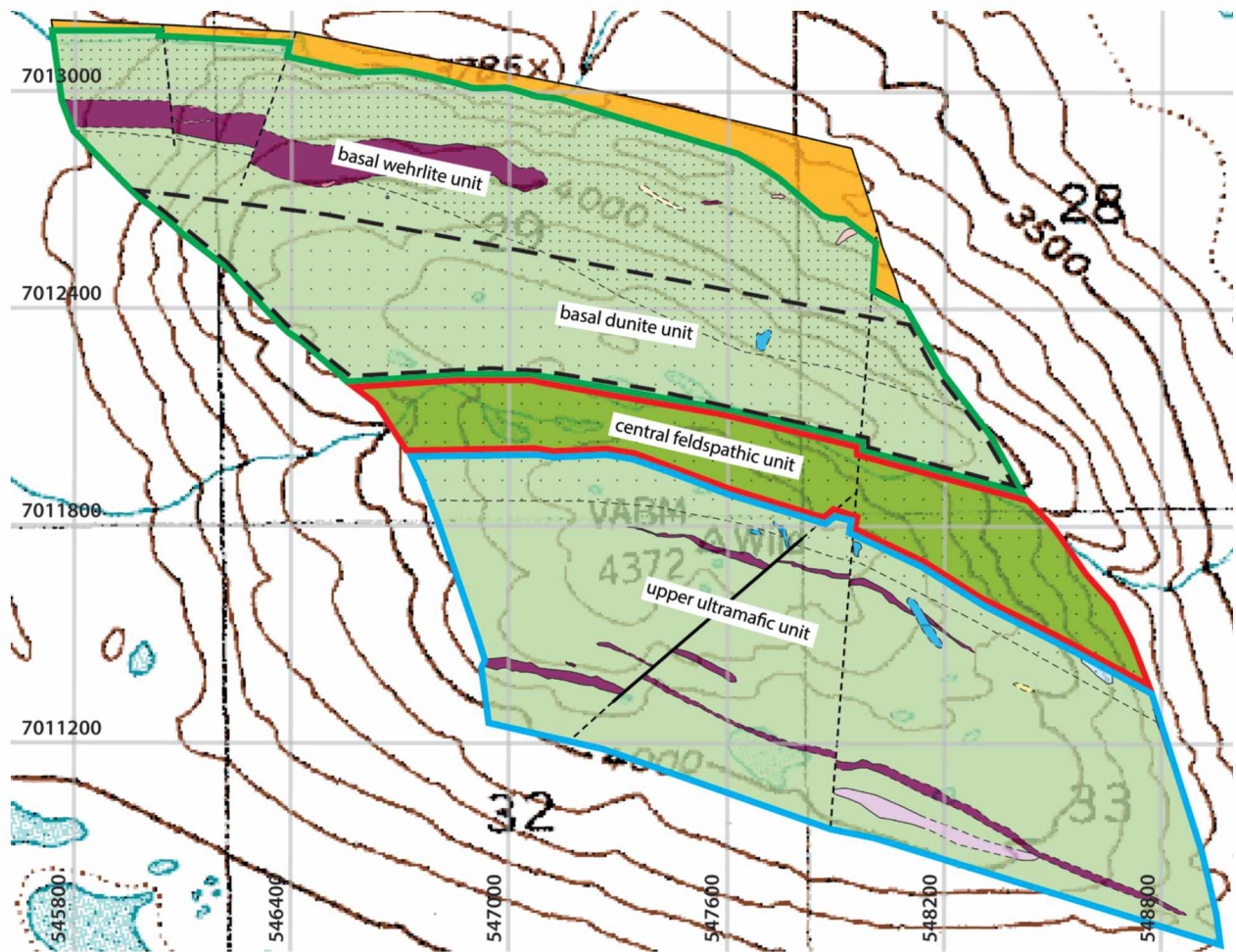
Figure 2-5. Geologic map showing the locations of the basal (green), central (red), and upper (blue) units referred to in the text. Legend for the map as in Figure 2-1.

2.1.2.1. Central feldspathic ultramafic unit

The feldspathic ultramafic unit is a sill-form body that extends for at least 2 km along strike and has an estimated thickness of approximately 200-220 m. The upper contact is with the upper wehrlite unit and the lower contact is with the basal dunite unit (Figure 2-5). The body is composed of feldspathic dunite along the margins that grades inward to troctolite at the center. Textures in this unit are somewhat heterogeneous and change from olivine orthocumulate along the marginal contacts inward to olivine and plagioclase adcumulate (Figure 2-6). Throughout the unit, plagioclase has been completely altered to sericite. Olivine is moderately altered to serpentine and clinopyroxene displays a small amount of orthopyroxene exsolution.

Dunite along the margins is an olivine cumulate with fine-grained, interstitial, postcumulate plagioclase (Figure 2-6A). Cumulate olivine is medium- to coarse-grained and subhedral to euhedral. Wehrlite closer to the center of the unit is an olivine cumulate with intercumulus plagioclase and

32

clinopyroxene. One sample at the center of the unit is troctolite; it contains cumulate olivine with minor cumulate clinopyroxene and orthopyroxene and interstitial (completely altered) plagioclase (Figure 2-6B). Pyroxene is medium- to coarse-grained (1-7 mm) and granular to subpoikilitic; the plagioclase was apparently fine grained (<1 mm) and interstitial. (Original textures are problematic given its extensive alteration.) Clinopyroxene and orthopyroxene become more abundant towards the center of the sill. Normative plagioclase ranges from 2.2% in the dunite to 15% in the troctolite. Normative clinopyroxene ranges from 30% in the wehrlite to 9% in the troctolite. The normative mineralogy of the troctolitic core has equal abundances of clinopyroxene and orthopyroxene (~12 wt.%), plagioclase (15 wt.%), olivine (57 wt.%), and spinel (5 wt.%). The troctolite is composed of medium-grained euhedral olivine with poikilitic plagioclase and pyroxene.

This unit has significantly higher Al_2O_3 content (1.34-3.9 wt.%) than the other ultramafic rocks (Table A-1). Ni contents are 1187-2650 ppm but don't follow a simple pattern across the body. Rock TiO_2 concentrations are low (<0.16 wt.%) throughout the unit. Magnetic susceptibilities are high, 20 to 90 x 10^{-3} SI. The unit is variably bounded by low-Ti gabbro along the upper edge.
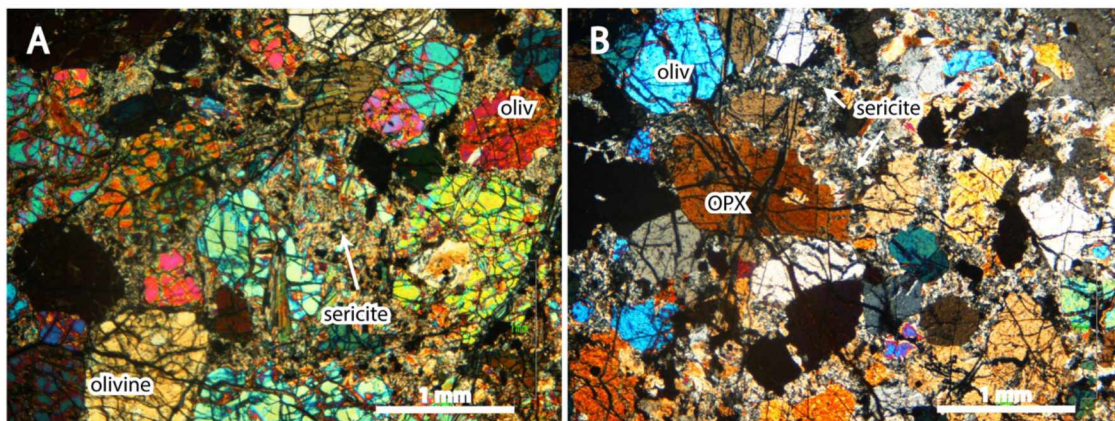
Figure 2-6. Cross polarized light photomicrographs of feldspathic ultramafic rocks showing: A) plagioclase dunite with olivine surrounded by plagioclase that has been completely altered to sericite and B) troctolite with olivine, orthopyroxene, and sericite (after plagioclase).

2.1.2.2. Upper ultramafic unit

The upper ultramafic unit consists of three thin wehrlite layers and a troctolite layer, which are surrounded by dunite and cut by high-Ti gabbro in multiple areas. This unit makes up the southernmost 950 m of the map area. The base of the unit is the contact with the feldspathic ultramafic unit. The upper contact of the unit is covered. The most abundant rock type is unserpentinized dunite, but several wehrlite (with rare clinopyroxenite) layers are present (Figure 2-5). Magnetic susceptibilities are the lowest in the

map area: 2-15 x 10^{-3} SI. Contacts between troctolite, clinopyroxenite, wehrlite, and dunite are sharp and visible in outcrop.

Mineral textures are predominately mesocumulate to adcumulate. Cumulate olivine is medium- to coarse-grained, granular, and subhedral to euhedral (Figure 2-7A). Clinopyroxene habit ranges from granular to poikilitic with 3-12 mm oikocrysts (Figure 2-7A,B). Plagioclase in the troctolite is medium-grained to very coarse-grained (>10 mm; Figure 2-7C,D). Olivine is mostly unaltered and clinopyroxene exhibits nearly pervasive orthopyroxene exsolution. Near the centers of wehrlite layers, clinopyroxene oikocrysts become coarser grained and contain more inclusions of olivine. Olivine grains included within clinopyroxene oikocrysts are more euhedral and finer grained than discrete olivine grains. Clinopyroxenite lenses in the unit are clinopyroxene-olivine adcumulates. Clinopyroxene is subhedral granular and no longer poikilitic. The upper wehrlite layers have somewhat coarser clinopyroxene oikocrysts than do layers lower in the unit.
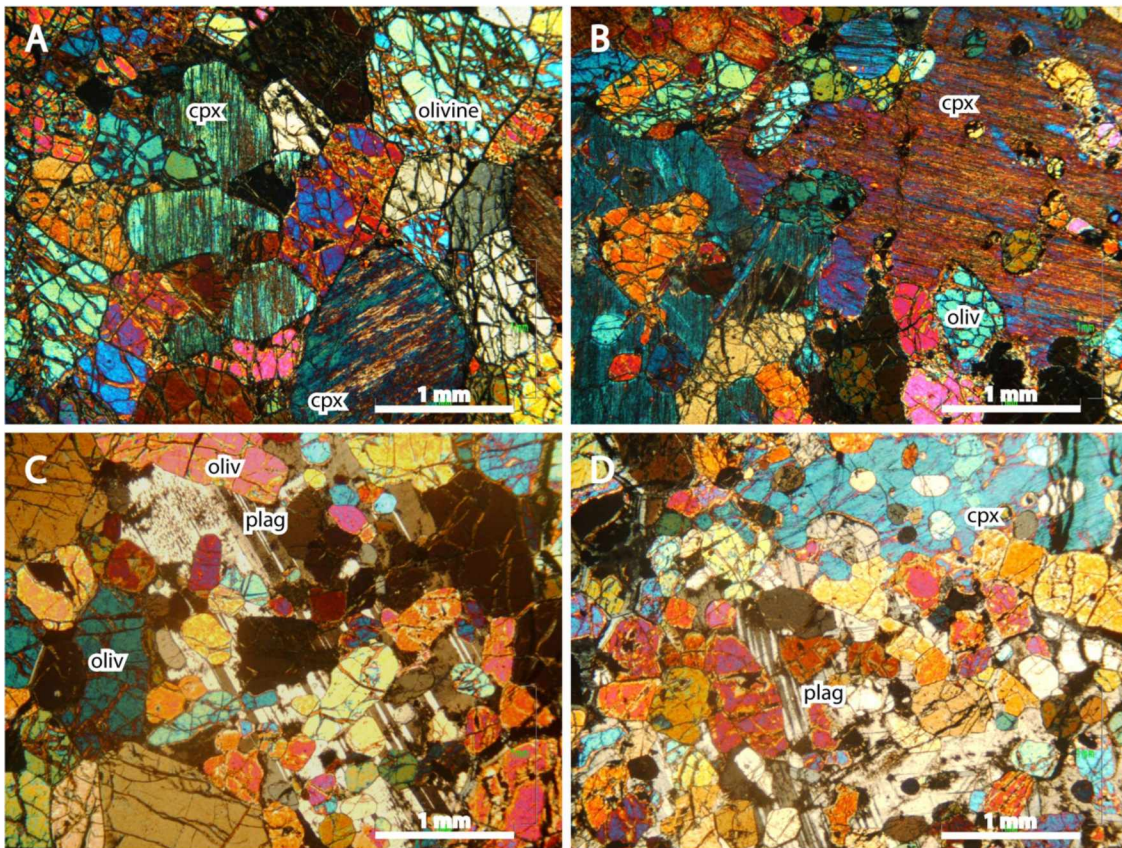
Figure 2-7. Cross polarized light photomicrographs of the upper ultramafic rocks showing wehrlite with A) weakly serpentinized olivine (oliv) with granular clinopyroxene (cpx), and B) poikilitic clinopyroxene with exsolution lamellae of orthopyroxene; and troctolite with C) poikilitic plagioclase (plag) with inclusions of olivine, and D) poikilitic clinopyroxene and plagioclase.

Rock Ni concentrations are 1000-1900 ppm in dunite and wehrlite (Table A-2), with no areas displaying significant depletion. Dunite and wehrlite contain 20-450 ppm Cu. One sample from the western troctolite has visible sulfide grains and contains 580 ppm Cu. The three remaining troctolite samples have low (45-70 ppm) Cu. Wehrlite and dunite contain <0.17 wt.% TiO_2; clinopyroxenite contains higher (0.3-0.4 wt.%) TiO_2 due to significant Ti in clinopyroxene (see ahead).

2.1.2.3. Basal dunite unit

The basal dunite unit is approximately 450 m thick, and immediately underlies the feldspathic ultramafic unit (Figure 2-5). This unit is composed of relatively homogeneous dunite with medium grained olivine and rare clinopyroxene (Figure 2-8B). Mineral textures are adcumulate throughout, with very rare intercumulate minerals. Olivine is euhedral to subhedral, granular, and moderately serpentinized. Clinopyroxene abundance increases slightly (up to ~5 wt.%) towards the center of the body, where it is present as medium grained clinopyroxene oikocrysts (Figure 2-8A). Clinopyroxene contains pervasive orthopyroxene exsolution. Magnetic susceptibilities in this unit are 15-30 x 10^{-3} SI. The top of the unit is in contact with the feldspathic ultramafic unit and the bottom is in contact with the basal wehrlite unit.

Rocks from this unit contain 600-2100 ppm Ni (Table A-3). Ni concentrations are highest along the margins of the unit and systematically decrease towards the center. Cu concentrations are 45-450 ppm. TiO_2 contents are low (<0.12 wt.%) throughout the unit.
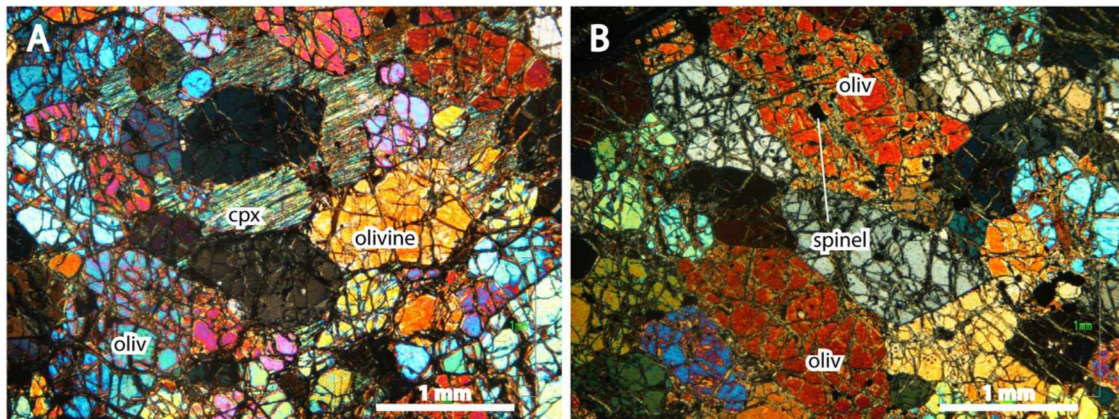
Figure 2-8. Cross polarized light photomicrographs of moderately altered olivine in the basal dunite unit with: A) ~2 mm diameter clinopyroxene (cpx) oikocrysts and B) spinel inclusions in olivine (oliv).

2.1.2.4. Basal wehrlite unit

The basal wehrlite unit makes up the lowest 300 m of the complex. It lies below the basal dunite unit and sits above Paleozoic rocks. Between the basal wehrlite and the northern boundary fault (Figure

2-5) is a complex and poorly-exposed zone dominated by serpentinite but containing a variety of sheared rock types. Serpentinite lies both immediately above and below basal wehrlite; the lower contact in particular might be a shear or fault zone. This unit contains 7-12 m thick clinopyroxenite layers within and near its edges. This wehrlite layer is significantly thicker than any other in the study area (Figure 2-5).

Mineral textures are mesocumulate to adcumulate throughout, with very little intercumulus material (Figure 2-9A). Clinopyroxene and olivine are both predominately granular and anhedral to subhedral, with very minor poikilitic clinopyroxene near the center of the unit. Clinopyroxene invariably contains orthopyroxene exsolution lamellae (Figure 2-9B). Olivine in wehrlite is moderately altered to serpentine. The serpentinite along the northern margin has no remnant olivine grains and abundant magnetite veinlets (<0.5 mm wide), giving these rocks a high magnetic susceptibility (50-100 x 10^{-3} SI). Dunite along the southern margin is less serpentinized and contains remnant olivine grains.

Rocks from the basal wehrlite unit contain 140-3500 ppm Ni (Table A-4). Ni is predominately in olivine, so clinopyroxene-rich rocks contain the least Ni. The rocks contain 50 to 375 ppm Cu. The unit also contains the highest (0.11-0.58 wt.%) TiO_2 concentrations, significantly higher than the upper ultramafic rocks.
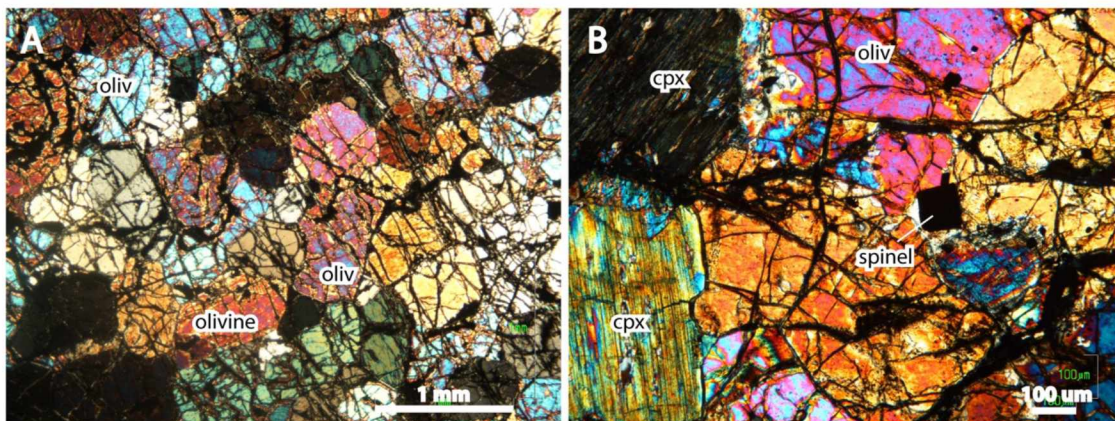
Figure 2-9. Cross polarized light photomicrographs of rocks from the basal wehrlite unit with: A) dunite with adcumulate olivine (oliv) with sutured grain boundaries and no interstitial minerals and B) wehrlite with clinopyroxene (cpx) that contains pervasive exsolution lamellae of orthopyroxene and interstitial, euhedral spinel.

2.1.2.5. Gabbroic dikes

Both high-Ti gabbro and low-Ti gabbro were sampled in the map area. High-Ti gabbro contains 1.5-2.2 wt.% TiO_2 whereas low-Ti gabbro contains 0.16-0.35 wt.% TiO_2 (Table A-5). The margins of gabbroic dikes that were sampled have higher wt.% MgO and lower SiO_2, Al_2O_3, and CaO than the interiors, suggesting that the dikes display chilled margins.

Low-Ti gabbro has a CIPW normative mineralogy of ~40% anorthite, 10% albite, 6-14% olivine, and 30% clinopyroxene. In contrast, the CIPW normative mineralogy of high-Ti gabbro includes 17-30% anorthite, 25-30% albite, 5-15% olivine, and 30% clinopyroxene. Both types of gabbro are usually fine to medium grained and granular (Figure 2-10), though all of the gabbros in the study area are moderately to highly altered. Only one outcrop of high-Ti gabbro near the base of the complex, within the intensely serpentinized region, exhibits a well-defined planar fabric (possibly metamorphic foliation).
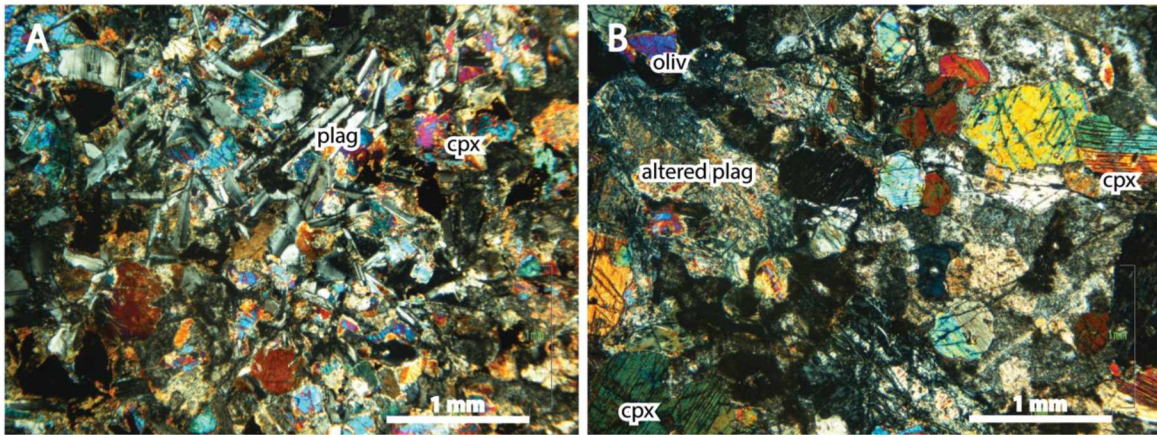
Figure 2-10. Cross polarized light photomicrographs of: A) high-Ti gabbro and B) low-Ti gabbro from the field area. The high-Ti gabbro sample contains visible plagioclase and moderately altered clinopyroxene and olivine. Feldspars in the low-Ti gabbro sample have been completely altered to a fine-grained mixture including sericite and possibly clays.

2.1.3. Trace element data

The results of the major and trace element analyses for samples in the complex are given in Table B-1 and Table B-2 in Appendix B.

The most highly mineralized samples are from the basal wehrlite, the basal dunite, the central feldspathic units, and the troctolite. These samples contain the highest Cu concentrations (251 to 367 ppm) and have 12 to 14 ppb Au. The two samples of dunite and wehrlite from the upper ultramafic unit have significantly lower Cu (87 to 99 ppm) and Au (2 to 7 ppb) concentrations. Two low-Ti gabbro samples contain 3 ppb Au and low Cu. All of the non-gabbro samples contain >40 ppb Pt+Pd values. The central feldspathic unit has the highest Pt+Pd value with 127 ppb and the lowest Pt:Pd ratio (0.41). Rocks from the other four units all have Pt:Pd ratios between 0.92 and 2.24.

The composite sample from the basal wehrlite unit has the highest TiO_2 (0.22 wt.%), consistent with XRF TiO_2 concentrations of 0.11-0.58 wt.%. This sample also contains the most clinopyroxene, so the high TiO_2 is likely due to high Ti in clinopyroxene. One sample from the upper unit has slightly higher Cr_2O_3 (0.81 wt.%) than samples from the other units, consistent with XRF Cr_2O_3 of 0.6-1.2 wt.%.

The composite sample from the central feldspathic unit has a significantly elevated Al_2O_3 concentration (2.58 wt.%), consistent with XRF data (1.3-3.9 wt.% Al_2O_3) for the unit.

2.2. Mineral compositions

As an ultramafic magma evolves, the Mg number (atomic $Mg/(Mg+Fe^{2+})$) of mafic minerals (olivine and pyroxene) progressively decreases. That is, minerals become more Fe-rich, as fractional crystallization progresses. Abrupt changes in Mg number of the same mineral indicate a change in magma composition (from sampling of a new sill or discrete magmatic body or due to a change in the parental magma source) or (less likely) a significant change in temperature. TiO_2 does not substitute readily into olivine, so Ti concentration in clinopyroxene and spinel can also be used to evaluate evolution of a magma. As a magma crystallizes, Ti concentration will increase in the melt if only olivine is removed. After Ti-bearing phases (e.g., clinopyroxene, spinel) begin to crystallize, Ti concentration in the remaining melt should decrease. To evaluate these processes, samples of the ultramafic rocks were collected for microprobe analysis at ~10-30 m intervals, perpendicular to mineral layering. Mineral compositions analyzed by electron microprobe are given in Appendix C.

2.2.1. Olivine compositions
2.2.1.1. Forsterite component

The forsterite (Fo = atomic $Mg/(Mg+Fe)$) component of olivine decreases as magma evolves, thus it is a good indicator of magma evolution. Within each unit in the map area, Fo decreases as clinopyroxene content increases. Concentric zones of olivine Fo values around wehrlite layers can be traced out with high forsterite margins that decrease towards the center of the layer, revealing individual sills (Figure 2-11).
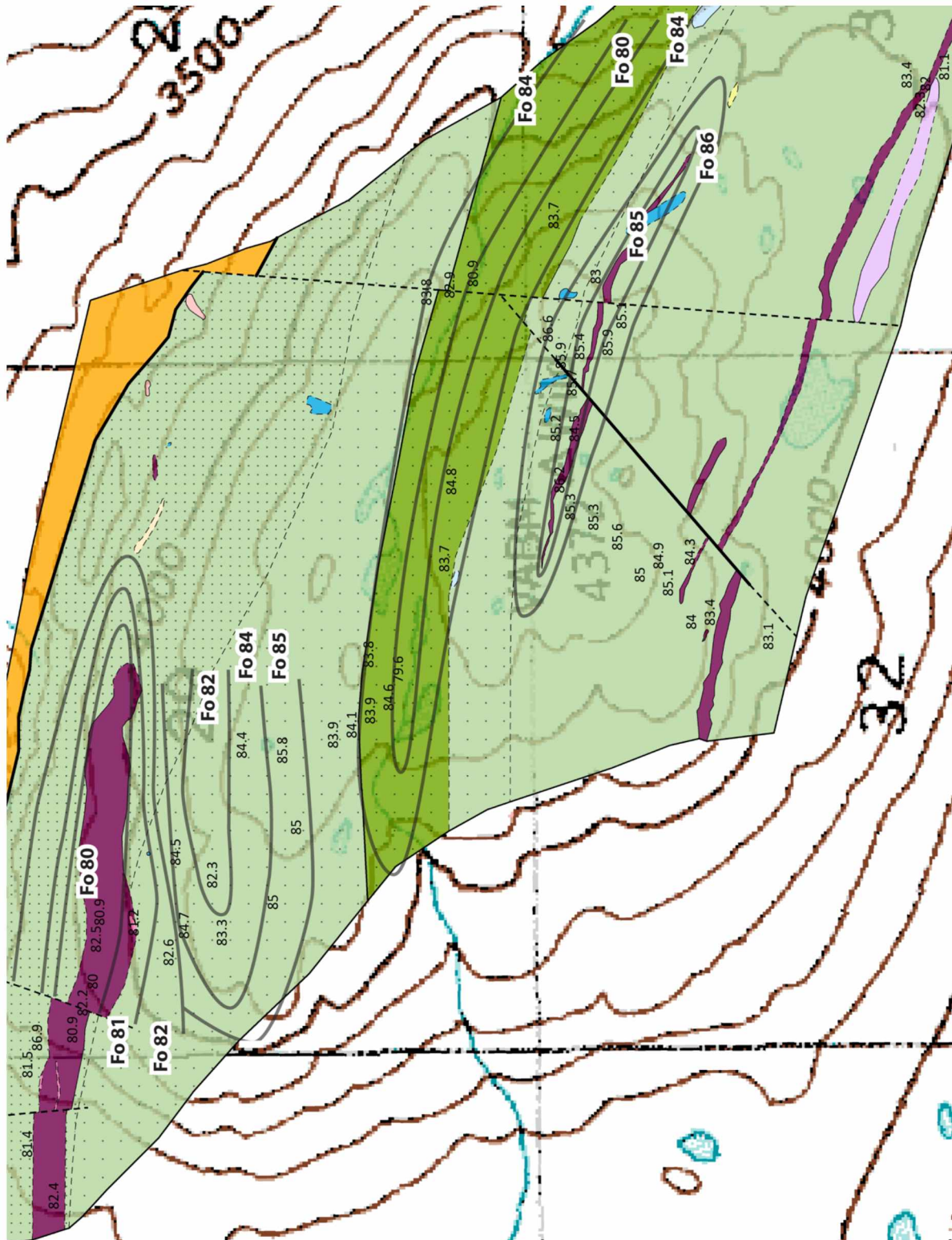
Figure 2-11. Geologic map of the Alpha complex with the average forsterite component of olivine plotted and contour lines traced around forsterite values. Each sill has a high forsterite margin that decreases towards the center. Data from this study is in Table C-1 in Appendix C.

The central feldspathic layer has the largest range of Fo values, from Fo 85.5 in dunite along the margins to Fo 79.1 in the troctolite core. The upper ultramafic unit has multiple layers but only one was sampled with tight sample spacing. This layer has the most primitive composition, with Fo 87.1 at the margins and decreasing to Fo 83 at the core. The basal dunite layer ranges from Fo 85.8 at the margins, to Fo 82.3 at the center. The basal wehrlite layer ranges from Fo 82.6 along the margin to Fo 80 at the center, with one errant sample at 86.1. This unit (on average) has the most evolved olivine compositions. Thicker layers within the complex show a larger range of olivine compositions than the thinner layers.

2.2.1.2. Nickel depletion

Nickel depletion in olivine is an important indicator of whether or not a melt reached sulfide saturation. Ni is more chalcophile than it is lithophile, thus it preferentially partitions into a sulfide melt over a silicate melt (Arndt et al., 2005). The partition coefficient (D) for Ni in sulfide is $\sim 10^2$-10^3 and for olivine, $D_{Ni}^{olivine-silicate}$ is around 2 in picritic liquids (Kinzler et al., 1990). Olivine grains that have been in contact with a sulfide liquid should be depleted in Ni for a given forsterite composition.

Across the Alpha complex, olivine shows variable degrees of Ni depletion (Figure 2-12). The modeled fractionation curve for olivine that crystallized from a sulfide undersaturated melt is shown for comparison (fractionation curve from the Geological Survey of Canada, unpublished data). Olivine compositions that fall below the curve likely grew from a Ni-depleted melt.

Individual olivine samples analyzed from the central feldspathic unit show little variation in Fo but significant variation in ppm Ni within and between grains. Patterns of Ni depletion in olivine in this unit are similar to patterns of Ni depletion in olivine from a mineralized sample of drill core (Figure 2-13). Sample 15LL158 has the greatest range in Ni (500 ppm difference) from 1640 ppm at Fo 83.5 to 2140 ppm at Fo 83.7. Between samples in the unit, Ni contents in olivine don't show a systematic decrease with decreasing Fo. As Fo decreases within the sill (from Fo 85 to Fo 80), the average Ni concentrations stay relatively constant.
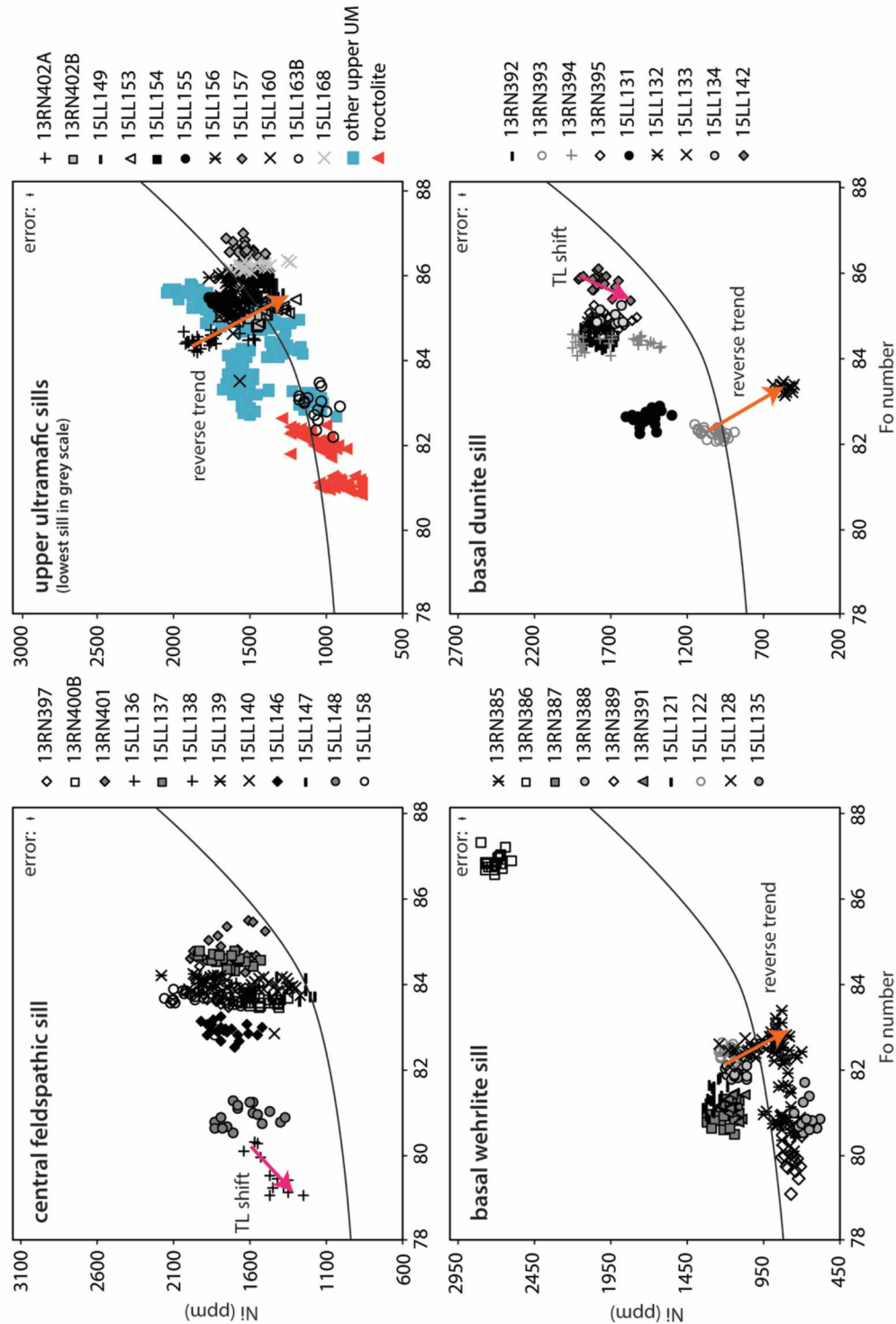
Figure 2-12. Olivine Fo versus ppm Ni for samples of olivine within each zone of the complex. Pink arrows show the direction of trapped liquid shift (TL) and orange arrows show the reverse zoning trend. The black curve is the calculated line for olivine from a sulfide undersaturated melt. Olivine that plots above the curve crystallized from a melt that was undersaturated in sulfide. Olivine that plots below the curve (Ni depleted) crystallized from a sulfide saturated melt.

41

Eight of ten samples from the upper ultramafic unit have almost no variation in Fo or Ni (Figure 2-12). The majority of samples are clustered close together at ~Fo 85.5 and ~1500 ppm Ni. The two outliers are samples 15LL163B and 13RN402A. Both of these samples are from wehrlite directly adjacent to clinopyroxenite bands. They have slightly more evolved Fo compositions and larger ranges in ppm Ni. The lowest (farthest north) sill is shown in grey scale in Figure 2-12 with individual samples denoted. Samples from other sills in this unit are in the background (blue and red points) without individual samples denoted. Graphing all of the sills together isn't as informative as showing data for the evolution of a single sill, so data from the above sills were separated. Olivine compositions from the other sills and from the troctolite layer are all slightly more evolved than olivine in the lowest sill. Samples of olivine from the troctolite have the most evolved, Fe-rich, Ni-depleted compositions (Figure 2-12; Figure 2-13).
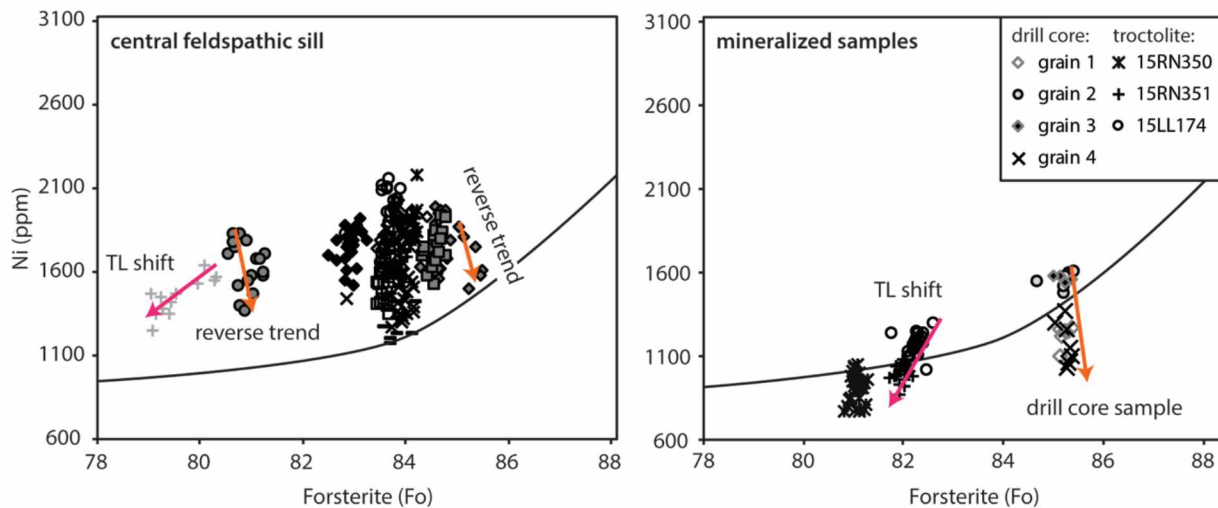
Figure 2-13. Olivine Fo versus ppm Ni for olivine in the central sill (left) and for a highly mineralized sample from outside of the map area plus samples from the troctolite of the upper ultramafic unit.

Samples from the basal dunite unit show little within-sample variation in Fo and ppm Ni (Figure 2-12). Samples from the margins of this zone contain olivine with higher Fo and ppm Ni. Olivine with the lowest ppm Ni occurs close to the center of this zone but it doesn't have the lowest Fo; the Ni pattern in this unit is more complicated. Sample 15LL142, with Fo 85.8, has the highest average Ni (1765 ppm).

Three samples from the basal dunite unit fall outside of the main compositional cluster defined by 6 samples; they exhibit lower Fo and variable Ni depletion. With the exceptions of samples 15LL133 and 13RN393, olivine grains from the basal dunite display a relatively linear trend of decreasing Ni with decreasing Fo. Sample 15LL133 displays enormous Ni depletion and falls well below the average trend with 560 ppm Ni for Fo 83.3 (Figure 2-12). Sample 13RN393 has the lowest Fo (82.3) and an average of 1010 ppm Ni. This combination falls slightly below the average trend.

Olivine from the basal wehrlite layer exhibit little within-sample Ni variation, but considerable between-sample variation. Samples from near the center of the unit are generally more Ni-depleted. The samples that are most depleted in Ni (13RN385, 13RN388, 13RN389) also show more variation in Fo content within a single sample. Sample 13RN385 has the greatest variation in Fo, ranging from Fo 80.1 to 83.4. Sample 13RN386 is the only major outlier, with with ~ Fo 86.5 and ~ 2700 ppm Ni.

2.2.1.3. Nickel in olivine compared to nickel in whole rock

Ni contents in olivine for the most part correlate with XRF Ni concentration in the rock, indicating that the majority of the Ni in a given rock is contained in the olivine and that both the microprobe and XRF analyses are relatively accurate (Figure 2-14). Two of my samples fall above the 1:1 line: 13RN391 (basal wehrlite) and 15LL137 (central feldspathic). Both contain Ni-bearing sulfide minerals. The other anomalous samples contain 0.4-0.7 wt.% S and are from an unpublished data set from the Geological Survey of Canada. Many of the samples appear to plot slightly above the 1:1 line, suggesting that they also contain minor amounts of additional Ni. One sample (13RN386 from the basal wehrlite unit) falls well below the 1:1 line, indicating that olivine in this sample is too primitive and has too high of a Ni composition to be in equilibrium with the rock from which it was sampled.
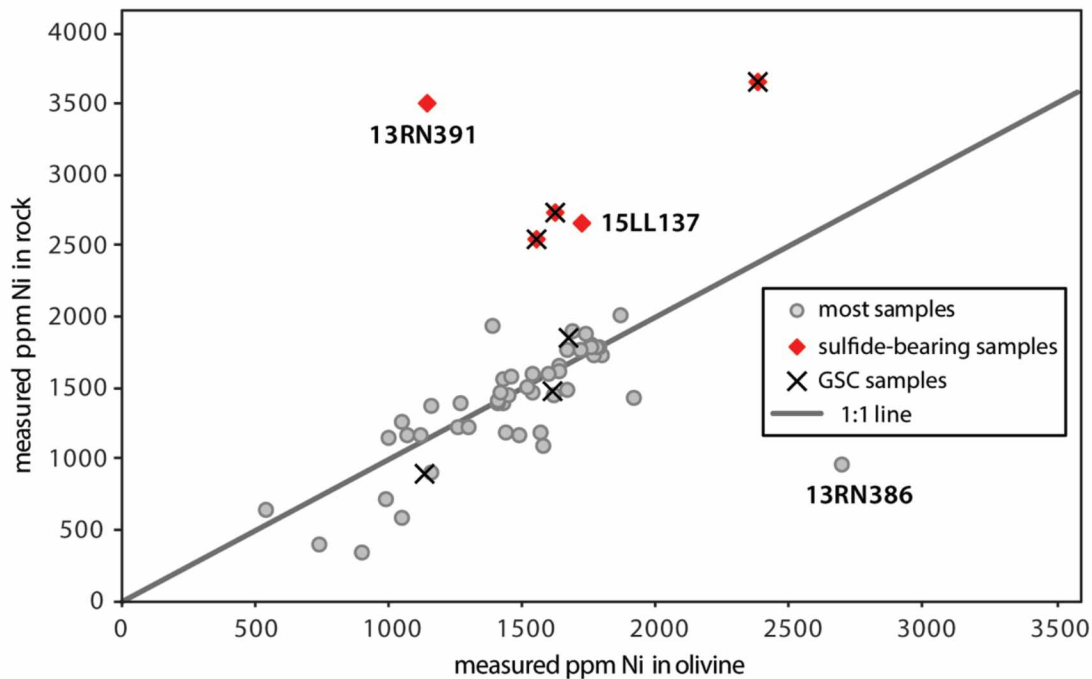
Figure 2-14. Measured concentrations of Ni in olivine versus Ni in rocks from the study area. Ni in rock was measured by XRF and Ni in olivine was measured by electron microprobe. Most of the data is from this study but includes 6 points from the Geological Survey of Canada (GSC), unpublished data.

2.2.2. Pyroxene compositions

Clinopyroxene in the Alpha complex is predominately diopside-augite solid solution. Clinopyroxenes in my samples display variable degrees of exsolution and widths of exsolution lamellae. I used a microprobe beam diameter of 5 microns, which is small enough that in some cases I analyzed pure clinopyroxene (from which the orthopyroxene component had exsolved) and in other cases I analyzed 'average' pre-exsolution clinopyroxene. Also, in some cases the beam was likely closer to an orthopyroxene lamella than others. Thus, it is unclear to what extent the clinopyroxene analyses (Figure 2-15) represent 'original' mineral vs. mixtures of exsolved minerals.

I found and analyzed both orthopyroxene and clinopyroxene from the central feldspathic unit. The center of this unit in particular contains appreciable orthopyroxene (which plots as "clinoenstatite" on Figure 2-15). I did not find orthopyroxene elsewhere in the map area.

Ca-rich pyroxenes from all units (Figure 2-15) appear to plot in narrow zones sub-parallel to lines of constant Mg number (atomic Mg/Mg+Fe), with total variation in Ca component from 50% ('pure diopside') to 35% (70% 'diopside' component). That is, the analyses contain 0-30% orthopyroxene component. This variation is about three times as great as the total variation in Mg number (~83-93). It is unclear to what extent the Ca variations represent differences in original pyroxene composition and to what extent they represent exsolution and analytical 'mixing' between Ca-rich and Ca-poor phases. Based on the limited orthopyroxene-clinopyroxene data from the central unit (Figure 2-15), I assume that the Mg numbers of both are about the same, hence the variation in Ca component has little effect on the net Mg number.
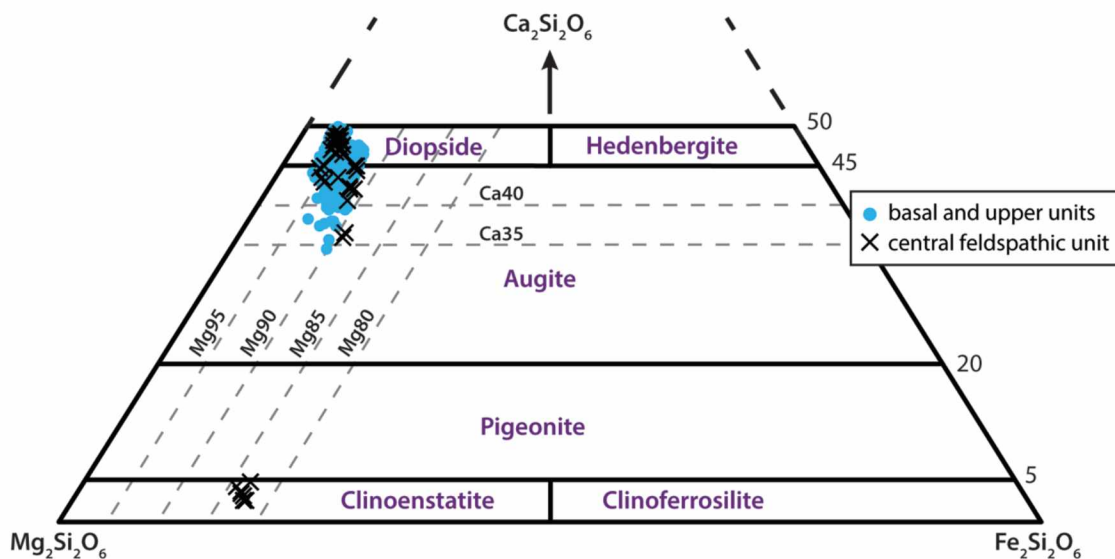
Figure 2-15. Classification diagram for pyroxene analyses from various units in the study area.

44

The Mg number and TiO_2 content of clinopyroxene can be used to differentiate between varieties of clinopyroxene within the Alpha complex (Figure 2-16). Clinopyroxene from the central feldspathic unit has the highest percent TiO_2 in the complex. Clinopyroxene from the basal ultramafic units falls in the intermediate range. Clinopyroxene from the upper ultramafic unit has the lowest percent TiO_2. If the trends on Figure 2-16 are caused by simple fractional crystallization of olivine $\rightarrow$ clinopyroxene, then clinopyroxene increases in percent TiO_2 with decreasing Mg number. Clinopyroxenes with similar Mg numbers but from different zones contain distinctly different concentrations of TiO_2.
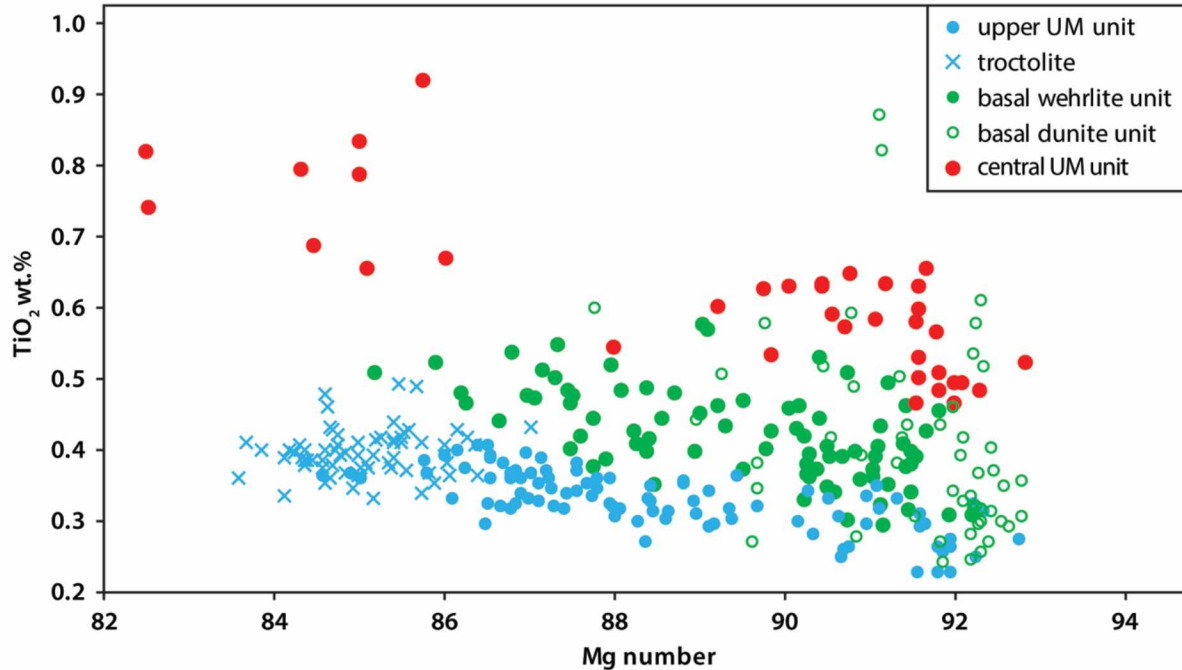
Figure 2-16. Wt.% TiO_2 versus Mg number for clinopyroxene from the study area. The systematic decrease of Mg number and the increase in TiO_2 monitors the evolution of the parent melt if changes in melt composition are mostly due to olivine crystallization.

2.2.3. Disequilibrium compositions and textures in olivine and clinopyroxene

Some non-poikilitic clinopyroxene phenocrysts in the basal unit are zoned with regard to major and minor elements, whereas clinopyroxene phenocrysts in the upper unit exhibit almost no zoning. The differences for major elements are small but the cores of phenocrysts have generally lower FeO, SiO_2, Al_2O_3, and TiO_2 than their rims (Figure 2-17). Concentrations of Cr are higher in the cores.

Sample 13RN393 from the center of the basal dunite unit exhibits the greatest variation in clinopyroxene compositions in the study area (Figure 2-18). A number of the grains analyzed follow the usual pattern of increasing TiO_2 with decreasing Mg number as demonstrated in Figure 2-16. However, some grains have distinctly higher TiO_2 rims (e.g., grain 2) than what would be observed from simple

fractional crystallization. Some of these clinopyroxene grains are also optically zoned with cores that have a slightly different birefringence than the grain margins (Figure 2-19A).
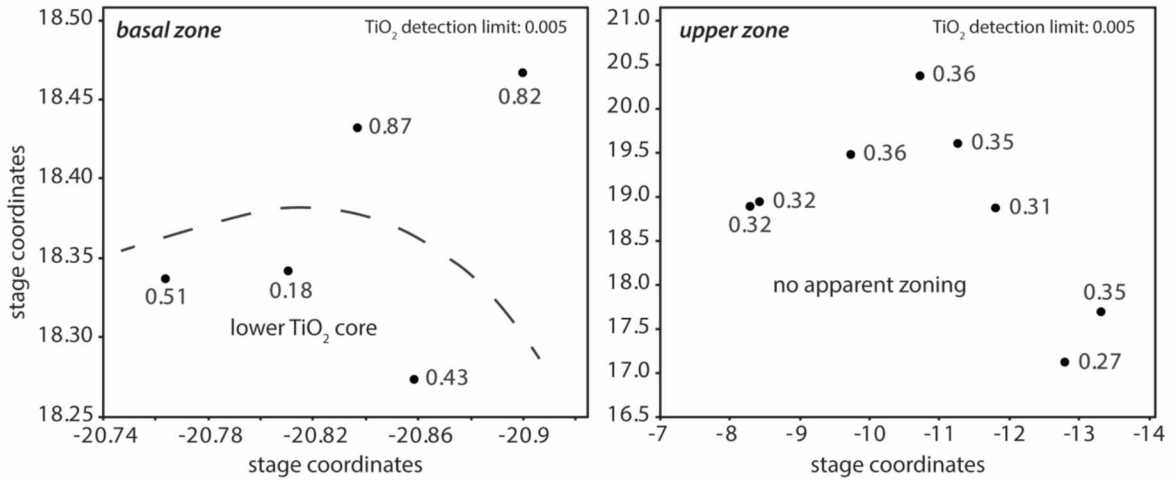
Figure 2-17. Two discrete grains of clinopyroxene from the basal dunite unit (13RN393) and the upper ultramafic unit (15ET191) with spot analyses labeled with their respective wt.% TiO_2 values. The X and Y axes are the stage coordinates on the microprobe such that 1 unit = 1 mm.
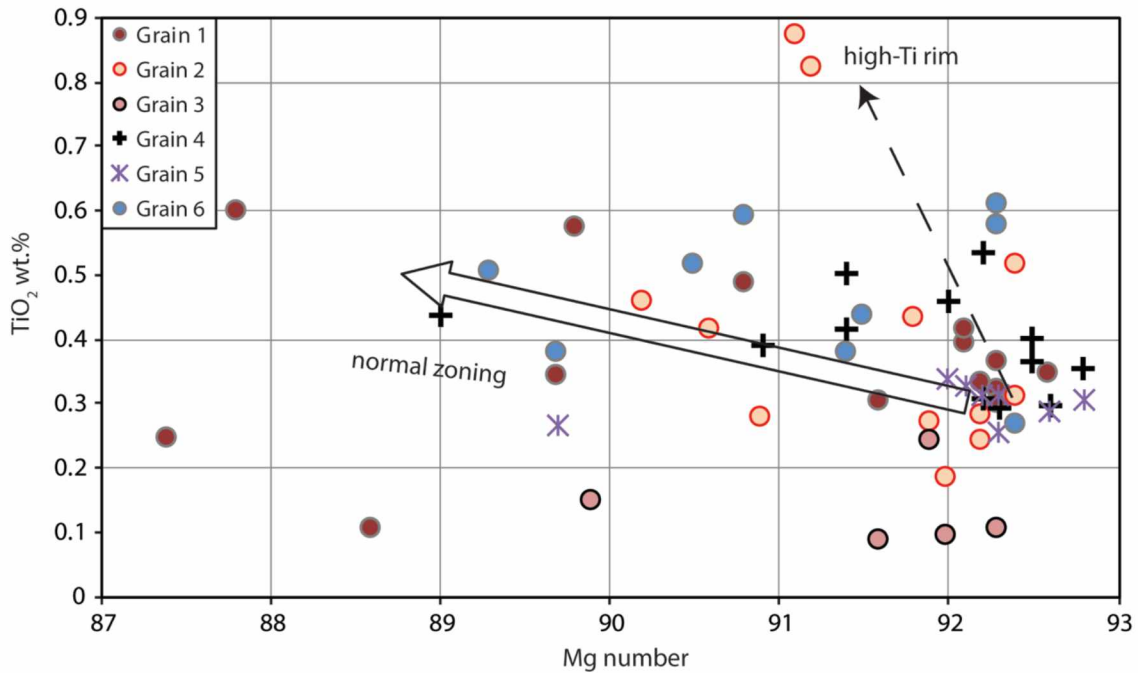
Figure 2-18. Compositions of six clinopyroxene grains from sample 13RN393. Grain 2 has a moderate-TiO_2 core and a high TiO_2 rim. Other grains in this sample display relatively consistent TiO_2 as Mg number decreases.

One sample in the basal unit also exhibits bimodal olivine compositions (Figure 2-20). Eight grains were analyzed from sample 13RN385, located at the base of the basal wehrlite unit. One group averages at Fo 82.5 and the other group at Fo 80.5. Samples throughout the complex generally have <1% variation in their Fo values (Figure 2-12). A range in Fo of over 3% within a single thin section, and a bimodal distribution, was not observed in any other samples in the map area. Olivine from sample 13RN386, taken nearby sample 13RN385, has olivine with up to Fo 86.6. Olivine grains in this sample have embayed margins (Figure 2-19B).
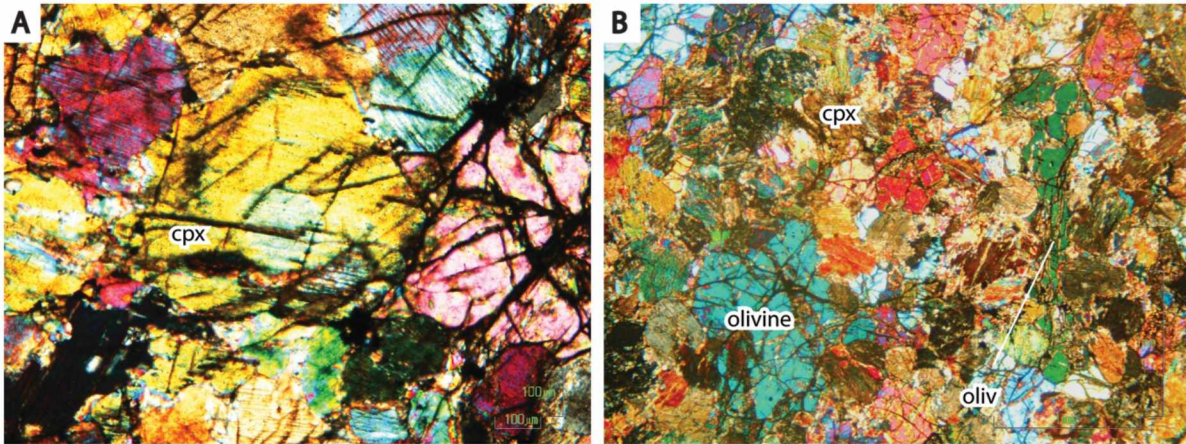
Figure 2-19. Photomicrographs of disequilibrium textures in wehrlite and dunite in the basal zone. A) A clinopyroxene grain that exhibits optical zoning. B) Embayed olivine in sample 13RN386 (Fo 86.6).
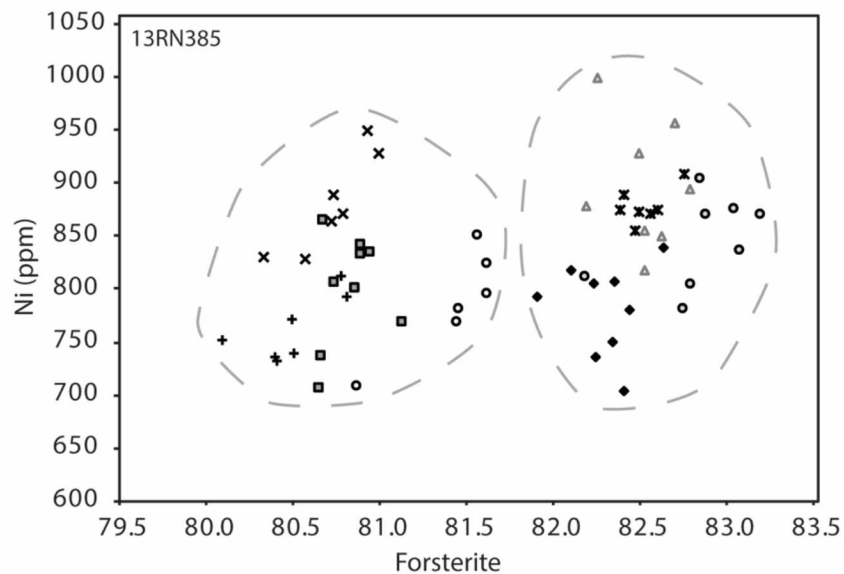
Figure 2-20. Forsterite versus Ni in olivine compositions for eight different grains in sample 13RN385. The dashed outlines trace the two separate olivine compositions that were identified.

2.2.4. Spinel compositions

Ultramafic rocks from the Alpha complex contain disseminated grains of chromium-rich spinel, which displays substantial variations in composition. Spinel is present as an accessory phase in all rock types, though it is less abundant in clinopyroxenite relative to dunite and wehrlite.

2.2.4.1. Compositional variations

Spinel compositions follow characteristic trends that can usually be observed within single thin sections (Figure 2-21). There are two clear trends, which can be classified according to the Fe^{2+} and Fe^{3+} contents of spinel. Spinels from different units in the complex follow different compositional trends. Spinels from the upper unit plot on trends 1 and 2. The samples with compositions that plot on trend 2 are from slightly more serpentinized rocks. Samples from the basal units have compositions that mostly plot on trend 2. Spinels from this group have high-Fe^{3+} and Cr/(Cr+Al) ratios ranging from 0.60 to 0.96. Not surprisingly, spinels of this group are in intensely serpentinized rocks. Spinels from the central feldspathic unit are distinctly different from spinels in the upper and basal units. These spinels are all low-Fe^{3+} and have elevated Al contents compared to other spinels in the complex (up to ~25 wt.% Al_2O_3).

The spinels that follow trend 1 start out with elevated Mg and Al (composition of approximately $(Mg_{30}Fe^{2+}{}_{70})Cr_{86}Fe^{3+}{}_{20}Al_{94})$. Al^{3+} is replaced by Cr^{3+} and this group evolves to a composition of approximately $(Mg_{15}Fe^{2+}{}_{85})Cr_{100}Fe^{3+}{}_{45}Al_{45}$. These spinels don't have a large compositional range and remain low in total Fe. Overall, the tendency is toward increasing Cr with increasing Fe^{2+}. The spinels in this group have compositions that define a steep trend on the TiO_2 versus $Fe^{3+}/(Fe^{3+}+Cr+Al)$ plot (Figure 2-21) due to increasing TiO_2 with little (~0.1-0.3 wt.%) relative increase in Fe^{3+}. Wt.% TiO_2 increases along this trend with increased coupled substitution of Ti^{4+} and Fe^{2+} for two Fe^{3+} cations. TiO_2 rises from about 0.2 to 3.2 wt.% (approximately 0.16-2.6 atomic %).

The spinels that follow trend 2 start out with high Mg and Al and low Fe (approximately $(Mg_{30}Fe^{2+}{}_{70})Cr_{95}Fe^{3+}{}_{20}Al_{85})$ and evolve to $Mg_{10}Fe^{2+}{}_{90}Ti_6Cr_{95}Fe^{3+}{}_{85}Al_7$, with the replacement of Mg^{2+} and Al^{3+} by Fe^{2+} and Fe^{3+}. For compositions in this group, Fe^{3+} replaces Al^{3+} at approximately constant Cr^{3+}. After reaching their maximum TiO_2 (5.5 wt.%), TiO_2 decreases as Ti^{4+} and Fe^{2+} are replaced by two Fe^{3+} cations. These spinels then evolve toward pure magnetite ($Fe^{2+}{}_{1.0}Fe^{3+}{}_{2.0}$) due to the exchange of Cr^{3+} and Al^{3+} for Fe^{3+} (and Mg^{2+} + Mn^{2+} by Fe^{2+}). This results in a final negative trend on the TiO_2 versus $Fe^{3+}/(Fe^{3+}+Cr+Al)$ plot (Figure 2-21, magenta arrows). These spinels occur in the intensely serpentinized zone and exhibit abundant alteration to magnetite (Figure 2-22, above). Magnetite occurs both as rims and as veinlets cutting through grains.
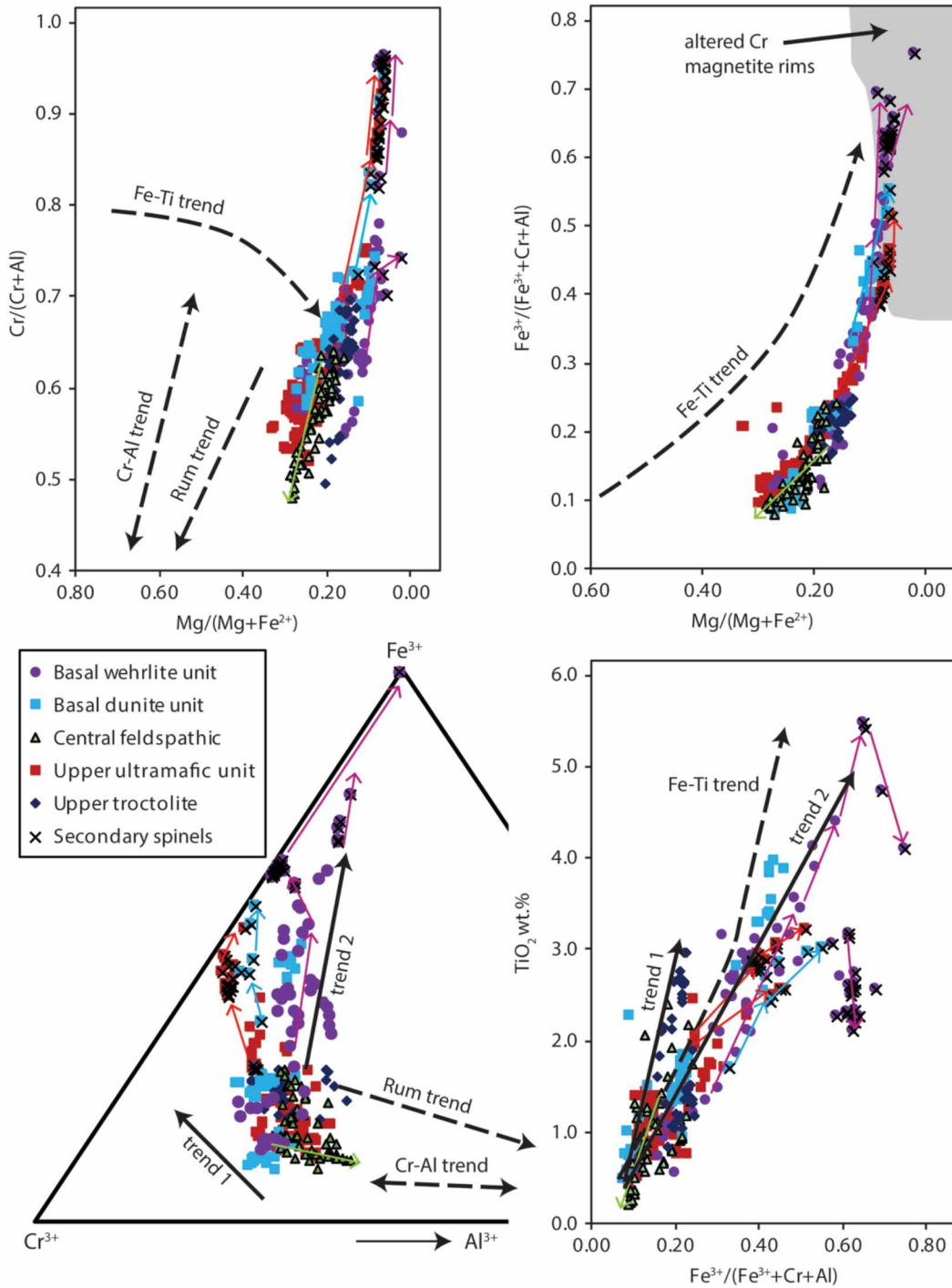
Figure 2-21. Spinel composition diagrams for spinels from the study area, with fields and dashed trend lines from Barnes and Roeder (2001). Trends 1 and 2 are discussed in the text. Colored arrows connect different compositions from the same sample, with arrows pointing in the direction of increased alteration, as indicated by microprobe compositional maps. Green arrow = 13RN398 (central feldspathic sill); red arrow = 15ET189 (upper ultramafic sills); blue arrow = 13RN394 (basal dunite); magenta arrows = several basal wehrlite samples. Secondary spinels were identified from their low Al-Mg compositions and textural relations.

49

Spinels from the feldspathic unit follow a different compositional trend from the spinels that follow trends 1 and 2 (Figure 2-21, green arrows). This group parallels trend 1 but the spinels increase in Al^{3+} as Al replaces Fe^{3+} and Cr^{3+}. These spinels are from variably serpentinized rocks with high magnetic susceptibilities but don't show the same Fe^{2+}-, Fe^{3+}- enrichment trends of the spinels along trend 2. The spinels from the upper troctolite in the upper ultramafic unit are most similar to the moderate-TiO_2 (~2 wt.%) spinels in this group. Both have a steep trend on the $Fe^{3+}/(Fe^{3+}+Al+Cr)$ vs. TiO_2 wt.% plot and remain low in total Fe.

2.2.4.2. Textural variations

Spinel grains are interstitial to silicate minerals and occur as euhedral to subhedral grains 20 to 200 microns in diameter. Grains with trend 1 compositions are euhedral and maintain their primary magmatic textures with little or no exsolution or alteration to magnetite. Spinel grains from the central feldspathic unit display cores that are Cr- and Ti-rich and Al-poor. Rims are depleted in Cr and enriched in Al (Figure 2-23, above; Figure 2-24, above). Some of these spinels also contain inclusions of ilmenite (Figure 2-24, above).

Less commonly, spinel grains exhibit oxidative exsolution of ilmenite. Ilmenite can be observed as tiny grains present along the {111} planes of the host spinel (Figure 2-23, below) and as irregular blebs that that are surrounded by spinel (Figure 2-24, above). In some cases, Ti blebs rim spinel grains (Figure 2-22, below). In intensely serpentinized rocks (trend 2 spinels) they occur as blebs with secondary magnetite (Figure 2-22, above). The ilmenite lamellae occur as elongate crystals, generally 5 to 20 microns in length and <5 microns in width. The irregular blebs of ilmenite are slightly coarser when they are inclusions in spinel grains (Figure 2-24, above) or when they rim spinel grains (Figure 2-22, below) and are much thinner and more irregular where present with secondary magnetite. They are generally elongate, although some appear to be anhedral. Spinel grains that have experienced ilmenite oxidative "exsolution" are generally lower in TiO_2 due to removal of TiO_2 from the spinel.
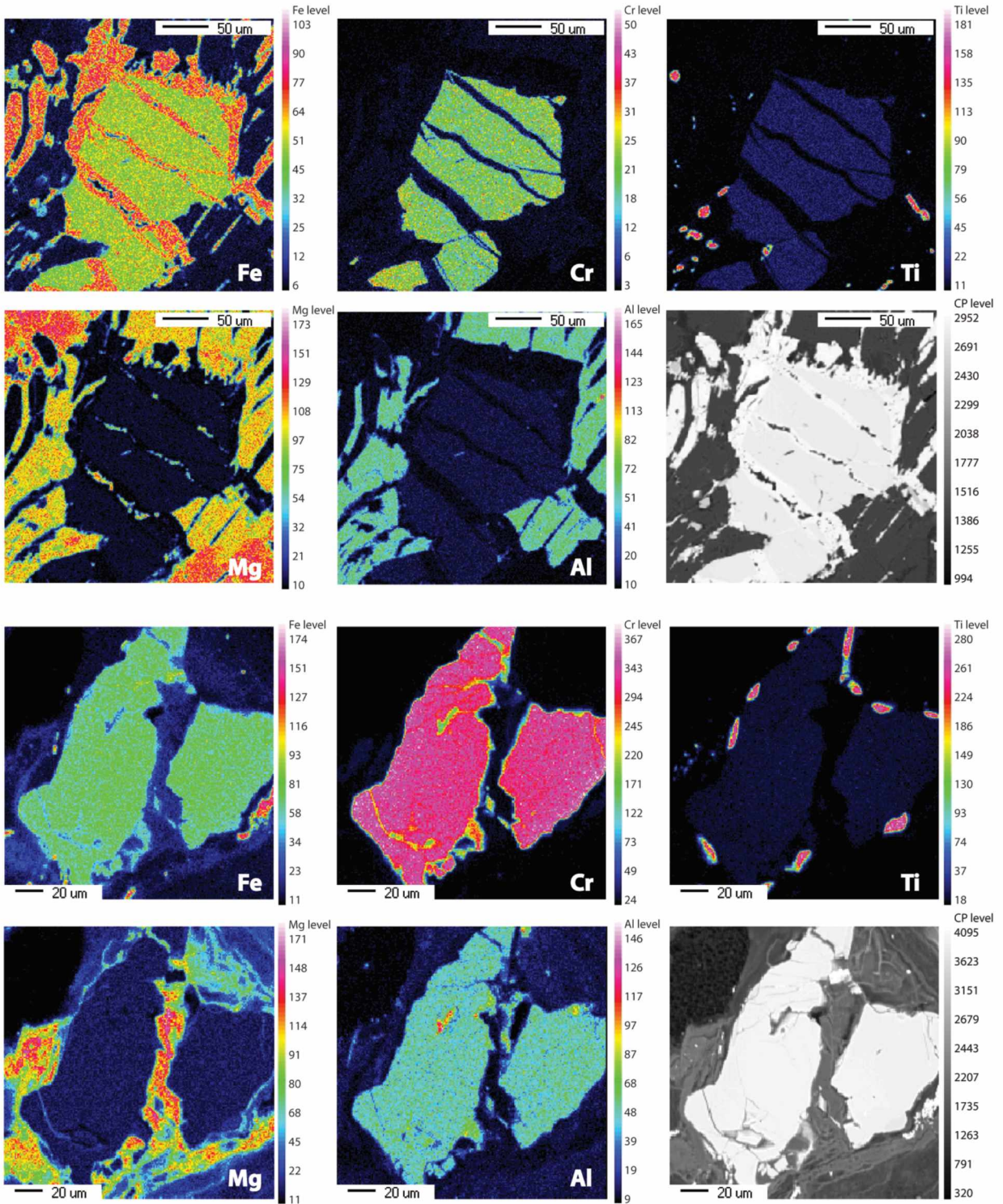
Figure 2-22. Elemental maps for Fe, Cr, Ti, Mg, and Al and the BSE image of: (above) chromite with pervasive veins and rims of magnetite and minor Ti-Fe oxide blebs in serpentinite (13RN384; basal wehrlite unit); (below) chromite with ilmenite along the grain margin (from PNI-05-08 drill core).
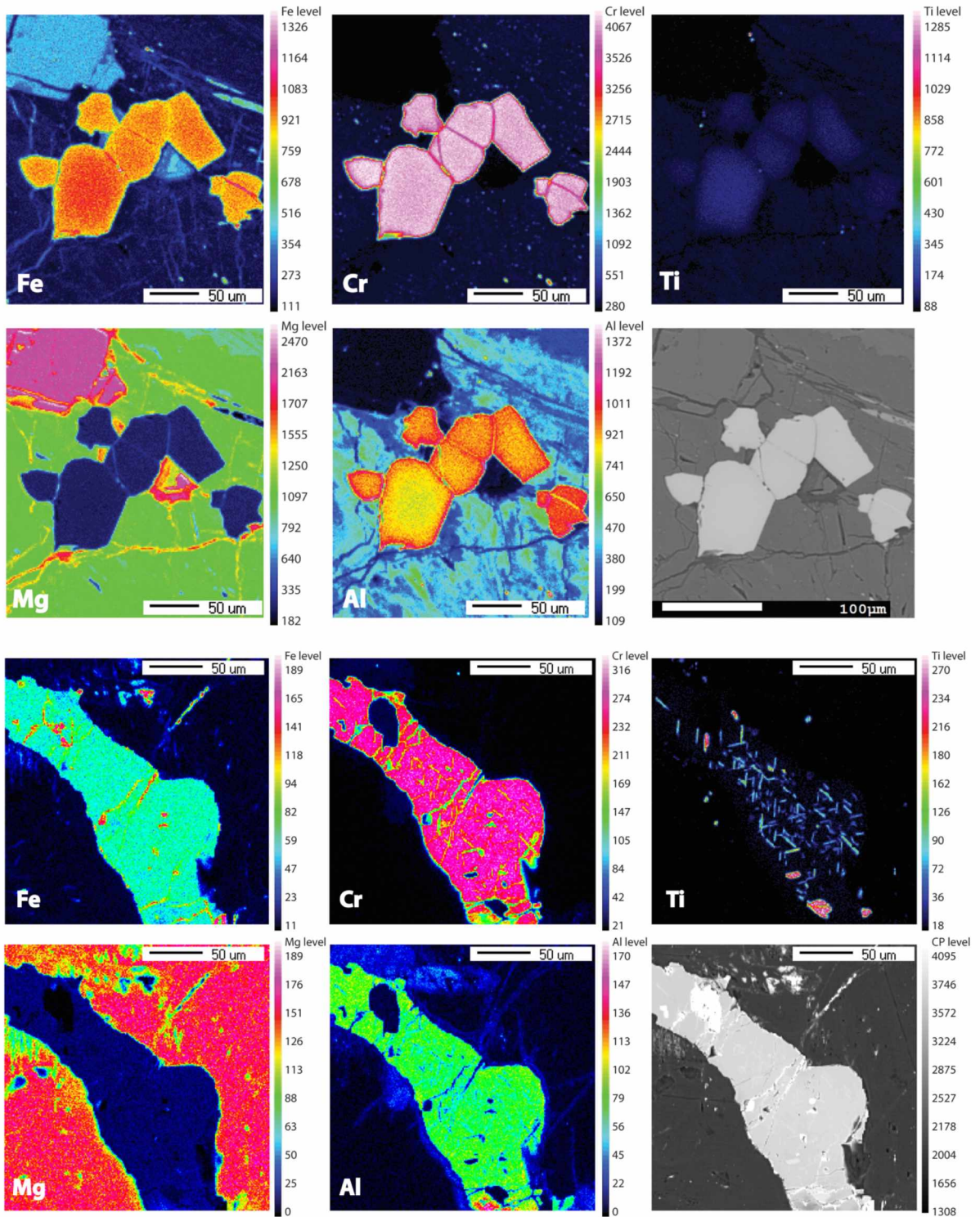
Figure 2-23. Elemental maps for Fe, Cr, Ti, Mg, and Al and the BSE image of: (above) three zoned, (higher-Al rims) euhedral chromite grains from a dunite sample (13RN400B; central feldspathic unit); (below) chromite with oxidative "exsolution" of ilmenite along the {111} zone, isolated ilmenite grains, and thin (1-5 micron wide) magnetite veinlets (from PNI-12-063 drill core).
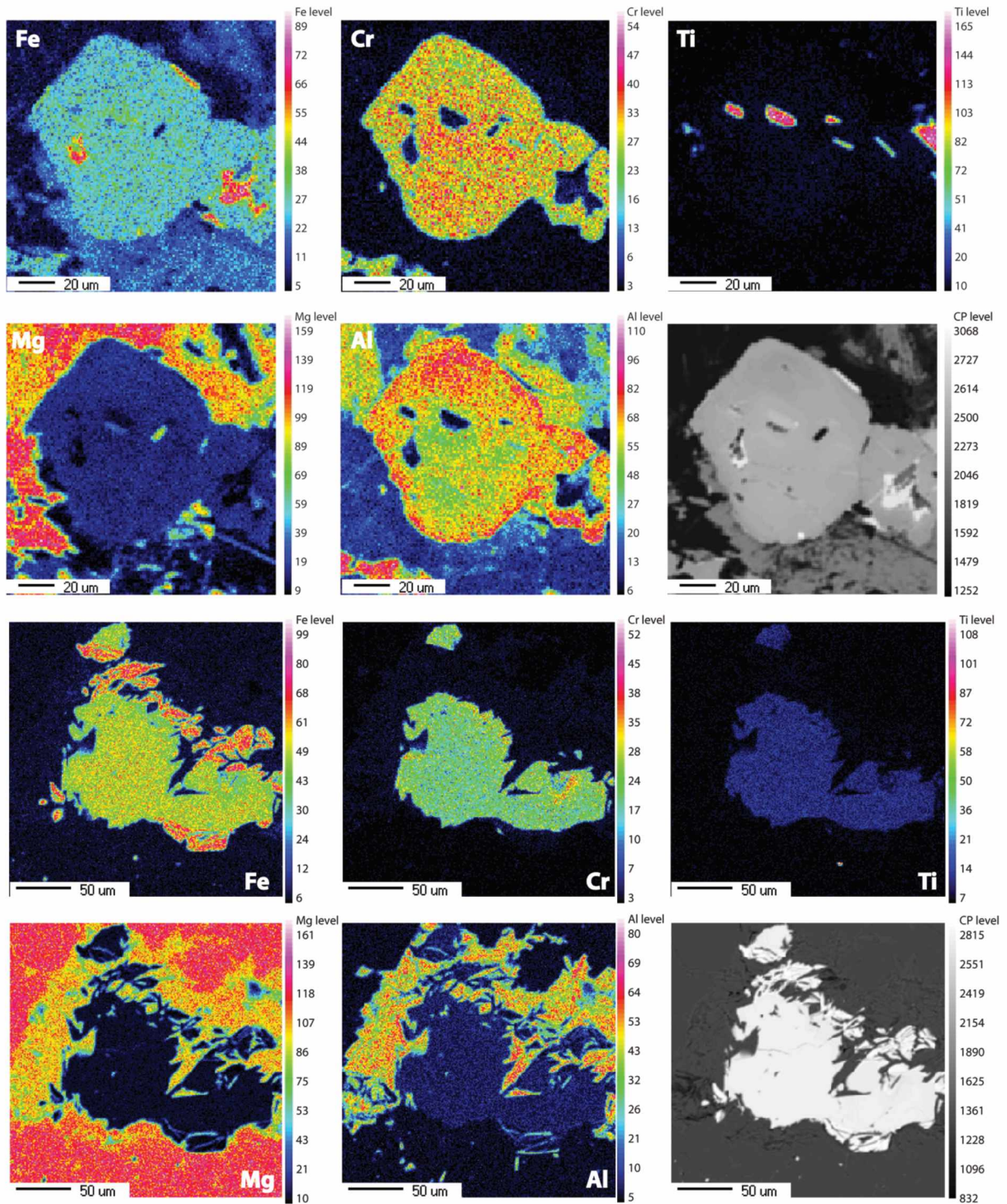
Figure 2-24. Elemental maps for Fe, Cr, Ti, Mg, and Al and the BSE image of: (above) chromite with distinctly higher Al rims and inclusions of ilmenite (13RN398; central feldspathic unit); (below) chromite being replaced by chlorite (Al-rich aureole) and magnetite in serpentinite (13RN384; basal wehrlite unit).

Chapter 3 Discussion

3.1. Crystallization sequence and cumulate emplacement

Three units in the complex can be identified according to their mineral compositions, major element compositions, and textures: the upper ultramafic unit, the central feldspathic unit, and the basal ultramafic unit. All of the ultramafic rocks in the Alpha complex exhibit cumulate textures (Figure 2-6, 2-7, 2-8, 2-9). In all ultramafic units, olivine is euhedral and variably contains inclusions of spinel. Consequently, olivine crystallized early with spinel. Clinopyroxene usually exhibits subpoikilitic to poikilitic textures (Figure 2-7, 2-8), hence, crystallized later. Textures in the feldspathic unit are problematic due to the pervasive alteration of plagioclase (Figure 2-6). However, at least a few rocks in this unit contain mostly olivine with minor (altered) interstitial plagioclase and little, if any, clinopyroxene. Clinopyroxene (and minor orthopyroxene) in rocks of this unit have anhedral, subpoikilitic textures and arguably contain altered plagioclase inclusions. Thus, the crystallization order in the feldspathic zone is olivine followed by plagioclase, followed by plagioclase and pyroxene.
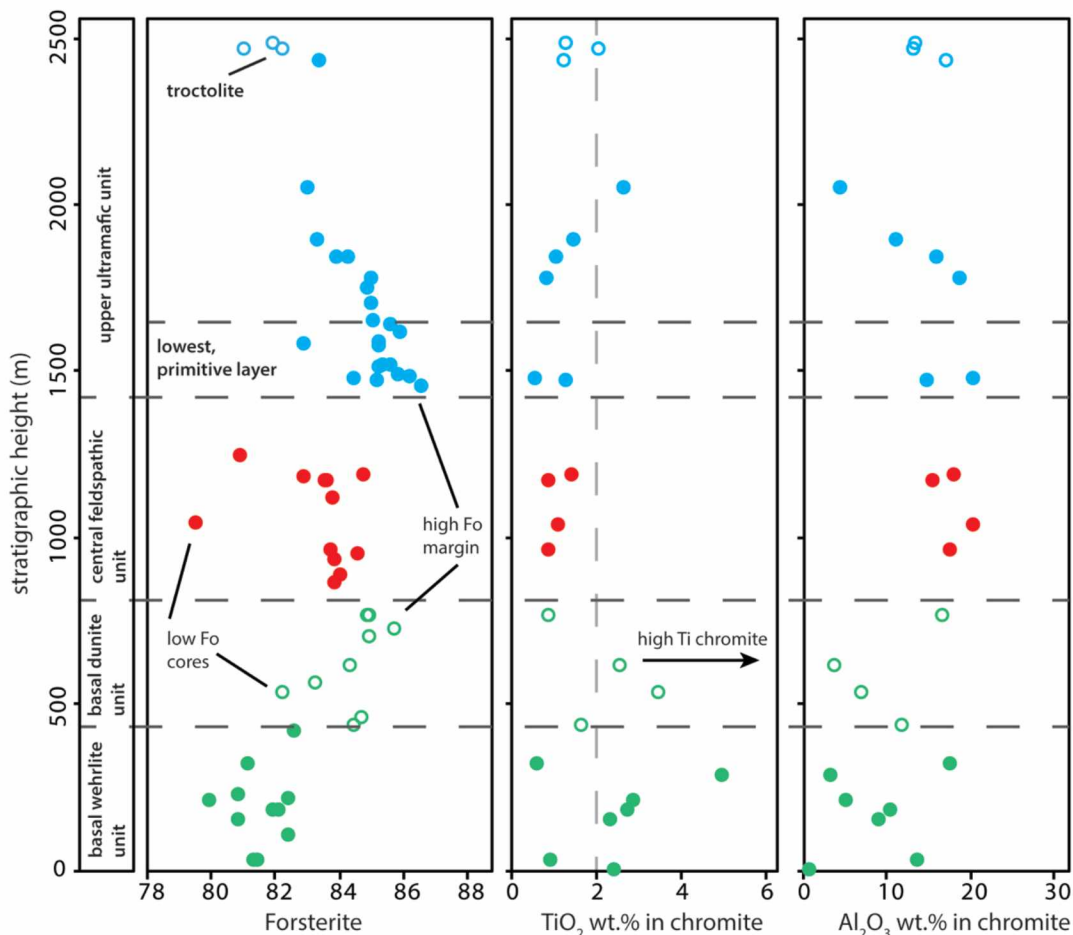
Figure 3-1. Variations in Fo content of olivine and wt.% TiO_2 and Al_2O_3 in spinel through the stratigraphy of the study area. Individual units exhibit inward zoning of olivine and spinel compositions.

3.1.1. Upper ultramafic unit

The upper ultramafic unit consists of three traceable wehrlite layers (Figure 2-1; Figure 2-5), with smaller olivine clinopyroxenite lenses. All of these are surrounded by dunite. I interpret each of these layers to be an individual sill: primitive olivine crystallized early along the margins and the center became progressively more evolved and more clinopyroxene enriched. This unit has the highest MgO content and the most primitive olivine (Figure 3-1) of the ultramafic sills. Wehrlite from this unit also has low TiO_2:CaO ratios compared to wehrlite from the basal unit (Figure 3-2). Ti^{4+} cannot substitute into olivine; consequently, TiO_2 should increase in concentration in a magma undergoing olivine fractionation. Thus, low-TiO_2 concentrations in wehrlite from the upper ultramafic unit suggest crystallization from a primitive magma that hadn't undergone a significant degree of fractionation and (or) crystallization from an intrinsically low TiO_2 magma.

A discontinuous troctolite body with orientation slightly discordant to the wehrlite bodies (Figure 2-5) occurs near the top of this unit. Troctolite clinopyroxene compositions group with those of the upper ultramafic sills (e.g., Mg number vs. wt.% TiO_2, Figure 2-16). Olivine compositions in the troctolite are Fo 81.1 to 82.3 (Figure 3-1), considerably more Fo-poor than any other olivine from this unit. They are also significantly depleted in Ni similar to the lowest Fo wehrlite from the first upper ultramafic sill (Figure 2-12).
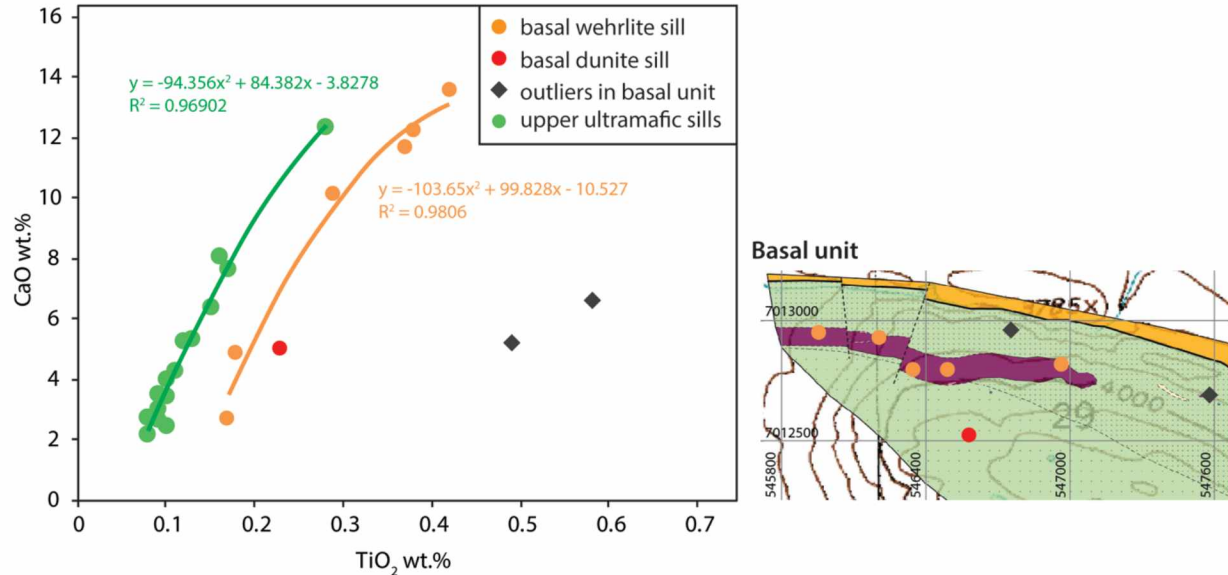
Figure 3-2. Wt.% CaO vs. TiO_2 for major element XRF analyses of wehrlite from the various units (left). On the right is a location map showing the distribution of samples in the basal unit. Green = serpentinized dunite, purple = basal wehrlite, orange = Paleozoic rocks. The very high TiO_2 in 'outlying wehrlite' samples must be due to significant amounts of a high-TiO_2 mineral, such as ilmenite.

Given the low Mg contents of olivine and clinopyroxene in the troctolite, the body was logically derived from a significantly fractionated magma. However, it is now mostly surrounded by dunite and strikes at a shallow angle to layering defined by wehrlite in the general vicinity (Figure 2-5). I speculate that this body represents the fractionated 'core' of an inward-crystallizing ultramafic sill. If such is the case, then the residual, fractionated magma escaped from its 'original' sill and migrated up into overlying olivine-rich rocks.

Olivine that was sampled adjacent to clinopyroxenite bands in these sills were identified having more Fe-rich, Ni-depleted compositions (e.g., 15LL163B, 13RN402A; Figure 2-12). Olivine crystallizing within or adjacent to clinopyroxenite will have more Fe-rich compositions, as it crystallized from a more highly fractionated melt than olivine that crystallized in dunite along sill margins. Additionally, some of the last residual magma may have been trapped between accumulating crystal phases. These small pockets of melt within the crystallized sill could have had slightly different Ni contents, resulting in olivine with a slightly larger range in Ni.

The upper ultramafic sills contain the most primitive olivine compositions observed in the map area and contain clinopyroxene with the lowest TiO_2 (0.3-0.4 wt.%). Average olivine compositions for the 20 samples analyzed are Fo 82.8-86.3 (Figure 3-1). Primitive olivine compositions in the lowest sill in this unit suggest the lowest sill was the first to intrude, and the stratigraphically higher sills intruded later. Only the lowest sill shows a clear zonation pattern, but this can be attributed to sampling density. The lowest sill was sampled at roughly 10 m intervals while the other sills were not.

The two blocks of schist identified in this area (Figure 2-1) are most likely blocks of basement rock that were preserved along a sill margin.

The upper ultramafic unit is cut by both high- and low-Ti gabbro dikes (Figure 2-1); the latter indicate that the upper ultramafic unit is related to earlier (low-Ti) Nikolai magmatism. Further evidence for this is the exclusive presence of clinopyroxene with the lowest TiO_2 concentrations (0.2-0.4 wt.%; Figure 2-16), both in the upper ultramafic sills *per se* and in the associated troctolite.

3.1.2. Central feldspathic unit

The central feldspathic unit can be mostly modeled as a single body (Figure 2-1), with dunitic margins that grade into wehrlite and then troctolite at the center. This unit contains dunite with the highest amount of Al_2O_3 (Figure 3-3) and the most evolved olivine (Fo 79-84.8; Figure 3-1) of the ultramafic sills. Based on the mineralogical patterns and olivine compositions, I interpret this unit to be a single sill. The central troctolite contains the most Fe-rich olivine (Fo 79); olivine with the second-lowest Fo (80.8) is present in a wehrlite just below the troctolite (Figure 2-11). Primitive (higher Fo) olivine crystallized along the margins and the center became progressively more evolved and more plagioclase enriched

during fractional crystallization. Overall the unit contains less clinopyroxene and more plagioclase than the other units. Notably this unit lacks significant wehrlite layers (Figure 2-1).
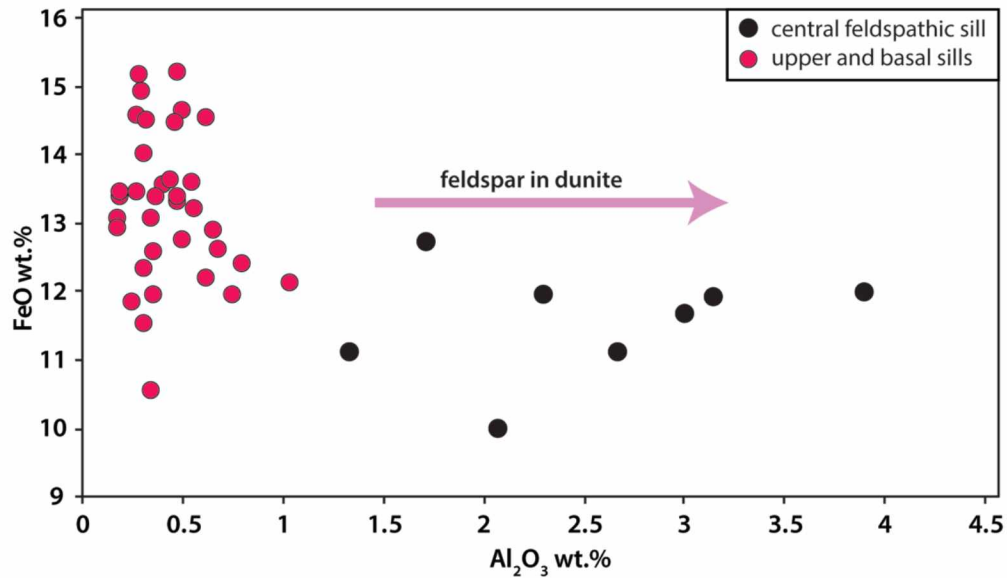
Figure 3-3. FeO wt.% versus Al_2O_3 wt.% for dunite in the central feldspathic sill compared to non-feldspathic dunite in the other sills.
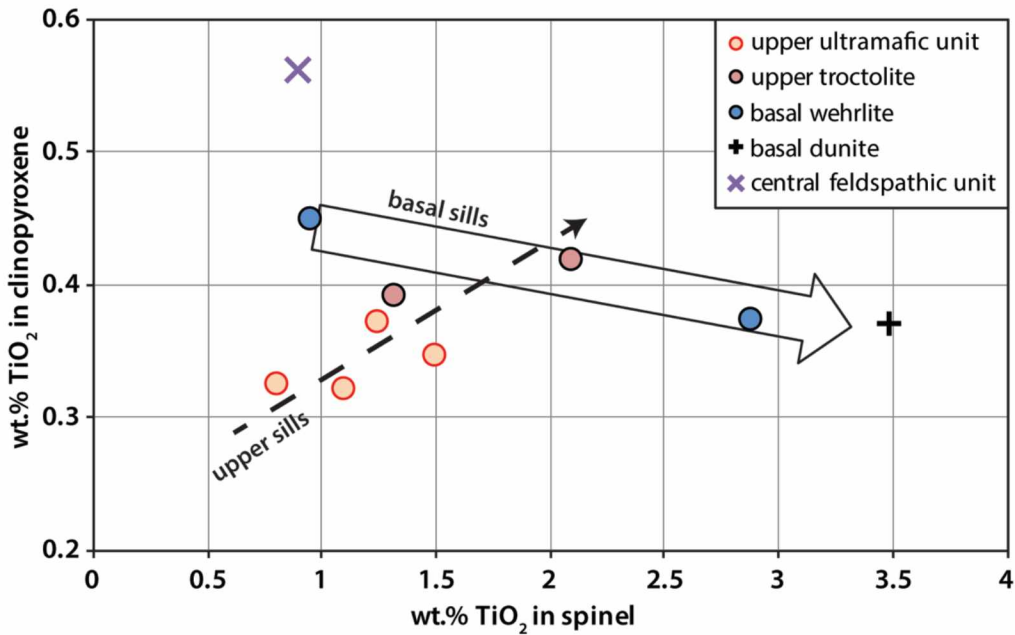
Figure 3-4. Average wt.% TiO_2 in spinel vs. wt.% TiO_2 in clinopyroxene from the same sample for rocks from the study area. Samples from the upper sills have a positive correlation between TiO_2 in spinel and clinopyroxene; samples from the basal sills have a negative correlation. The single sample from the central sill for which both spinel and clinopyroxene compositions are available does not fall into either group.

58

Olivine compositions range from Fo 85.5 along the margins to Fo 79.1 at the core (Figure 3-1). This range in Fo most likely reflects significant fractional crystallization that took place within the sill. This is suggestive of a closed system where the residual melt was depleted in MgO as it fractionated due to crystallization of olivine (mostly) and lesser clinopyroxene and plagioclase. The change in Fo from sill margins to the core (6.4) is nearly twice that (86.5-82.8 = 3.7; Figure 3-1) in the upper sills.

Clinopyroxene in this sill has the lowest Mg number (82.5) and highest average TiO_2 (>0.8 wt.%) of those I've analyzed (Figure 2-16). The high-TiO_2 concentrations in clinopyroxene suggest derivation from a TiO_2-rich magma. Analyzed spinels from this sill, however, have relatively low TiO_2. Based on the limited data for TiO_2 in clinopyroxene and in spinel from the same rock, however, relations are not straightforward (Figure 3-4). Samples from the upper sills show increasing TiO_2 in clinopyroxene is associated with increased TiO_2 in spinel. In contrast, the basal sills show a negative correlation between TiO_2 in clinopyroxene and TiO_2 in spinel.

3.1.3. Basal ultramafic unit

The basal unit consists of of the basal dunite sill and the basal wehrlite sill, both of which are interpreted to be sills based on their mineralogical textures and whole rock chemistries.
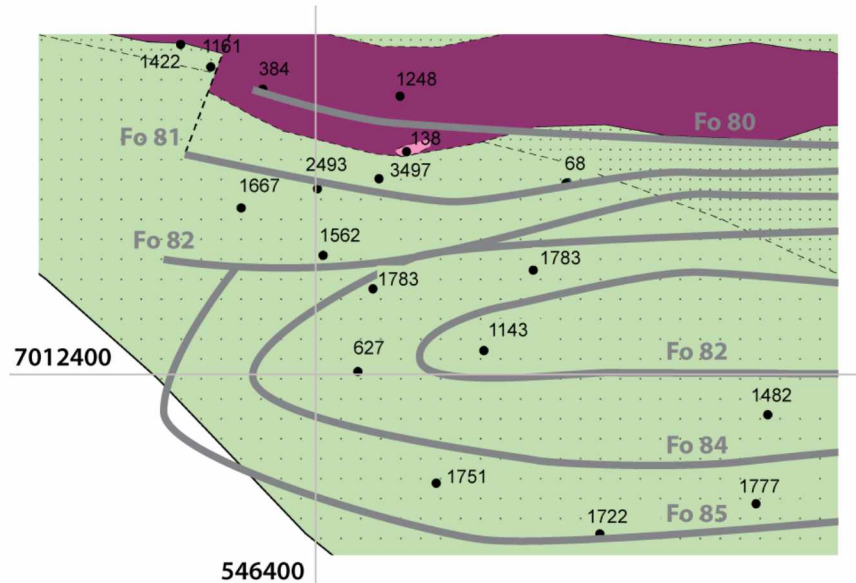
Figure 3-5. Sample locations for the basal dunite sill with Ni (ppm) values from XRF analysis labeled. The grey contour lines are the olivine contours traced in Figure 2-11.

The dunite sill is almost completely free of clinopyroxene. This sill is thicker and had greater space to undergo in situ differentiation, so olivine exhibits a greater range in Fo compositions. Olivine ranges from Fo 85.8 along the margins to Fo 82.3 at the center of the sill. Ni values from XRF analyses decrease systematically towards the center of the sill, suggesting the center of the sill was more evolved

than the margins (Figure 3-5). The absence of intercumulus minerals throughout most of the sill indicates it was likely emplaced at a high temperature and underwent slow cooling in order for the interstitial material to have been able to escape.

Individual samples of olivine have almost no variation in Ni values (Figure 2-12). The majority of samples in this sill have a positive correlation between decreasing forsterite and decreasing Ni values. This indicates Ni was being depleted due to fractional crystallization of olivine rather than a large sulfur saturation event. Olivine in the lowest Ni sample (sample 15LL133) has ~550 ppm Ni and Fo 83.5. Olivine in the sample with the lowest Fo (Fo 82.3 in sample 13RN393) has ~1050 ppm Ni. It is possible that the Ni depletion observed in 15LL133 is due to Ni being removed from the melt by a late stage, small sulfur saturation event. There are small disseminated sulfides in the core of the sill but the majority of the sill lacks any sulfide mineralization.

The basal wehrlite sill forms the base of the Alpha complex. This sill has margins of serpentinized dunite that grade inwards to wehrlite and clinopyroxenite. The wehrlite is much thicker in this sill indicating that clinopyroxene saturation was reached early on in the residual melt during crystallization. Clinopyroxene increases in grain size and abundance towards the sill center. Clinopyroxene saturation having been reached early on is also evidenced by the absence of intercumulus clinopyroxene. This resulted in olivine-clinopyroxene adcumulate textures. The clinopyroxene from this sill has intermediate TiO_2 values between the central feldspathic sill and the upper ultramafic sills. Values range from 0.3 to 0.6 wt.% TiO_2.

The two samples that fall above and below the positive correlation between Ni in whole rock and Ni in olivine are from this sill (Figure 2-14). Sample 13RN391 has high Ni in the whole rock analysis and lower Ni in olivine. This is due to the presence of extra Ni in sulfide in the sample. Sample 13RN386 is more complicated. This sample has high Ni in olivine and low Ni in the whole rock analysis. This sample is from a wehrlite with high clinopyroxene content and <30% olivine, so low olivine in the sample resulted in low Ni in the rock. However, this sample is also a major outlier among other samples within the sill, having significantly higher Fo and Ni values. Such primitive olivine within wehrlite implies that the olivine in this sample was in disequilibrium with the surrounding melt at the time of solidification of the sill.

3.2. Spinel as a petrogenetic indicator

3.2.1. Primary composition

Trend 1 (Figure 2-21) may represent primary magmatic changes in spinel. Spinels that fall along trend 1 all have <3.0 wt.% TiO_2 and <0.3 wt.% Fe^{3+}. The earliest spinels to crystallize from the upper ultramafic sills are slightly more Cr-rich and Ti-poor. Chrome spinels from the upper troctolite fall along trend to spinels from the upper ultramafic sills. These spinels are slightly higher in TiO_2 than the upper sills because they crystallized from the residual melt that was slightly more fractionated and enriched in TiO_2. Primary spinels from the central feldspathic sill have a slightly more Al-rich, Cr-poor primitive composition. While spinels from this sill generally have low Ti contents (Figure 3-1), many of them have inclusions of a Ti-rich mineral, likely ilmenite (Figure 2-24, above). The ilmenite inclusions are different from the ilmenite lamellae that result from oxidative exsolution (as is in Figure 2-23, below) and rather appear to have crystallized first, with later spinel crystallizing around these grains. This is potentially evidence for a high-Ti parental magma to the central feldspathic sill.

3.2.2. Post-cumulus alteration

Spinels that follow trend 2 (Figure 2-21) are most likely not magmatic and are hydrothermal. The Ti-enrichment in spinels along this trend is likely the result of post-magmatic enrichment from hydrothermal fluids. Cumulus chrome spinels have been shown to react rapidly with interstitial evolving liquid (Roeder and Campbell, 1985; Roeder, 1994). Spinel can be altered even when enclosed in olivine, though alterations are strongest when chrome spinel directly reacts with interstitial liquid (Roeder and Campbell, 1985). Its composition can be substantially changed including a decrease of the Mg, Cr, and Al contents and an increase in Fe and Ti contents.

The Alpha chrome spinels along trend 2 have considerable variation in TiO_2 contents. Distribution of the Alpha spinels on the $Fe^{3+}/(Fe^{3+}+Cr+Al)$ vs. TiO_2 diagram in Figure 2-21 shows that the Alpha spinels along trend 2 were enriched in up to 5.5 wt.% TiO_2. Ti-rich spinel solid solution is stable at high temperature, however, during cooling in oxidizing conditions Ti is released from the spinel structure, forming ilmenite lamellae (Figure 2-23, below; Spencer and Lindsley, 1981) according to the equation:

$$6Fe^{2+}{}_2TiO_4 + O_2 \rightarrow 2Fe_3O_4 + 6FeTiO_3$$
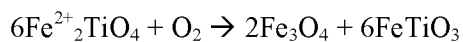
These lamellae occur in a number of the Alpha spinels and are not restricted to a single type of sill. Formation of the ilmenite lamellae is also accompanied by redistribution of other elements. None of the grains that contain ilmenite lamellae exhibit significant zoning. Fe_2O_3 content increases as oxidative-exsolution proceeds so Cr, Mg, and Al were depleted in the mineral and zoning is no longer apparent.

Spinels from highly serpentinized rocks fall along the more Fe^{3+}-rich end of trend 2 and are usually overgrown by magnetite rims and veinlets. The magnetite formed during serpentinization of

olivine. These grains show no evidence of elemental zoning but can have ilmenite lamellae or rims with ilmenite blebs (Figure 2-22, below). Spinels in the most highly serpentinized rocks exhibit the most intensive alteration to magnetite and have sharp increases in Fe^{3+} and Cr (Figure 2-21). Many of these grains also exhibit chlorite aureoles (i.e., intergrown chlorite, serpentine, and magnetite; Figure 2-22, above; Figure 2-24, below). The chlorite areole is the result of Al diffusing out of magmatic spinel, which promotes the formation of chlorite around the grain and leaves behind an Fe-, Cr-rich spinel. Mellini et al. (2005) described the process according to the reaction:

$$MAl_2O_4 + 1.5\ M_3Si_2O_5(OH)_4 + H_2O + 0.083\ O_2 \rightarrow M_5AlSi_3AlO_{10}(OH)_8 + 0.167\ M_3O_4$$

Al-spinel   serpentine   chlorite   Cr-magnetite
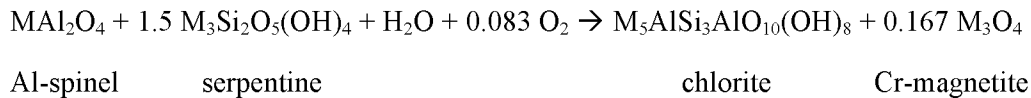
The formation of chlorite can be solely derived from Al-spinel alteration and does not require involvement of plagioclase. Thus, the chloritic aureoles don't indicate a plagioclase bearing protolith (Mellini et al., 2005). This may be why only the highly serpentinized rocks exhibit chlorite aureoles, while spinels from the feldspathic sill do not exhibit these aureoles.

Spinels from the central feldspathic sill exhibit a different trend from other spinels in the complex. These spinels are from variably serpentinized rocks but they don't have the same Fe^{2+}-Fe^{3+} enrichment trend that spinels from other serpentinized rocks exhibit. These spinels exhibit Al-rich rims (Figure 2-23, above; Figure 2-24, above) and have decreasing Mg, Cr, and Ti (Figure 2-21, green arrow). The trend of these spinels is similar to the Rum trend (Figure 2-21) described by Barnes and Roeder (2001) and initially observed by Henderson (1975) and Henderson and Wood (1981) for spinels from the Rum layered intrusion. The trend involves an increase in Al as Al replaces Cr and Fe^{3+}. This is accompanied by decreasing $Fe^{2+}/(Fe^{2+}+Mg)$. This trend has been attributed to reequilibration between spinel, intercumulus liquid, plagioclase, and olivine. The decrease in Fe, which is the opposite from normal alteration processes, is a result of the changing Cr/Al ratio in spinel. This affects the activity coefficients of Fe^{2+} and Mg which in turn changes the Fe^{2+}/Mg exchange coefficient (Kd) with the surrounding silicates (Barnes and Roeder, 2001). The central feldspathic sill is high-Al and contains abundant interstitial plagioclase. The exceptionally high-Al contents of rocks in this sill when compared to other rocks in the complex (Figure 3-3) may be the reason for the different trend observed in these spinels.

3.2.3. Implication for tectonic setting

Spinels have been considered important petrogenetic indicators because of their ability to to subtly change according to physico-chemical conditions (e.g., Irvine, 1965; Irvine, 1967; Arai, 1992; Barnes and Roeder, 2001). The relative abundance of Cr and Al in chrome spinel varies significantly with the degree of partial melting and fractional crystallization of the melt and the ratio of Fe^{2+} to Fe^{3+} in the mineral is sensitive to variations in f_{O2}. These diagnostic geochemical characteristics mean chrome spinels are an important petrogenetic indicator (Barnes and Roeder, 2001).

Spinels from the Alpha complex have a strong tholeiitic affinity and plot within the field for spinels from intra-plate basalts (Figure 3-6). Spinels from intra-plate basalts have significantly higher TiO_2 than spinels from MORB and arc magmas (Arai, 1992). Alpha spinels also plot within the fields defined by Barnes and Roeder (2001) for subvolcanic intrusions from flood basalt terrains and layered mafic intrusions (Figure 3-7). These two fields are difficult to distinguish geochemically. Both are characterized by high TiO_2 contents due to cumulus chrome spinel interacting with trapped intercumulus liquid. Included in the category for subvolcanic mafic intrusions from continental flood basalt terrains are the Siberian and Karoo flood basalt provinces, which include the Noril'sk and Talnakh intrusions in Siberia and the Insizwa (Mt. Ayliff intrusion) in the Karoo. The Alpha chrome spinels have significant overlap with spinels from these other large intrusions.
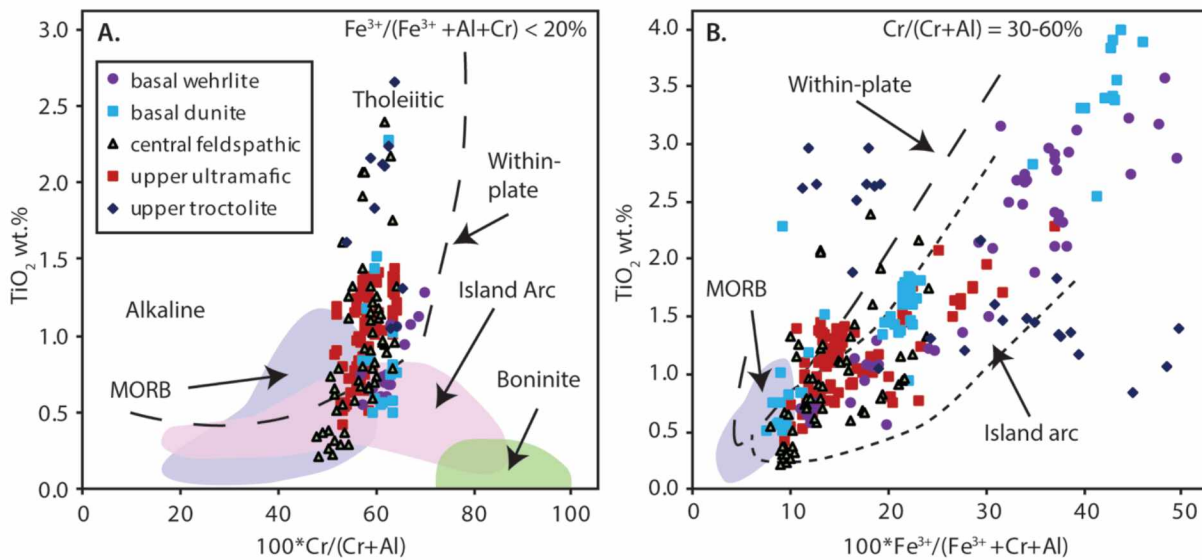
Figure 3-6. Spinel compositions from the study area plotted on spinel tectonic classification diagrams from Arai (1992). Note the poor correspondence, mostly due to the high Fe^{3+} contents of the study area spinels.
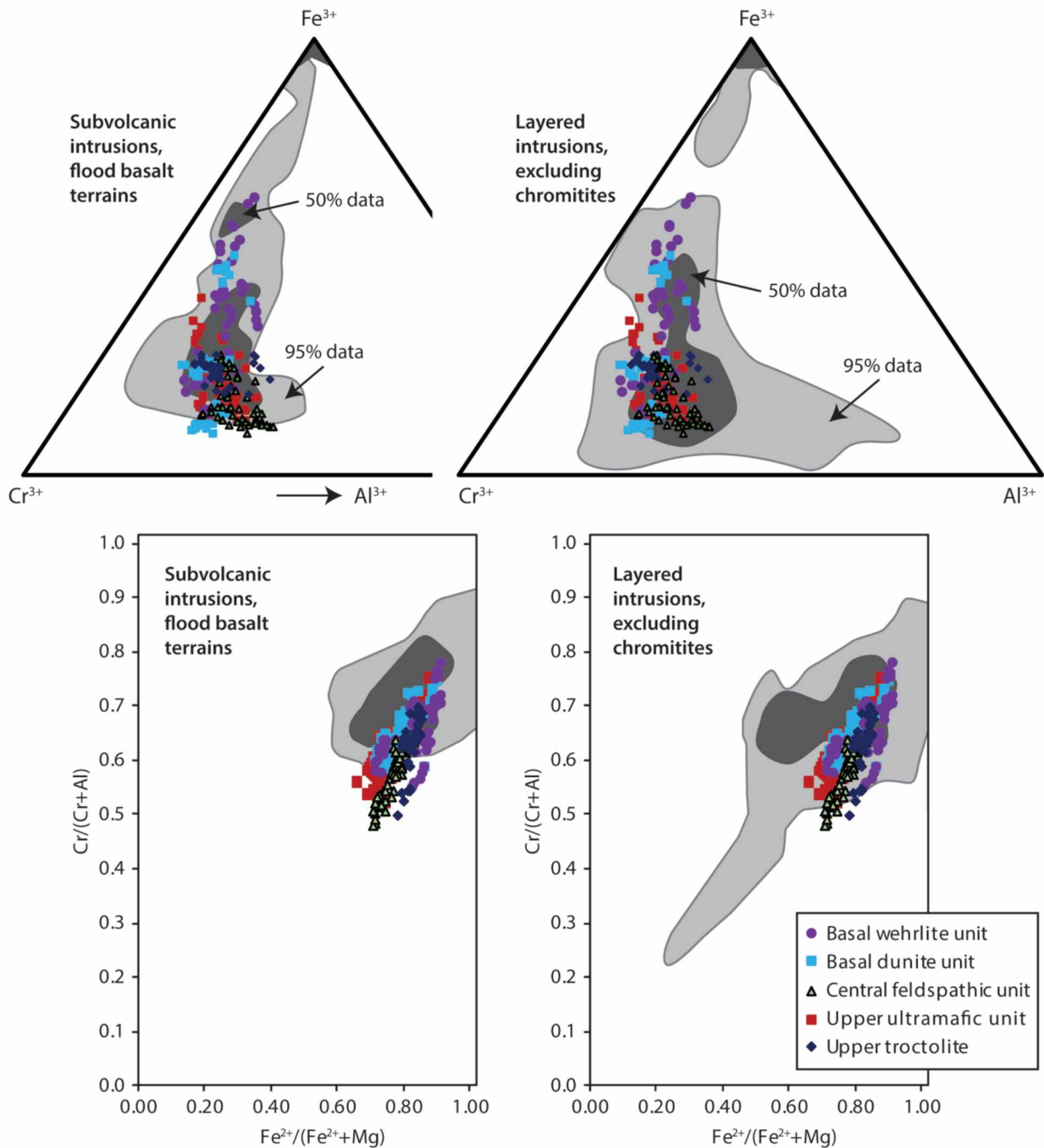
Figure 3-7. Spinel compositions (excluding secondary ferritchromite) from the study area plotted on compositional diagrams of Barnes and Roeder (2001). The data fit better with non-flood basalt related than flood-basalt related subvolcanic intrusions on the ternary diagrams. The data doesn't fit as well within either field on the $Fe^{2+}/(Fe^{2+}+Mg)$ versus $Cr/(Cr+Al)$ plot.

However, spinels are also highly susceptible to alteration. Spinels from the project area have been through variable degrees of alteration, thus they don't fit well on the tectonic classification diagrams from Arai (1992) and Barnes and Roeder (2001; Figure 3-6; Figure 3-7). The composition of chrome spinel can undergo drastic changes during postcumulus interactions, subsolidus exsolution or re-equilibration, low-temperature alteration (serpentinization), and metamorphism (Arai, 1992; Barnes and Roeder, 2001). Common hydrothermal alteration results in increasing $Cr/(Cr+Al)$ and $Fe^{3+}/(Fe^{3+}+Cr+Al)$ in spinel (Mellini et al., 2005). Therefore, spinel compositions can't be interpreted solely in terms of igneous processes.

3.3. Parental magma composition and comparison to the Nikolai magma series

Variations in rock and mineral compositions indicate that the Alpha complex was formed from multiple magmatic inputs that created a complex of sills stacked on top of one another. Given the three different TiO_2-Mg number trends observed in clinopyroxene, it seems plausible that the three units were formed from three different parental melt compositions.

3.3.1. Estimation of the parental melt composition

The composition of early cumulus olivine can be modified by fractional crystallization, subsolidus re-equilibration with trapped interstitial silicate liquid, and re-equilibration with a sulfide liquid (Li et al., 2003). Ni and Mg are compatible in olivine, and accordingly decrease in a melt with fractional crystallization. Fe is less compatible in comparison to Mg, thus olivine crystallizing from a trapped silicate liquid will become poorer in forsterite (Fo) component as the trapped liquid fractionates further. Postcumulus diffusion of Fe and Mg in olivine will result in olivine that is poorer in Fo than the original cumulus material. This is referred to as the "trapped silicate liquid shift" (Barnes, 1986). Discrete and poikilitic olivine cumulate crystals are inevitably subjected to this alteration effect, resulting in lower Fo contents.

As a magma crystallizes, the MgO/FeO ratios of the melt and the crystallizing olivine decrease. Partitioning of Fe and Mg between olivine and the melt can be used to estimate the MgO/FeO molar ratio of the melt in equilibrium with olivine in the Alpha complex. Roeder and Emslie (1970) found the partition coefficient between olivine and melt (in mol):

$$Kd = (FeO/MgO)^{olivine}/(FeO/MgO)^{magma} = 0.3 \pm 0.03$$

However, considerable work in the last 40 years (e.g., Toplis, 2005) shows that a single value for all olivine compositions and temperatures is unrealistic. Using equations given in Toplis (2005) I estimate a value of Kd for a high-Fo olivine (Fo 80-90) at approximately 0.32. Applying this Kd to the Alpha complex sills can help estimate the MgO/FeO ratio of the parental magma.

By rearranging this equation, the Mg number of the parental melt can be calculated. Substituting Mg number $(100*\text{atomic Mg/Mg+Fe}^{2+})$ to the equation, the equation for the parental melt becomes:

$$\text{Mg no.}^{\text{liquid}} = 100 / ((1/Kd) \times (\text{FeO/MgO})^{\text{olivine}} + 1)$$

Applying this equation to the most primitive olivine from each of the major sills indicates that the parental melts require Mg numbers of 64-68 (Table 3-1) to produce the Alpha complex olivine compositions.

Table 3-1. Calculated* Mg number for parental melts of ultramafic rocks in the study area.

Unit	Maximum Olivine Mg#	Calculated Melt Mg#	
upper ultramafic	86.5	67	+/-2
central feldspathic	84.6	64	+/-2
basal dunite	85.7	66	+/-2
basal wehrlite	86.9	68	+/-2

* Calculated using Kd = 0.32

In order to compare the calculated Mg numbers to those for Nikolai Greenstone, I used a database made from a collection of all available analyses, including those from Greene et al. (2008), Twelker et al. (2014), Wypych et al. (2014), and Wypych et al. (2015a). Calculating a Mg number for a rock requires knowing the amount of iron as FeO, and not simply the total iron content. As most of the data only give total iron, and basalts are commonly oxidized (so their current Fe_2O_3/FeO ratios do not reflect their original ratios), it has been customary to assign a standard ratio of Fe_2O_3/FeO. Brooks and Platt (1975), following earlier workers, suggested using 0.15 for the ratio. That value is commonly employed (e.g., Reichow et al., 2005). Consequently, I used Fe_2O_3/FeO of 0.15 in calculating Mg number for the various Nikolai basalt analyses in my database.

Because the bulk of the Ni in most of the rocks is present in the olivine, I also calculated the Ni content of a melt in equilibrium with the olivines I analyzed. Recently determined experimental values for Kd Ni in olivine (= ppm Ni in olivine/ppm Ni in melt) range from 5 to 15 (Mysen, 1978; Pedersen, 1979; Nabelek, 1980; Seifert et al., 1988; Kloeck and Palme, 1988). I chose a value of 10 as the midpoint of the range, and a value given by several studies (e.g., Nabelek, 1980).

A plot of Mg number vs. Ni concentration (Figure 3-8) shows that in general Ni increases in Nikolai basalt with increasing Mg number. Although the data is sparse at low Mg number, the data suggest that Upper Nikolai was derived from a higher Ni parent than was Lower Nikolai. The drop in Ni with increasing Mg number suggests that typical Nikolai basalt was derived from a primitive Nikolai basalt by olivine fractionation. All of my olivine compositions are in equilibrium with a basaltic melt with

66

a reasonable Ni concentration, suggesting that these olivines crystallized from a Nikolai-like melt. Most olivine from the upper sills is relatively low in Ni (Figure 2-12), thus Ni concentration for the melt that was in equilibrium with this olivine is accordingly low for a given Mg number (Figure 3-8). Conversely, olivine from the central feldspathic sill was in equilibrium with a melt of higher Ni content, most similar to the data for Upper Nikolai (Figure 3-8). Olivine compositions from the basal sills are more complicated. The most primitive olivine from the study area is from the basal wehrlite (Figure 2-12); it plots with the high-Ni group. Many of the other olivines plot variably with the higher- or lower-Ni groups.
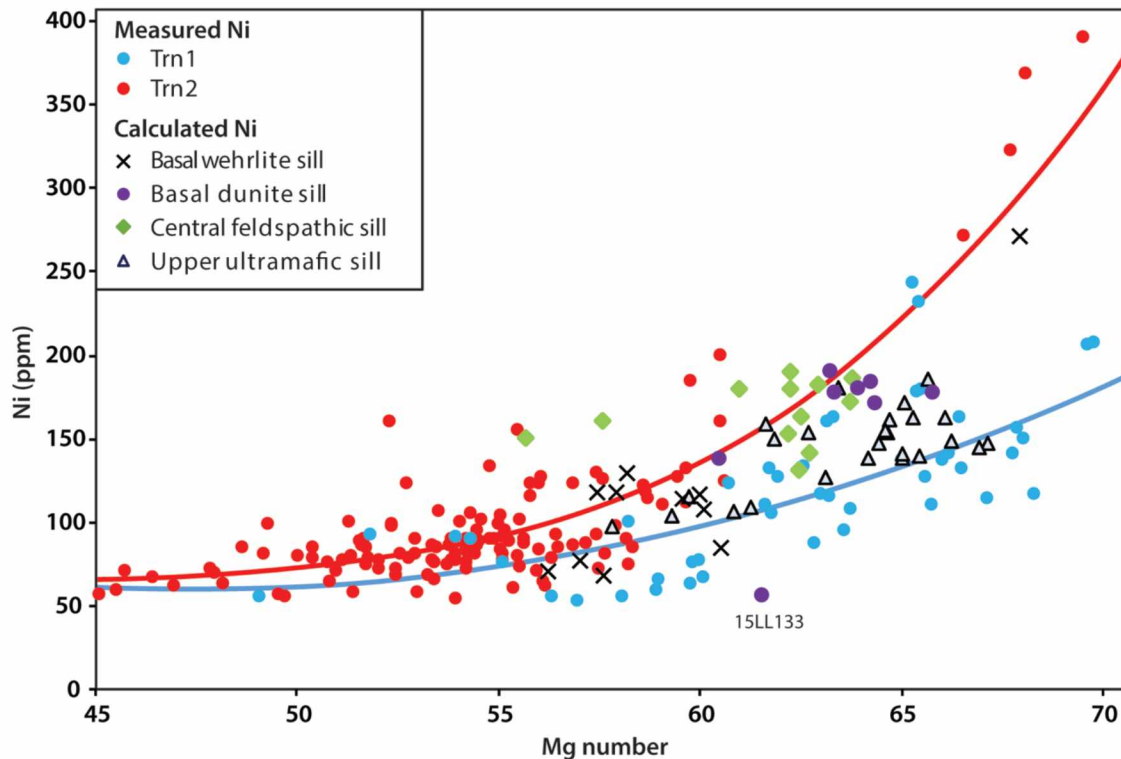
Figure 3-8. Calculated Mg number vs. Ni concentration in least-altered Nikolai basalt samples with calculated melt compositions in equilibrium with analyzed olivine from the study area. The red line is the best-fit curve through the Upper Nikolai data; the blue line is the best fit through the Lower Nikolai data. Nikolai basalt data is from Greene et al. (2008), Twelker et al. (2014), Wypych et al. (2014), and Wypych et al. (2015a). Sample 15LL133 has olivine with anomalously low Ni (Figure 2-12) and plots well below the others.

Matching olivine compositions in the ultramafic rocks of the study area with specific Nikolai basalt compositions may be problematic, as olivine compositions in the study area have been potentially modified by reaction with magmatic sulfide (see ahead). However, with the exception of sample 15LL133 (Figure 3-8) with anomalously low Ni (Figure 2-12), all the study area olivines have compositions

permissible for equilibrium with a basaltic-composition melt. This data implies that the ultramafic rocks of the study area are the products of fractional crystallization from a primitive basaltic melt.

3.3.2. Clinopyroxene as a monitor of the parental melt

Clinopyroxene is present in all rock types and sills in the study area, thus it is an ideal tracer for magma evolution. Clinopyroxene has a significant compositional range with Mg numbers of 83-93 and TiO_2 of 0.3-0.95 wt.% (Figure 3-9). The ranges in clinopyroxene composition are related to both differences in the bulk composition of the parental melt and to magmatic fractionation. Clinopyroxene monitors the course of crystallization: with a decrease in Mg number, the average wt.% TiO_2 increases (Figure 3-9). Clinopyroxene compositions can be related to both different parental magmas and to different Nikolai basalts, due to the intrinsic differences in TiO_2 content (Greene et al., 2008), between the Lower Nikolai (low-TiO_2) and Upper Nikolai (high-TiO_2). Clinopyroxene compositions can be related to basaltic magma compositions through Kd values.
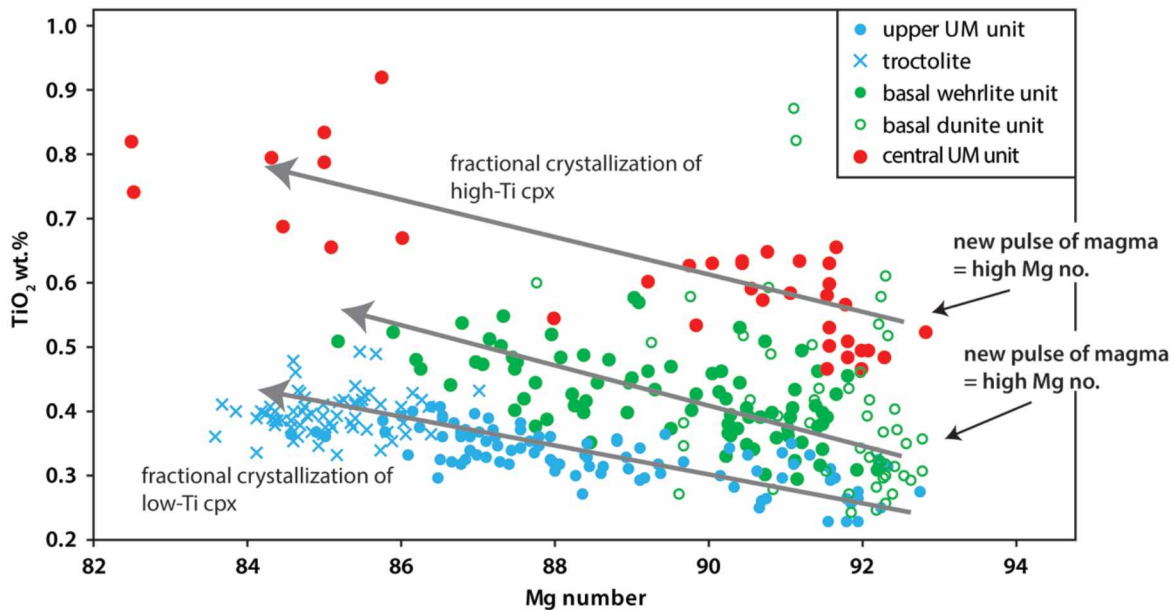
Figure 3-9. Clinopyroxene compositions from the study area with three apparently different parental magmas identified. Note that the single sample from the basal dunite has compositions that overlap both the high-Ti and low-Ti groups.

Unfortunately, as with Ni and Fe/Mg in olivine, Kd values for clinopyroxene also vary. Figure 3-10, for example, shows a wide range of experimentally-determined values for Kd (TiO_2) in clinopyroxene (= TiO_2 in clinopyroxene/TiO_2 in basaltic melt). In part this spread in values represents different compositions of pyroxene, different temperatures, different pressures, and different oxidation

states. I have chosen the Kd of 0.45 determined by Hauri et al. (1994) as approximately mid-way between the various measurements, but recognize that any value between approximately 0.2 and 0.6 is feasible.
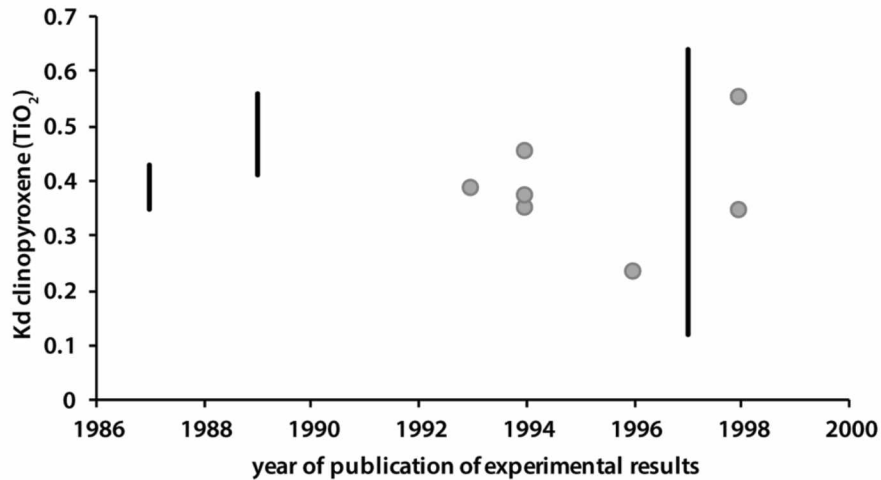
Figure 3-10. Published Kd values for TiO_2 in clinopyroxene and basalt vs. year of publication. Data from: Dunn (1987), Johnson and Kinzler (1989), Hart and Dunn (1993), Johnson (1994), Jenner et al. (1994), Hauri et al. (1994), Skulski et al. (1994), Johnson (1998), and Vannucci et al. (1998). Solid line indicates a range of values were given.

Similarly, experimentally determined Kd (Fe/Mg) for clinopyroxene values vary widely, although it is common to assume a constant value of 0.23-0.28, based on studies by Grove and Bryan (1983) and Sisson and Grove (1993). Bédard (2010) reviewed the extensive literature and provided equations for estimating this Kd employing temperature, pressure, melt, and clinopyroxene composition. I estimate a value of 0.2 as most appropriate for the low-pressure, moderately-high temperature crystallization conditions and for the high Mg number clinopyroxene in my study area.

Using the Kd of 0.45 (TiO_2) and 0.2 (Fe/Mg), I calculated the magma composition in equilibrium with each of my average clinopyroxene compositions (Figure 3-11) and plotted these on a plot of Nikolai basalt compositions. I used the same Nikolai basalt data set described earlier and the same calculated Mg numbers. Combining these two data sets shows that the upper sills contain clinopyroxene that equilibrated with magmas similar in composition to the Lower Nikolai basalt. Conversely, the central feldspathic sill contains clinopyroxene that equilibrated with a high-TiO_2 magma, similar to that of the Upper Nikolai basalt. Gabbroic dikes in the upper sills (Figure 2-1) occur just above the contact with the central feldspathic sill. The compositions of these gabbros are compatible with derivation from the most evolved part of the central sill (Figure 3-11). Clinopyroxene from the basal sills have compositions intermediate between those of the upper and central sills. The calculated melt with which they equilibrated is in-between typical Upper Nikolai and typical Lower Nikolai basalt. In summary, this data shows that the

upper ultramafic sills could have crystallized from a Lower Nikolai basalt and the central feldspathic sill could have crystallized from an Upper Nikolai basalt.

The intermediate trend is more problematic because it falls between the two magma series. The intermediate trend appears to overlap the compositions of many low-TiO$_2$ basalts. I do not know the relative ages of the basalt samples that follow the intermediate trend, but they might be transitional in time between the clearly low-TiO$_2$ Lower Nikolai and the clearly high-TiO$_2$ Upper Nikolai. That is, the intermediate trend could have been the result of magma mixing between the last phase of Lower Nikolai basalt and the early stages of Upper Nikolai basalt magmatism.
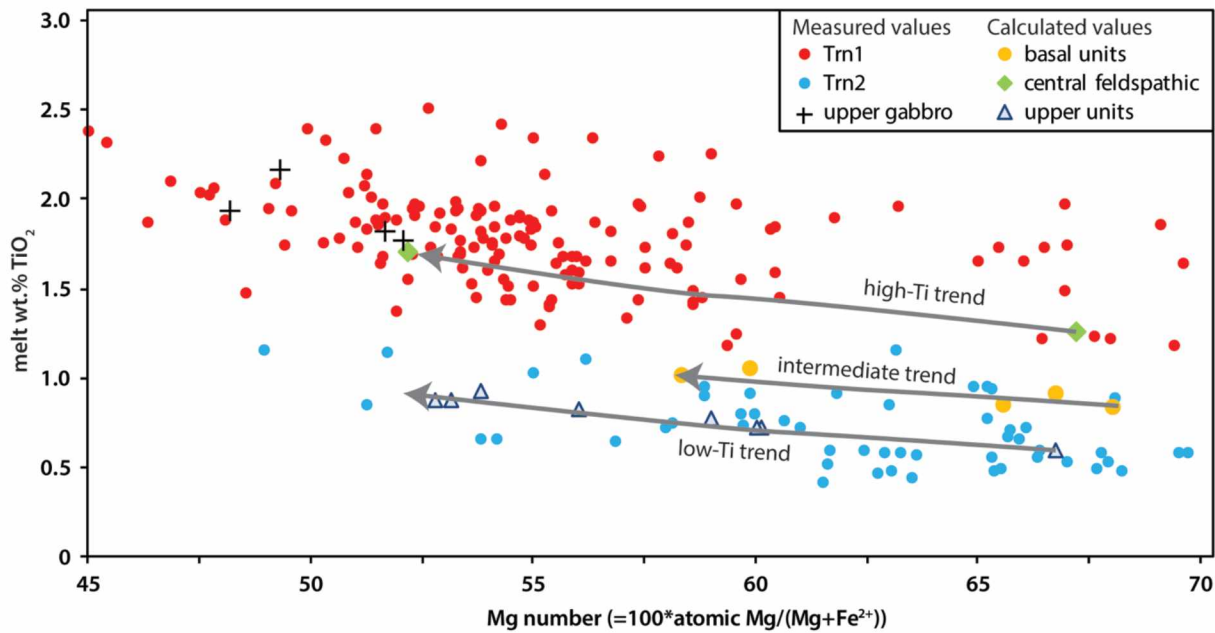
Figure 3-11. Mg number versus wt.% TiO$_2$ for Upper and Lower Nikolai basalt and for high-TiO$_2$ gabbro dikes in the upper sills compared to the theoretical equilibrium melt compositions calculated from average clinopyroxene compositions in the study area samples. Nikolai basalt data from sources listed with Figure 3-8. Clinopyroxene calculations are described in the text.

Evidence for multiple magma types with different pyroxene compositions is shown by a plot of normative diopside versus wt.% TiO$_2$ for ultramafic (non-gabbroic) rocks of the study area (Figure 3-12). The clearest trends are seen with rocks of the upper sills and the basal wehrlite: rock wt.% TiO$_2$ is directly related to the amount of normative diopside, hence to the abundance of clinopyroxene. The non-zero intercepts are due to TiO$_2$ in non-clinopyroxene minerals, presumably spinel and ilmenite. The slopes provide an estimate of the TiO$_2$ concentration in clinopyroxene (and broadly match those shown on Figure 3-9). While the data for the central feldspathic sill do not extend to very large clinopyroxene abundances, the limited data yield a steeper slope than the others, consistent with higher-TiO$_2$ clinopyroxene in that unit (Figure 3-9; Figure 3-12). The data for the basal dunite sill do not yield a

simple line, rather the two rocks with >5% normative clinopyroxene (including sample 13RN393) have anomalously higher TiO$_2$. Sample 13RN393 also contains early clinopyroxene with lower TiO$_2$ cores rimmed by high-TiO$_2$ clinopyroxene margins (Figure 2-17).
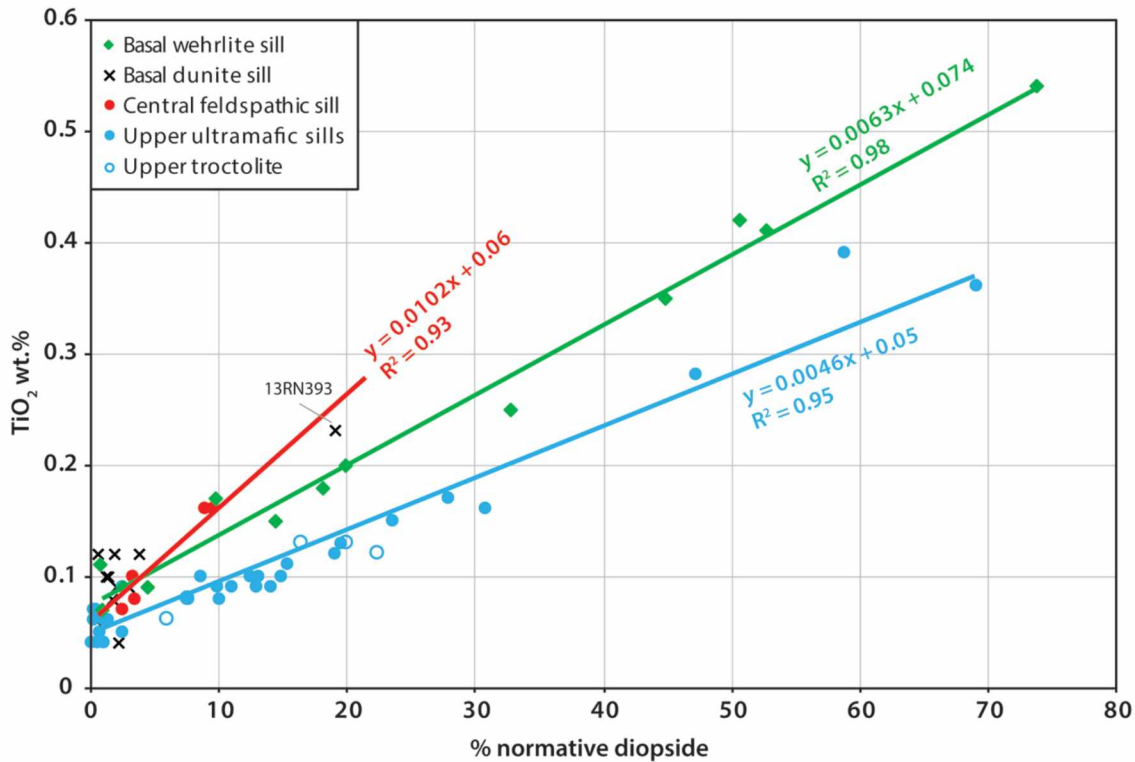
Figure 3-12. CIPW normative diopside vs. wt.% TiO$_2$ for ultramafic rocks of the study area. Sample 13RN393 contains both very high- and low-TiO$_2$ clinopyroxene.

3.3.3. Evidence for magma mixing in the basal units

I have previously shown that two samples from the basal wehrlite sill contain anomalous olivine. Sample 13RN386 contains olivine with the highest percent Fo and with the highest Ni and shows evidence for resorption (Figure 2-12; Figure 2-19). Sample 13RN385 contains two populations of olivine: Fo 80.7±0.6 and Fo 82.7±0.6 (Figure 2-20). However, neither olivine is in compositional equilibrium with the clinopyroxene (Figure 3-13A). Sample 15LL121 is unique among my analyses as it contains two types of clinopyroxene with Mg numbers of 89±1 and 86±1 (Figure 3-13A,B). The clinopyroxene grains from 15LL121 display compositional variation from Mg number 91 and low (0.35 wt.%) TiO$_2$ to lower Mg number and higher (0.5 wt.%) TiO$_2$. The grains with higher Mg number and lower TiO$_2$ are close to compositional equilibrium with the nearby olivine. The grain with lower Mg number and constant TiO$_2$ contains too little Mg to be in equilibrium with the olivine. In contrast, all other clinopyroxene grains from the basal wehrlite display little variation in either Mg number or wt.% TiO$_2$.

71

Based on the clinopyroxene compositions, the new magma had a Mg number of approximately 58 (i.e., was moderately fractionated). The proposed magma mixing took place after olivine crystallization (which is why the olivine is not in equilibrium with most clinopyroxene) and before all the clinopyroxene in sample 13RN386 crystallized. (Clinopyroxene in 13RN386 shows no significant variation in wt.% TiO_2.) Such a melt would definitely not be in equilibrium with the high-Fo olivine in sample 13RN386 and would cause olivine to dissolve into the new melt. Somewhere in this process the Ni concentration (in the melt) dropped drastically, as olivine in 15LL121 contains approximately 1300 ppm Ni and that in 13RN386 contains only 800 ppm (Figure 3-13C). Because the proposed 'contaminant' magma was of the high-TiO_2 variety, and because low-Fo olivine from the central feldspathic sill (representative of the high-TiO_2 type) contains olivine with 1440-1600 ppm Ni (Figure 3-13C), it seems unlikely that magma mixing alone was responsible for this drop. An alternative is that mixing caused sulfide melt exsolution, which robbed Ni from the silicate melt, and caused low-Ni olivine to form.

Olivine and clinopyroxene in samples 13RN389 and 15LL135 evidently formed after the proposed mixing was complete, as these minerals are in compositional equilibrium (Figure 3-13A) and possess low (approximately 700 ppm) Ni. Both rocks contain more than 50% clinopyroxene and were among the last rocks to crystallize in the basal wehrlite sill.

Evidence for magma mixing in the basal dunite sill comes from the wide range in wt.% TiO_2 in clinopyroxene from sample 13RN393 (Figure 2-17; Figure 2-18; Figure 3-13A). This wide range (Figure 3-9) suggests that at least one clinopyroxene (with low wt.% TiO_2) grew before mixing, one high-TiO_2 grain grew from high-TiO_2 melt, and the majority (with intermediate TiO_2) grew after the mixing was complete. However, because all the clinopyroxenes from the sample have the same range in Mg number (~ 89.5-92.5; Figure 3-9), the contaminant magma must have possessed the same Mg number (of approximately 68) as that of the melt (and crystals) that it mixed with (Figure 3-11). That is, both the old and new clinopyroxene grains in the sample are in approximate Fe/Mg equilibrium (Figure 3-13A) with the olivine. New olivine that grew in the mixed melt would be compositionally indistinguishable from the olivine present before mixing (Figure 3-13D). As sample 13RN393 is in the center of the basal dunite sill, I infer that this mixing event took place after the bulk of this sill had crystallized.
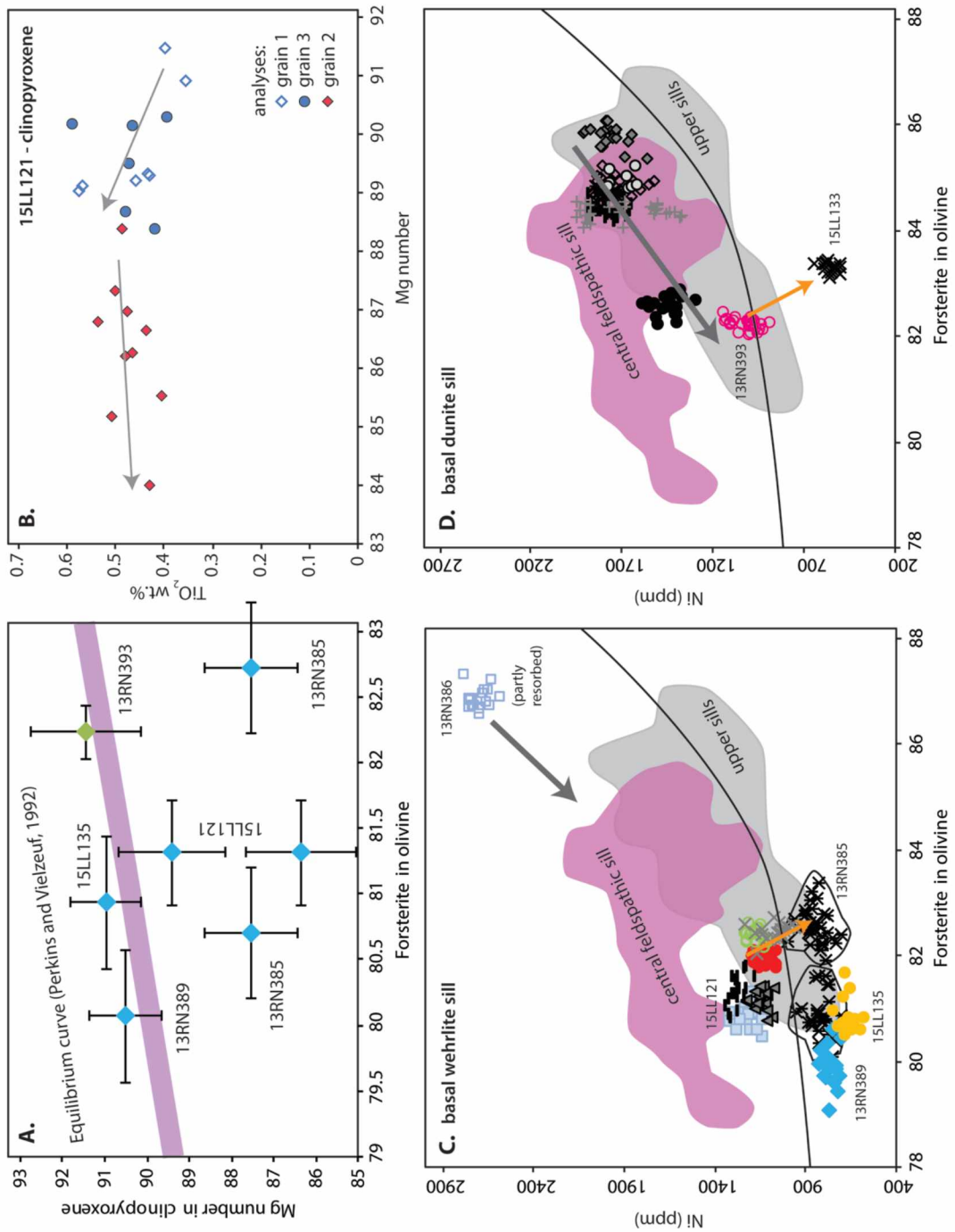
Figure 3-13. Olivine and clinopyroxene compositional systematics in the basal sills of the study area. A) Olivine % Fo vs. Mg number in clinopyroxene of the same sample. The equilibrium curve for olivine-clinopyroxene is taken from Perkins and Vielzeuf (1992). B) Mg number vs. wt.% TiO_2 in three clinopyroxene grains from sample 15LL121, showing two different compositional types. C) Olivine % Fo vs. ppm Ni for olivine samples from the basal wehrlite sill. The outlines of olivine data for the central feldspathic sill (purple) and the upper ultramafic and troctolitic sills (grey) are shown for comparison. D) Olivine % Fo vs. ppm Ni for samples from the the basal dunite sill.

3.4. Ni concentrations in olivine and magmatic sulfide exsolution

Ni concentrations in olivine exhibit patterns (e.g., Figure 2-12) not easily explained. Li et al. (2003) investigated olivine compositions in samples from sulfide-bearing and sulfide absent dikes and sills of the Noril'sk magmatic sulfide deposit, Russia. They showed (Figure 3-14) two major trends: in sulfide-poor rocks (<600 ppm S), Ni in olivine decreases with decreasing Fo and in sulfide-rich rocks (>800 ppm S), Ni tends to increase with decreasing Fo. They explained the former as due to a combination of re-equilibration of olivine with intercumulate magma (so called 'trapped liquid' effect) and continued crystallization of olivine from successively Ni- and Mg-depleted melt. They explained the latter as due to exchange of Ni and Fe between olivine and magmatic sulfide: for a given Ni/Fe ratio in sulfide, olivine will (at equilibrium) possess a constant Ni/Fe ratio. Hence, higher Fe (lower % Fo) olivine will contain more Ni than lower Fe olivine (Li et al., 2003). Figure 3-14 shows typical trends for olivine from Li et al. (2003) superimposed on olivine data from the study area. Olivine data from an unpublished data set from the Geological Survey of Canada (GSC) is shown for samples with sulfur concentrations of 0.13-0.7 wt.% (Figure 3-14A). My data for olivine from the central feldspathic sill (Figure 3-14B) shows patterns similar to those of Figure 3-14A, but with more data points.

One sample in each of Figure 3-14A and B displays the decrease in Ni with decreasing percent Fo trend characteristic of low-sulfide samples from Li et al. (2003). In contrast, none of the samples displays the high sulfide trend. The highest sulfide rocks analyzed by the GSC have 3500-7000 ppm S (0.35-0.7 wt.% S is equivalent to 1-2 wt.% sulfide minerals). Instead, olivine from sulfide-bearing samples exhibits a near-vertical trend: Ni changes considerably with little change in percent Fo (Figure 3-14). This is true for my own data and for data collected by the GSC. Notably, 15LL137 displays a major change in Ni, but 13RN391 from the basal wehrlite sill exhibits no such change.

I propose that olivines from my rocks do not display the same compositional patterns as those of Li et al. (2003) because the olivine from my rocks did not re-equilibrate with magmatic sulfide, as insufficient magmatic sulfide was created. Rather, I propose that the samples with radical changes in Ni concentrations represent olivine grains that grew in melts undergoing Ni depletion through magmatic sulfide exsolution and (or) variably re-equilibrated with silicate magma that became depleted in Ni. Because Ni is strongly fractionated (Kd = 200-400; Rajamani and Naldrett, 1978; Gaetani and Grove, 1997) from silicate melt into sulfide melt, exsolution of 1% sulfide would cause the residual silicate melt to contain approximately 1/3 of its original Ni concentration. For an initial melt with 200 ppm Ni, this would change the equilibrium Ni concentration in olivine to drop from about 2000 ppm to 700 ppm. In other words, exsolution of a small amount of magmatic sulfide would cause a major change in Ni content of the silicate melt, but it would be impossible for this tiny amount of sulfide to equilibrate with very many olivine grains. However, the amount of Ni-depleted silicate melt would be large enough to either

grow new, Ni-poor olivine or to re-equilibrate with previously-formed olivine. In other words, the substantial range in Ni concentrations (at approximately constant percent Fo) seen in many of my olivine grains is evidence for both exsolution of magmatic sulfide and exsolution of only tiny amounts of magmatic sulfide.
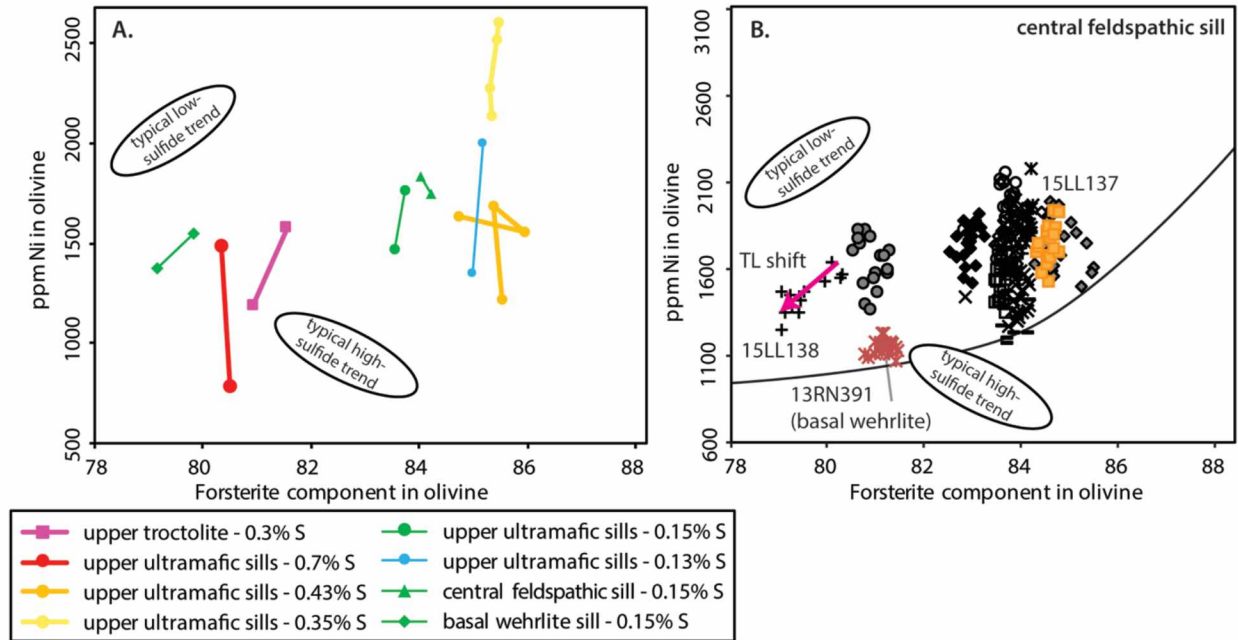
Figure 3-14. Olivine compositional trends from the study area with typical trends for samples from high-sulfide and low-sulfide rocks from Li et al. (2003). A) Olivine data for rocks from the study area from the Geological Survey of Canada (unpublished) with sulfide concentrations in the rocks. B) My data from the central feldspathic sill (+ data from sulfide-bearing sample 13RN391). Sample 15LL137 contains significant excess Ni (Figure 2-12) as sulfide. The sample from the basal wehrlite in A and 15LL138 in B parallel the low sulfide trends of Li et al. (2003).

3.5. Mineralization

Magmatic sulfide is enriched in Ni, Cu, and PGE. It is not easy to distinguish Ni in olivine from Ni in sulfide (or other forms) and PGE analyses are expensive. My best estimate on the original distribution of magmatic mineralization is thus from Cu concentrations in rock. A compilation of surface samples (Figure 3-15) from the Geological Survey of Canada and Pure Nickel Inc. indicates that rocks with anomalous (> 200 ppm) Cu are widely distributed through the map area. Higher values are apparently more common in the upper ultramafic and central feldspathic sills and in the intensely serpentinized rocks near the faulted base of the complex. Such is consistent with my model (based on Ni distributions in olivine) for widespread, but low grade, magmatic sulfide in many of the units.
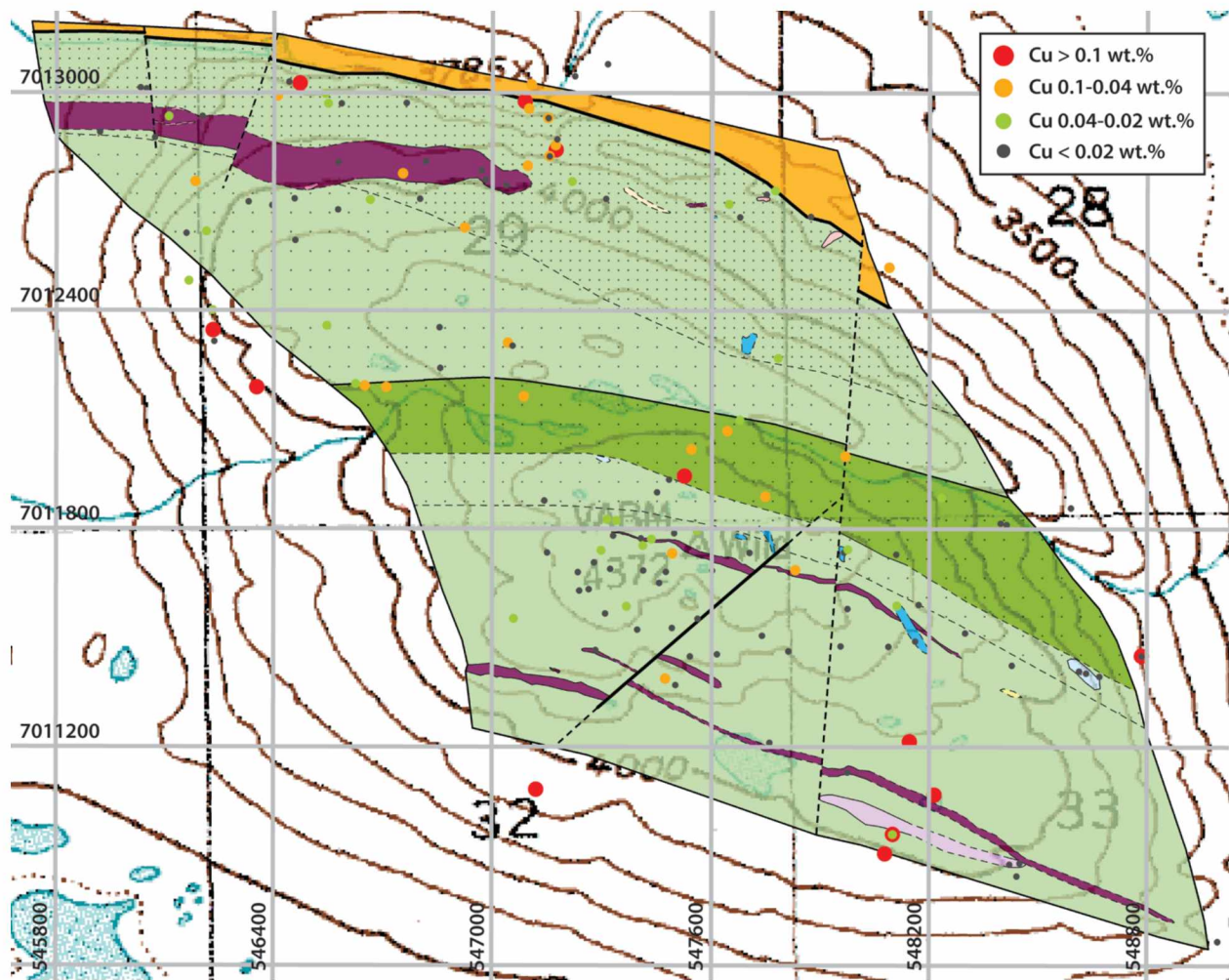
Figure 3-15. Distribution of Cu in surface samples, based on a compilation of samples from the Geological Survey of Canada (unpublished data) and Pure Nickel Inc. (unpublished data).
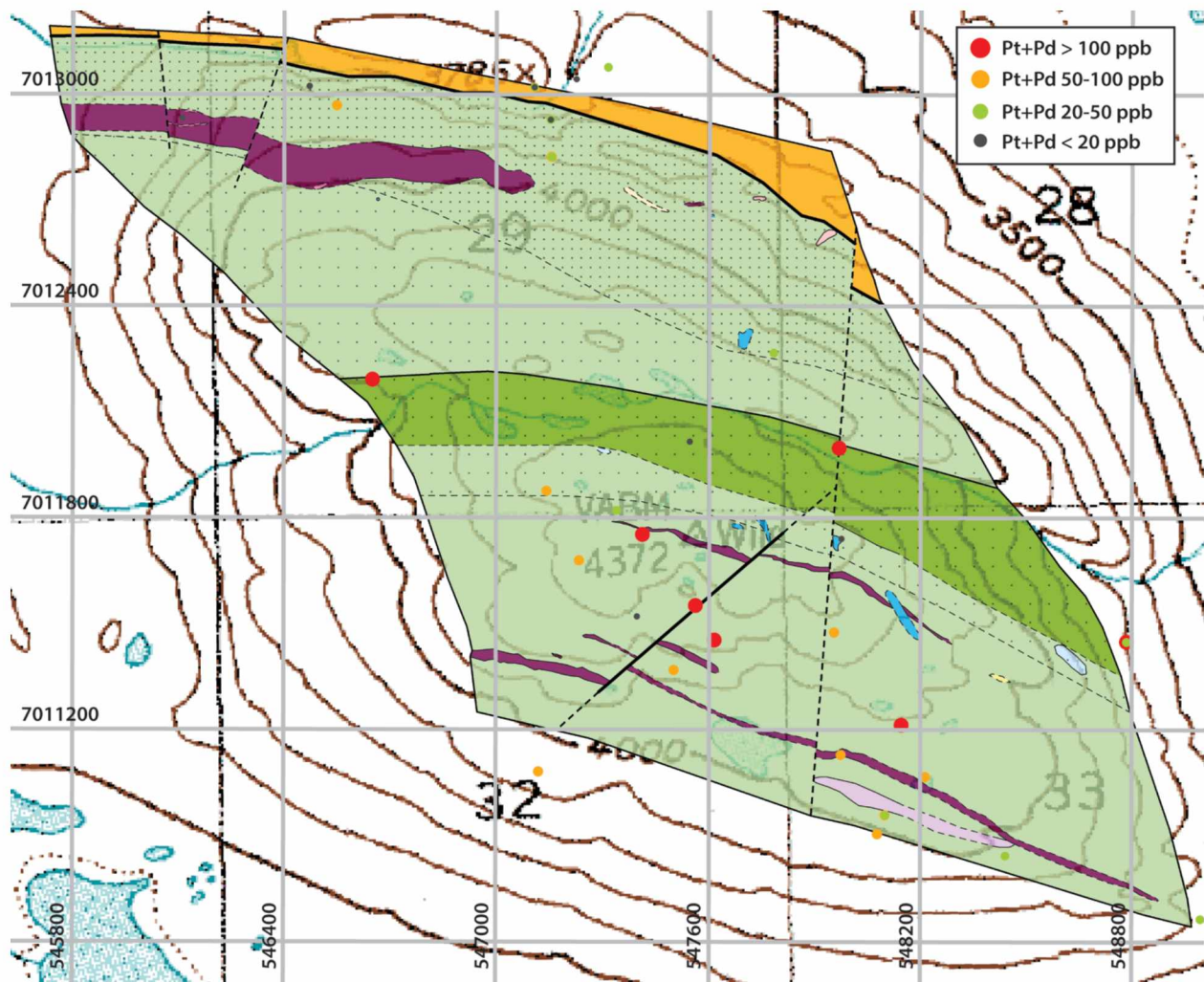
Figure 3-16. Distribution of Pt+Pd in surface samples from the map area. Data is compiled from the Geological Survey of Canada (unpublished data).

Based on a much smaller sample set, higher PGM concentrations in surface rocks of the study area are restricted to the central feldspathic sill and the upper ultramafic sills. In particular, an area near the north margin of the body, the so-called 'ravine gossan' (Figure 1-2) has been intensely sampled by several companies. Pt+Pd concentrations from several dozen samples have been uniformly low.

A compilation of Pd/Pt ratios for all available surface samples from the Alpha Complex (Figure 3-17) shows a potentially significant increase in Pd/Pt with increasing fractionation. The lowest ratios are in dunite (geometric mean = 0.6) and the highest in gabbro (geometric mean = 1.4). Ratios from massive sulfide samples have uniformly high Pd/Pt ratios, with a geometric mean of 80 (Figure 3-17). However, massive sulfide in the Alpha complex has only been identified in the Tres Equis prospect (Figure 1-2), so these samples are only from a small area and are not representative of all mineralization within the

complex. I ascribe the very high Pd/Pt of the Tres Equis prospect to hydrothermal activity, as Pd is considerably more soluble in hydrothermal fluids than is Pt.
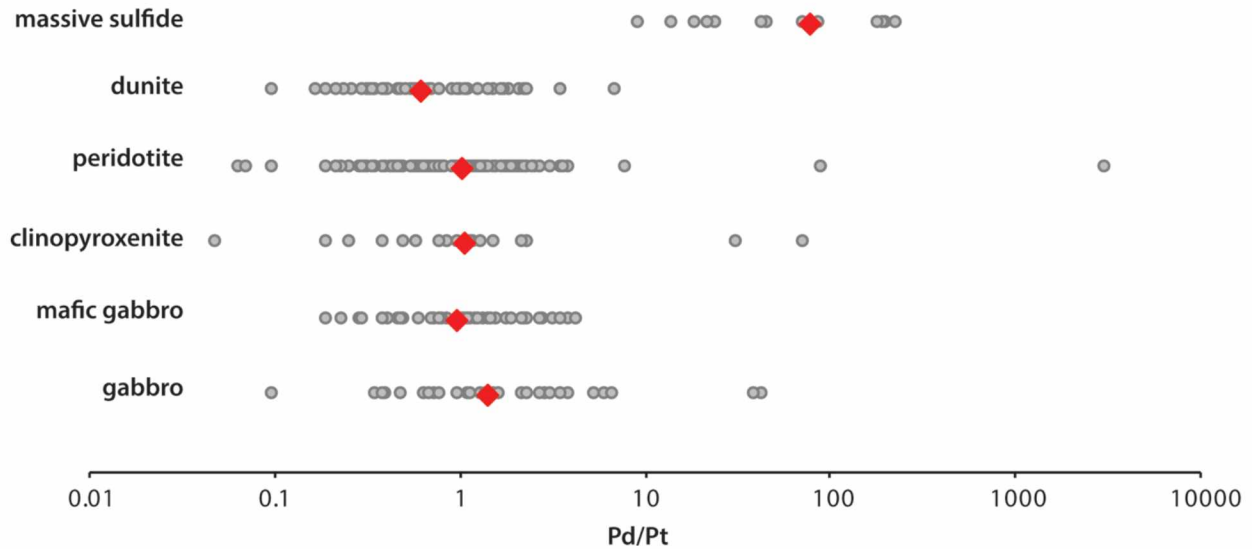
Figure 3-17. Pd/Pt ratios for several hundred surface samples from the Alpha complex. Grey circles represent individual samples; red diamonds are the geometric means of all the samples for a given lithology. Unpublished data from Pure Nickel Inc. and the Geological Survey of Canada.

If not modified by hydrothermal activity, Pd/Pt ratios in rocks can give information about the source. Prior to magmatic sulfide exsolution, Pt and Pd tend to remain in a silicate melt. Once a sulfide melt is formed, the two are equally fractionated into that melt (Barnes et al., 1985).

Data for Nikolai volcanic and gabbroic rocks (Figure 3-18A) seemingly define two different trends: one trend of increasing Pt with increasing Pd (trend 1) and another trend of increasing Pd with decreasing Pt (trend 2). It is not clear what causes this difference. Trend 1 is defined by Lower Nikolai picrite, basalt, and gabbro, as well as by Upper Nikolai picrite and a few samples of Upper Nikolai basalt and gabbro. Trend 2 is solely defined by samples of Upper Nikolai basalt and gabbro. What stands out is that the Lower Nikolai magma series remains along trend 1 over the entire course of its evolution. However, at some point during evolution of the Upper Nikolai magma series, the basalt follows trend 2 and increases in Pd content as Pt decreases. While it has not been determined why these two patterns are present between the Upper and Lower Nikolai basalts, it is likely related to some fundamental difference between the two magma series.
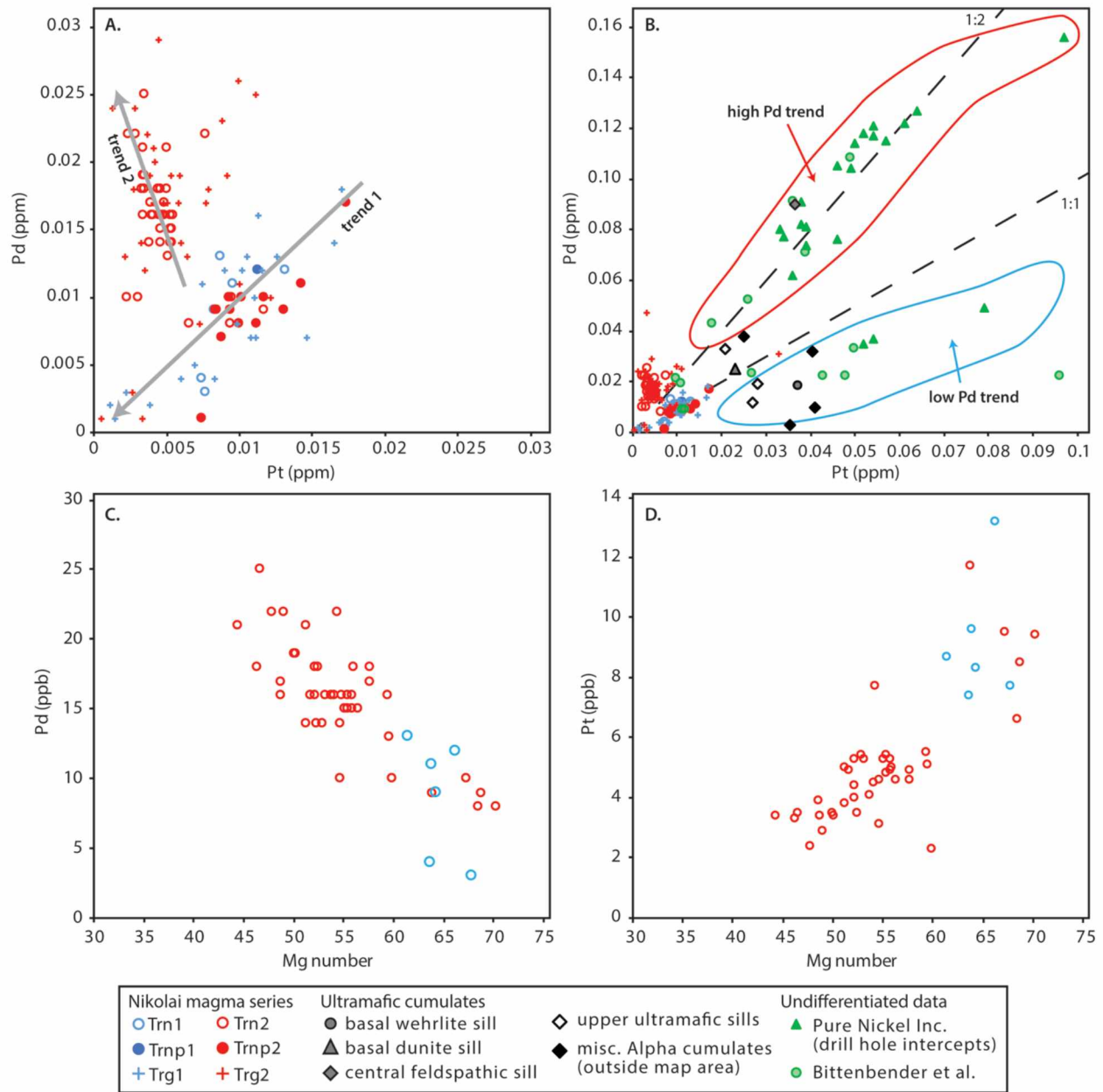
Figure 3-18. Pt versus Pd for (A) samples from the Nikolai magma series and (B) samples from the Alpha complex plotted with Nikolai samples for comparison. Samples with higher PGE concentrations are from more sulfide rich samples. C) Mg number versus Pd for Upper and Lower Nikolai basalt. D) Mg number versus Pt for Upper and Lower Nikolai basalt. Data is from this study, the sources listed in Figure 3-8, Pure Nickel Inc. (2013), and from Bittenbender et al. (2007).

The first trend shows that both Pt and Pd behave as incompatible elements during mantle partial melting. They are initially high and have a positive correlation as they both are removed from the mantle during mantle melting. With increased partial melting they become diluted in the silicate magma. In the presence of an immiscible sulfide liquid, Pt and Pd will partition into the sulfide, recording the original

Pd:Pt ratio of the silicate melt during partial melting. The opposite trend (trend 2) emphasizes the differential behavior of Pt. Pt belongs to the incompatible PGE group, which is characterized by relatively high solubility in mafic silicate magmas (Barnes et al., 1985). However, Pt changes from incompatible during mantle partial melting into compatible during the early stages of crystal fractionation. Thus, Pt is initially extracted from the melt, while Pd remains in the melt until late stages of crystallization. This process produces the negative correlation between Pd and Pt that is recorded in the Upper Nikolai basalt (trend 2; Figure 3-18A). This also results in the positive correlation between decreasing Pt in the melt with decreasing Mg number (increasing fractionation; Figure 3-18D). On the contrary, Pd remains in the silicate melt and increases in concentration with degree of fractionation (Figure 3-18C). Unfortunately, there are only a few analyses that have Pt-Pd data for the Lower Nikolai basalt, so these trends are only clear for the Upper Nikolai basalt.

The ultramafic cumulate samples also exhibit two different trends (Figure 3-18B), one with lower Pd:Pt (< 1.2) and the other with higher Pd:Pt (~2). The low Pd:Pt group falls along the 1:1 Pd:Pt line. Samples in this trend are predominately from the upper ultramafic (low-TiO_2) sills and the basal wehrlite (intermediate TiO_2) sill. The high Pd group is characterized by a 2:1 Pd:Pt ratio. It is important to note this ratio is significantly lower than the Pd:Pt ratios in samples from the Tres Equis prospect (Figure 3-17). The composite sample and two additional samples from the central feldspathic (high-TiO_2) sill are in this group. Other sample analyses in the Alpha complex from Pure Nickel Inc. (2013) and Bittenbender et al. (2007) help to define these two trends, though it is unknown which type of sills these other samples are from.

The two trends presumably record different magma sources for the low- and high-Ti melts. In the map area, the central feldspathic sill is no more or less fractionated than the others, based on olivine with similar Fo compositions from all four sill groups (Figure 2-11; Figure 2-12). However, clinopyroxene compositions demonstrated that this sill was derived from a melt that was higher in TiO_2 than other sills in the map area (Figure 2-16). This was attributed to crystallization from a high-TiO_2, Upper Nikolai parental melt. Thus, the high Pd:Pt ratio in this sill may be attributed to crystallization from the Upper Nikolai basalt, which is higher in Pd relative to the Lower Nikolai basalt (Figure 3-18C).

Samples from the basal and upper sills mostly occur in the low Pd group. Mineralization in the upper ultramafic sills (low TiO_2) is complex. The maximum Cu concentration in rocks generally increases with decreasing normative olivine (Figure 3-19), but each rock type (dunite, clinopyroxenite, wehrlite, and troctolite) exhibits major variation in Cu content. Unfortunately, there is no correlation between Cu and Pt+Pd in these rocks (Figure 3-19). The highest Pt+Pd concentrations are in both dunite and troctolite, with no obvious pattern.
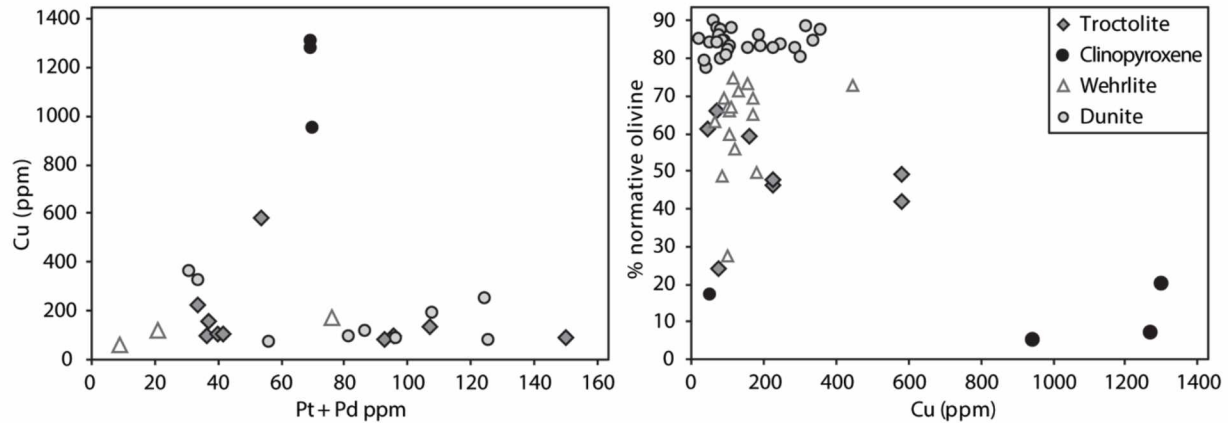
Figure 3-19. Cu and PGM relations in the upper sills of the study area. Data from this study and from unpublished data from Pure Nickel Inc. and the Geological Survey of Canada.

Samples from the basal sills, also fall in the low Pd:Pt group. One sample from the basal wehrlite sill has slightly higher Pt (37 ppb) and Cu (272 ppm) than samples from the upper sills (Figure 3-18). Given the wide range in concentrations for the upper sills, however, the basal wehrlite sample is not unique. The basal sills were derived from mixing of Upper and Lower Nikolai melts; however, they do not define an intermediate trend on the Pt-Pd plot. Figure 3-18C showed that early Upper Nikolai melt is low Pd and Pd only increases as Mg number decreases. If the basal sills were derived from mixing of a late Lower Nikolai melt and an early Upper Nikolai melt, they would remain in the low Pd:Pt group rather than defining an intermediate group.

To summarize, all of the sills exhibit some degree of mineralization, though in most cases it appears that sulfide saturation occurred late in crystallization of the sills. The Pd:Pt ratios of the cumulate samples seem to be mainly affected by the parental melt composition and sulfide accumulation. A low Pd:Pt ratio in the upper and basal sills is consistent with these sills having been derived from Lower Nikolai melt and from magma mixing with an early Upper Nikolai melt. A high Pd:Pt ratio in the central feldspathic sill is consistent with this sill having been solely derived from an Upper Nikolai melt.

Chapter 4 Conclusions

4.1. Petrological model

Field, petrographic, and geochemical results from this study are interpreted to indicate that the Alpha complex is composed of multiple ultramafic sills intruded from two different emplacement episodes involving the Lower and Upper Nikolai basalts.

High forsterite in olivine and low TiO_2 compositions in clinopyroxene from the upper ultramafic sills indicate that these sills were intruded first, as a part of the Lower Nikolai magmatic series. These sills formed through fractional crystallization of the ultramafic extract of the low-TiO_2 series basalt associated with the Lower Nikolai (Figure 4-1A). The absence of chilled margins between sills is likely the result of a high temperature of emplacement. These sills were presumably intruded around the same time as one another based on the similarity of their textures and chemistry, thus the dunitic margins between the different sills are difficult to distinguish. Subsequent to crystallization of the ultramafic sills, the residual, evolved melt migrated out of the sills and was erupted as the Lower Nikolai basalt. The troctolite layer in the upper sills represents one layer where the evolved residual melt was trapped and crystallized plagioclase oikocrysts instead of migrating out of the sill. In a few areas, just below the upper sills, the Lower Nikolai basalt was trapped in the crust and crystallized gabbroic dikes.

The basal, mid-TiO_2 sills were intruded next. Disequilibrium textures and intermediate TiO_2 values in clinopyroxene imply that these sills formed as a result of mixing between the Lower and Upper Nikolai melts. This unit formed during the last stages of the Lower Nikolai magma series and the early phase of the Upper Nikolai magma series (Figure 4-1B). The Lower and Upper Nikolai magma series likely shared some magmatic plumbing, so it's probable these sills represent early pulses of the Upper Nikolai basalts that mixed with late remnants of the Lower Nikolai basalt. These sills then underwent fractional crystallization and the residual melt migrated out of these sills and was extruded as early pulses of the Upper Nikolai basalt.

Lower Fo contents in olivine and high TiO_2 contents in clinopyroxene suggest the central, high-TiO_2 sill was the last to be emplaced. This sill was intruded during the eruption of the Upper Nikolai magma series (Figure 4-1C). During crystallization the sill became highly fractionated and enriched in Al_2O_3 and FeO. This resulted in crystallization of low Fo olivine and orthopyroxene near the core and abundant interstitial feldspar throughout the sill. In several areas, the high-TiO_2, Upper Nikolai basalt was trapped in the crust and formed crosscutting gabbroic dikes. These dikes crosscut both the upper and basal sills.
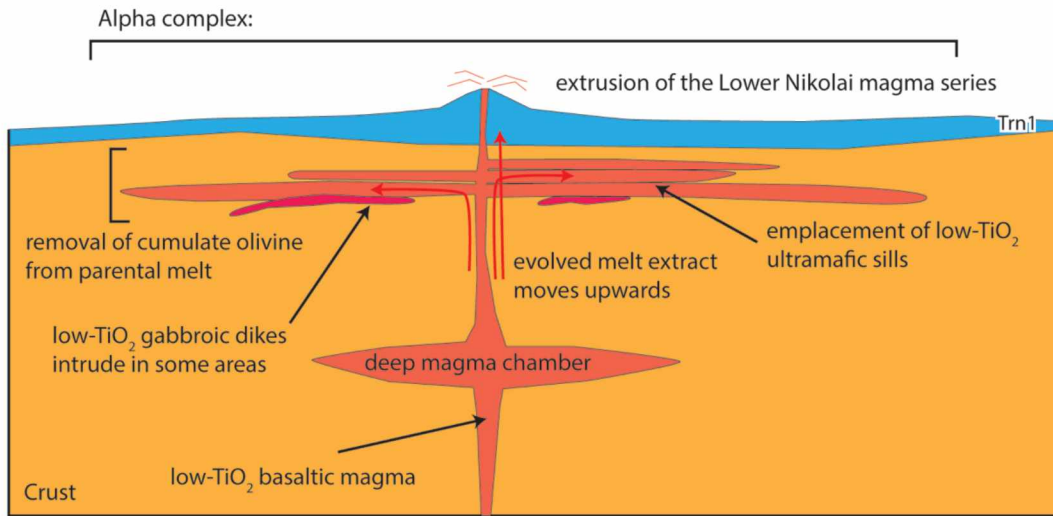
Figure 4-1. A) During the early magmatic stage, extrusive volcanism of the Lower Nikolai magma series dominated. Ultramafic cumulates were extracted from the Lower Nikolai basalt and crystallized the low-TiO$_2$ ultramafic sills. Low-TiO$_2$ gabbroic dikes intruded at the base of these sills.
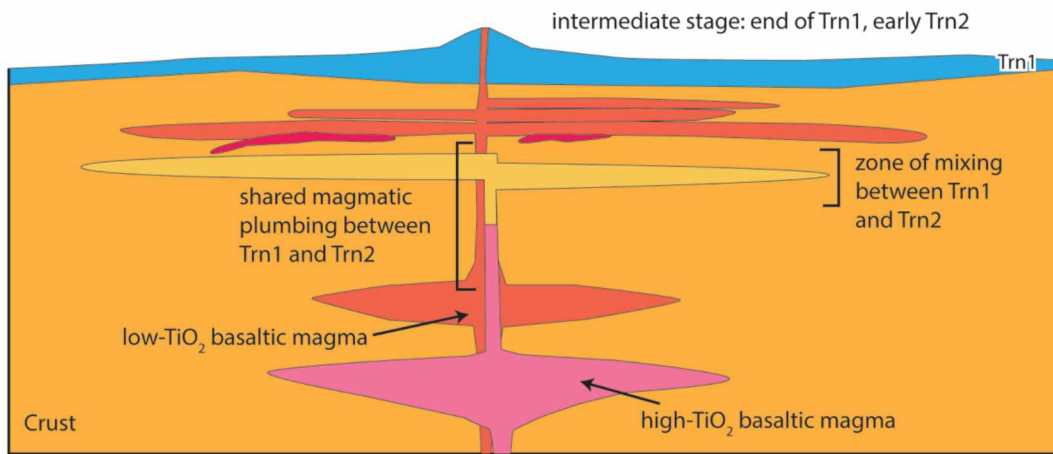
Figure 4-1. B) The intermediate TiO$_2$ sills were intruded next. These sills formed as a result of shared magmatic plumbing between Trn1 and Trn2 and formed as Trn1 magmatism was coming to an end and Trn2 magmatism was just beginning.
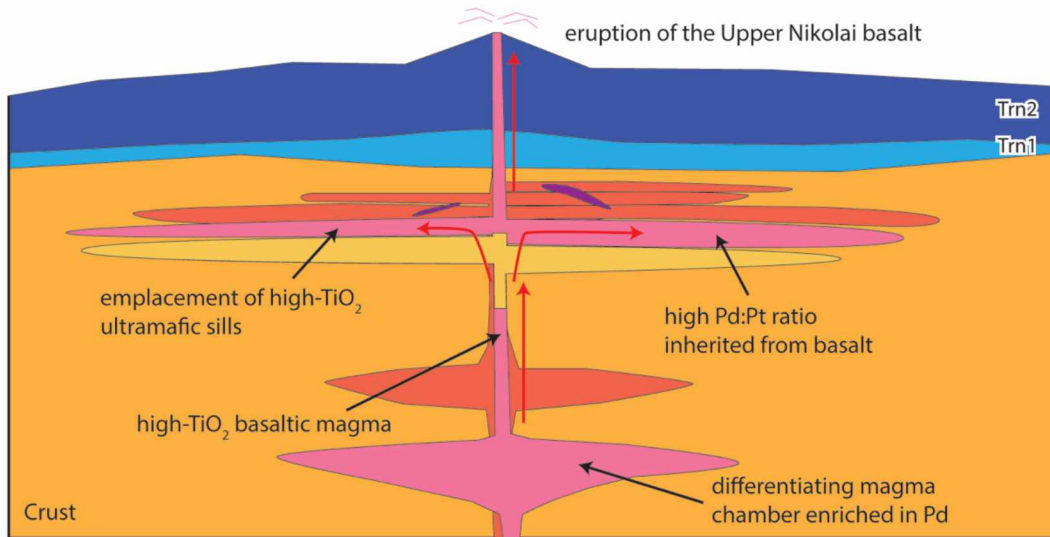
Figure 4-1. C) After emplacement of the intermediate TiO$_2$ sills, the high-TiO$_2$ sills were intruded. These were derived from the Upper Nikolai basalt. Ultramafic cumulates were extracted from the Upper Nikolai basalt and the evolved melt extract migrated to the surface. High-TiO$_2$ gabbroic dikes (dark purple) intruded and crosscut the upper ultramafic sills.

4.2. Conclusions

The major observations and conclusions of this study are as follows:

- High Fo contents in olivine (up to Fo 87) and high Cr/(Cr+Al) in spinel (0.46-0.96) suggest the ultramafic cumulates in the Alpha complex were derived from a primitive basaltic parental magma.

- Field mapping, whole rock analyses, and petrographic observations suggest the map area consists of three major units: (1) the upper ultramafic unit, which is comprised of multiple thin sills grading from unserpentinized dunite into wehrlite and clinopyroxenite at the cores; (2) the central feldspathic ultramafic unit, which consists of feldspar bearing dunite, wehrlite, and troctolite; and (3) the basal unit, which consists of two sills composed of variably serpentinized dunite and wehrlite.

- Olivine mineral chemistry confirms the presence of individual sills. These sills have high forsterite margins that decrease inwards, indicating an inward crystallization sequence. Each sill within the complex has dunitic margins that increase in clinopyroxene content towards the center.

- Ni concentrations and Mg numbers in the Lower and Upper Nikolai basalt suggest that the Upper Nikolai was derived from a higher Ni parent than the Lower Nikolai. Ni concentrations in olivine show that olivine from the central feldspathic sill was in equilibrium with a higher Ni melt, similar to the Upper Nikolai and olivine from the upper ultramafic sills was in equilibrium with a lower Ni melt, similar to the Lower Nikolai basalt. Olivine compositions from the basal sills were variably in equilibrium with both a higher and lower Ni melt.

85

- TiO$_2$ concentrations and Mg numbers in clinopyroxene suggests these sills were derived from the Lower and Upper Nikolai magma series. Low-TiO$_2$ compositions in clinopyroxene from the upper sills indicate their parental magma was the low-TiO$_2$, Lower Nikolai magma series. High-TiO$_2$ clinopyroxene in the central feldspathic sill indicate this sill was derived from the high-TiO$_2$, Upper Nikolai magma series. Intermediate TiO$_2$ compositions in clinopyroxene in the two basal sills indicate these sills were derived from a mix of the Upper and Lower Nikolai magma series.

- Disequilibrium textures and compositions in both olivine and clinopyroxene in the two basal sills confirm that these two sills were derived from mixing of the Upper and Lower Nikolai melts.

- According to the volcanic stratigraphy of the Upper and Lower Nikolai magma series, the upper sills were emplaced first, followed by the basal dunite sill and the basal wehrlite sill. The central feldspathic sill was emplaced last.

- Forsterite and Ni concentrations in olivine indicate that olivine in my samples did not re-equilibrate with magmatic sulfide. Samples that have radical changes in Ni concentration likely grew from a melt that was undergoing Ni depletion due to a small amount of magmatic sulfide exsolution.

- Low Pd in the upper ultramafic sills and in the basal sills suggests crystallization from the Lower Nikolai basalt. The basal sills likely crystallized from a mix of the late Lower Nikolai basalt with early Upper Nikolai basalt in order for Pd values to remain low. Elevated Pd values in the central feldspathic sill can be attributed to crystallization from the Pd-enriched Upper Nikolai basalt.

References

Arai, S., 1992, Chemistry of chromian spinel in volcanic rocks as a potential guide to magma chemistry: Mineralogical Magazine, v. 56, p. 173-184, doi: 10.1180/minmag.1992.056.383.04.

Arndt, N., Lesher, C.M., and Czamanske, G.K., 2005, Mantle-derived magmas and magmatic Ni-Cu-(PGE) deposits: Economic Geology 100th Anniversary Volume, p. 5-24.

Barnes, S.J. and Lightfoot, P.C., 2005, Formation of Magmatic Nickel Sulfide Deposits and Processes Affecting their Copper and Platinum Group Element Contents: Economic Geology 100th Anniversary Volume, p. 179-213.

Barnes, S.J. and Roeder, P.L., 2001, The Range of Spinel Compositions in Terrestrial Mafic and Ultramafic Rocks: Journal of Petrology, v. 42, no. 12, p. 2279-2302, doi: 10.1093/petrology/42.12.2279.

Barnes, S.J., 1986, The effect of trapped liquid crystallization on cumulus mineral compositions in layered intrusions: Contributions to Mineralogy and Petrology, v. 93, no. 4, p. 524–531.

Barnes, S.J., Naldrett, A.J., and Gorton, M.P., 1985, The origin of the fractionation of platinum-group elements in terrestrial magmas: Chemical Geology, v. 53, p. 303-323, doi: 10.1016/0009-2541(85)90076-2.

Bédard, J.H., 2010, Parameterization of the Fe = Mg exchange coefficient (Kd) between clinopyroxene and silicate melts: Chemical Geology, v. 274, no. 3–4, p. 169-176.

Bittenbender, P.E., Bean, K.B., Kurtak, J.M., and Deininger, J., 2007, Mineral assessment of the Delta River Mining District area, east-central Alaska: U.S. Bureau of Land Management, Alaska Technical Report 57, 697 p.

Brooks, C.K. and Platt, R.G., 1975, Kaersutite-bearing gabbroic inclusions and the late dike swarm of Kangerdlugssuaq, East Greenland: Mineralogical magazine, v. 40, p. 259-83.

Cawthorn, R.G., Barnes, S.J., Ballhaus, C., and Malitch, K.N., 2005, Platinum group elements, chromium, and vanadium deposits in mafic and ultramafic rocks: Economic Geology 100th Anniversary Volume, p. 215-249.

Colpron, M. and Nelson, J.L., 2011, A Digital Atlas of Terranes for the Northern Cordillera: British Columbia Ministry of Energy and Mines, BCGS GeoFile 2011-11.

Dunn, T., 1987, Partitioning of Hf, Lu, Ti, and Mn between Olivine, Clinopyroxene and Basaltic Liquid: Contributions to Mineralogy and Petrology, v. 96, no. 4, p. 476-484.

Eckstrand, O.R., and Hulbert, L.J., 2007, Magmatic nickel-copper-platinum group element deposits, in Goodfellow, W.D., ed., Mineral Deposits of Canada: A Synthesis of Major Deposit Types, District Metallogeny, the Evolution of Geological Provinces, and Exploration Methods: Geological Association of Canada, Mineral Deposits Division, Special Publication No. 5, p. 205-222.

Gaetani, G.A. and Grove, T.L., 1997, Partitioning of moderately siderophile elements among olivine, silicate melt, and sulfide melt: constraints on core formation in the Earth and Mars: Geochimica et Cosmochimica Acta, v. 61, no. 9, p. 1829-1846.

Glen, J.M., Schmidt, J.M., and Connard, G.G., 2011, Three-dimensional model of an ultramafic feeder system to the Nikolai Greenstone mafic large igneous province, central Alaska Range: Geochemistry, Geophysics, Geosystems, v. 12, no. 6, p. 1-24, doi: 10.1029/2011GC003508.

Greene, A.R., Scoates, J.S., and Weis, D., 2008, Wrangellia flood basalts in Alaska: A record of plume-lithosphere interaction in a Late Triassic accreted oceanic plateau: Geochemistry, Geophysics, Geosystems, v. 9, no. 12, p. 1-34, doi: 10.1029/2008GC002092.

Grove, T.L. and Bryan, W.B., 1983, Fractionation of pyroxene phyric MORB at low pressure: an experimental study: Contributions to Mineralogy and Petrology, v. 84, p. 293–309.

Hart, S.R. and Dunn, T., 1993, Experimental cpx/melt partitioning of 24 trace elements: Contributions to Mineralogy and Petrology, v. 113, p. 1-8.

Hauri, E.H., Wagner, T.P., and Grove, T.L., 1994, Experimental and natural partitioning of Th, U, Pb and other trace elements between garnet, clinopyroxene and basaltic melts: Chemical Geology, v. 117, p. 149-166, doi: 10.1016/0009-2541(94)90126-0.

Henderson, P. and Wood, R.J., 1981, Reaction relationships of chrome-spinels in igneous rocks - further evidence from the layered intrusions of Rhum and Mull, Inner Hebrides, Scotland: Contributions to Mineralogy and Petrology, v. 78, p. 225-229.

Henderson, P., 1975, Reaction trends shown by chrome-spinels of the Rhum layered intrusion: Geochimica et Cosmochimica Acta, v. 39, no. 6-7, p. 1035-1044.

Hulbert, L. and Stone, W., 2006, Eastern Wrangellia - a new Ni-Cu-PGE metallogenic terrane in North America: Australian Society of Exploration Geophysicists Extended Abstracts 2006, v. 1, p. 1-7, doi:10.1071/ASEG2006ab070.

Hulbert, L.J., 1997, Geology and metallogeny of the Kluane mafic-ultramafic belt, Yukon Territory, Canada: eastern Wrangellia - a new Ni-Cu-PGE metallogenic terrane: Geological Survey of Canada Bulletin, v. 506, p. 265.

Irvine, T.N., 1965, Chromian spinel as a petrogenetic indicator, Part 1. Theory: Canadian Journal of Earth Sciences, v. 2, no. 6, p. 648-672.

Irvine, T.N., 1967, Chromian spinel as a petrogenetic indicator, Part 2. Petrologic applications: Canadian Journal of Earth Sciences, v. 4, no. 1, p. 71-103, doi: 10.1139/e67-004.

Jenner, G.A., Foley, S.F., Jackson, S.E., Green, T.H., Fryer, B.J., and Longerich, H.P., 1994, Determination of partition coefficients for trace elements in high pressure-temperature experimental run products by laser ablation microprobe-inductively coupled plasma-mass spectrometry (LAM-ICP-MS): Geochimica et Cosmochimica Acta, v. 57, no. 23-24, p. 5,099-5,103, doi: 10.1016/0016-7037(93)90611-Y.

Johnson, K.T.M. and Kinzler, R.J., 1989, Partitioning of REE, Ti, Zr, Hf, and Nb between clinopyroxene and basaltic liquid: an ion microprobe study: EOS, Transactions of the American Geophysical Union, v. 70, p. 1,388.

Johnson, K.T.M., 1994, Experimental cpx/ and garnet/melt partitioning of REE and other trace elements at high pressures; petrogenetic implications: Mineralogical Magazine, v. 58, p. 454-455.

Johnson, K.T.M., 1998, Experimental determination of partition coefficients for rare earth and high-field-strength elements between clinopyroxene, garnet, and basaltic melt at high pressures: Contributions to Mineralogy and Petrology, v. 133, no. 1-2, p. 60-68.

Jones, D.L., Silberling N.J., and Hillhouse J., 1977, Wrangellia - A displaced terrane in northwestern North America: Canadian Journal of Earth Sciences, v. 14, p. 2565-2577, doi: 10.1139/e77-222.

Kinzler, R.J., Grove, T.L., and Recca, S.I., 1990, An experimental study on the effect of temperature and melt composition on the partitioning of nickel between olivine and silicate melt: Geochimica et Cosmochimica Acta, v. 54, p. 1255-1265, doi: 10.1016/0016-7037(90)90151-A.

Kloeck, W. and Palme, H., 1988, Partitioning of siderophile and chalcophile elements between sulfide, olivine, and glass in a naturally reduced basalt from Disko Island, Greenland: Proceedings of the Lunar and Planetary Science Conference, v. 18, p. 471-483.

Li, C., Ripley, E.W., and Naldrett, A.J., 2003, Compositional variations of olivine and sulfur isotopes in the Noril'sk and Talnakh intrusions, Siberia: implications for ore-forming processes in dynamic magma conduits: Economic Geology, v. 98, p. 69-86, doi: 0361-0128/01/3316/69-18.

Mavrogenes, J.A. and O'Neill, H.St.C., 1999, The relative effects of pressure, temperature and oxygen fugacity on the solubility of sulfide in magmas: Geochimica et Cosmochimica Acta, v. 63, no. 7/8, p. 1173-1180 doi: 0016-7037/99.

Mellini, M., Rumori, C., and Viti, C., 2005, Hydrothermally reset magmatic spinels in retrograde serpentinites: formation of "ferritchromit" rims and chlorite aureoles: Contributions to Mineralogy and Petrology, v. 149, no. 3, p. 266-275.

Mysen, B., 1978, Experimental determination of nickel partition coefficients between liquid, pargasite and garnet peridotite minerals and concentration limits of behavior according to Henry's Law at high pressure and temperature: American Journal of Science, v. 278, p. 217-243.

Nabelek, P.I., 1980, Nickel partitioning between olivine and liquid in natural basalts: Henry's Law behavior: Earth and Planetary Science Letters, v. 48, p. 293-302, doi: 10.1016/0012-821X(80)90193-4.

Naldrett, A.J., 2010, Secular variation of magmatic sulfide deposits and their source magmas: Economic Geology and the Bulletin of the Society of Economic Geologists, v. 105, no. 3, p. 669-688, doi: 0361-0128/10/3893/669-20.

Naldrett, A.J., 2011, Fundamentals of magmatic sulfide deposits: Reviews in Economic Geology, v. 17, p. 1-50.

Nokleberg, W.J., Jones, D.L., and Silberling, N.J., 1985, Origin and tectonic evolution of the Maclaren and Wrangellia terranes, eastern Alaska Range, Alaska: Geological Society of America Bulletin, v. 96, p. 1251-1270, doi: 10.1130/0016-7606(1985)96<1251:OATEOT>2.0.CO;2.

Pedersen, A.K., 1979, Basaltic Glass with High-Temperature Equilibrated Immiscible Sulfide Bodies with Native Iron from Disko, Central West Greenland: Contributions to Mineralogy and Petrology, v. 69, no. 4, p. 397-407.

Perkins, D. and Vielzeuf, D., 1992, Reinvestigation of fayalite+anorthite=garnet: Contributions to Mineralogy and Petrology, v. 111, no. 2, p. 260-263.

Pure Nickel Inc., 2013, Pure Nickel Inc. confirms extensive Ni-Cu-Co-PGE mineralization on the MAN property, Alaska, October 29, 2013 [Press release]. Retrieved from http://www.purenickel.com/s/NewsReleases.asp?ReportID=609291.

Pure Nickel Inc., 2014, Pure Nickel Inc. reports favorable results for nickel deportment study at MAN property, April 22, 2014 [Press release]. Retrieved from http://www.purenickel.com/s/NewsReleases.asp?ReportID=648641.

Rajamani, V. and Naldrett, A.J., 1978, Partitioning of Fe, Co, Ni, and Cu between sulfide liquid and basaltic melts and the composition of Ni-Cu sulfide deposits: Economic Geology, v. 73, no. 1, p. 82-93.

Rankin, L.J., 2005, Man NiS Project – The Fish Lake Mafic-Ultramafic Sill Complex Wrangell Belt, Southern Alaska: Structural Geology from Airborne Magnetic Data: Private report prepared for Angloamerican Exploration Canada.

Reichow, M.D., Saunders, A.D., White, R.V., Al'Mukhamedov, A.I., and Medvedev, A.Ya., 2005, Geochemistry and petrogenesis of basalts from the West Siberian Basin: an extension of the Permo–Triassic Siberian Traps, Russia: Lithos, v. 79, no. 3-4, p. 425-452.

Richter, D.H. and Jones, D.L., 1970, Structure and Stratigraphy of Eastern Alaska Range [abs.]: AAPG Bulletin, v. 54, no. 12, p. 2502.

Roeder, P.L. and Campbell, I.H., 1985, The effect of postcumulus reactions on composition of chrome-spinels from the Jimberlana intrusion: Journal of Petrology, v. 26, no. 3, p. 763-786, doi: 10.1093/petrology/26.3.763.

Roeder, P.L. and Emslie, R.F., 1970, Olivine–liquid equilibrium: Contributions to Mineralogy and Petrology, v. 29, p. 275–289.

Roeder, P.L., 1994, Chromite: From the Fiery Rain of Chondrules to the Kilauea Iki Lava Lake: The Canadian Mineralogist, v. 32, p. 729-746.

Schmidt, J.M., and Rogers, R.K., 2007, Metallogeny of the Nikolai large igneous province (LIP) in southern Alaska and its influence on the mineral potential of the Talkeetna Mountains, in Ridgway, K.D., Trop, J.M., Glen, J.M.G., and O'Neill, J.M., eds., Tectonic Growth of a Collisional Continental Margin: Crustal Evolution of Southern Alaska: Geological Society of America Special Paper, v. 431, p. 623–648, doi: 10.1130/2007.2431(24).

Schmidt, J.M., Pellerin, L., Glen, J.M.G., Bittenbender, P., Ellis, W.T., and Sampson, J., 2002, What lies beneath the Amphitheater Mountains? Geophysical investigations shed light on the structural setting and PGE-Ni-Cu potential of the Nikolai magmatic system [abs.]: A Focus on the Americas: Northwest Mining Association's 108th Annual Meeting, Spokane, Washington, p. 17.

Seifert, S., Oneill, H.S., and Brey, G., 1988, The Partitioning of Fe, Ni and Co between Olivine, Metal, and Basaltic Liquid - an Experimental and Thermodynamic Investigation, with Application to the Composition of the Lunar Core: Geochimica et Cosmochimica Acta, v. 52, no. 3, p. 603-616, doi: 10.1016/0016-7037(88)90322-5.

Sisson, T.W. and Grove, T.L., 1993, Experimental investigations of the role of H_2O in calc- alkaline differentiation and subduction zone magmatism: Contributions to Mineralogy and Petrology, v. 113, p. 143–166.

Skulski, T., Minarik, W., and Watson, E.B., 1994, High-Pressure Experimental Trace-Element Partitioning between Clinopyroxene and Basaltic Melts: Chemical Geology, v. 117, no. 1-4, p. 127-147, doi: 10.1016/0009-2541(94)90125-2.

Spencer, K.J. and Lindsley, D.H., 1981, A solution model for coexisting iron–titanium oxides: American Mineralogist, v. 66, p. 1189–1201.

Stout, J.H., 1976, Geology of the Eureka Creek area, east-central Alaska Range: Alaska Division of Geological & Geophysical Surveys Geologic Report 46, 32 p., 1 sheet, scale 1:63,360, doi:10.14509/374.

Taylor, C.D., Premo, W.R., Meier, A.L., and Taggart, J.E., 2008, The metallogeny of Late Triassic rifting of the Alexander terrane in southeastern Alaska and northwestern British Columbia: Economic Geology, v. 103, p. 89-115.

Toplis, M.J., 2005, The thermodynamics of iron and magnesium partitioning between olivine and liquid: criteria for assessing and predicting equilibrium in natural and experimental systems: Contributions to Mineralogy and Petrology, v. 149, no. 1, p. 22-39.

Twelker, E., Bachmann, E.N., Freeman, L.K., Newberry, R.J., Reioux, D.A., Sicard, K.R., Tuzzolino, A.L., Wright, T.C., and Wypych, A., 2014, Major-oxide, minor-oxide, and trace-element geochemical data from rocks and stream sediments in the Wrangellia mineral assessment area, Gulkana, Healy, Mount Hayes, and Talkeetna Mountains quadrangles, Alaska: Alaska Division of Geological & Geophysical Surveys Raw Data File 2014-3, 6 p., doi:10.14509/27181.

Vannucci, R., Bottazzi, P., Wulffpedersen, E., and Neumann, E., 1998, Partitioning of REE, Y, Sr, Zr and Ti between clinopyroxene and silicate melts in the mantle under La Palma (Canary Islands): implications for the nature of the metasomatic agents: Earth and Planetary Science Letters, v. 158, p. 39-51, doi: 10.1016/S0012-821X(98)00040-5.

Wypych, A., Twelker, E., Freeman, L.K., Lande, L., Newberry, R.J., Reioux, D.A., and Sicard, K.R., 2014, Major-oxide and trace-element geochemical data from rocks collected in 2014 in the Wrangellia mineral assessment area, Talkeetna Mountains C-4, C-3, and B-4 quadrangles, Alaska: Alaska Division of Geological & Geophysical Surveys Raw Data File 2014-22, 4 p., doi:10.14509/29140.

Wypych, A., Twelker, E., Freeman, L.K., Lande, L., Newberry, R.J., Reioux, D.A., and Sicard, K.R., 2015a, Major-oxide and trace-element geochemical data from rocks collected in 2015 in the Wrangellia mineral assessment area, Alaska: Alaska Division of Geological & Geophysical Surveys Raw Data File 2015-16, 4 p., doi:10.14509/29518.

Wypych, A., Twelker, E., Lande, L.L., and Newberry, R.J., 2015b, Along-strike geochemical variations in the Late Triassic Nikolai magmatic system, Wrangellia, central Alaska (poster number V31D-3059): American Geophysical Union 2015 Fall Meeting, December 14-18, 2015: Alaska Division of Geological & Geophysical Surveys, 1 sheet, doi:10.14509/29567.

Appendix A.

X-ray fluorescence analyses

The following tables are whole rock x-ray fluorescence analyses (XRF) separated by units within the complex. Major oxide values are in weight percent and trace elements are in parts per million (ppm).

Table A-1. Feldspathic ultramafic unit analyses.

Sample	SiO2	TiO2	Al2O3	FeO	MnO	MgO	CaO	Na2O	K2O	P2O5	BaO	LOI
13RN397A	43.07	0.16	2.67	11.10	0.18	36.92	3.71	0.19	0.01	0.01		
13RN398A	44.73	0.16	1.72	6.96	0.14	42.78	0.85	0.00	0.01	0.01		
15LL136	42.27	0.15	4.82	13.38	0.22	31.13	5.11	0.39	0.01	0.01	0.01	
15LL137	41.94	0.10	2.07	9.99	0.15	39.91	0.81	0.07	0.01	0.02		
15LL138	41.63	0.10	3.90	11.98	0.18	37.71	2.75	0.30	0.01	0.02		
15LL139	42.32	0.09	0.75	11.95	0.20	41.95	0.57	0.04	0.01	0.01		
15LL146	41.58	0.08	2.30	11.94	0.20	38.55	2.00	0.14	0.01	0.01		
15LL147	40.22	0.11	1.34	11.10	0.20	41.09	2.54	0.06	0.00	0.02	0.00	
15LL148	44.17	0.16	2.08	12.81	0.22	36.75	3.27	0.19	0.01	0.01		
15LL158	39.47	0.07	3.15	11.90	0.20	39.67	1.67	0.05	0.01	0.02	0.01	
15LL159	40.15	0.07	3.01	11.68	0.19	39.43	2.23	0.08	0.00	0.01	0.00	

Sample	Cu	Ni	Cr	Ga	Nb	Pb	Rb	Sr	V	Y	Zn	Zr	Lith.	Sum
13RN397A	266	1774	2318					28	69		61		DU	98.5
13RN398A	375	3114	3727					8	79		55		DU	98.1
15LL136	406	1187	2104	5	1.3	2	0	53	79	2.4	177	7	TR	97.9
15LL137	668	2650	4096					14	55		76		DU	95.8
15LL138	148	1889	2418					30	48		151		DU	99.0
15LL139	45	1995	2440					10	42		60		DU	98.3
15LL146	303	1879	2043					17	35		68		DU	97.2
15LL147	108	1211	2487	2	0.5	1	0	10	50	1	58	6	DU	97.1
15LL148	59	1439	2114					24	77		64		WH	100.0
15LL158	67	1420	2359	4	0.3	0	1	18	34	0.9	68	6	WH	96.6
15LL159	52	1699	2597	2	0.5	2	0	19	46	1.6	66	5	DU	97.3

Table A-2. Upper ultramafic unit analyses.

Sample	SiO2	TiO2	Al2O3	FeO	MnO	MgO	CaO	Na2O	K2O	P2O5	BaO	LOI
13RN402A	44.62	0.15	0.84	11.41	0.19	35.38	6.36	0.11	0.00	0.02		
13RN402B	39.35	0.08	0.31	14.00	0.21	41.91	0.91	0.03	0.00	0.02		
15ET189	39.33	0.04	0.62	14.54	0.22	41.58	0.49	0.03	0.01	0.02		
15ET191	43.59	0.13	0.77	11.89	0.22	37.26	5.32	0.08	0.01	0.01		
15ET192	41.44	0.08	0.42	13.70	0.21	40.77	2.15	0.04	0.01	0.02		
15ET193	41.39	0.08	0.41	12.85	0.20	40.00	2.72	0.05	0.01	0.02		
15LL149	42.91	0.09	0.55	12.20	0.19	38.74	3.52	0.07	0.01	0.02		
15LL150	41.85	0.10	0.46	12.89	0.20	38.41	3.47	0.06	0.00	0.01		
15LL151	39.92	0.09	0.41	12.72	0.19	35.85	3.52	0.05	0.00	0.02		

Sample											
15LL152	42.09	0.10	0.53	12.86	0.20	38.65	4.01	0.06	0.01	0.02	
15LL153	39.19	0.04	0.19	13.38	0.20	41.42	0.13	0.01	0.01	0.02	
15LL154	40.42	0.04	0.18	12.93	0.19	44.45	0.38	0.02	0.01	0.02	
15LL155	39.01	0.05	0.18	13.08	0.20	40.79	0.69	0.03	0.01	0.02	
15LL156	39.93	0.05	0.31	12.33	0.20	41.44	0.34	0.03	0.01	0.02	
15LL157	41.46	0.06	0.31	11.53	0.19	44.25	0.41	0.03	0.01	0.02	
15LL160	39.79	0.05	0.19	13.45	0.23	43.75	0.26	0.02	0.01	0.02	
15LL161	40.03	0.09	0.40	13.56	0.20	43.19	0.83	0.03	0.01	0.02	
15LL162	42.12	0.09	0.52	12.72	0.20	38.47	3.00	0.04	0.01	0.01	
15LL163A	50.74	0.36	1.63	6.70	0.14	21.04	18.18	0.22	0.01	0.01	
15LL163B	48.08	0.28	1.31	8.98	0.16	26.28	12.36	0.15	0.01	0.01	
15LL168	40.48	0.09	0.68	12.62	0.19	44.28	0.69	0.05	0.00	0.02	
15LL169	40.51	0.07	0.56	13.21	0.21	44.10	0.40	0.04	0.01	0.02	
15LL172	39.75	0.06	0.37	13.37	0.20	42.89	0.53	0.04	0.00	0.02	
15LL173	42.56	0.13	9.89	11.78	0.18	22.96	9.13	0.43	0.01	0.02	
15LL174	41.72	0.08	5.96	13.06	0.20	32.35	4.95	0.29	0.00	0.02	
15RN336	43.01	0.11	0.67	12.52	0.21	38.57	4.25	0.06	0.01	0.02	
15RN338	44.56	0.16	0.89	11.14	0.18	32.24	8.08	0.09	0.01	0.01	
15RN339	38.57	0.06	0.44	13.63	0.21	41.25	0.28	0.03	0.01	0.03	
15RN340	39.89	0.07	0.55	13.60	0.21	42.69	0.37	0.02	0.01	0.02	
15RN341	40.16	0.06	0.27	13.47	0.21	43.55	0.47	0.04	0.01	0.02	
15RN342	39.58	0.06	0.47	13.32	0.21	41.87	0.32	0.02	0.01	0.02	
15RN343	42.39	0.10	0.59	13.46	0.21	39.00	3.43	0.09	0.00	0.02	
15RN344	41.63	0.09	0.46	13.84	0.21	39.76	2.70	0.05	0.01	0.02	
15RN345	39.19	0.06	0.27	14.58	0.22	41.59	0.46	0.04	0.01	0.02	
15RN346	44.23	0.12	0.81	12.12	0.19	36.86	5.28	0.06	0.01	0.01	
15RN348	49.36	0.39	4.26	7.60	0.16	19.94	16.81	0.33	0.10	0.02	
15RN349	45.59	0.17	1.07	12.23	0.20	32.78	7.62	0.10	0.01	0.02	
15RN350	46.33	0.12	16.28	7.43	0.13	14.75	13.63	1.07	0.07	0.01	0.01
15RN351	41.19	0.06	8.08	12.80	0.20	31.90	5.62	0.42	0.00	0.02	
15RN352	41.69	0.10	0.63	13.88	0.21	39.36	2.48	0.07	0.00	0.02	

Sample	Cu	Ni	Cr	Ga	Nb	Pb	Rb	Sr	V	Y	Zn	Zr	Lith.	Sum
13RN402A	156	1184	3414					14	71		76		WH	99.6
13RN402B	156	1793	5988					8	52		75		DU	97.6
15ET189	287	1167	1222					10	23		92		DU	97.2
15ET191	65	1158	2740					12	64		73		WH	99.7
15ET192	113	1450	3811					9	43		80		WH	99.4
15ET193	153	1380	2933					12	43		68		WH	98.2
15LL149	104	1383	3643					10	54		53		WH	98.8
15LL150	58	1778	4583					10	59		64		WH	98.1
15LL151	135	1420	3436					11	54		71		WH	93.3
15LL152	89	1318	4454					11	70		58		WH	99.1
15LL153	305	1922	2900					6	30		78		DU	95.1
15LL154	90	1432	2842					6	27		61		DU	99.1
15LL155	81	1647	3334					6	34		66		DU	94.6
15LL156	42	1601	4028					6	35		71		DU	95.2
15LL157	36	1489	4374					6	37		74		DU	98.9
15LL160	22	1593	4256					7	33		84		DU	98.4
15LL161	195	1762	7926					9	72		59		DU	99.4

Sample	Cu	Ni	Cr	Ga	Nb	Pb	Rb	Sr	V	Y	Zn	Zr	Lith.	Sum
15LL162	99	1710	3333					10	49		57		WH	97.7
15LL163A	42	221	4981					23	207		43		CP	99.6
15LL163B	98	573	4293					21	146		53		WH	98.1
15LL168	339	1564	5603					7	51		65		DU	99.9
15LL169	53	1411	4283					7	38		78		DU	99.7
15LL172	109	1597	4073					8	37		64		DU	97.8
15LL173	582	852	1900					136	76		62		TR	97.5
15LL174	45	888	1214					84	41		76		TR	98.9
15RN336	110	1210	2992					11	62		66		WH	99.9
15RN338	178	1031	3109					16	89		62		WH	97.8
15RN339	227	1496	3564					7	36		84		DU	95.1
15RN340	102	1382	3619					7	40		83		DU	98.0
15RN341	71	1275	2489					7	28		76		DU	98.7
15RN342	96	1462	3492					7	35		77		DU	96.4
15RN343	171	1287	2754					11	50		88		WH	99.7
15RN344	446	1648	3779					9	54		74		WH	99.4
15RN345	157	992	2463					9	34		79		DU	96.8
15RN346	102	1127	3402					11	76		59		WH	100.2
15RN348	52	216	5013					66	236		52		CP	99.5
15RN349	83	1079	3193					15	93		69		WH	100.2
15RN350	72	331	820	13	0.2	3	4	286	71	2.3	42	13	TR	100.0
15RN351	66	713	868					120	32		68		TR	100.5
15RN352	127	1238	3623					11	56		68		WH	99.0

Table A-3. Basal dunite unit analyses.

Sample	SiO2	TiO2	Al2O3	FeO	MnO	MgO	CaO	Na2O	K2O	P2O5	BaO	LOI
13RN392A	37.56	0.10	0.47	13.39	0.21	39.69	0.57	0.04	0.00	0.02		
13RN393A	41.13	0.23	1.12	13.42	0.21	31.58	4.99	0.16	0.03	0.03		
13RN394A	38.44	0.06	1.72	12.71	0.18	37.68	0.99	0.08	0.01	0.01		
13RN395A	40.18	0.12	0.36	12.59	0.19	41.36	1.11	0.04	0.00	0.02		
15LL130	39.44	0.12	0.62	12.21	0.20	41.58	0.44	0.05	0.00	0.02		
15LL131	38.59	0.10	0.29	14.93	0.23	40.28	0.46	0.04	0.00	0.02		
15LL132	39.66	0.12	0.50	12.77	0.20	41.27	0.70	0.04	0.00	0.02		
15LL133	39.30	0.10	0.50	14.64	0.21	40.17	0.56	0.05	0.00	0.02		
15LL134	37.20	0.08	0.34	13.07	0.20	39.92	0.58	0.05	0.00	0.04		
15LL140	41.41	0.09	0.80	12.41	0.20	41.33	0.88	0.07	0.01	0.02		
15LL141#1	39.83	0.07	0.65	12.89	0.20	43.77	0.45	0.03	0.01	0.03		
15LL141#2	40.86	0.18	1.03	12.12	0.19	38.20	1.69	0.10	0.00	0.02		
15LL142	38.93	0.09	0.35	11.93	0.17	41.25	0.90	0.03	0.00	0.02		
15LL143	40.10	0.04	0.32	12.38	0.23	39.94	0.68	0.03	0.01	0.01		

Sample	Cu	Ni	Cr	Ga	Nb	Pb	Rb	Sr	V	Y	Zn	Zr	Lith.	Sum
13RN392A	326	1791	3450					10	37		81		DU	92.6
13RN393A	330	1143	2989					29	77		79		WH	93.4
13RN394A	258	1482	1680					23	26		77		DU	92.2
13RN395A	386	1722	2680					10	44		65		DU	96.5
15LL130	46	1667	3116					12	40		67		DU	95.2
15LL131	191	1562	3626					18	37		63		DU	95.5

15LL132	128	1783	3905	19	44	73	DU	95.9
15LL133	228	627	3249	12	42	79	DU	96.0
15LL134	447	1751	1837	12	30	84	DU	91.9
15LL140	68	1396	2051	10	39	58	DU	97.6
15LL141#1	114	2046	4376	8	43	82	DU	98.6
15LL141#2	231	2097	4404	11	73	67	DU	95.1
15LL142	263	1777	2245	9	34	72	DU	94.1
15LL143	54	1543	1022	12	16	77	DU	94.0

Table A-4. Basal wehrlite unit analyses.

Sample	SiO2	TiO2	Al2O3	FeO	MnO	MgO	CaO	Na2O	K2O	P2O5	BaO	LOI
13RN384A	43.66	0.17	0.97	8.00	0.15	41.85	0.13	0.00	0.01	0.02		
13RN386A	46.31	0.29	0.95	11.86	0.19	29.69	10.08	0.14	0.00	0.01		
13RN387A	41.16	0.15	0.47	15.21	0.23	34.73	3.75	0.06	0.00	0.02		
13RN388A	38.55	0.09	0.28	15.17	0.23	38.07	1.18	0.04	0.00	0.02		
13RN389A	48.29	0.42	1.44	10.18	0.18	25.81	13.56	0.18	0.00	0.01		
13RN390A	49.72	0.54	1.80	5.80	0.14	17.62	18.62	0.21	0.01	0.01		
13RN391A	38.35	0.11	0.34	10.55	0.17	39.56	0.36	0.03	0.00	0.02		
15LL121	43.29	0.18	0.69	13.44	0.21	35.04	4.84	0.07	0.01	0.02		
15LL122	40.23	0.09	0.32	14.52	0.23	39.90	0.79	0.04	0.00	0.02		
15LL123	42.30	0.15	0.46	14.47	0.23	35.81	3.79	0.06	0.00	0.02		
15LL124	47.59	0.35	1.17	11.64	0.20	26.98	11.94	0.15	0.00	0.01		
15LL125	48.64	0.41	1.31	9.88	0.17	25.32	13.98	0.16	0.00	0.01		
15LL126	45.98	0.25	0.82	12.14	0.18	30.72	8.63	0.11	0.00	0.01		
15LL127	43.18	0.20	0.67	12.46	0.19	34.54	5.22	0.07	0.00	0.02		
15LL128	41.96	0.17	0.48	14.24	0.22	38.58	2.68	0.04	0.00	0.03		
15LL129	41.00	0.07	0.25	11.84	0.19	44.36	0.36	0.01	0.01	0.02		
15LL181#1	46.15	0.38	1.47	10.33	0.17	28.31	12.20	0.14	0.02	0.02	0.01	
15LL181#2	46.45	0.37	1.62	10.43	0.17	29.07	11.66	0.15	0.02	0.02	0.01	
15RN354	44.67	0.58	2.33	12.03	0.20	31.52	6.63	0.07	0.01	0.04	0.00	
15RN359	43.80	0.49	3.14	9.92	0.15	34.77	5.20	0.07	0.01	0.08	0.00	

Sample	Cu	Ni	Cr	Ga	Nb	Pb	Rb	Sr	V	Y	Zn	Zr	Lith.	Sum
13RN384A	376	2110	2195					9	37		36		DU	95.4
13RN386A	334	944	3373					31	100		69		WH	100.0
13RN387A	356	1422	2245					16	59		93		DU	96.2
13RN388A	99	1161	1293					9	31		104		DU	93.9
13RN389A	112	384	3281					33	153		63		WH	100.5
13RN390A	210	138	5754					36	220		53		CP	95.1
13RN391A	82	3497	4166					11	38		87		DU	90.3
15LL121	244	1214	2311					16	67		86		WH	98.2
15LL122	200	1370	426					10	22		96		DU	96.4
15LL123	99	1236	2428					13	59		91		DU	97.7
15LL124	169	619	2972					28	134		64		CP	100.4
15LL125	48	380	2969					29	156		55		CP	100.2
15LL126	284	726	2876					30	90		73		CP	99.2
15LL127	333	989	2774					26	68		84		CP	97.0
15LL128	224	1248	582					15	39		89		WH	98.6

Sample	Cu	Ni	Cr	Ga	Nb	Pb	Rb	Sr	V	Y	Zn	Zr	Lith.	Sum
15LL129	57	2493	3661					7	33		62		DU	98.7
15LL181#1	110	587	3198	2	1.7	2	2	30	157	7	54	12	WH	99.6
15LL181#2	129	639	3132	2	1.1	4	1	30	162	6.5	59	11	WH	100.4
15RN354	197	612	2076	4	3.3	11	0	39	138	7.7	82	29	WH	98.4
15RN359	369	920	2444	5	2.5	30	1	25	102	5.9	66	33	WH	98.0

Table A-5. Analyses of gabbroic dikes.

Sample	SiO2	TiO2	Al2O3	FeO	MnO	MgO	CaO	Na2O	K2O	P2O5	BaO	LOI
13RN399A	49.57	0.21	18.06	5.65	0.11	8.07	15.27	2.24	0.02	0.03	0.01	
13RN400A	46.64	0.27	14.54	7.94	0.08	12.64	17.04	0.48	0.06	0.01	0.01	
15RN335A	47.54	0.16	18.04	5.37	0.10	10.50	15.73	1.14	0.25	0.01	0.02	
15RN335B	43.70	0.16	5.91	13.23	0.22	25.20	8.75	0.57	0.04	0.00	0.00	0.30
15LL119A	48.06	1.75	12.91	12.52	0.21	8.32	8.93	3.10	0.80	0.17	0.07	
15LL119B	46.41	2.16	11.71	13.32	0.27	6.41	18.66	0.78	0.10	0.17	0.01	
15LL119C	48.72	1.80	13.20	12.16	0.20	7.61	9.81	3.13	0.60	0.16	0.02	
15LL119D	50.69	1.81	14.70	11.50	0.20	6.08	10.72	2.71	0.26	0.17	0.01	
15LL119E	48.90	1.56	12.79	11.19	0.18	7.92	9.09	3.99	0.10	0.13	0.01	
15LL119F	44.80	2.12	10.70	14.18	0.22	8.83	18.51	0.25	0.10	0.14	0.01	
15LL120	49.56	1.93	14.14	12.59	0.22	5.79	10.15	2.71	0.28	0.24	0.01	
15LL144	48.74	1.62	13.17	11.96	0.18	6.11	9.99	3.44	0.57	0.20	0.02	
15LL145A	49.58	1.97	13.62	4.66	0.08	8.89	19.42	1.17	0.03	0.27	0.01	
15LL145B	48.42	1.49	13.62	12.67	0.20	6.37	8.54	3.62	0.92	0.17	0.05	
15LL177	49.25	1.45	11.65	11.72	0.22	6.52	12.35	2.74	0.74	0.15	0.03	
15LL182	48.88	1.60	12.65	12.16	0.22	6.34	12.34	2.98	0.40	0.14	0.01	
15RN333	49.02	1.84	14.04	11.99	0.20	6.04	10.37	3.40	0.57	0.15	0.02	
15RN334	48.58	1.68	13.03	12.08	0.19	6.93	9.43	3.36	0.47	0.15	0.02	

Sample	Cu	Ni	Cr	Ga	Nb	Pb	Rb	Sr	V	Y	Zn	Zr	Lith.	Sum
13RN399A	79	133	431	15	0.2	1	3	437	115	2.6	41	15	low-Ti GB	99.4
13RN400A	121	354	234	14	0.2	2	7	1354	228	0.5	30	37	low-Ti GB	99.9
15RN335A	62	162	761	14	0.2	1	9	346	86	1.8	33	13	low-Ti GB	99.0
15RN335B	83	639	2820	5.8	0.2	3	0.8	90	111	3.2	76	4	low-Ti GB	98.5
15LL119A	185	58	48	18	9.4	0	32	331	394	28	95	114	high-Ti GB	97.0
15LL119B	26	66	34	19	12.9	0	6	84	476	34	80	141	high-Ti GB	100.1
15LL119C	224	66	68	19	8.6	2	18	423	393	28	100	119	high-Ti GB	97.6
15LL119D	233	55	50	21	8.5	2	6	194	386	30	101	114	high-Ti GB	99.0
15LL119E	324	62	52	17	7.9	1	4	292	350	25	84	102	high-Ti GB	96.0
15LL119F	182	61	48	18	11.3	1	7	41	445	31	115	123	high-Ti GB	100.0
15LL120	213	50	34	21	9.5	1	6	188	396	31	114	122	high-Ti GB	97.7
15LL144	106	62	59	19	8.8	0	23	329	390	23	62	119	high-Ti GB	96.1
15LL145A	91	96	43	14	8.7	0	7	1259	368	16	24	179	high-Ti GB	99.9
15LL145B	96	68	65	21	9.5	1	34	155	393	26	90	111	high-Ti GB	96.2
15LL177	15	64	133	17	9	24	23	351	340	26	68	114	high-Ti GB	96.9
15LL182	250	68	87	18	9	1	13	388	375	26	97	118	high-Ti GB	97.9
15RN333	214	55	45	21	9.3	2	17	290	383	27	98	107	high-Ti GB	97.8
15RN334	192	61	64	18	8.6	2	13	303	392	26	74	108	high-Ti GB	96.0

Appendix B.

Major-Trace-REE-PGE analyses

Table B-1. A) Major and minor element analyses.

Sample	15ET160	15ET162	15ET163	15ET164	15ET165	15ET168	15ET194	15ET195	15ET201
Type	dunite	wehrlite	wehrlite	gabbro	gabbro	dunite	gabbro	olivine gabbro	gabbro
SiO2	38.1	38	38.8	41.7	47.3	37.4	48	43	49.9
Al2O3	0.7	1.05	3.62	5.8	14.7	0.75	17.8	6.77	12.8
Fe2O3	16.4	13.55	14.15	11.2	4.64	15.5	5.17	10.4	15.35
CaO	0.35	0.93	3.41	8.25	16.2	0.5	16.25	10.05	8.61
MgO	41.1	36.6	34.7	27.2	11.25	39.9	9.77	25.1	6.02
Na2O	0.03	0.06	0.04	0.36	1.32	0.02	0.98	0.4	3.29
K2O	0.01	0.02	<0.01	0.07	0.14	0.01	0.05	0.04	0.68
Cr2O3	0.44	0.72	0.1	0.29	0.28	0.21	0.06	0.32	0.01
TiO2	0.04	0.13	0.07	0.18	0.24	0.06	0.21	0.16	2.07
MnO	0.25	0.15	0.2	0.16	0.09	0.2	0.1	0.15	0.22
P2O5	0.01	0.01	0.01	0.01	<0.01	0.01	<0.01	0.01	0.18
SrO	<0.01	<0.01	<0.01	0.01	0.03	<0.01	0.04	0.01	0.03
BaO	<0.01	<0.01	<0.01	<0.01	<0.01	<0.01	<0.01	<0.01	0.02
LOI	2.08	8	5.39	4.4	2.43	4.59	2.02	1.81	1.03
Total	99.51	99.22	100.49	99.63	98.62	99.15	100.45	98.22	100.21
C	0.04	0.1	0.04	0.04	0.01	0.08	0.2	0.02	0.01
S	0.02	0.03	0.08	0.22	0.01	0.07	0.13	0.18	<0.01

Values in weight percent.

Table B-1. B) Trace element analyses.

Sample	15ET160	15ET162	15ET163	15ET164	15ET165	15ET168	15ET194	15ET195	15ET201
Type	dunite	wehrlite	wehrlite	gabbro	gabbro	dunite	gabbro	olivine gabbro	gabbro
Au	0.002	0.009	0.001	0.005	0.002	0.002	0.002	0.005	0.006
Pt	0.0354	0.0405	0.0251	0.0113	0.009	0.041	0.0005	0.0146	0.0037
Pd	0.003	0.032	0.038	0.016	0.012	0.01	0.001	0.007	0.022
Ba	5.1	9.7	4.6	34.7	41.7	4	25.8	29.3	171
Ce	0.5	1.5	0.8	1.9	2	0.7	1.6	1	21
Cr	3130	4940	740	2050	2040	1520	420	2300	50
Cs	0.06	0.38	0.06	1.02	0.33	0.18	0.17	0.11	0.25
Dy	<0.05	0.18	0.18	0.65	0.95	0.09	0.64	0.65	5.42
Er	0.05	0.14	0.13	0.36	0.5	0.07	0.37	0.33	3.08
Eu	<0.03	0.08	0.06	0.2	0.35	0.04	0.27	0.18	1.56
Ga	1.9	2.5	3.3	5.5	10.9	1.4	13.7	5.4	18.6
Gd	<0.05	0.23	0.2	0.63	0.86	0.16	0.81	0.63	5.59
Ge	<5	<5	<5	<5	<5	<5	<5	<5	<5
Hf	<0.2	0.2	<0.2	0.2	0.3	<0.2	<0.2	0.2	3.1
Ho	0.01	0.04	0.03	0.12	0.2	0.03	0.18	0.13	1.18
La	<0.5	0.6	<0.5	0.8	0.8	<0.5	0.6	<0.5	8.1

98

Lu	0.01	0.01	0.02	0.04	0.06	<0.01	0.03	0.04	0.39
Nb	<0.2	0.2	<0.2	0.3	0.2	0.2	<0.2	<0.2	10.2
Nd	0.2	0.8	0.6	1.5	1.9	0.4	1.5	1.1	15.7
Pr	0.04	0.18	0.12	0.33	0.34	0.12	0.3	0.15	3.17
Rb	0.2	0.6	0.2	1.2	3.1	0.2	2.4	0.9	13.2
Sm	<0.03	0.24	0.17	0.52	0.68	0.05	0.61	0.47	5.05
Sn	<1	<1	<1	<1	<1	<1	<1	<1	1
Sr	2.2	16.5	9.7	87.9	273	3.6	302	94.7	197
Ta	<0.1	<0.1	<0.1	<0.1	<0.1	<0.1	<0.1	<0.1	0.6
Tb	0.01	0.04	0.03	0.11	0.16	0.02	0.11	0.1	0.89
Th	0.05	0.09	0.06	0.1	0.06	0.07	<0.05	<0.05	0.81
Tm	0.01	0.01	0.02	0.05	0.08	<0.01	0.06	0.04	0.42
U	<0.05	<0.05	<0.05	0.05	<0.05	<0.05	<0.05	<0.05	0.24
V	43	57	44	101	164	30	128	99	424
W	<1	<1	<1	<1	<1	<1	<1	<1	<1
Y	<0.5	1.1	1	3.1	4.7	0.7	3.9	3.1	28.1
Yb	0.06	0.13	0.2	0.33	0.43	0.1	0.41	0.24	2.76
Zr	2	5	4	7	7	3	5	5	117
As	2.4	5	0.4	5.3	0.5	1	0.5	0.8	0.5
Bi	0.05	0.03	0.02	0.05	0.01	0.02	0.05	0.05	0.03
Hg	0.008	0.011	0.018	0.03	<0.005	0.056	0.006	0.027	0.007
In	0.015	0.009	0.008	0.007	0.006	0.011	0.032	0.008	0.018
Re	0.001	0.001	0.001	0.002	<0.001	0.001	<0.001	0.001	<0.001
Sb	0.12	0.05	0.1	0.1	0.06	0.05	0.11	<0.05	0.07
Se	<0.2	0.8	0.3	0.8	<0.2	0.9	0.6	0.7	0.7
Te	0.02	0.09	0.02	0.03	0.01	0.04	0.01	0.04	<0.01
Tl	<0.02	0.08	<0.02	<0.02	<0.02	<0.02	<0.02	<0.02	<0.02
Ag	<0.5	<0.5	<0.5	<0.5	<0.5	<0.5	<0.5	<0.5	<0.5
Cd	<0.5	<0.5	<0.5	<0.5	<0.5	<0.5	1.4	<0.5	<0.5
Co	153	167	156	111	32	176	38	93	48
Cu	18	190	48	167	109	88	69	153	202
Li	<10	<10	<10	<10	20	<10	10	10	10
Mo	<1	<1	<1	<1	<1	<1	1	1	<1
Ni	1080	2440	1010	899	242	1160	163	738	71
Pb	7	2	<2	<2	<2	<2	3	<2	<2
Sc	7	6	10	23	39	6	33	27	40
Zn	116	86	82	58	29	97	96	51	109

Values in ppm.

Table B-2. A) Major and minor element analyses.

Sample	15ET 203	15LL 173	15LL 175	15LL 201	15LL 202	15LL 203	15LL 204	15LL 205	15RN 335A	15RN 335B
Type	porphyry	troctolite	granodi. porphyry						gabbro	gabbro
SiO_2	57.4	41.8	64.9	40.6	36.7	37.2	37.9	38.7	46.2	43.7
Al_2O_3	16.45	6.59	15.95	1.06	0.66	2.58	0.61	0.72	17.15	5.91
Fe_2O_3	6.28	13.5	3.91	14.85	16.35	15.3	14.9	16.05	5.25	14.7
CaO	5.4	8.23	4.11	5.91	0.66	2.42	1.89	2.7	15.95	8.75
MgO	4.24	26.8	2.78	32.1	40.2	35.5	39.9	38.7	10.85	25.2
Na_2O	4.97	0.36	3.88	0.1	0.05	0.17	0.04	0.07	1.18	0.57
K_2O	2.87	0.01	2.09	0.05	0.04	0.03	0.02	0.02	0.21	0.04
Cr_2O_3	0.01	0.35	0.01	0.33	0.61	0.44	0.81	0.35	0.14	0.38
TiO_2	0.36	0.13	0.46	0.22	0.11	0.1	0.08	0.09	0.16	0.16
MnO	0.15	0.18	0.07	0.21	0.21	0.2	0.2	0.23	0.1	0.22
P_2O_5	0.2	0.01	0.25	0.02	0.02	0.01	0.01	0.02	<0.01	<0.01
SrO	0.06	0.01	0.1	<0.01	<0.01	<0.01	<0.01	<0.01	0.04	0.01
BaO	0.12	<0.01	0.1	<0.01	<0.01	<0.01	<0.01	<0.01	0.01	<0.01
LOI	1.28	0.08	2.02	3.46	5.21	5.93	3.89	1.5	2.41	0.3
Total	99.79	98.05	100.63	98.91	100.82	99.88	100.25	99.15	99.65	99.94
C	0.01	0.02	0.06	0.12	0.13	0.12	0.1	0.1	0.05	0.03
S	0.01	0.53	0.01	0.04	0.07	0.12	0.07	0.07	0.03	0.17

Values in weight percent.

Table B-2. B) Trace element analyses.

Sample	15ET 203	15LL 173	15LL 175	15LL 201	15LL 202	15LL 203	15LL 204	15LL 205	15RN 335A	15RN 335B
Type	porphyry	troctolite	granodi. porphyry						gabbro	gabbro
Au	0.001	0.011	0.001	0.012	0.014	0.012	0.007	0.002	0.003	0.003
Pt	0.0015	0.0207	<0.0005	0.0372	0.023	0.0366	0.0281	0.0269	0.0098	0.0014
Pd	0.001	0.033	<0.001	0.018	0.025	0.09	0.019	0.012	0.008	0.001
Ba	1085	14.9	914	19.7	9.9	14.2	5.3	7.2	75.8	23
Ce	16.4	1	41.1	2.3	1.4	1	0.6	1.1	4.4	1.1
Cr	80	2510	70	2450	4430	3280	5890	2570	1070	2820
Cs	0.37	0.04	1.63	1.6	0.49	0.55	0.27	0.38	3.52	0.23
Dy	1.74	0.42	2.14	0.7	0.22	0.22	0.23	0.23	0.58	0.54
Er	1.39	0.27	1.13	0.28	0.1	0.15	0.1	0.09	0.37	0.33
Eu	0.66	0.14	0.91	0.2	0.06	0.07	0.06	0.08	0.31	0.19
Ga	14.1	5	17.5	2.4	1.9	3.4	1.7	1.6	11.9	5.8
Gd	2.12	0.38	2.76	0.67	0.21	0.32	0.18	0.33	0.56	0.6
Ge	<5	<5	<5	<5	<5	<5	<5	<5	<5	<5
Hf	1.5	<0.2	3.1	0.3	0.2	<0.2	<0.2	<0.2	<0.2	0.2
Ho	0.4	0.09	0.46	0.13	0.03	0.06	0.03	0.06	0.13	0.13
La	8.8	<0.5	19.8	0.9	0.7	0.4	0.4	0.5	0.5	<0.5
Lu	0.17	0.02	0.17	0.04	0.01	0.02	0.02	0.03	0.04	0.07
Nb	4.4	<0.2	8.8	0.5	0.5	0.2	0.2	0.3	<0.2	0.2
Nd	9.1	1	19.6	1.8	0.9	0.8	0.4	0.9	1.3	1.1
Pr	1.97	0.19	4.96	0.35	0.18	0.14	0.09	0.18	0.21	0.19

Rb	42.6	0.4	34.7	2.6	2.3	1.3	1	0.9	4.7	0.8
Sm	2.19	0.28	3.45	0.59	0.2	0.27	0.05	0.22	0.4	0.46
Sn	1	<1	1	<1	<1	<1	<1	<1	6	<1
Sr	536	89.9	834	17.7	9.2	18.6	4.2	6.5	331	90
Ta	0.1	<0.1	0.5	<0.1	<0.1	<0.1	<0.1	<0.1	<0.1	<0.1
Tb	0.27	0.06	0.37	0.11	0.03	0.04	0.03	0.04	0.11	0.08
Th	1.62	<0.05	4.31	0.19	0.13	0.06	0.05	0.09	<0.05	<0.05
Tm	0.17	0.04	0.15	0.04	0.02	0.02	0.02	0.04	0.06	0.06
U	0.8	<0.05	1.99	0.09	<0.05	<0.05	<0.05	<0.05	<0.05	<0.05
V	176	83	68	91	57	67	67	57	115	111
W	<1	<1	1	1	15	1	2	<1	<1	<1
Y	10.7	2.3	11.3	2.9	0.9	1.3	0.9	1.4	3.4	3.2
Yb	1.23	0.21	1.02	0.29	0.16	0.13	0.1	0.13	0.34	0.31
Zr	53	4	114	6	4	2	<2	3	4	4
As	10.1	0.4	2.5	6.3	27.1	2.2	3.3	0.6	0.3	2
Bi	0.03	0.09	0.03	0.07	0.1	0.06	0.04	0.02	0.01	0.04
Hg	<0.005	<0.005	0.01	0.018	0.019	0.021	0.01	0.007	0.007	<0.005
In	0.009	0.012	0.015	0.013	0.012	0.016	0.013	0.01	<0.005	0.006
Re	<0.001	0.003	<0.001	<0.001	0.001	0.002	0.001	0.001	<0.001	0.001
Sb	0.44	<0.05	0.24	0.11	0.1	0.08	0.05	0.06	<0.05	<0.05
Se	0.4	1.7	0.3	0.5	0.5	0.9	0.3	0.5	0.2	0.3
Te	0.01	0.09	<0.01	0.11	0.1	0.1	0.04	0.04	0.01	0.01
Tl	0.02	<0.02	0.07	<0.02	<0.02	<0.02	<0.02	<0.02	<0.02	<0.02
Ag	<0.5	0.6	<0.5	<0.5	<0.5	<0.5	<0.5	<0.5	<0.5	<0.5
Cd	<0.5	<0.5	<0.5	<0.5	<0.5	<0.5	<0.5	<0.5	<0.5	<0.5
Co	15	125	11	150	163	151	151	154	39	94
Cu	42	580	16	272	251	367	99	87	24	83
Li	10	<10	30	<10	<10	<10	<10	<10	40	<10
Mo	1	1	1	<1	<1	<1	<1	<1	<1	<1
Ni	13	1060	58	1115	1760	2040	1785	1405	151	639
Pb	3	<2	<2	2	<2	<2	<2	<2	<2	3
Sc	20	21	7	21	6	9	10	13	31	29
Zn	61	64	53	90	103	102	94	96	23	76

Values in ppm.

Appendix C.

Electron microprobe mineral compositions

Table C-1. Select olivine compositions by EPMA.

Sample ID	Rock type	NiO	MnO	FeO	MgO	SiO2	Total	Fo %
13RN385A	clinopyroxenite	0.098	0.258	18.3	42.3	39.3	100.3	80.5
		0.101	0.253	17.8	42.1	39.3	99.6	80.8
		0.093	0.248	18.4	42.3	39.3	100.3	80.4
		0.108	0.195	16.3	43.6	40.0	100.3	82.6
		0.109	0.203	16.5	43.6	39.5	99.9	82.5
		0.106	0.193	16.0	44.1	40.3	100.7	83.1
13RN386A	wehrlite	0.344	0.203	12.8	46.6	40.2	100.2	86.7
		0.350	0.197	12.6	46.3	40.3	99.8	86.7
		0.346	0.203	12.7	46.6	40.1	99.9	86.8
		0.336	0.198	12.7	46.5	40.5	100.1	86.8
		0.337	0.215	12.4	46.7	40.2	99.8	87.0
		0.354	0.185	12.2	47.2	40.3	100.2	87.3
13RN387A	dunite	0.151	0.258	18.1	43.2	38.5	100.2	81.0
		0.144	0.263	18.2	43.0	38.0	99.5	80.8
		0.144	0.270	18.4	42.7	37.9	99.4	80.5
		0.141	0.252	17.9	43.1	38.8	100.2	81.1
		0.167	0.263	18.2	43.0	38.3	100.0	80.8
		0.153	0.280	18.0	43.0	38.7	100.1	80.9
13RN388A	wehrlite	0.149	0.266	17.2	44.0	39.4	101.0	82.0
		0.147	0.252	17.3	43.8	39.5	101.0	81.9
		0.140	0.248	16.9	44.1	39.3	100.8	82.3
		0.145	0.244	16.9	43.7	39.7	100.7	82.2
		0.146	0.237	16.8	44.2	39.7	101.1	82.4
		0.140	0.257	17.1	44.1	39.4	101.0	82.1
13RN389A	wehrlite	0.087	0.313	18.6	41.7	39.1	99.8	80.0
		0.085	0.327	18.5	42.0	39.1	100.0	80.2
		0.104	0.314	18.6	41.8	39.2	100.0	80.1
		0.085	0.313	18.6	41.9	39.1	100.1	80.1
		0.087	0.323	18.6	41.8	39.2	100.1	80.0
		0.089	0.320	18.6	41.9	39.1	100.1	80.0
13RN391A	dunite	0.148	0.282	17.7	42.5	39.1	99.7	81.1
		0.156	0.271	17.6	42.5	39.2	99.8	81.1
		0.156	0.291	17.7	42.8	38.9	99.8	81.2
		0.149	0.291	17.6	42.4	39.4	99.9	81.1
		0.146	0.294	17.7	42.8	39.1	100.0	81.2
		0.148	0.288	17.7	42.7	39.4	100.2	81.1

Sample ID	Rock type	NiO	MnO	FeO	MgO	SiO2	Total	Fo %
13RN392A	dunite	0.233	0.231	14.8	44.8	39.9	100.0	84.4
		0.238	0.233	14.7	45.0	39.8	100.0	84.5
		0.239	0.238	14.8	45.0	39.7	99.9	84.4
		0.211	0.227	14.8	44.9	39.9	100.0	84.4
		0.213	0.230	14.8	44.8	39.9	100.0	84.3
		0.220	0.230	14.9	44.9	39.7	99.9	84.3
13RN393A	wehrlite	0.145	0.271	16.5	43.6	40.2	100.7	82.5
		0.126	0.253	16.8	43.5	40.0	100.6	82.2
		0.117	0.256	16.8	43.3	40.0	100.5	82.2
		0.120	0.263	16.9	43.5	39.9	100.7	82.1
		0.125	0.268	16.8	43.3	39.8	100.4	82.1
		0.128	0.245	16.7	43.7	39.9	100.7	82.3
13RN394A	dunite	0.238	0.223	15.0	44.6	39.6	99.8	84.1
		0.239	0.232	14.9	44.8	39.7	99.9	84.3
		0.243	0.229	15.1	44.7	39.7	100.0	84.1
		0.239	0.213	14.7	44.8	39.9	99.8	84.5
		0.248	0.219	14.6	44.8	39.9	99.7	84.5
		0.242	0.203	14.7	45.1	39.9	100.1	84.5
13RN395A	dunite	0.230	0.193	14.3	45.3	39.8	99.9	84.9
		0.237	0.197	14.4	45.2	39.9	99.9	84.8
		0.237	0.194	14.3	45.3	39.9	99.9	84.9
		0.240	0.198	14.3	45.3	39.8	99.9	84.9
		0.206	0.206	14.4	45.4	39.9	100.0	84.9
		0.250	0.192	14.3	45.4	39.9	100.1	85.0
13RN397A	dunite	0.248	0.213	15.3	44.5	39.7	100.0	83.8
		0.222	0.220	15.4	44.5	39.6	99.9	83.7
		0.232	0.238	15.5	44.4	39.6	100.0	83.6
		0.215	0.239	15.1	44.4	40.0	100.0	83.9
		0.227	0.216	15.4	44.5	39.7	100.0	83.8
		0.231	0.215	15.5	44.5	39.7	100.1	83.7
13RN400B	dunite	0.192	0.249	15.3	44.4	39.9	100.0	83.7
		0.176	0.241	15.5	44.2	39.9	100.0	83.6
		0.204	0.226	15.4	44.5	39.8	100.1	83.7
		0.205	0.239	15.4	44.5	39.8	100.1	83.7
		0.196	0.241	15.5	44.4	39.8	100.1	83.7
		0.191	0.238	15.3	44.6	39.9	100.2	83.8
13RN401A	wehrlite	0.247	0.212	14.7	45.3	39.5	99.9	84.6
		0.221	0.225	14.8	45.0	39.8	100.0	84.5
		0.233	0.208	14.7	45.0	39.7	99.8	84.5
		0.250	0.223	14.5	44.9	40.1	100.0	84.7
		0.250	0.220	14.5	45.4	39.7	100.1	84.8
		0.216	0.205	14.6	45.3	39.8	100.1	84.7

Sample ID	Rock type	NiO	MnO	FeO	MgO	SiO2	Total	Fo %
13RN402A	wehrlite	0.195	0.205	14.0	45.7	40.0	100.1	85.3
		0.202	0.213	14.0	45.5	40.2	100.1	85.3
		0.201	0.220	14.1	45.2	40.4	100.2	85.1
		0.189	0.213	14.3	45.6	39.9	100.2	85.1
		0.183	0.221	14.4	45.3	39.8	99.9	84.9
		0.203	0.225	14.3	45.4	40.1	100.2	85.0
13RN402B	dunite	0.224	0.225	14.5	45.1	39.9	100.0	84.7
		0.224	0.229	14.8	45.1	39.9	100.3	84.4
		0.233	0.200	15.0	45.0	39.9	100.2	84.3
		0.240	0.213	14.7	44.8	40.0	100.0	84.5
		0.235	0.216	15.0	44.9	39.7	100.1	84.2
		0.225	0.211	14.9	45.0	40.0	100.3	84.4
15ET189	dunite	0.143	0.250	15.8	44.1	39.7	99.9	83.3
		0.139	0.242	15.9	44.0	39.5	99.8	83.1
		0.138	0.228	15.8	44.0	39.6	99.8	83.3
		0.135	0.244	16.0	44.0	39.5	99.9	83.1
		0.149	0.247	16.1	44.0	39.7	100.1	83.0
		0.130	0.250	15.8	43.8	39.8	99.8	83.2
15ET191	wehrlite	0.198	0.240	15.3	44.2	39.8	99.8	83.8
		0.187	0.216	15.4	44.4	39.7	99.9	83.7
		0.195	0.255	15.4	44.3	39.7	99.9	83.7
		0.175	0.268	15.7	43.9	39.8	99.8	83.3
		0.192	0.249	15.7	44.0	39.6	99.8	83.3
		0.193	0.258	15.8	43.9	39.7	99.8	83.2
15ET192	wehrlite	0.208	0.231	15.6	44.4	39.8	100.1	83.6
		0.204	0.230	15.3	44.4	40.0	100.1	83.8
		0.196	0.210	15.1	44.7	39.8	100.1	84.1
		0.201	0.246	15.0	44.7	39.8	99.9	84.2
		0.171	0.228	14.9	44.8	39.9	100.0	84.3
		0.192	0.223	15.1	44.8	39.8	100.1	84.1
15ET193	wehrlite	0.185	0.219	14.4	45.5	39.7	100.0	84.9
		0.189	0.204	14.5	45.4	39.7	100.0	84.8
		0.189	0.209	14.3	45.5	39.9	100.1	85.0
		0.181	0.230	14.2	45.7	39.9	100.2	85.1
		0.184	0.208	14.3	45.6	39.8	100.1	85.1
		0.196	0.206	14.2	45.6	39.7	99.9	85.1
15LL121	wehrlite	0.163	0.249	17.2	42.9	39.4	100.0	81.6
		0.165	0.266	17.2	42.9	39.4	99.9	81.7
		0.162	0.255	17.8	42.5	39.3	100.0	81.0
		0.168	0.262	17.8	42.5	39.2	100.0	80.9
		0.166	0.263	17.5	42.8	39.2	99.9	81.3
		0.162	0.269	17.4	42.8	39.3	100.0	81.4

Sample ID	Rock type	NiO	MnO	FeO	MgO	SiO2	Total	Fo %
15LL122	dunite	0.143	0.249	16.7	43.3	39.4	99.8	82.2
		0.147	0.273	16.4	43.5	39.5	99.8	82.6
		0.152	0.247	16.5	43.4	39.4	99.8	82.4
		0.145	0.264	16.6	43.6	39.6	100.1	82.4
		0.144	0.251	16.5	43.4	39.6	99.9	82.4
		0.156	0.241	16.5	43.6	39.5	100.0	82.5
15LL128	wehrlite	0.131	0.252	16.5	43.5	39.6	100.0	82.5
		0.136	0.249	16.3	43.8	39.5	99.9	82.7
		0.142	0.248	16.6	43.5	39.5	100.0	82.3
		0.150	0.241	16.6	43.6	39.5	100.0	82.4
		0.129	0.235	16.5	43.5	39.7	100.1	82.5
		0.130	0.261	16.6	43.4	39.6	100.0	82.4
15LL131	dunite	0.178	0.243	16.5	43.5	39.6	100.0	82.5
		0.174	0.244	16.1	43.7	39.5	99.7	82.9
		0.164	0.235	16.2	43.6	39.6	99.8	82.7
		0.178	0.240	16.3	43.4	39.8	100.0	82.6
		0.186	0.234	16.2	43.6	39.8	100.0	82.8
		0.173	0.231	16.1	43.6	39.6	99.8	82.8
15LL132	dunite	0.232	0.219	14.4	45.0	40.1	99.9	84.8
		0.229	0.224	14.4	45.0	40.2	100.1	84.8
		0.231	0.214	14.6	44.9	40.0	99.9	84.6
		0.229	0.202	14.5	45.0	40.2	100.1	84.7
		0.232	0.222	14.4	44.9	40.1	99.9	84.7
		0.223	0.224	14.5	45.0	40.1	100.0	84.7
15LL133	dunite	0.068	0.239	15.7	44.0	39.5	99.5	83.3
		0.082	0.243	15.7	44.1	39.6	99.7	83.4
		0.070	0.220	15.7	43.9	39.5	99.5	83.3
		0.076	0.230	15.6	43.9	39.7	99.5	83.4
		0.064	0.235	15.7	43.9	39.6	99.5	83.3
		0.068	0.251	15.7	44.0	39.6	99.7	83.3
15LL134	dunite	0.209	0.192	14.4	45.2	39.9	99.8	84.9
		0.211	0.214	14.4	45.2	39.9	99.9	84.8
		0.208	0.217	14.3	45.1	39.9	99.9	84.9
		0.223	0.192	14.3	45.1	39.9	99.7	84.9
		0.226	0.198	14.3	45.0	39.9	99.7	84.9
		0.224	0.210	14.1	45.3	40.0	99.8	85.2
15LL135	wehrlite	0.086	0.276	17.9	42.3	39.2	99.7	80.8
		0.090	0.293	18.0	42.3	39.1	99.8	80.7
		0.082	0.282	18.1	42.6	39.2	100.1	80.8
		0.082	0.292	18.1	42.2	39.1	99.7	80.6
		0.094	0.261	17.7	42.3	39.4	99.7	81.0
		0.086	0.255	17.1	43.0	39.4	99.9	81.7

Sample ID	Rock type	NiO	MnO	FeO	MgO	SiO2	Total	Fo %
15LL136	troctolite	0.172	0.285	19.2	40.9	38.9	99.5	79.1
		0.184	0.307	19.1	41.0	39.0	99.6	79.2
		0.186	0.282	19.3	40.8	39.0	99.5	79.1
		0.209	0.282	18.4	41.5	39.1	99.4	80.1
		0.200	0.274	18.3	41.8	39.1	99.7	80.3
		0.197	0.256	18.2	41.6	39.2	99.5	80.3
15LL137	dunite	0.199	0.238	14.7	44.8	39.7	99.6	84.5
		0.215	0.207	14.8	44.8	39.7	99.8	84.3
		0.215	0.204	14.4	45.2	39.9	99.9	84.8
		0.225	0.223	14.6	45.0	39.8	99.9	84.6
		0.217	0.224	14.5	45.1	39.9	100.0	84.7
		0.245	0.220	14.4	44.9	39.8	99.6	84.7
15LL138	dunite	0.200	0.231	15.2	44.4	39.7	99.7	83.9
		0.201	0.244	15.2	44.4	39.9	100.0	83.9
		0.205	0.226	15.3	44.3	39.7	99.7	83.8
		0.243	0.228	15.1	44.3	39.8	99.7	84.0
		0.205	0.204	15.1	44.3	39.8	99.7	83.9
		0.195	0.229	15.1	44.4	39.8	99.7	83.9
15LL139	dunite	0.231	0.217	15.0	44.6	39.6	99.7	84.1
		0.234	0.219	14.9	44.6	39.8	99.8	84.2
		0.232	0.235	15.2	44.5	39.7	99.9	83.9
		0.227	0.222	14.9	44.7	39.7	99.8	84.2
		0.236	0.236	15.0	44.6	39.7	99.7	84.2
		0.230	0.239	15.0	44.8	39.8	100.1	84.2
15LL140	dunite	0.172	0.227	15.0	44.8	39.8	100.0	84.1
		0.181	0.233	15.3	44.6	39.6	99.9	83.9
		0.195	0.235	15.0	44.7	39.8	99.9	84.1
		0.199	0.218	15.1	44.8	39.7	100.0	84.1
		0.172	0.224	15.2	44.8	39.8	100.1	84.0
		0.165	0.224	15.2	44.6	39.7	99.9	83.9
15LL142	dunite	0.230	0.177	13.7	45.4	40.2	99.6	85.6
		0.232	0.199	13.7	45.6	40.3	100.0	85.6
		0.212	0.203	13.7	46.0	39.6	99.8	85.7
		0.229	0.213	13.5	46.0	40.0	99.9	85.9
		0.231	0.204	13.5	46.0	40.1	100.0	85.9
		0.221	0.204	13.6	45.8	39.9	99.7	85.7
15LL146	dunite	0.224	0.225	16.0	43.6	39.7	99.8	83.0
		0.228	0.242	16.1	44.0	39.5	100.0	83.0
		0.235	0.238	16.1	43.7	39.5	99.8	82.9
		0.234	0.238	15.9	44.1	39.4	99.8	83.2
		0.230	0.247	16.1	43.8	39.6	100.1	82.9
		0.225	0.222	16.1	43.9	39.5	100.0	82.9

Sample ID	Rock type	NiO	MnO	FeO	MgO	SiO2	Total	Fo %
15LL147	dunite	0.181	0.226	15.3	44.3	39.4	99.4	83.8
		0.183	0.229	15.5	44.1	39.6	99.6	83.6
		0.152	0.241	15.3	44.3	39.6	99.6	83.7
		0.149	0.231	15.4	44.4	39.6	99.7	83.7
		0.180	0.226	15.0	44.8	39.6	99.8	84.2
		0.156	0.229	15.1	44.9	39.7	100.0	84.2
15LL148	wehrlite	0.232	0.257	18.0	42.4	39.5	100.4	80.8
		0.224	0.278	18.1	42.4	39.3	100.4	80.7
		0.212	0.248	17.8	42.9	39.5	100.6	81.1
		0.199	0.286	17.8	42.7	39.4	100.5	81.0
		0.186	0.279	17.8	42.6	39.5	100.4	81.1
		0.173	0.258	17.7	42.1	38.8	99.0	80.9
15LL149	wehrlite	0.185	0.187	13.6	45.8	40.1	99.8	85.7
		0.175	0.195	13.7	45.9	40.2	100.1	85.7
		0.170	0.212	13.7	46.0	40.2	100.2	85.7
		0.181	0.215	14.0	45.9	40.0	100.2	85.4
		0.172	0.195	14.2	45.5	40.1	100.2	85.1
		0.185	0.211	13.7	46.0	40.1	100.2	85.7
15LL153	dunite	0.185	0.209	13.8	45.7	40.0	100.0	85.5
		0.181	0.203	14.0	45.7	40.0	100.0	85.4
		0.178	0.205	13.8	45.5	40.2	100.0	85.4
		0.192	0.207	14.1	45.6	40.0	100.0	85.3
		0.162	0.216	14.1	45.6	39.9	100.0	85.2
		0.158	0.215	14.2	45.6	39.8	100.0	85.1
15LL154	dunite	0.190	0.209	13.2	46.0	40.1	99.8	86.1
		0.197	0.203	13.4	46.0	40.0	99.8	86.0
		0.196	0.220	13.4	46.1	40.1	100.0	85.9
		0.186	0.197	13.8	45.9	40.0	100.1	85.6
		0.186	0.211	13.3	46.2	40.3	100.2	86.1
		0.181	0.198	13.3	46.3	40.3	100.3	86.2
15LL155	dunite	0.192	0.207	13.9	45.9	39.8	100.1	85.5
		0.216	0.220	13.8	45.8	40.1	100.1	85.5
		0.218	0.205	13.9	45.5	40.2	100.1	85.4
		0.202	0.207	13.9	45.7	40.2	100.2	85.4
		0.220	0.202	13.9	45.7	40.2	100.2	85.4
		0.188	0.228	13.8	45.7	40.2	100.1	85.6
15LL156	dunite	0.202	0.215	13.3	46.1	40.2	100.0	86.1
		0.210	0.217	13.6	45.8	40.2	100.0	85.8
		0.203	0.211	13.7	45.9	40.1	100.1	85.6
		0.207	0.214	13.4	46.2	40.1	100.1	86.0
		0.208	0.207	13.4	46.0	40.2	100.0	85.9
		0.213	0.194	13.4	46.3	39.9	99.9	86.0

Sample ID	Rock type	NiO	MnO	FeO	MgO	SiO2	Total	Fo %
15LL157	dunite	0.180	0.220	13.0	46.4	40.2	100.0	86.5
		0.179	0.194	12.9	46.4	40.4	100.1	86.5
		0.197	0.219	13.1	46.3	40.3	100.1	86.3
		0.185	0.181	12.9	46.5	40.4	100.2	86.5
		0.188	0.202	12.9	46.6	40.4	100.2	86.6
		0.198	0.211	13.1	46.4	40.4	100.3	86.3
15LL158	dunite	0.242	0.250	15.2	44.4	39.8	100.0	83.9
		0.257	0.239	15.3	44.5	39.8	100.1	83.8
		0.248	0.245	15.4	44.3	39.8	100.0	83.7
		0.251	0.224	15.3	44.4	39.7	99.9	83.8
		0.229	0.237	15.4	44.3	39.7	99.9	83.7
		0.221	0.226	15.5	44.2	39.8	100.0	83.6
15LL160	dunite	0.204	0.227	14.3	45.2	40.1	100.1	84.9
		0.207	0.231	14.2	45.4	39.9	99.9	85.1
		0.207	0.232	14.0	45.4	40.0	99.9	85.3
		0.211	0.245	14.2	45.5	40.0	100.1	85.1
		0.200	0.230	14.1	45.4	40.1	100.0	85.2
		0.198	0.216	14.1	45.5	40.0	100.0	85.2
15LL161	dunite	0.213	0.195	14.2	45.5	39.8	99.9	85.1
		0.214	0.205	13.8	45.5	40.0	99.8	85.4
		0.217	0.202	13.9	45.6	40.2	100.1	85.4
		0.212	0.200	14.0	45.5	40.1	100.0	85.3
		0.229	0.200	13.8	45.6	40.1	99.9	85.5
		0.227	0.205	14.0	45.4	40.1	99.9	85.3
15LL163B	wehrlite	0.145	0.247	16.0	43.9	39.6	99.8	83.0
		0.148	0.224	15.9	44.0	39.4	99.8	83.1
		0.130	0.242	15.7	44.3	39.7	100.1	83.4
		0.132	0.212	15.6	44.2	39.7	99.7	83.5
		0.134	0.255	16.5	43.3	39.5	99.7	82.4
		0.120	0.270	16.7	43.2	39.5	99.8	82.2
15LL168	dunite	0.183	0.200	13.2	46.4	40.3	100.2	86.3
		0.196	0.190	13.0	46.3	40.4	100.1	86.4
		0.194	0.202	13.1	46.3	40.3	100.2	86.3
		0.178	0.218	13.1	46.3	40.3	100.1	86.3
		0.160	0.190	13.1	46.4	40.4	100.2	86.4
		0.198	0.223	13.2	46.4	40.3	100.3	86.3
15LL169	dunite	0.174	0.236	14.0	45.5	40.1	100.1	85.3
		0.186	0.212	13.9	45.5	40.3	100.1	85.3
		0.182	0.205	14.0	45.6	40.1	100.1	85.4
		0.186	0.219	14.0	45.6	40.0	100.1	85.3
		0.179	0.208	14.0	45.6	40.0	100.0	85.3
		0.172	0.239	14.1	45.5	40.0	100.0	85.2

Sample ID	Rock type	NiO	MnO	FeO	MgO	SiO2	Total	Fo %
15LL171	dunite	0.239	0.219	13.5	45.9	40.2	100.0	85.8
		0.232	0.221	13.6	45.8	40.2	100.1	85.7
		0.229	0.222	13.8	45.7	40.0	99.9	85.6
		0.257	0.220	13.6	45.9	39.9	99.9	85.7
		0.225	0.223	13.7	45.8	40.0	99.9	85.6
		0.237	0.228	13.8	45.9	39.8	100.0	85.6
15LL172	dunite	0.214	0.214	14.1	45.0	40.2	99.7	85.0
		0.190	0.214	14.3	45.1	40.0	99.8	84.9
		0.210	0.194	14.1	45.0	40.3	99.8	85.1
		0.176	0.200	13.8	45.3	40.4	99.9	85.4
		0.190	0.199	14.2	45.2	40.2	100.0	85.0
		0.207	0.229	14.1	45.2	40.3	100.1	85.1
15LL174	troctolite	0.149	0.245	16.5	43.2	39.7	99.8	82.4
		0.143	0.249	16.7	43.3	39.5	99.9	82.2
		0.148	0.243	16.7	43.2	39.6	99.9	82.2
		0.145	0.248	16.6	43.3	39.7	100.0	82.3
		0.142	0.260	16.8	43.2	39.6	100.0	82.1
		0.156	0.243	16.6	43.3	39.8	100.1	82.3
15RN340	dunite	0.146	0.246	15.0	44.7	40.0	100.1	84.2
		0.175	0.247	15.0	44.7	39.9	100.1	84.1
		0.162	0.225	15.0	44.8	39.9	100.1	84.2
		0.148	0.226	14.8	44.8	39.9	99.9	84.4
		0.164	0.225	14.8	44.8	40.1	100.0	84.3
		0.170	0.211	14.9	44.9	40.0	100.1	84.3
15RN342	dunite	0.197	0.225	14.5	45.1	39.9	99.9	84.7
		0.173	0.219	14.4	45.2	40.1	100.1	84.8
		0.180	0.221	14.3	45.4	40.1	100.1	85.0
		0.178	0.223	14.4	45.4	40.0	100.1	84.9
		0.169	0.209	14.3	45.4	40.1	100.2	85.0
		0.161	0.225	14.5	45.2	40.0	100.2	84.7
15RN349	wehrlite	0.204	0.226	15.6	44.1	39.7	99.8	83.4
		0.207	0.240	15.6	44.1	39.7	99.9	83.4
		0.202	0.235	15.7	44.1	39.8	100.0	83.4
		0.204	0.242	15.8	44.1	39.7	100.0	83.2
		0.202	0.231	15.7	44.1	39.8	100.0	83.4
		0.190	0.239	15.6	44.1	39.9	100.0	83.5
15RN350	troctolite	0.133	0.266	17.6	42.3	39.3	99.7	81.1
		0.119	0.279	17.6	42.5	39.2	99.7	81.2
		0.127	0.244	17.6	42.3	39.4	99.7	81.1
		0.125	0.264	17.7	42.3	39.3	99.7	80.9
		0.115	0.257	17.6	42.4	39.3	99.8	81.1
		0.125	0.243	17.7	42.4	39.3	99.8	81.0

Sample ID	Rock type	NiO	MnO	FeO	MgO	SiO2	Total	Fo %
15RN351	troctolite	0.131	0.260	16.7	42.9	39.6	99.6	82.1
		0.133	0.259	16.7	43.0	39.5	99.6	82.1
		0.126	0.234	16.9	42.8	39.5	99.6	81.9
		0.137	0.255	16.8	42.9	39.5	99.6	82.0
		0.132	0.240	16.9	42.8	39.6	99.7	81.9
		0.130	0.254	16.9	42.9	39.5	99.7	81.9
10-36-229.2	drill core	0.161	0.210	13.9	45.6	39.9	99.7	85.4
		0.158	0.208	13.9	45.2	39.8	99.2	85.3
		0.201	0.215	14.1	44.9	39.6	99.0	85.0
		0.199	0.212	13.9	45.3	40.2	99.7	85.4
		0.140	0.208	13.8	45.2	39.7	99.1	85.4
		0.146	0.216	13.9	45.2	39.7	99.2	85.3

Table C-2. Pyroxene compositions by EPMA.

Sample	FeO	MnO	Cr2O3	CaO	TiO2	SiO2	Na2O	MgO	Al2O3	Total	Mg number
13RN385A											
Grain 1:	4.61	0.131	0.803	20.3	0.375	53.6	0.195	18.6	1.73	100.3	87.8
	5.30	0.146	0.993	20.2	0.520	52.5	0.163	18.1	1.79	99.7	85.9
	5.66	0.126	0.716	17.9	0.346	53.8	0.213	19.1	1.66	99.6	85.7
	3.98	0.155	0.901	22.5	0.424	52.9	0.245	16.8	1.83	99.7	88.3
	4.39	0.118	0.913	21.4	0.417	53.0	0.261	17.4	1.82	99.7	87.6
	3.87	0.171	0.889	21.8	0.449	53.1	0.253	17.6	2.05	100.2	89.0
Grain 2:	4.67	0.145	0.805	20.3	0.475	53.5	0.268	18.4	1.88	100.4	87.5
	4.21	0.147	0.784	21.6	0.406	53.7	0.230	17.8	1.77	100.6	88.3
	4.61	0.152	0.880	20.9	0.399	53.5	0.250	18.1	1.91	100.7	87.5
	5.33	0.174	0.716	18.8	0.351	54.0	0.195	19.7	1.61	100.8	86.8
	4.72	0.140	0.952	20.9	0.470	53.2	0.253	17.8	2.24	100.7	87.1
	4.53	0.148	0.825	21.4	0.509	53.6	0.237	17.2	2.42	100.9	87.2
	4.32	0.123	0.814	21.3	0.517	53.6	0.264	17.7	2.36	101.0	88.0
	4.24	0.128	0.832	21.3	0.482	53.9	0.264	17.6	2.28	101.0	88.1
	6.66	0.176	0.771	16.5	0.653	54.3	0.177	20.1	1.60	101.0	84.3
Grain 3:	4.55	0.144	0.963	20.6	0.441	53.6	0.237	18.3	2.13	100.9	87.8
	3.97	0.111	0.887	20.9	0.396	54.0	0.285	18.0	2.06	100.6	89.0
	3.99	0.137	0.878	22.1	0.442	53.5	0.268	17.3	2.05	100.7	88.6
	4.62	0.148	0.963	20.7	0.546	53.1	0.231	17.9	1.98	100.2	87.3
	4.56	0.147	0.923	20.9	0.463	53.3	0.227	17.9	1.98	100.3	87.5
	4.16	0.115	0.831	21.8	0.396	53.7	0.244	17.7	1.75	100.7	88.4
	4.43	0.154	0.777	20.9	0.385	53.8	0.217	18.1	1.82	100.5	87.9
13RN389A											
Grain 1:	3.36	0.082	0.735	22.3	0.365	53.1	0.231	17.5	2.68	100.3	90.3
	2.89	0.110	0.610	24.5	0.350	53.7	0.074	16.9	1.69	100.8	91.2
	2.94	0.111	0.536	24.4	0.321	53.8	0.078	17.0	1.54	100.7	91.1
	3.21	0.120	0.878	23.2	0.346	53.1	0.198	17.2	2.35	100.5	90.5
	3.29	0.137	0.719	21.8	0.340	53.3	0.259	17.8	2.58	100.2	90.6
	3.78	0.098	0.820	20.8	0.372	52.7	0.251	18.1	2.80	99.7	89.5
Grain 2:	3.39	0.121	0.917	23.9	0.399	52.7	0.112	16.8	2.14	100.5	89.8
	2.88	0.088	0.500	22.5	0.461	52.9	0.212	17.3	2.86	99.7	91.4
	3.02	0.099	0.530	21.2	0.313	53.4	0.274	18.1	2.54	99.6	91.5
	3.12	0.114	0.729	24.3	0.404	52.9	0.075	16.7	2.03	100.4	90.5
	3.10	0.097	0.609	23.6	0.299	53.3	0.128	17.1	1.77	100.0	90.8
	2.93	0.116	0.655	24.5	0.370	53.2	0.064	16.7	1.68	100.2	91.1
	3.29	0.110	0.762	23.5	0.326	53.2	0.144	17.1	1.82	100.2	90.2

	FeO	MnO	Cr2O3	CaO	TiO2	SiO2	Na2O	MgO	Al2O3	Total	Mg number
	2.88	0.090	0.604	24.5	0.350	53.5	0.073	16.8	1.60	100.4	91.2
Grain 3:	3.19	0.108	0.625	24.3	0.370	53.3	0.074	16.8	1.73	100.6	90.4
	3.23	0.098	0.668	24.3	0.376	53.3	0.050	16.8	1.71	100.5	90.3
	4.23	0.113	1.014	23.9	0.483	52.4	0.054	16.5	1.91	100.7	87.5
	2.85	0.121	0.662	23.7	0.406	53.2	0.147	17.0	2.29	100.4	91.4
	2.96	0.092	0.689	24.0	0.360	53.4	0.146	16.9	2.02	100.5	91.1
	3.07	0.097	0.738	24.4	0.389	53.4	0.096	16.7	1.93	100.8	90.7
	3.38	0.108	0.769	24.1	0.424	53.3	0.090	16.8	1.88	100.8	89.8
	3.02	0.118	0.688	24.3	0.394	53.2	0.102	16.7	1.97	100.5	90.8
	3.22	0.114	0.631	24.3	0.359	53.4	0.062	16.8	1.72	100.6	90.3

Sample	FeO	MnO	Cr2O3	CaO	TiO2	SiO2	Na2O	MgO	Al2O3	Total	Mg number
13RN393											
Grain 1:	3.21	0.109	0.827	22.3	0.484	52.8	0.183	17.8	2.18	100.0	90.8
	4.38	0.145	0.841	21.5	0.595	52.5	0.160	17.7	2.26	100.0	87.8
	3.46	0.148	0.806	22.7	0.573	52.5	0.182	17.1	2.48	99.9	89.8
	2.47	0.100	0.699	24.5	0.345	53.4	0.146	17.4	2.10	101.0	92.6
	2.61	0.077	0.825	24.3	0.390	52.9	0.160	17.1	2.24	100.6	92.1
	3.90	0.116	0.345	23.8	0.102	54.8	0.127	16.9	1.41	101.6	88.6
	4.56	0.137	0.491	22.1	0.245	52.6	0.170	17.7	1.98	100.0	87.4
	2.60	0.093	0.910	23.5	0.318	52.9	0.176	17.4	2.00	99.9	92.3
	2.60	0.054	0.909	23.6	0.297	53.0	0.197	17.5	2.16	100.3	92.3
	3.47	0.130	0.598	23.3	0.342	53.3	0.172	16.9	2.26	100.5	89.7
	2.73	0.099	0.715	21.7	0.363	53.5	0.297	18.4	2.64	100.3	92.3
	2.65	0.106	0.714	23.5	0.414	53.4	0.196	17.4	2.49	100.9	92.1
	2.59	0.099	0.882	24.1	0.331	53.0	0.169	17.2	2.08	100.4	92.2
	2.79	0.090	0.910	25.0	0.302	52.8	0.092	17.0	1.74	100.7	91.6
Grain 2:	2.58	0.092	0.843	24.6	0.278	52.8	0.141	17.2	1.91	100.4	92.2
	2.68	0.085	0.945	25.1	0.268	52.7	0.107	17.0	1.62	100.5	91.9
	3.17	0.110	1.040	22.6	0.275	52.4	0.207	17.7	2.22	99.7	90.9
	2.58	0.099	0.800	23.6	0.310	52.9	0.212	17.7	2.15	100.3	92.4
	2.60	0.071	0.850	24.4	0.241	53.0	0.153	17.3	1.87	100.5	92.2
	2.57	0.071	0.697	23.9	0.515	53.1	0.240	17.4	2.77	101.3	92.4
	2.74	0.060	0.651	24.8	0.431	53.5	0.154	17.3	2.17	101.8	91.8
	3.02	0.089	0.841	23.9	0.870	53.2	0.161	17.4	2.12	101.6	91.1
	2.79	0.096	0.363	23.8	0.184	54.4	0.227	17.9	1.79	101.5	92.0
	3.24	0.093	1.193	23.5	0.414	52.6	0.194	17.4	2.32	100.9	90.6
	3.12	0.059	0.567	22.3	0.819	53.0	0.281	18.1	2.65	100.9	91.2
	3.42	0.092	0.752	22.7	0.456	52.6	0.229	17.6	2.75	100.7	90.2

Sample	FeO	MnO	Cr2O3	CaO	TiO2	SiO2	Na2O	MgO	Al2O3	Total	Mg number
Grain 3:	2.84	0.104	0.162	25.2	0.085	53.9	0.118	17.3	0.69	100.4	91.6
	2.65	0.095	0.189	25.4	0.091	53.8	0.103	17.2	0.50	100.1	92.0
	2.56	0.079	0.162	25.2	0.104	53.7	0.125	17.3	0.70	99.9	92.3
	3.36	0.120	0.373	25.2	0.147	54.1	0.194	16.7	0.96	101.2	89.9
	2.72	0.089	0.498	24.9	0.239	53.8	0.102	17.3	1.84	101.5	91.9
Grain 4:	2.55	0.084	0.700	25.4	0.307	53.0	0.103	17.0	1.66	100.8	92.2
	2.70	0.104	0.870	23.6	0.457	52.6	0.194	17.4	2.30	100.2	92.0
	2.38	0.086	0.559	24.8	0.353	53.2	0.129	17.2	1.81	100.5	92.8
	3.77	0.107	1.475	23.2	0.438	51.9	0.181	17.1	2.21	100.3	89.0
	2.92	0.132	0.841	23.1	0.415	52.1	0.187	17.4	2.23	99.4	91.4
	2.45	0.082	0.655	24.8	0.297	52.8	0.116	17.1	1.61	99.9	92.6
	2.54	0.067	0.766	24.6	0.293	52.8	0.136	17.1	1.73	99.9	92.3
	2.89	0.094	0.807	23.1	0.501	51.5	0.235	17.2	2.77	99.1	91.4
	2.44	0.086	0.587	24.8	0.399	51.0	0.186	16.8	2.32	98.6	92.5
	2.52	0.099	0.616	23.7	0.366	52.4	0.239	17.4	2.30	99.5	92.5
	3.21	0.123	0.838	21.9	0.389	52.6	0.169	18.1	2.14	99.4	90.9
	2.55	0.095	0.795	24.1	0.532	51.9	0.174	17.0	2.42	99.5	92.2
Grain 5:	2.68	0.109	0.839	23.8	0.339	52.7	0.175	17.3	2.09	100.1	92.0
	2.59	0.106	0.847	24.4	0.313	53.0	0.128	17.2	1.92	100.5	92.2
	2.36	0.049	0.644	25.1	0.303	52.8	0.095	17.1	1.84	100.3	92.8
	2.40	0.052	0.716	25.0	0.288	52.8	0.087	17.0	1.78	100.2	92.6
	2.59	0.105	0.725	24.9	0.325	52.9	0.112	17.1	1.68	100.4	92.1
	2.54	0.078	0.791	24.8	0.312	52.8	0.092	17.2	1.84	100.5	92.3
	2.53	0.061	0.693	25.3	0.253	53.1	0.094	17.1	1.55	100.7	92.3
	3.66	0.070	0.576	22.5	0.265	52.4	0.221	17.8	1.94	99.3	89.7
Grain 6:	2.54	0.089	0.607	24.3	0.576	52.3	0.168	17.0	2.51	100.0	92.3
	3.76	0.080	1.061	22.1	0.504	51.6	0.281	17.6	2.82	99.8	89.3
	2.56	0.114	0.681	23.7	0.607	52.5	0.165	17.3	2.46	100.1	92.3
	2.92	0.079	0.762	23.3	0.433	52.1	0.326	17.6	2.82	100.3	91.5
	3.55	0.071	0.731	23.4	0.378	51.7	0.112	17.4	2.52	99.7	89.7
	3.05	0.045	0.705	25.4	0.588	52.8	0.045	16.9	1.61	101.1	90.8
	2.63	0.061	0.478	23.1	0.266	53.0	0.217	18.1	2.41	100.2	92.4
	2.87	0.084	0.707	25.2	0.377	52.9	0.088	17.0	1.58	100.9	91.4
	3.16	0.087	0.887	24.7	0.514	52.2	0.109	16.8	1.95	100.4	90.5
13RN402A											
Grain 1:	2.78	0.095	1.051	22.4	0.379	52.8	0.294	17.5	2.70	100.0	91.8
	2.96	0.104	1.034	22.7	0.399	52.7	0.249	17.7	2.84	100.6	91.4
	2.65	0.110	0.900	23.6	0.319	54.5	0.192	17.6	1.87	101.7	92.2
	2.98	0.148	1.002	22.8	0.328	53.4	0.227	17.7	2.39	101.0	91.4

Sample	FeO	MnO	Cr2O3	CaO	TiO2	SiO2	Na2O	MgO	Al2O3	Total	Mg number
Grain 2:	4.45	0.144	0.902	20.3	0.320	51.8	0.196	18.3	2.12	98.5	88.0
	3.11	0.133	0.808	18.9	0.225	54.0	0.252	19.0	1.87	98.3	91.6
	3.41	0.130	0.915	22.1	0.337	53.1	0.255	17.8	2.15	100.3	90.3
Grain 3:	5.34	0.171	0.851	18.4	0.291	52.8	0.286	19.2	2.14	99.5	86.5
	4.11	0.150	0.963	21.9	0.296	52.9	0.272	17.4	2.16	100.2	88.3
	3.92	0.109	0.996	22.1	0.298	53.2	0.270	17.2	2.10	100.2	88.6
	3.81	0.147	0.968	22.0	0.305	52.9	0.271	17.3	2.13	99.8	89.0
	4.39	0.128	0.927	20.1	0.311	52.9	0.221	18.9	2.07	99.9	88.5
	4.24	0.140	0.943	20.2	0.310	53.7	0.260	18.6	2.13	100.5	88.7
	3.64	0.162	0.979	21.8	0.360	53.2	0.311	17.4	2.35	100.2	89.5
Grain 4:	2.67	0.124	0.939	22.5	0.245	52.8	0.193	17.9	2.11	99.5	92.3
	2.74	0.133	0.867	23.3	0.251	53.5	0.168	17.4	1.56	99.9	91.9
	3.65	0.138	1.001	21.9	0.300	53.0	0.248	17.3	2.13	99.6	89.4
	2.72	0.146	0.852	23.4	0.258	54.2	0.170	17.5	1.59	100.8	92.0
	2.77	0.104	1.257	23.1	0.223	53.6	0.210	17.8	1.82	100.9	92.0
	3.08	0.113	0.990	22.3	0.333	53.4	0.275	17.5	2.19	100.1	91.0
	2.98	0.119	1.001	23.1	0.314	53.3	0.250	17.2	2.13	100.4	91.1
	2.84	0.126	0.937	22.9	0.287	53.6	0.257	17.4	1.89	100.2	91.6
	3.21	0.109	0.951	22.5	0.327	53.5	0.261	17.2	2.09	100.2	90.5
	3.05	0.131	0.952	22.2	0.346	53.6	0.310	17.5	2.25	100.4	91.1
	2.45	0.128	0.754	23.7	0.270	53.2	0.189	17.7	1.74	100.2	92.8
	2.60	0.117	0.722	23.4	0.309	53.9	0.250	17.6	1.59	100.5	92.4
	2.84	0.125	0.876	23.2	0.305	53.7	0.280	17.4	1.88	100.5	91.6
	2.92	0.149	1.045	20.9	0.272	52.9	0.327	18.8	2.63	99.9	92.0
Grain 5:	3.19	0.125	0.929	23.1	0.246	53.9	0.248	17.4	1.76	101.0	90.7
	2.75	0.141	1.044	23.6	0.261	53.8	0.165	17.3	1.69	100.8	91.8
	3.41	0.126	0.976	22.4	0.277	53.6	0.308	17.9	1.94	100.9	90.3
	3.27	0.132	1.001	21.8	0.256	54.5	0.271	17.9	2.08	101.3	90.7
	2.88	0.114	0.889	21.7	0.223	54.2	0.266	18.1	1.88	100.3	91.8
	3.22	0.113	0.896	22.4	0.304	53.5	0.300	17.5	1.97	100.2	90.6
	3.16	0.125	0.825	23.1	0.260	53.6	0.231	17.4	1.65	100.4	90.8
	3.51	0.148	0.964	21.5	0.294	53.5	0.301	18.1	2.20	100.4	90.2
	3.73	0.156	0.963	22.0	0.315	53.6	0.318	17.6	2.18	100.8	89.4
	3.11	0.116	0.904	20.2	0.291	54.0	0.356	19.2	2.33	100.4	91.7

Sample	FeO	MnO	Cr2O3	CaO	TiO2	SiO2	Na2O	MgO	Al2O3	Total	Mg number
15ET191											
Grain 1:	3.93	0.111	0.855	21.1	0.346	53.0	0.266	16.9	2.46	98.9	88.5
	3.69	0.104	0.901	22.3	0.354	52.2	0.255	16.5	2.70	99.0	88.8
	4.56	0.153	0.889	20.7	0.364	52.7	0.308	17.2	2.51	99.3	87.0
	3.74	0.132	0.828	21.6	0.323	52.5	0.305	16.9	2.45	98.7	88.9
	3.46	0.111	0.798	20.5	0.316	53.9	0.293	16.9	2.52	98.8	89.7
Grain 2:	3.73	0.120	0.918	21.9	0.349	51.8	0.261	16.7	2.98	98.6	88.8
	4.74	0.139	0.898	20.0	0.367	52.5	0.275	17.6	2.53	99.1	86.9
	4.77	0.135	0.925	20.7	0.402	52.5	0.269	17.0	2.70	99.3	86.4
	4.81	0.145	0.822	20.5	0.320	52.8	0.231	17.3	2.07	99.0	86.5
	4.77	0.129	0.812	20.7	0.319	53.0	0.233	17.4	2.07	99.4	86.7
15ET192											
Grain 1:	4.31	0.125	0.824	20.2	0.302	53.0	0.255	17.8	2.19	99.0	88.0
	3.69	0.131	0.977	21.5	0.339	52.7	0.304	17.0	2.60	99.2	89.1
	4.50	0.124	0.922	20.9	0.348	52.7	0.310	17.1	2.44	99.3	87.1
	4.10	0.147	0.948	21.4	0.355	52.6	0.328	16.8	2.42	99.1	88.0
	4.27	0.146	0.967	20.2	0.316	53.1	0.306	17.6	2.29	99.2	88.0
Grain 2:	4.27	0.137	0.933	21.0	0.332	53.3	0.304	17.2	2.40	99.8	87.8
	4.07	0.123	0.905	21.5	0.314	53.1	0.240	16.9	2.21	99.3	88.1
	3.68	0.071	0.910	21.2	0.290	53.1	0.315	17.1	2.35	99.0	89.2
	3.69	0.101	0.874	21.5	0.289	53.2	0.269	17.0	2.22	99.0	89.1
15ET193											
Grain 1:	4.84	0.149	0.909	19.6	0.328	52.7	0.252	18.2	2.36	99.3	87.0
	4.92	0.143	0.884	19.5	0.321	52.8	0.247	18.3	2.34	99.5	86.9
	4.45	0.150	0.851	20.3	0.339	52.3	0.299	17.6	2.33	98.5	87.6
	5.39	0.169	0.870	18.2	0.328	52.7	0.263	18.8	2.64	99.2	86.1
	4.80	0.151	0.985	19.5	0.324	52.8	0.243	18.2	2.29	99.3	87.1
	4.23	0.130	0.943	21.6	0.367	52.4	0.243	16.7	2.45	99.1	87.6
Grain 2:	4.10	0.145	0.918	21.9	0.343	52.5	0.316	16.6	2.43	99.2	87.8
	4.49	0.137	0.934	20.4	0.334	52.7	0.312	17.6	2.33	99.2	87.5
	5.15	0.115	0.904	18.0	0.312	53.0	0.272	19.0	2.33	99.2	86.8
	4.17	0.121	0.933	21.6	0.350	52.5	0.311	16.6	2.48	99.2	87.7
	4.36	0.143	0.867	20.6	0.357	52.8	0.306	17.6	2.50	99.6	87.8
Grain 3:	4.48	0.118	0.900	20.8	0.316	52.6	0.262	17.3	2.33	99.1	87.3
	4.54	0.162	0.920	20.2	0.312	52.8	0.275	17.7	2.24	99.2	87.4
	4.89	0.149	0.953	19.2	0.335	52.7	0.262	18.2	2.38	99.2	86.9
	4.59	0.121	0.866	20.3	0.343	52.8	0.292	17.7	2.39	99.3	87.3
	4.69	0.132	0.860	19.7	0.368	52.7	0.302	18.0	2.57	99.3	87.2
	4.71	0.129	0.860	19.9	0.386	52.6	0.269	17.9	2.61	99.4	87.1

Sample	FeO	MnO	Cr2O3	CaO	TiO2	SiO2	Na2O	MgO	Al2O3	Total	Mg number
15LL121											
Grain 1:	3.65	0.112	0.776	22.2	0.568	52.2	0.274	16.7	2.93	99.4	89.1
	3.83	0.157	0.769	21.0	0.431	52.8	0.223	18.0	2.45	99.7	89.3
	3.69	0.140	0.786	22.2	0.575	52.2	0.278	16.8	2.91	99.6	89.0
	3.84	0.160	0.771	21.0	0.431	52.9	0.218	18.0	2.46	99.8	89.3
	3.99	0.134	0.842	19.9	0.459	52.0	0.241	18.5	2.58	98.7	89.2
	2.90	0.111	0.744	22.3	0.397	52.6	0.245	17.5	2.34	99.2	91.5
	3.16	0.102	0.981	21.5	0.355	52.7	0.251	17.7	2.66	99.4	90.9
Grain 2:	5.80	0.173	0.730	18.7	0.508	52.8	0.216	18.7	2.39	100.0	85.2
	6.59	0.187	0.809	17.5	0.428	52.8	0.185	19.4	2.25	100.1	84.0
	5.36	0.163	0.891	20.3	0.405	52.6	0.222	17.8	2.12	99.8	85.5
	4.74	0.133	0.704	21.5	0.438	53.0	0.188	17.3	1.88	99.8	86.7
	4.88	0.132	0.925	20.3	0.537	52.3	0.202	18.0	2.67	100.0	86.8
	5.25	0.161	0.811	19.2	0.464	52.7	0.191	18.5	2.43	99.7	86.3
	4.41	0.141	0.880	21.6	0.499	52.7	0.247	17.0	2.43	100.0	87.3
	4.64	0.199	0.929	21.1	0.474	52.8	0.241	17.4	2.37	100.1	87.0
	4.11	0.166	0.989	21.0	0.484	52.7	0.193	17.6	2.70	99.9	88.4
Grain 3:	3.39	0.159	0.629	22.5	0.390	53.2	0.121	17.7	1.86	99.9	90.3
	3.28	0.144	0.866	22.5	0.586	52.2	0.250	16.9	3.01	99.8	90.2
	3.80	0.161	0.836	21.2	0.468	53.1	0.200	18.2	2.52	100.4	89.5
	4.11	0.168	0.839	20.9	0.477	52.7	0.198	18.1	2.31	99.7	88.7
	4.12	0.177	0.655	21.1	0.415	52.9	0.177	17.6	2.05	99.3	88.4
	3.39	0.118	0.893	22.2	0.460	52.2	0.180	17.4	2.37	99.3	90.2
	5.28	0.131	0.828	19.3	0.479	52.2	0.219	18.5	2.53	99.4	86.2
15LL135											
Grain 1:	3.34	0.113	0.792	21.7	0.527	52.5	0.149	17.7	2.70	99.5	90.4
	3.25	0.079	0.848	23.7	0.428	52.3	0.107	16.7	2.10	99.6	90.2
	3.21	0.102	0.772	21.4	0.508	52.5	0.206	17.7	2.68	99.1	90.8
	2.69	0.096	0.741	24.1	0.426	52.9	0.107	16.7	2.08	99.7	91.7
	3.37	0.138	0.765	21.5	0.441	52.9	0.175	17.8	2.37	99.4	90.4
	2.87	0.109	0.707	22.9	0.374	52.8	0.181	17.2	2.41	99.5	91.4
	2.77	0.104	0.626	24.4	0.340	53.0	0.077	16.7	1.65	99.7	91.5
Grain 2:	2.65	0.079	0.599	22.0	0.307	53.4	0.210	17.6	2.37	99.1	92.2
	2.71	0.106	0.849	23.0	0.451	52.7	0.201	17.1	2.69	99.7	91.8
	3.42	0.139	0.866	22.3	0.458	52.9	0.110	17.4	2.34	100.0	90.1
	2.94	0.089	0.758	22.9	0.493	52.9	0.148	17.2	2.15	99.6	91.2
	2.76	0.083	0.778	24.5	0.376	52.9	0.072	16.7	1.86	100.0	91.5

	FeO	MnO	Cr2O3	CaO	TiO2	SiO2	Na2O	MgO	Al2O3	Total	Mg number
	3.27	0.077	0.838	23.5	0.419	52.7	0.149	17.0	2.23	100.2	90.2
	2.71	0.090	0.544	23.5	0.305	53.6	0.143	17.3	1.77	100.0	91.9
Grain 3:	2.96	0.135	0.699	23.8	0.293	53.5	0.144	17.1	1.82	100.5	91.2
	2.91	0.103	0.729	24.5	0.389	52.9	0.074	16.6	1.90	100.1	91.1
	2.89	0.109	0.917	23.9	0.430	52.4	0.119	16.6	2.45	99.9	91.1
	3.13	0.122	0.971	23.7	0.388	52.4	0.095	16.8	2.12	99.8	90.5
	2.92	0.072	0.843	24.1	0.402	52.5	0.116	16.7	2.14	99.8	91.1
	4.18	0.079	1.115	20.0	0.349	51.8	0.283	18.0	2.82	98.7	88.5
	2.75	0.129	0.777	24.3	0.388	53.2	0.086	16.8	1.90	100.3	91.6

Sample	FeO	MnO	Cr2O3	CaO	TiO2	SiO2	Na2O	MgO	Al2O3	Total	Mg number
15LL136											
Grain 1:	11.19	0.244	0.376	1.9	0.474	54.7	0.017	29.6	1.44	99.9	82.5
	11.16	0.254	0.397	2.0	0.514	54.7	0.060	29.4	1.55	100.0	82.4
	10.99	0.254	1.198	2.5	0.185	53.6	0.067	28.0	2.26	99.0	82.0
Grain 2:	11.73	0.276	0.328	1.4	0.328	54.3	-0.016	29.3	1.51	99.2	81.7
	11.21	0.246	0.405	2.0	0.348	54.9	0.018	29.4	1.51	100.0	82.4
	10.59	0.308	0.341	2.3	0.351	52.5	0.009	29.3	1.36	97.2	83.1
	11.65	0.315	0.459	1.4	0.312	54.0	-0.003	29.4	1.53	99.1	81.8
	11.17	0.253	0.365	1.8	0.337	54.5	0.008	29.4	1.41	99.2	82.4
	11.20	0.222	0.407	1.8	0.343	54.4	0.065	29.1	1.47	99.0	82.3
	11.26	0.281	0.402	1.8	0.366	54.6	0.017	29.5	1.55	99.8	82.4
	11.32	0.260	0.349	1.7	0.324	54.5	0.002	29.2	1.50	99.2	82.2
Grain 3:	4.94	0.159	0.626	22.3	0.918	51.7	0.233	16.7	2.64	100.2	85.8
	5.27	0.135	0.647	22.0	0.787	52.2	0.265	16.8	2.36	100.4	85.0
	6.92	0.211	0.631	18.0	0.738	52.1	0.137	18.3	2.34	99.4	82.5
	5.74	0.158	0.645	21.0	0.794	52.2	0.220	17.3	2.36	100.4	84.3
	5.85	0.197	0.674	20.3	0.685	51.9	0.137	17.9	2.49	100.0	84.5
	5.45	0.194	0.706	21.1	0.833	52.2	0.209	17.3	2.64	100.6	85.0
	7.16	0.220	0.667	17.9	0.817	52.0	0.118	18.9	2.35	100.3	82.5
	5.44	0.187	0.925	20.9	0.654	52.1	0.169	17.4	3.02	100.8	85.1
	4.81	0.198	0.817	22.3	0.667	52.2	0.150	16.6	3.02	100.7	86.0
15LL158											
Grain 1:	2.34	0.090	0.859	24.7	0.520	52.3	0.148	17.0	2.82	100.8	92.8
	2.74	0.121	0.953	24.7	0.529	52.1	0.146	16.7	2.89	101.0	91.6
	2.68	0.095	0.986	24.4	0.565	51.9	0.170	16.8	3.19	100.8	91.8
	2.57	0.092	0.853	24.4	0.482	52.6	0.150	17.3	2.40	100.9	92.3
	2.94	0.147	1.015	24.1	0.583	51.8	0.151	16.9	2.86	100.6	91.1
	2.74	0.108	0.955	24.4	0.596	52.0	0.143	16.8	2.99	100.8	91.6

	2.79	0.095	0.961	24.2	0.578	52.1	0.198	17.0	3.00	100.9	91.5
Grain 2:	2.69	0.109	1.006	24.5	0.483	52.2	0.143	17.0	2.61	100.7	91.8
	2.72	0.119	0.894	23.9	0.462	52.1	0.144	17.6	2.76	100.6	92.0
	2.90	0.109	0.764	24.6	0.631	52.5	0.189	16.9	2.41	101.0	91.2
	3.23	0.143	0.705	24.0	0.633	52.7	0.150	17.2	2.42	101.1	90.5
	3.17	0.158	0.931	23.6	0.648	52.3	0.159	17.5	2.69	101.1	90.8
	3.42	0.154	0.910	23.9	0.530	52.6	0.194	17.0	2.37	101.1	89.8
	2.74	0.097	1.020	24.0	0.507	52.5	0.159	17.3	2.53	100.8	91.8
	2.60	0.125	0.967	24.6	0.492	52.4	0.128	17.0	2.48	100.9	92.1
	2.78	0.106	1.044	24.3	0.654	52.4	0.178	17.1	2.54	101.1	91.7
	4.29	0.159	1.019	21.6	0.543	52.3	0.251	17.6	2.87	100.7	88.0
Grain 3:	3.60	0.131	0.951	21.3	0.628	51.2	0.192	18.3	3.11	99.4	90.0
	3.35	0.136	0.948	21.9	0.570	51.1	0.133	18.4	2.63	99.1	90.7
	2.79	0.118	0.783	24.7	0.499	52.6	0.104	17.0	2.23	100.8	91.6
	3.20	0.162	1.072	23.5	0.628	52.0	0.198	17.0	2.81	100.6	90.5
	3.65	0.154	0.960	23.2	0.600	52.3	0.188	17.0	2.70	100.8	89.2
	2.80	0.095	0.850	22.1	0.491	52.0	0.209	18.1	2.70	99.4	92.0
	2.76	0.139	0.975	24.5	0.629	52.2	0.163	16.9	2.65	100.9	91.6
	3.21	0.133	0.889	23.5	0.590	52.5	0.197	17.3	2.60	100.9	90.6
	3.47	0.136	0.963	23.6	0.623	52.3	0.181	17.1	2.73	101.0	89.8
	2.95	0.143	0.955	22.5	0.465	52.0	0.338	17.9	3.40	100.7	91.6

Sample	FeO	MnO	Cr2O3	CaO	TiO2	SiO2	Na2O	MgO	Al2O3	Total	Mg number
15LL174											
Grain 1:	4.85	0.171	0.858	21.7	0.382	52.4	0.216	16.8	2.44	99.8	86.0
	4.73	0.144	0.869	21.8	0.365	52.5	0.239	16.8	2.47	100.0	86.4
	6.62	0.166	0.741	17.0	0.335	53.3	0.174	19.7	2.28	100.3	84.1
	6.37	0.146	0.958	17.3	0.405	52.7	0.172	19.2	2.74	100.0	84.3
	4.67	0.124	1.010	22.3	0.426	52.0	0.257	16.3	2.85	99.9	86.1
	5.71	0.162	0.943	20.1	0.400	52.5	0.233	17.8	2.77	100.6	84.7
	4.79	0.114	1.007	21.9	0.406	52.1	0.243	16.5	2.87	99.9	86.0
	4.69	0.131	0.976	21.9	0.408	52.3	0.256	16.6	2.81	100.1	86.4
	4.95	0.146	1.001	22.1	0.410	51.8	0.186	16.2	2.98	99.9	85.4
Grain 2:	4.34	0.146	0.886	22.7	0.433	52.1	0.319	16.3	2.68	100.0	87.0
	5.02	0.136	0.932	21.6	0.489	52.3	0.228	16.8	2.85	100.4	85.7
	6.79	0.137	0.757	17.1	0.397	53.5	0.185	19.7	2.57	101.2	83.8
	5.93	0.193	0.861	18.3	0.478	52.8	0.222	18.3	2.88	99.9	84.6
	5.05	0.125	0.885	21.6	0.493	52.3	0.250	16.6	2.79	100.0	85.5
	5.70	0.159	0.828	20.0	0.462	52.5	0.218	17.6	2.69	100.1	84.6

	FeO	MnO	Cr2O3	CaO	TiO2	SiO2	Na2O	MgO	Al2O3	Total	Mg number
	5.03	0.158	0.929	21.5	0.419	52.0	0.283	16.6	2.87	99.8	85.5
	5.38	0.179	0.880	20.5	0.380	52.6	0.290	17.2	2.66	100.1	85.1

Sample	FeO	MnO	Cr2O3	CaO	TiO2	SiO2	Na2O	MgO	Al2O3	Total	Mg number
15RN349											
Grain 1:	4.71	0.139	0.964	21.1	0.378	52.3	0.227	17.3	2.63	99.8	86.7
	4.50	0.124	0.967	22.5	0.387	52.2	0.260	16.3	2.70	99.9	86.6
	4.53	0.135	1.022	22.2	0.386	52.3	0.293	16.4	2.78	100.1	86.6
	6.09	0.148	0.866	18.5	0.363	53.4	0.195	19.2	2.41	101.2	84.9
Grain 2:	4.63	0.149	0.974	21.4	0.362	52.9	0.253	17.1	2.50	100.3	86.8
	4.44	0.140	0.970	22.1	0.351	52.7	0.249	16.8	2.46	100.2	87.1
	4.30	0.128	0.977	22.6	0.358	52.4	0.279	16.5	2.46	100.0	87.2
	4.69	0.163	0.960	21.5	0.355	52.7	0.230	17.5	2.45	100.6	86.9
	4.43	0.137	0.920	22.4	0.391	52.5	0.275	16.6	2.69	100.3	87.0
	4.62	0.122	0.893	22.0	0.402	52.4	0.261	16.7	2.67	100.0	86.5
	4.13	0.113	0.957	22.8	0.377	52.5	0.283	16.3	2.56	100.0	87.6
	6.22	0.202	0.786	17.3	0.361	52.8	0.202	19.2	2.41	99.4	84.6
Grain 3:	4.53	0.140	0.991	22.5	0.357	52.1	0.225	16.7	2.65	100.2	86.8
	4.99	0.115	0.994	21.0	0.388	52.3	0.243	17.2	2.72	100.0	86.0
	4.85	0.161	1.001	21.4	0.397	51.9	0.211	17.0	2.83	99.8	86.2
	6.05	0.167	0.902	18.5	0.358	52.3	0.174	19.3	2.57	100.3	85.0
	5.01	0.142	0.979	21.0	0.382	52.1	0.233	16.9	2.78	99.5	85.8
	4.69	0.134	1.007	21.5	0.371	52.3	0.237	16.5	2.58	99.4	86.3
	4.03	0.134	0.859	20.7	0.328	52.8	0.269	17.2	2.51	98.9	88.4
	4.65	0.097	0.979	21.7	0.357	52.2	0.259	16.8	2.56	99.5	86.5
	5.43	0.152	0.926	19.4	0.363	52.6	0.181	18.4	2.52	100.0	85.8
15RN350											
Grain 1:	5.13	0.151	0.237	22.7	0.393	52.0	0.175	16.3	2.68	99.8	85.0
	5.29	0.152	0.310	22.3	0.359	51.7	0.161	16.4	2.86	99.5	84.6
	5.44	0.140	0.334	21.7	0.384	52.5	0.193	16.6	2.37	99.6	84.4
	5.19	0.127	0.595	22.8	0.385	52.3	0.195	16.0	2.53	100.1	84.6
	6.22	0.176	0.743	19.4	0.360	52.4	0.165	17.7	2.55	99.8	83.6
	4.74	0.138	0.683	23.1	0.352	52.0	0.175	16.2	2.62	99.9	85.9
	4.93	0.179	0.587	22.9	0.412	52.2	0.205	16.2	2.49	100.0	85.4
	4.88	0.122	0.611	23.1	0.411	52.5	0.212	16.4	2.57	100.8	85.7
	5.32	0.155	0.597	21.6	0.405	52.2	0.186	16.6	2.48	99.5	84.7
	5.18	0.152	0.529	22.6	0.420	52.2	0.181	16.1	2.50	99.9	84.7
	4.92	0.151	0.392	23.0	0.410	52.5	0.168	16.1	2.20	99.9	85.4
	5.15	0.147	0.324	22.0	0.414	52.6	0.164	16.6	2.21	99.6	85.2

	FeO	MnO	Cr2O3	CaO	TiO2	SiO2	Na2O	MgO	Al2O3	Total	Mg number
	4.94	0.153	0.694	23.0	0.332	52.2	0.187	15.9	2.65	100.1	85.1
Grain 2:	4.75	0.155	0.455	23.3	0.367	52.6	0.176	16.1	1.98	99.9	85.8
	5.17	0.167	0.479	22.7	0.368	52.4	0.182	16.2	2.01	99.7	84.8
	5.12	0.178	0.429	22.8	0.365	52.8	0.215	16.3	1.91	100.0	85.0
	5.29	0.170	0.473	22.6	0.352	52.7	0.180	16.3	2.01	100.0	84.6
	5.52	0.149	0.465	21.8	0.380	52.5	0.185	16.7	2.16	99.8	84.4
Grain 3:	5.38	0.159	0.526	21.3	0.411	52.4	0.177	17.1	2.38	99.8	85.0
	5.50	0.149	0.385	21.3	0.428	52.6	0.191	17.0	2.43	100.1	84.7
	5.85	0.158	0.424	20.6	0.397	53.0	0.168	17.5	2.40	100.5	84.2
	6.21	0.137	0.592	19.2	0.410	52.3	0.152	17.9	2.57	99.4	83.7
	5.16	0.154	0.467	22.2	0.394	52.4	0.184	16.6	2.41	99.9	85.1
	5.58	0.166	0.450	21.2	0.428	52.8	0.161	17.3	2.37	100.5	84.7

Sample	FeO	MnO	Cr2O3	CaO	TiO2	SiO2	Na2O	MgO	Al2O3	Total	Mg number
15RN351											
Grain 1:	5.35	0.146	0.935	20.9	0.391	52.0	0.241	16.7	2.84	99.6	84.8
	5.35	0.146	0.935	20.9	0.391	52.0	0.241	16.7	2.84	99.6	84.8
	4.95	0.123	0.986	22.1	0.409	52.0	0.234	16.4	2.94	100.1	85.5
	4.90	0.133	0.951	21.9	0.371	51.9	0.240	16.3	2.92	99.6	85.5
	4.75	0.137	0.977	22.9	0.428	51.7	0.247	15.8	2.96	100.0	85.6
	4.84	0.124	0.976	22.5	0.424	51.9	0.242	16.0	2.89	99.9	85.5
	5.79	0.144	0.967	20.5	0.398	52.4	0.191	17.3	2.85	100.5	84.2
	5.84	0.139	0.979	19.3	0.399	51.5	0.211	17.7	2.95	99.0	84.3
	4.85	0.135	0.979	22.6	0.439	51.6	0.249	15.9	2.97	99.7	85.4
Grain 2:	5.38	0.141	0.912	20.7	0.400	52.1	0.257	16.6	2.83	99.3	84.6
	5.85	0.148	0.870	19.9	0.387	52.5	0.222	17.6	2.70	100.2	84.3
	4.85	0.149	0.759	22.5	0.339	52.5	0.232	16.4	2.21	99.8	85.7
	4.88	0.138	1.073	22.4	0.418	51.6	0.249	15.8	3.03	99.7	85.3
	5.22	0.137	1.037	21.6	0.430	51.7	0.243	16.1	3.03	99.5	84.7
	5.56	0.148	0.933	20.5	0.395	53.5	0.229	17.5	2.77	101.5	84.8
	6.21	0.143	0.849	18.1	0.388	53.3	0.198	18.5	2.52	100.2	84.1
	4.84	0.147	0.769	22.4	0.362	54.0	0.211	16.7	2.30	101.7	86.0
	5.68	0.157	0.775	19.4	0.345	53.3	0.214	18.0	2.43	100.3	84.9
	5.08	0.162	0.888	21.7	0.389	53.4	0.221	16.6	2.76	101.2	85.4
	5.68	0.151	0.897	20.3	0.375	53.6	0.186	17.5	2.76	101.4	84.6
	5.63	0.153	0.978	20.4	0.385	53.3	0.247	17.0	2.99	101.1	84.4
	5.15	0.147	0.977	21.7	0.376	53.2	0.244	16.4	2.94	101.1	85.0
	4.52	0.129	1.000	23.2	0.418	53.2	0.254	15.9	3.04	101.6	86.3

Sample	FeO	MnO	Cr2O3	CaO	TiO2	SiO2	Na2O	MgO	Al2O3	Total	Mg number
Grain 3:	5.26	0.158	0.821	20.7	0.373	51.8	0.201	17.2	2.45	99.0	85.4
	5.26	0.158	0.821	20.7	0.373	51.8	0.201	17.2	2.45	99.0	85.4
	5.03	0.128	0.888	21.8	0.380	51.9	0.219	16.4	2.73	99.6	85.3
	5.49	0.147	0.882	20.8	0.378	52.2	0.225	17.0	2.75	99.9	84.7
	5.46	0.160	0.958	21.0	0.386	52.1	0.227	16.5	2.96	99.7	84.4
	5.01	0.166	0.968	22.2	0.373	51.6	0.246	16.1	2.90	99.5	85.1

Table C-3. Spinel compositions by EPMA.

Sample	FeO	Fe2O3	Cr2O3	MnO	TiO2	MgO	Al2O3	Total	Cr/(Cr+Al)
13RN384	31.2	40.7	22.5	0.415	2.50	1.26	0.79	99.5	0.95
	31.3	40.9	22.8	0.438	2.54	1.26	0.76	100.0	0.95
	31.2	40.7	22.8	0.437	2.25	1.18	0.67	99.2	0.96
	32.0	40.0	21.6	0.440	3.16	1.35	1.42	99.9	0.91
	31.5	41.1	22.0	0.443	2.10	1.18	1.11	99.4	0.93
	31.1	40.6	23.4	0.426	2.31	1.21	0.82	99.9	0.95
	30.6	41.6	22.4	0.442	2.19	1.31	0.65	99.2	0.96
	30.8	40.1	23.4	0.419	2.29	1.27	0.75	99.1	0.95
	31.4	40.9	21.8	0.453	2.56	1.27	0.74	99.1	0.95
	31.4	39.4	21.7	0.381	2.25	1.39	3.00	99.6	0.83
	31.4	37.9	21.5	0.467	3.06	1.44	3.20	99.0	0.82
	31.8	39.8	21.4	0.388	3.11	1.44	1.62	99.7	0.90
	31.4	41.0	22.5	0.418	2.61	1.23	0.74	99.9	0.95
	31.5	41.1	22.4	0.408	2.54	1.23	0.74	99.9	0.95
	31.5	41.0	21.6	0.448	2.74	1.43	0.73	99.4	0.95
	31.1	40.6	23.5	0.479	2.31	1.18	0.62	99.8	0.96
	31.9	41.6	22.0	0.418	2.32	1.12	0.68	99.9	0.96
	31.2	40.7	23.0	0.435	2.59	1.20	0.79	99.9	0.95
	31.6	41.2	22.3	0.434	2.60	1.19	0.75	100.0	0.95
	31.6	41.2	22.0	0.415	2.63	1.23	0.76	99.9	0.95
	31.5	41.1	22.4	0.429	2.61	1.22	0.78	100.0	0.95
	31.2	40.7	22.7	0.418	2.49	1.20	0.79	99.5	0.95
	31.2	42.3	21.6	0.431	2.27	1.14	0.67	99.6	0.96
13RN385	28.4	12.3	39.9	0.396	1.12	3.13	11.90	97.1	0.69
	29.0	13.8	39.6	0.408	1.27	3.00	11.07	98.2	0.71
	28.8	13.7	36.7	0.421	1.05	3.03	13.55	97.3	0.65
	28.7	14.3	36.1	0.425	1.06	3.14	13.95	97.7	0.63
	28.9	9.6	39.7	0.441	0.74	3.74	15.80	99.0	0.63
	29.0	13.2	38.2	0.402	0.93	3.01	12.97	97.8	0.66
	29.3	13.3	39.1	0.421	1.07	2.82	12.62	98.7	0.68
	27.4	8.6	40.5	0.400	0.69	4.02	15.86	97.4	0.63
	28.5	8.9	39.3	0.405	0.68	3.59	15.90	97.3	0.62
13RN386	31.8	28.9	25.4	0.505	3.22	1.71	5.80	97.4	0.75
	30.3	18.1	36.3	0.536	1.18	2.60	10.63	99.7	0.70
	32.1	34.3	21.2	0.525	3.90	1.46	4.55	98.0	0.76
	31.6	31.2	24.6	0.535	3.15	1.58	5.20	97.9	0.76
13RN387	29.6	21.9	30.4	0.461	1.48	2.47	11.65	98.1	0.64
	31.5	25.4	28.6	0.515	2.39	1.73	8.01	98.2	0.71
	31.2	39.1	17.6	0.416	2.69	1.34	5.07	97.4	0.70
	31.4	23.3	28.2	0.497	2.67	2.21	10.82	99.2	0.64
	31.5	23.3	29.4	0.529	2.72	2.13	8.86	98.5	0.69
	31.6	23.4	29.4	0.492	2.67	2.13	8.81	98.5	0.69
	31.6	25.4	28.3	0.543	2.85	1.84	8.35	98.9	0.69

	FeO	Fe2O3	Cr2O3	MnO	TiO2	MgO	Al2O3	Total	Cr/(Cr+Al)
	31.6	23.4	28.1	0.495	2.46	2.08	10.27	98.5	0.65
	31.9	24.6	28.2	0.526	2.95	1.85	8.40	98.5	0.69
	31.4	26.4	28.2	0.504	2.30	1.74	8.40	99.0	0.69
	30.9	25.9	28.2	0.515	2.32	1.76	8.52	98.0	0.69
	31.5	26.4	27.5	0.528	2.09	1.76	8.48	98.2	0.69
	31.1	26.0	28.0	0.488	2.10	1.84	9.17	98.7	0.67
	31.6	25.4	27.6	0.469	2.75	1.80	8.52	98.1	0.68
	30.9	25.9	28.0	0.590	2.37	1.81	8.69	98.2	0.68
	30.3	18.1	32.7	0.456	1.20	2.92	13.87	99.5	0.61

Sample	FeO	Fe2O3	Cr2O3	MnO	TiO2	MgO	Al2O3	Total	Cr/(Cr+Al)
13RN388	32.1	30.3	24.5	0.457	2.73	1.63	7.14	98.8	0.70
	31.9	32.7	24.6	0.474	2.86	1.35	4.71	98.6	0.78
	31.5	26.4	24.6	0.470	2.92	2.21	10.32	98.5	0.62
	31.9	26.7	24.6	0.479	3.11	2.02	9.73	98.6	0.63
	31.8	21.6	27.8	0.487	3.14	2.44	11.05	98.3	0.63
	31.5	24.3	25.0	0.489	2.81	2.37	11.99	98.4	0.58
	31.0	23.9	25.1	0.481	2.66	2.57	12.60	98.4	0.57
	30.9	22.9	25.4	0.478	2.48	2.71	13.36	98.3	0.56
	30.8	24.8	25.5	0.451	1.86	2.32	12.20	97.9	0.58
	30.2	22.4	26.3	0.453	2.08	3.00	14.17	98.6	0.56
	31.7	25.5	25.5	0.497	2.90	2.15	10.30	98.6	0.62
	32.9	33.8	21.1	0.488	4.10	1.46	4.77	98.7	0.75
	30.0	21.3	26.4	0.480	2.12	3.08	14.73	98.2	0.55
13RN389	32.2	33.0	21.8	0.553	3.44	1.69	6.45	99.1	0.69
	32.2	31.8	22.6	0.657	3.55	1.65	6.30	98.8	0.71
	32.2	42.0	12.9	0.485	4.72	1.69	3.17	97.2	0.73
	31.4	44.4	14.3	0.401	2.55	1.22	3.65	97.9	0.72
	32.9	36.5	17.6	0.652	4.38	1.28	4.66	98.0	0.72
	31.0	20.2	31.6	0.539	1.34	2.29	12.21	99.2	0.63
	30.7	69.3	0.4	0.040	0.20	0.32	0.04	101.0	0.88
13RN390	33.6	38.8	13.6	0.629	5.41	1.16	3.87	97.1	0.70
	33.5	38.8	13.8	0.613	5.46	1.17	3.93	97.3	0.70
	33.0	44.8	10.6	0.600	4.10	0.38	2.47	96.0	0.74
13RN391	26.6	12.7	35.4	0.462	0.73	5.05	17.62	98.6	0.57
	25.9	15.5	33.7	0.413	0.54	5.35	16.55	97.9	0.58
	27.0	9.5	40.4	0.429	0.67	4.88	15.84	98.8	0.63
	27.2	9.5	40.3	0.442	0.66	4.85	15.71	98.7	0.63
	27.0	9.5	39.0	0.411	0.57	4.93	16.87	98.3	0.61
	26.8	9.4	39.0	0.453	0.59	4.77	16.48	97.5	0.61
	26.6	9.3	38.7	0.431	0.64	5.50	17.79	98.9	0.59
	26.8	9.4	38.7	0.409	0.64	5.39	17.62	98.9	0.60
	27.1	9.5	40.3	0.424	0.59	4.83	16.21	99.0	0.63
	26.6	9.9	39.3	0.452	0.71	5.27	16.72	99.0	0.61
	26.7	9.9	39.6	0.421	0.73	5.24	16.52	99.1	0.62

Sample	FeO	Fe2O3	Cr2O3	MnO	TiO2	MgO	Al2O3	Total	Cr/(Cr+Al)
13RN392	28.6	16.4	36.1	0.495	1.62	3.36	11.71	98.3	0.67
	28.8	16.5	36.0	0.491	1.59	3.34	11.62	98.3	0.68
	29.1	16.6	35.6	0.489	1.63	3.36	11.51	98.3	0.67
	29.4	16.8	34.9	0.542	1.81	3.12	11.37	98.0	0.67
	31.5	24.3	25.0	0.489	2.81	2.37	11.99	98.4	0.58
	29.4	16.1	38.2	0.553	1.46	2.62	9.73	98.0	0.72
	28.6	15.0	38.0	0.481	1.48	3.42	11.65	98.6	0.69
	28.9	15.1	37.4	0.494	1.42	3.24	11.55	98.2	0.69
	28.0	14.6	38.1	0.470	1.44	3.80	12.25	98.7	0.68
	28.0	14.6	38.0	0.481	1.44	3.83	12.20	98.6	0.68
	27.7	14.5	37.8	0.480	1.32	3.82	12.49	98.2	0.67
	28.6	16.3	35.2	0.443	0.93	3.15	12.58	97.3	0.65
	28.6	15.7	35.7	0.482	1.59	3.84	12.33	98.2	0.66
	29.0	15.9	35.4	0.457	1.72	3.82	12.38	98.7	0.66
	28.9	15.8	35.1	0.476	1.77	3.84	12.39	98.2	0.66
	28.6	16.4	35.0	0.469	1.81	3.89	12.43	98.6	0.65
	29.0	15.9	35.0	0.423	1.78	3.97	12.64	98.6	0.65
	28.9	15.8	34.8	0.451	1.77	3.95	12.75	98.4	0.65
	28.5	16.3	34.6	0.476	1.74	4.01	12.83	98.4	0.64
	28.9	15.8	35.0	0.439	1.73	4.03	12.93	98.8	0.64
	28.4	16.3	34.7	0.487	1.74	4.01	12.93	98.6	0.64
	29.0	15.9	35.2	0.458	1.75	3.99	12.85	99.1	0.65
	28.4	16.3	34.7	0.507	1.75	3.96	12.71	98.4	0.65
	28.5	16.3	34.9	0.475	1.76	3.91	12.62	98.5	0.65
	28.7	16.4	34.9	0.500	1.75	3.94	12.51	98.7	0.65
	28.5	16.3	35.0	0.502	1.72	3.88	12.41	98.3	0.65
	28.7	15.7	35.4	0.441	1.65	3.85	12.31	98.1	0.66
	29.0	15.8	37.5	0.556	1.69	2.98	9.94	97.4	0.72
	28.9	15.8	37.7	0.489	1.83	3.33	9.92	97.9	0.72
	29.0	15.9	37.8	0.506	1.82	3.30	9.96	98.3	0.72
	28.7	15.7	36.5	0.485	1.35	3.44	12.49	98.6	0.66
	28.7	15.7	36.4	0.468	1.36	3.40	12.44	98.5	0.66
13RN393	32.1	26.9	26.4	0.530	3.29	1.96	7.80	99.1	0.69
	32.0	26.8	26.6	0.508	3.29	1.96	7.85	98.9	0.69
	31.6	28.7	25.9	0.531	3.36	1.88	6.55	98.5	0.73
	32.3	28.2	25.5	0.568	3.82	1.84	6.82	99.0	0.72
	31.9	27.8	25.2	0.521	3.38	1.82	7.39	98.0	0.70
	30.9	28.0	25.5	0.474	2.53	2.07	8.10	97.6	0.68
	31.3	28.4	25.0	0.517	3.40	1.93	7.21	97.8	0.70
	31.7	28.8	25.1	0.515	3.54	1.92	7.03	98.6	0.71
	32.8	27.5	25.6	0.527	3.88	1.63	6.01	97.8	0.74
	31.6	29.9	22.9	0.523	3.87	2.30	6.87	97.9	0.69
	32.4	28.3	24.3	0.526	3.97	1.96	6.78	98.3	0.71

Sample	FeO	Fe2O3	Cr2O3	MnO	TiO2	MgO	Al2O3	Total	Cr/(Cr+Al)
13RN394	32.7	36.3	26.3	0.570	3.00	1.24	1.11	101.2	0.94
	32.5	34.7	27.9	0.537	2.96	1.35	1.79	101.8	0.91
	30.5	23.6	33.0	0.445	1.70	2.47	8.49	100.2	0.72
	32.0	29.1	31.7	0.571	2.41	1.47	3.55	100.8	0.86
	32.3	30.6	30.0	0.570	2.86	1.87	4.03	102.3	0.83
	31.8	28.9	31.1	0.620	2.69	1.91	4.57	101.5	0.82
13RN395	27.1	7.1	42.1	0.440	0.73	4.88	16.30	98.6	0.63
	27.4	7.6	40.1	0.430	0.57	4.66	17.66	98.5	0.60
	27.0	7.0	42.3	0.452	1.01	4.69	16.22	98.7	0.64
	26.1	6.8	41.4	0.420	0.54	5.25	17.45	98.0	0.61
	26.4	6.9	42.6	0.398	0.57	5.01	16.23	98.1	0.64
	27.5	7.6	41.7	0.434	0.80	4.64	15.90	98.6	0.64
	26.6	7.4	43.0	0.405	0.49	4.67	16.30	98.9	0.64
	26.5	6.0	41.0	0.389	0.49	5.46	18.54	98.3	0.60
	27.3	7.6	41.3	0.450	0.55	4.48	17.00	98.6	0.62
	26.9	6.6	43.3	0.453	0.75	4.75	16.04	98.8	0.64
	27.7	9.2	37.3	0.386	1.17	4.94	17.70	98.5	0.59
	28.2	16.9	33.0	0.404	1.42	3.82	14.53	98.2	0.60
	28.9	7.1	40.5	0.422	2.26	4.42	15.91	99.5	0.63
	27.0	9.0	38.2	0.437	0.82	4.91	18.62	98.9	0.58
	27.9	10.3	37.7	0.462	1.50	4.76	16.47	99.1	0.61
	27.6	8.6	38.7	0.428	0.82	4.66	17.66	98.4	0.60
13RN397	28.9	11.9	36.8	0.478	1.12	3.94	16.17	99.4	0.60
	28.1	11.6	34.1	0.427	1.11	4.40	19.18	98.9	0.54
	28.7	9.0	40.5	0.500	0.96	3.58	15.38	98.6	0.64
	27.9	8.7	38.7	0.437	0.74	4.32	17.32	98.1	0.60
	29.4	17.6	33.5	0.433	1.75	3.17	12.97	98.7	0.63
	28.1	8.3	38.6	0.450	1.15	4.45	18.22	99.3	0.59
	28.0	9.3	33.6	0.421	0.74	5.07	22.04	99.2	0.51
	29.1	12.0	35.7	0.479	1.02	3.56	16.49	98.3	0.59
	27.7	10.2	37.8	0.438	0.70	4.10	17.15	98.1	0.60
	27.6	10.2	38.0	0.454	0.79	4.25	17.50	98.9	0.59
	27.0	10.0	36.1	0.426	0.58	4.74	19.36	98.2	0.56
	27.3	9.1	37.0	0.430	0.71	4.68	19.03	98.3	0.57
	26.6	7.4	37.8	0.379	0.29	5.10	21.19	98.7	0.54
13RN398	27.0	10.0	34.4	0.429	0.61	5.25	21.62	99.3	0.52
	28.5	12.3	36.0	0.461	1.32	4.22	16.75	99.5	0.59
	26.5	7.8	37.0	0.405	0.30	5.47	22.16	99.7	0.53
	26.6	7.8	36.0	0.400	0.22	5.57	22.99	99.6	0.51
	26.5	7.4	34.6	0.402	0.21	5.78	24.71	99.5	0.48
	27.0	8.5	35.5	0.422	0.32	5.32	22.37	99.4	0.52
	26.2	8.2	35.3	0.366	0.27	5.66	23.48	99.5	0.50
	26.5	8.3	37.0	0.358	0.37	5.33	21.52	99.4	0.54

125

	FeO	Fe2O3	Cr2O3	MnO	TiO2	MgO	Al2O3	Total	Cr/(Cr+Al)
	26.5	8.3	35.8	0.393	0.51	5.78	22.33	99.7	0.52
	26.1	7.7	35.5	0.388	0.38	5.90	23.49	99.5	0.50
	28.3	9.9	37.0	0.416	0.92	4.64	18.17	99.3	0.58
	28.2	11.6	36.5	0.439	1.10	4.37	17.14	99.3	0.59
	27.9	9.2	34.7	0.439	0.79	5.04	21.11	99.2	0.52
	26.7	7.4	33.9	0.361	0.34	5.91	24.65	99.2	0.48
	27.0	7.5	34.4	0.403	0.37	5.83	23.88	99.5	0.49
	27.8	10.3	39.5	0.452	0.90	4.36	16.15	99.4	0.62
	28.1	9.3	40.7	0.493	0.78	4.24	15.68	99.2	0.64

Sample	FeO	Fe2O3	Cr2O3	MnO	TiO2	MgO	Al2O3	Total	Cr/(Cr+Al)
13RN400B	28.8	17.2	34.3	0.484	1.17	3.87	14.92	100.7	0.61
	28.7	16.4	34.3	0.475	0.91	3.85	16.00	100.6	0.59
	28.6	16.4	35.3	0.424	0.94	3.66	14.53	99.9	0.62
	28.9	16.5	35.1	0.459	0.96	3.69	14.79	100.5	0.61
	28.5	13.6	35.8	0.513	0.68	3.88	17.00	99.9	0.59
	28.6	13.6	35.8	0.505	0.66	3.89	16.98	100.1	0.59
	28.9	12.5	36.6	0.549	0.59	3.79	16.70	99.5	0.60
	28.8	18.0	34.9	0.554	1.33	3.59	13.12	100.2	0.64
	28.7	15.0	35.4	0.467	0.83	3.78	15.95	100.2	0.60
	29.5	16.1	34.4	0.525	1.15	3.64	14.86	100.2	0.61
	28.7	15.0	34.3	0.408	0.80	4.01	17.07	100.3	0.57
13RN401A	29.1	10.2	38.1	0.449	1.22	4.37	17.45	100.8	0.59
	29.2	10.2	38.2	0.500	1.26	4.20	16.85	100.4	0.60
	27.6	8.7	36.5	0.392	1.26	5.15	20.49	100.0	0.54
	26.9	6.6	37.8	0.382	0.55	5.61	22.49	100.3	0.53
	29.7	9.8	35.7	0.481	2.07	4.58	17.83	100.2	0.57
	29.7	9.9	35.9	0.445	2.07	4.52	17.75	100.3	0.58
	28.4	7.9	36.9	0.412	1.32	4.98	19.94	99.8	0.55
	29.2	14.6	33.6	0.465	1.92	4.23	16.71	100.7	0.57
	28.3	14.1	31.9	0.429	1.61	4.72	18.78	99.8	0.53
	29.6	13.4	35.3	0.472	2.39	4.00	14.78	100.0	0.62
	28.2	12.8	35.0	0.435	1.43	4.46	17.58	99.8	0.57
	28.9	7.5	38.8	0.389	0.67	4.48	19.78	100.6	0.57
	28.7	9.5	39.7	0.468	0.96	4.33	16.67	100.4	0.61
	29.8	17.1	33.9	0.484	2.17	3.68	13.31	100.5	0.63
	27.1	8.0	35.8	0.402	0.66	5.39	22.64	100.1	0.52
13RN402A	27.2	8.0	36.5	0.417	0.52	5.40	20.93	99.1	0.54
	26.6	9.9	38.6	0.453	0.79	5.30	17.32	98.9	0.60
	26.8	9.9	35.6	0.399	0.56	5.23	20.25	98.7	0.54
	26.9	7.9	36.4	0.424	0.50	5.50	21.27	98.9	0.53
	27.5	9.6	36.4	0.461	0.62	5.15	19.86	99.7	0.55
	26.4	7.8	36.9	0.391	0.51	5.95	21.73	99.6	0.53
	25.9	7.7	37.2	0.390	0.56	6.06	21.98	99.8	0.53
	26.0	7.7	37.1	0.395	0.40	6.17	21.65	99.4	0.53

26.6	7.9	37.4	0.428	0.54	5.64	20.95	99.4	0.54
27.2	8.0	37.1	0.465	0.71	5.51	20.36	99.3	0.55
27.8	10.8	36.0	0.451	0.75	4.77	18.84	99.5	0.56
27.7	10.3	40.6	0.453	1.35	4.82	15.12	100.3	0.64
27.6	10.2	40.3	0.424	1.37	4.76	15.12	99.8	0.64
27.6	10.2	40.1	0.443	1.28	5.02	15.13	99.8	0.64
27.8	10.3	40.1	0.426	1.11	4.66	15.27	99.7	0.64
28.0	10.4	40.0	0.417	1.31	4.51	15.11	99.8	0.64
27.9	10.3	39.8	0.461	1.33	4.68	15.07	99.5	0.64
27.6	11.4	39.3	0.462	1.16	4.42	14.85	99.1	0.64
28.4	11.7	38.9	0.468	1.26	4.15	14.51	99.4	0.64
28.0	10.4	40.1	0.461	1.20	4.38	14.67	99.2	0.65
27.5	10.2	40.2	0.453	1.35	4.95	15.07	99.7	0.64
27.2	10.1	40.3	0.445	1.43	5.15	15.14	99.8	0.64
27.1	10.0	40.2	0.432	1.37	5.25	15.20	99.6	0.64

Sample	FeO	Fe2O3	Cr2O3	MnO	TiO2	MgO	Al2O3	Total	Cr/(Cr+Al)
15ET189	30.0	17.9	35.6	0.475	1.99	2.88	9.98	97.0	0.71
	29.7	17.8	35.8	0.469	1.96	3.03	10.44	97.5	0.70
	29.7	17.7	35.6	0.484	1.95	3.04	10.53	97.3	0.69
	29.8	17.8	35.7	0.496	1.95	2.98	10.33	97.4	0.70
	30.1	17.2	35.3	0.501	2.45	2.85	10.23	97.0	0.70
	31.5	27.5	31.7	0.582	2.86	1.43	3.13	95.8	0.87
	32.0	32.8	27.7	0.521	3.20	1.19	1.43	95.6	0.93
	30.9	30.5	31.5	0.588	2.56	1.17	1.30	95.5	0.94
	31.6	28.7	30.8	0.574	3.06	1.36	2.58	95.8	0.89
	31.3	28.5	32.6	0.567	2.50	1.24	1.92	95.7	0.92
	31.3	29.7	31.4	0.568	2.55	1.19	1.59	95.4	0.93
	31.5	26.4	32.5	0.577	2.84	1.43	3.12	95.8	0.87
	31.2	26.1	32.7	0.573	2.85	1.54	3.69	96.0	0.86
	31.5	25.4	33.0	0.556	2.85	1.60	3.90	96.2	0.85
	31.6	25.4	32.9	0.570	2.88	1.58	3.82	96.2	0.85
	31.2	26.1	33.0	0.599	2.77	1.49	3.45	96.0	0.87
	31.5	26.4	32.2	0.569	2.93	1.55	3.62	96.1	0.86
	31.5	26.4	32.4	0.578	2.93	1.54	3.54	96.3	0.86
	31.7	26.5	32.3	0.610	2.83	1.45	3.19	96.0	0.87
	31.7	26.6	32.4	0.584	2.76	1.43	3.08	95.8	0.88
	31.9	29.0	31.4	0.558	3.00	1.29	2.15	96.5	0.91
15ET191	30.4	19.9	31.8	0.525	1.60	2.75	11.83	96.9	0.64
	30.0	19.6	32.2	0.516	1.48	2.86	12.43	97.1	0.63
	30.0	20.4	34.2	0.568	1.72	2.43	9.19	96.5	0.71
	30.2	20.5	34.7	0.559	1.74	2.41	9.11	97.1	0.72
	27.9	13.9	36.1	0.462	1.03	4.02	15.12	97.2	0.62
	28.2	14.1	37.3	0.456	0.99	3.78	14.26	97.6	0.64
	28.8	14.4	37.0	0.479	1.15	3.43	13.60	97.4	0.65

Sample	FeO	Fe2O3	Cr2O3	MnO	TiO2	MgO	Al2O3	Total	Cr/(Cr+Al)
	29.1	15.2	34.9	0.513	0.96	3.52	14.85	97.5	0.61
	29.1	17.4	33.6	0.519	1.23	3.28	13.48	96.9	0.63
	30.9	25.9	31.1	0.580	2.27	1.96	6.93	97.0	0.75
	30.2	21.5	33.2	0.582	1.94	2.16	9.15	96.6	0.71
	30.4	22.6	34.3	0.575	1.70	2.06	7.78	97.1	0.75
	30.1	19.6	34.9	0.559	1.64	2.44	9.35	96.7	0.71
	29.7	19.4	35.5	0.585	1.62	2.41	9.59	96.8	0.71

Sample	FeO	Fe2O3	Cr2O3	MnO	TiO2	MgO	Al2O3	Total	Cr/(Cr+Al)
15ET192	21.0	19.8	35.7	0.434	0.76	4.22	17.55	97.4	0.58
	18.9	17.9	36.7	0.403	0.79	5.14	19.79	97.9	0.55
	19.1	18.1	36.7	0.430	0.74	5.07	19.62	98.0	0.56
	29.4	16.1	36.0	0.508	1.49	2.98	12.29	97.2	0.66
	27.0	10.5	37.9	0.433	1.13	4.92	17.08	98.0	0.60
	27.2	10.1	37.4	0.429	1.08	4.98	17.76	97.9	0.59
	28.4	12.9	34.8	0.441	1.03	4.29	16.88	97.4	0.58
	29.2	16.0	33.8	0.444	1.52	3.60	14.19	97.1	0.62
	29.9	16.4	34.5	0.482	1.75	3.23	12.32	97.0	0.65
	27.4	10.7	37.6	0.410	1.04	4.71	16.73	97.6	0.60
	28.1	13.4	35.8	0.452	0.99	4.02	16.03	97.5	0.60
	29.0	13.8	35.4	0.450	1.14	3.79	15.26	97.4	0.61
	27.9	11.4	36.0	0.412	0.73	4.41	18.19	97.9	0.57
	27.8	12.6	35.8	0.432	0.90	4.31	17.16	97.7	0.58
	28.1	12.8	35.7	0.449	0.91	4.16	16.76	97.6	0.59
	27.8	11.4	35.9	0.423	0.75	4.52	18.11	97.8	0.57
	28.1	12.8	35.5	0.442	0.90	4.12	16.98	97.5	0.58
	28.3	11.6	35.7	0.454	0.82	4.35	17.59	97.7	0.58
	29.9	17.9	34.8	0.511	2.07	2.81	10.26	96.5	0.70
	29.3	16.0	35.1	0.496	1.43	3.34	13.39	97.5	0.64
15ET193	25.6	10.0	38.2	0.402	0.82	5.95	18.74	98.7	0.58
	25.6	10.0	38.4	0.390	0.77	5.89	18.64	98.7	0.58
	25.7	9.5	38.5	0.386	0.69	5.99	19.11	99.0	0.57
	26.2	10.2	37.4	0.376	0.97	5.79	18.82	98.6	0.57
	26.1	10.2	37.6	0.404	0.73	5.62	18.97	98.6	0.57
	26.1	10.2	37.2	0.417	0.69	5.48	19.16	98.2	0.57
	26.5	9.8	38.2	0.413	0.73	5.40	18.39	98.4	0.58
	26.7	10.4	37.1	0.434	0.82	5.25	18.83	98.5	0.57
	26.6	9.8	37.2	0.419	0.65	5.37	19.32	98.4	0.56
	27.1	9.0	37.5	0.406	0.63	5.08	19.37	98.2	0.57
	27.2	9.0	38.0	0.431	1.08	5.53	18.19	98.6	0.58
	27.2	9.5	37.0	0.408	0.79	5.37	19.09	98.5	0.57
	27.2	9.0	37.1	0.435	0.96	5.43	19.08	98.3	0.57
	27.4	9.1	37.3	0.411	0.98	5.38	18.91	98.6	0.57
	27.3	9.1	37.5	0.410	0.95	5.44	18.91	98.6	0.57
	27.1	9.5	35.4	0.392	0.79	5.50	20.62	98.4	0.54

	FeO	Fe2O3	Cr2O3	MnO	TiO2	MgO	Al2O3	Total	Cr/(Cr+Al)
	27.2	9.6	37.3	0.441	0.80	5.17	19.10	98.6	0.57
	26.9	9.4	37.4	0.428	0.71	5.14	19.30	98.3	0.57
	26.9	10.5	36.8	0.455	0.80	5.11	18.77	98.3	0.57
	27.6	9.7	36.4	0.422	0.76	5.04	19.12	98.1	0.56
	26.5	9.3	37.9	0.414	0.81	5.63	18.86	98.4	0.57
	26.6	9.3	37.7	0.407	0.81	5.56	18.95	98.4	0.57
	26.8	9.4	37.6	0.399	0.85	5.51	18.51	98.1	0.58
	27.5	9.6	37.1	0.410	0.72	5.21	18.94	98.5	0.57
	26.0	9.1	39.4	0.400	0.50	5.85	18.32	98.7	0.59
	26.6	8.3	39.5	0.382	1.37	5.79	17.57	98.7	0.60
	26.0	9.1	39.1	0.409	0.63	5.90	18.69	98.9	0.58

Sample	FeO	Fe2O3	Cr2O3	MnO	TiO2	MgO	Al2O3	Total	Cr/(Cr+Al)
15LL174	30.8	15.4	33.5	0.478	2.51	2.94	12.64	96.6	0.64
	30.6	15.3	33.7	0.499	2.42	2.98	13.09	97.0	0.63
	29.2	12.0	35.2	0.462	1.83	3.52	15.93	97.0	0.60
	30.4	13.8	34.4	0.486	2.24	3.22	13.70	96.8	0.63
	30.1	15.0	34.0	0.469	2.70	3.18	12.74	96.7	0.64
	30.2	15.1	34.1	0.493	2.75	3.16	12.56	96.9	0.65
	30.8	14.0	34.2	0.494	2.65	3.17	13.03	96.9	0.64
	30.7	15.3	34.3	0.508	2.65	2.92	11.77	96.6	0.66
	30.8	15.4	34.3	0.494	2.66	2.88	11.53	96.5	0.67
	31.0	15.5	34.5	0.524	2.62	2.69	11.26	96.6	0.67
	30.6	15.3	34.3	0.493	2.64	2.91	11.71	96.4	0.66
	28.5	14.9	35.7	0.410	1.05	3.85	14.16	97.1	0.63
	28.0	16.1	34.9	0.417	1.19	3.82	14.13	97.0	0.62
	28.6	15.0	35.1	0.412	1.10	3.81	14.21	96.8	0.62
	29.0	13.2	37.4	0.448	1.32	3.63	13.33	97.0	0.65
	27.9	14.6	36.9	0.427	1.06	3.73	13.81	97.0	0.64
	28.6	14.9	35.9	0.442	1.21	3.65	13.51	96.7	0.64
	28.4	16.3	34.7	0.434	1.05	3.29	13.77	96.3	0.63
	30.3	17.3	33.3	0.503	1.89	2.68	12.30	96.5	0.65
	30.1	12.4	33.6	0.492	2.16	3.40	15.80	96.6	0.59
	29.5	12.1	35.8	0.484	2.10	3.42	14.86	97.1	0.62
	29.3	16.7	36.0	0.449	1.47	2.98	11.29	96.5	0.68
	30.8	15.4	33.9	0.491	2.63	3.01	12.22	96.9	0.65
	30.5	15.2	33.8	0.489	2.46	3.11	12.85	96.8	0.64
	30.8	15.4	33.4	0.512	2.97	2.84	11.37	95.7	0.66
	30.9	15.4	33.2	0.507	2.97	2.83	12.05	96.4	0.65
	30.2	13.7	34.0	0.477	2.12	3.15	14.31	96.6	0.61
	30.4	15.2	34.1	0.522	2.66	2.93	12.47	96.7	0.65
	28.8	11.8	32.7	0.430	1.60	3.90	18.65	96.8	0.54

Sample	FeO	Fe2O3	Cr2O3	MnO	TiO2	MgO	Al2O3	Total	Cr/(Cr+Al)
15RN349	27.4	11.3	33.0	0.429	1.12	4.93	20.14	97.2	0.52
	27.5	11.3	32.9	0.405	1.17	4.90	20.11	97.1	0.52
	27.3	11.2	33.1	0.421	0.89	4.85	20.29	96.9	0.52
	27.3	11.2	32.9	0.417	0.86	4.84	20.52	96.9	0.52
	27.6	11.4	36.1	0.428	1.31	4.45	16.99	97.1	0.59
	27.7	11.4	36.2	0.435	1.37	4.45	16.84	97.3	0.59
	27.7	11.4	36.3	0.461	1.30	4.40	16.96	97.3	0.59
	27.7	11.4	36.1	0.451	1.33	4.43	16.85	97.0	0.59
	27.9	11.5	35.6	0.447	1.31	4.43	17.25	97.3	0.58
	27.8	11.4	35.9	0.445	1.37	4.53	17.18	97.5	0.58
	27.8	11.4	35.7	0.432	1.38	4.49	17.06	97.1	0.58
	27.8	11.4	35.5	0.455	1.29	4.45	17.21	97.0	0.58
	28.0	11.5	35.5	0.457	1.17	4.38	17.60	97.4	0.58
	27.9	11.4	35.7	0.455	1.37	4.50	17.05	97.3	0.58
	27.8	11.4	35.7	0.459	1.36	4.54	17.17	97.3	0.58
	27.9	10.3	37.7	0.408	1.07	4.44	16.43	97.2	0.61
	28.7	11.8	36.3	0.446	1.39	4.23	15.68	97.3	0.61
	28.0	12.7	36.1	0.445	1.34	4.21	15.84	97.3	0.60
	27.1	11.1	35.8	0.412	1.30	5.02	16.83	96.5	0.59
	27.4	11.3	36.1	0.426	1.30	5.03	17.12	97.6	0.59
	27.2	11.2	36.0	0.416	1.24	5.09	17.18	97.3	0.58
	28.0	11.5	35.3	0.432	1.26	4.49	17.37	97.1	0.58
	27.9	11.5	35.4	0.438	1.33	4.65	17.26	97.3	0.58
	28.0	11.5	35.1	0.427	1.28	4.59	17.32	97.1	0.58
	28.0	11.5	35.1	0.446	1.26	4.62	17.40	97.2	0.58
	27.9	11.5	35.3	0.411	1.35	4.62	17.31	97.2	0.58
	28.1	11.5	34.6	0.414	1.14	4.43	18.12	97.2	0.56
	28.0	11.5	34.9	0.447	1.18	4.46	18.03	97.5	0.57
	28.0	11.5	35.1	0.439	1.16	4.48	17.92	97.4	0.57
	28.4	11.7	34.5	0.410	1.22	4.34	17.80	97.2	0.57
	28.0	11.5	35.0	0.442	1.21	4.47	17.94	97.4	0.57
	27.5	11.3	36.1	0.438	1.08	4.47	17.34	97.1	0.58
	28.4	11.7	35.7	0.431	1.37	4.38	16.38	97.1	0.59
	28.3	11.6	34.7	0.446	1.26	4.42	17.28	96.9	0.57
	28.3	11.6	35.8	0.436	1.34	4.38	16.23	96.9	0.60
	28.2	11.6	35.7	0.431	1.35	4.43	16.53	97.1	0.59
	27.9	11.5	35.0	0.402	1.15	4.55	17.36	96.7	0.57
	27.9	11.5	35.9	0.439	1.24	4.35	16.84	97.0	0.59
	27.7	11.4	35.9	0.445	1.13	4.36	17.13	96.9	0.58
	27.9	11.5	36.1	0.437	1.23	4.33	16.82	97.1	0.59
	27.9	11.5	35.9	0.441	1.22	4.36	16.89	97.1	0.59
	28.0	11.5	35.9	0.435	1.26	4.36	16.79	97.1	0.59

Sample	FeO	Fe2O3	Cr2O3	MnO	TiO2	MgO	Al2O3	Total	Cr/(Cr+Al)
15RN351	28.9	17.3	35.8	0.457	1.35	2.90	11.04	95.9	0.68
	28.5	17.1	35.7	0.431	1.33	3.25	11.04	95.7	0.68
	28.9	17.3	35.8	0.458	1.31	2.95	11.05	96.0	0.68
	29.2	17.5	29.4	0.473	1.52	3.34	16.25	96.0	0.55
	28.8	15.8	29.8	0.461	1.13	3.72	18.19	96.3	0.52
	28.1	14.0	29.7	0.421	0.84	4.09	20.25	96.1	0.50
	29.1	17.4	29.7	0.446	1.41	3.45	16.74	96.4	0.54
	29.6	16.2	29.8	0.483	1.36	3.45	16.77	96.1	0.54
	29.4	17.6	35.0	0.475	1.17	2.48	10.70	95.0	0.69
	29.7	16.2	36.5	0.461	1.47	2.80	10.71	96.2	0.70
	29.6	16.2	36.6	0.492	1.45	2.80	10.66	96.2	0.70
	29.8	16.3	36.4	0.473	1.49	2.81	10.67	96.2	0.70

Normalized to 4 oxygens.

Appendix D.

Petrographic descriptions of field samples

Table D-1. Petrographic descriptions of field samples taken during the summers of 2013 and 2015.

Sample	Rock type	Cumulate type	Petrographic descriptions	Mineral mode	Degree of alteration	Easting	Northing
13RN384A	serpentinite		Olivine has been fully serpentinized. Magnetite occurs within serpentine veinlets.	97% serpentine 3% magnetite	very strong	546139.6	7012978.5
13RN385A	clinopyroxenite	adcumulate	Olivine is fine to medium grained (0.5-2.5 mm). Grains are anhedral with cuspate grain boundaries. Weak serpentine veining in olivine. Clinopyroxene is granular, anhedral, and fine to medium grained (0.5-2 mm). All clinopyroxene has pervasive orthopyroxene exsolution lamellae. Some of the pyroxene grains are zoned. Spinels are mainly interstitial.	89% clinopyroxene 10% olivine 1% opaque minerals	moderate	546145.6	7012954.0
13RN386A	wehrlite	adcumulate	Olivine is fine to coarse grained and 0.5-3 mm. Grains are anhedral with very pronounced cuspate grain boundaries. Weak serpentine veining in olivine. Clinopyroxene is granular, anhedral, and fine to medium grained (0.5-2 mm). On average clinopyroxene grains are smaller than olivine grains. All clinopyroxene has very strong alteration. Chromite is mainly interstitial but some occurs as fine grained inclusions in olivine.	57% clinopyroxene 40% olivine 3% spinel	moderate	546200.7	7012931.5
13RN387A	wehrlite	adcumulate	Olivine is fine to coarse grained (0.5-3 mm) and subhedral to euhedral. Olivine is mostly granular but rare grains are poikilitic with inclusions of fine grained pyroxene. Moderate serpentine veining in olivine. Clinopyroxene is fine to medium grained and on average is finer grained than olivine (0.25-1 mm). Grains are anhedral to subhedral and show significant orthopyroxene exsolution lamellae. Spinel occurs both interstitial and as inclusions in olivine. Less commonly as inclusions in clinopyroxene.	60% olivine 35% clinopyroxene 5% opaque minerals	moderate to strong	546257.1	7012850.1
13RN388A	dunite	mesocumulate	Olivine is medium grained (0.5-1 mm), euhedral, and equigranular. Very weak serpentine alteration of olivine. Rare clinopyroxene is poikilitic and coarse grained (2-9 mm) with inclusions of olivine. Chromite occurs both interstitial and as inclusions in olivine.	92% olivine 5% clinopyroxene 3% opaque minerals	weak	546289.0	7012826.1
13RN389A	wehrlite	adcumulate	Olivine is fine to medium grained (0.5-1.5 mm) and anhedral. Grain boundaries are cuspate and some grains are poikilitic with inclusions of clinopyroxene (CPX). Olivine is moderately serpentinized. Clinopyroxene is anhedral to subhedral and medium to medium coarse grained (0.5-2.5 mm). CPX has pervasive orthopyroxene exsolution lamellae. Some pyroxene grains exhibit amphibole alteration. Several tabular grains show simple twins. Spinel is mostly interstitial.	65% clinopyroxene 30% olivine 5% opaque minerals	strong	546344.0	7012802.5

Sample	Rock type	Cumulate	Description	Mineralogy	Alteration	Easting	Northing
13RN389B	dunite		no sample			546344.0	7012802.5
13RN390A	clinopyroxenite	adcumulate	Clinopyroxene is medium to coarse grained and anhedral to subhedral. Grain boundaries are more strongly altered and red brown. Some CPX have coarse exsolution lamellae and some have more pervasive, fine exsolution lamellae. A few grains have simple twins. Rare olivine is fine grained (0.5 mm) and anhedral. Dark red brown opaque mineral is possibly rutile (or high Ti chromite?). Opaques are mainly interstitial. Two veins in thin section are highly altered CPX or amphibole.	91% clinopyroxene 5% olivine 4% opaque minerals	strong	546496.6	7012736.3
13RN391A	dunite	mesocumulate	Olivine has been almost fully serpentinized. Multiple 0.5-1 mm wide serpentine veins cut through thin section. Remnant fine grained olivine is highly altered. Grains are fine to medium grain (0.25-1 mm) and anhedral. Very rare clinopyroxene grains are also highly altered. Clinopyroxene is medium grained (2-3 mm) and poikilitic. Abundant magnetite veinlets and chromite.	88% olivine 8% clinopyroxene 4% magnetite	very strong	546467.3	7012707.4
13RN392A	dunite	adcumulate	Olivine is moderately to highly serpentinized. Olivine is fine to medium grained (0.5-3 mm) and subhedral to euhedral. Rare clinopyroxene is interstitial to olivine grains and fine grained (0.5 mm). Fairly abundant opaques are both interstitial and included in olivine.	88% olivine 8% clinopyroxene 4% magnetite	moderate to strong	546631.0	7012610.6
13RN393A	wehrlite	adcumulate	Olivine is medium grained and 0.5-3 mm. Grains are subhedral to euhedral and have fairly strong serpentinite alteration. Clinopyroxene is medium grained (1-1.5 mm). CPX grains are anhedral to subhedral and highly altered with pervasive exsolution lamellae. Fairly abundant euhedral chromite occurs as inclusions in both clinopyroxene and olivine, some is interstitial.	50% clinopyroxene 45% olivine 5% opaque minerals	strong	546578.5	7012525.1
13RN394A	dunite	adcumulate	Very pervasive serpentinization of olivine, remnant olivine grain boundaries are barely visible. Several grains have been fully altered to serpentine. Prior to alteration olivine was medium grained (1-3 mm) and euhedral. Opaques are coarse grained, interstitial, and almost fully enclose some olivine grains. In transmitted light opaques are slightly translucent red brown.	90% olivine 5% clinopyroxene 5% opaque minerals	very strong	546879.6	7012456.9
13RN395A	dunite	adcumulate	Olivine is medium grained (1-3 mm), equant, and euhedral. Serpentine is concentrated along grain boundaries and helps to outline individual grains. Serpentinization of the interior of grains is weak. One or two 1 mm wide veins of serpentine in thin section. Opaques are mostly interstitial, some are included in serpentine veinlets within olivine.	90% olivine 5% clinopyroxene 5% opaque minerals	moderate	546701.7	7012330.5
13RN396A	altered gabbro	NC	Sample is highly altered. Most of the sample is altered to clays. Remnant clinopyroxene has pervasive exsolution lamellae. No other visible minerals.	60% alteration material 40% altered clinopyroxene	very strong	546920.3	7012238.9

133

13RN397A	feldspathic wehrlite	mesocumulate	Olivine is anhedral to subhedral and fine to medium grained (0.5-2 mm). Moderate serpentinization of olivine. Clinopyroxene is medium grained (1-2.5 mm), granular to poikilitic. Minor plagioclase has been fully altered to clays. Magnetite veinlets are abundant throughout sample. Chromite mostly occurs as inclusions in olivine, though some grains are interstitial or in serpentine veinlets.	65% olivine 23% clinopyroxene 9% altered plagioclase 3% spinel	moderate to strong	547089.5	7012162.4
13RN398A	serpentinite		Olivine has been fully serpentinized. Significant magnetite veining within serpentine.	96% serpentine 4% magnetite	very strong	547193.3	7012098.7
13RN399A	altered gabbro	NC	Sample is highly altered. Most of the sample is altered to clays. Remnant clinopyroxene has pervasive exsolution lamellae. No other visible minerals.	70% alteration material 30% altered clinopyroxene	strong	547299.2	7011996.4
13RN400A	olivine gabbro	NC	Sample is highly altered. Remnant clinopyroxene is anhedral and fine grained (0.25-0.75 mm) with pervasive exsolution lamellae. Feldspars have been fully altered to sericite and clay. Olivine is fine grained (0.25-0.75 mm), anhedral, and embayed.	45% altered plagioclase 40% clinopyroxene 12% olivine 3% opaque minerals	strong	547312.1	7011990.4
13RN400B	feldspathic dunite	orthocumulate	Olivine is pervasively serpentinized. Multiple 1 mm wide serpentine veinlets in sample. Remnant olivine is medium grained and 1-3 mm. Grains are anhedral to subhedral. Grains range from granular to poikilitic with inclusions of altered plagioclase. Plagioclase has been fully altered to sericite and is interstitial to olivine. Very minor clinopyroxene is fine grained (0.5-0.75 mm) and granular. CPX has pervasive exsolution lamellae of OPX and exsolution of opaque minerals. Opaque minerals are both included in silicates and interstitial.	62% olivine 30% plagioclase 5% clinopyroxene 3% opaque minerals	very strong	547312.1	7011990.4
13RN401A	feldspathic dunite	orthocumulate	Olivine is subhedral to euhedral and fine to medium grained (0.75-1.5 mm). Olivine is moderately serpentinized and has inclusions of an opaque mineral. Plagioclase has been fully altered to sericite and is interstitial to olivine. One grain of amphibole is potentially primary but may have formed from alteration of pyroxene. Amphibole is fine grained (0.5 mm), subhedral, and interstitial to olivine.	75% olivine 20% plagioclase 4% opaque minerals 1% amphibole	moderate	547490.4	7011970.5
13RN402A	wehrlite	orthocumulate	Olivine is fine to medium grained (0.75-1.5 mm) and subhedral to euhedral. Individual grains are moderately serpentinized. Clinopyroxene is medium grained (1-3 mm) and ranges from subpoikilitic to poikilitic. Inclusions in CPX are fine grained olivine (<0.5 mm). Clinopyroxene shows abundant exsolution lamellae. Opaque minerals are both interstitial and included in silicates.	55% olivine 40% clinopyroxene 5% opaque minerals	moderate	547613.8	7011728.1
13RN402B	dunite	adcumulate	Olivine is granular, subhedral to euhedral, and is fine to coarse grained (0.5-5 mm). Olivine has moderate alteration to serpentine throughout the sample. A few of the larger grains are poikilitic with inclusions of finer grained olivine. Rare clinopyroxene is medium grained (1.5 mm) and poikilitic. Euhedral spinel is common as both inclusions in olivine and in interstitial spaces.	90% olivine 5% clinopyroxene 5% opaque minerals	moderate	547613.8	7011728.1

15ET189	dunite	adcumulate	Olivine is medium grained (0.75-3 mm) and forms subhedral to euhedral equant grains. One grain has a fine grained inclusion of clinopyroxene. Olivine exhibits weak serpentinization. Opaque minerals are mainly interstitial.	90% olivine 5% clinopyroxene 5% opaque minerals	weak	547131.3	7011235.1
15ET190	dunite		no sample			547095.8	7011337.5
15ET191	wehrlite	orthocumulate	Olivine is fine to medium grained (0.75-3 mm) and subhedral to euhedral with weak serpentinization. Clinopyroxene is medium to coarse grained (1-10 mm) and poikilitic. CPX exhibits pervasive exsolution lamellae of orthopyroxene. Spinel mainly occurs as inclusions in olivine.	67% olivine 31% clinopyroxene 5% opaque minerals	weak	547187.3	7011372.8
15ET192	wehrlite	orthocumulate	Olivine is fine to medium grained (0.75-3 mm) and subhedral to euhedral with weak serpentinization. Aggregates of olivine have equant, triple junction grain boundaries. Clinopyroxene is medium to coarse grained (1.5-13 mm) and poikilitic. Inclusions are fine grained olivine (<0.25 mm). CPX exhibits pervasive exsolution lamellae of orthopyroxene. Spinel mainly occurs as inclusions in olivine.	80% olivine 17% clinopyroxene 3% opaque minerals	weak	547178.3	7011413.8
15ET193	wehrlite	adcumulate	Olivine is fine to medium grained (0.25-1.5 mm) and subhedral to euhedral. Olivine is weakly to moderately serpentinized. Clinopyroxene is fine grained (0.5-0.75 mm), subhedral, and granular. Spinel occurs mainly as inclusions in olivine.	80% olivine 17% clinopyroxene 3% opaque minerals	moderate	547280.9	7011467.4
15LL118	wehrlite		no sample			547977.0	7011715.3
15LL119A	gabbro	NC	no sample			547961.8	7011747.2
15LL119B	gabbro	NC	no sample			547968.9	7011710.0
15LL119C	gabbro	NC	no sample			547957.3	7011730.7
15LL119D	gabbro	NC	no sample			547959.4	7011738.8
15LL119E	gabbro	NC	no sample			547958.6	7011751.4
15LL119F	gabbro	NC	no sample			547974.9	7011740.3
15LL120	gabbro	NC	no sample			548116.8	7011589.6
15LL121	wehrlite	adcumulate	Olivine is medium to coarse grained (0.5-2 mm) and subhedral to euhedral. A few grains have cuspate grain boundaries but the majority have equant grain boundaries. Olivine is moderately serpentinized. Clinopyroxene is fine to medium grained (0.25-1 mm), subhedral, and granular. Clinopyroxene has abundant exsolution lamellae. Opaque minerals occur as inclusions in olivine and along grain boundaries.	60% olivine 37% clinopyroxene 3% opaque minerals	moderate	545953.9	7012954.4

15LL122	dunite	adcumulate	Olivine is fine to medium grained (0.75-1 mm) and subhedral. Olivine is moderately serpentinized. Rare clinopyroxene is poikilitic and medium grained (2.5 mm) or fine grained (<0.5 mm), interstitial, and anhedral. CPX has exsolution of oxides and orthopyroxene. Opaque minerals are mainly interstitial but sometimes occur within the silicates.	88% olivine 8% clinopyroxene 4% opaque minerals	moderate	545833.7	7012893.1
15LL123	wehrlite		no sample			546073.3	7012889.3
15LL124	clinopyroxenite		no sample			546072.7	7012900.0
15LL125	olivine clinopyroxenite		no sample			546074.0	7012919.9
15LL126	clinopyroxenite		no sample			546107.8	7012910.2
15LL127	clinopyroxenite		no sample			546183.1	7012916.7
15LL128	wehrlite	adcumulate	Olivine is fine to medium grained (0.5-1 mm) and subhedral to euhedral. Olivine is pervasively serpentinized. Clinopyroxene is fine to medium grained (0.5-1 mm), granular, and subhedral. CPX has abundant exsolution lamellae. Opaque minerals mainly occur within serpentinite veinlets.	70% olivine 25% clinopyroxene 5% opaque minerals	strong	546489.6	7012795.2
15LL129	wehrlite		no sample			546402.1	7012696.9
15LL130	dunite		no sample			546321.3	7012676.4
15LL131	dunite	adcumulate	Olivine is fine to medium grained (0.5-2 mm) and subhedral. Grains are pervasively serpentinized, though individual grains haven't been completely destroyed. Clinopyroxene is fine grained (0.5 mm) and anhedral. Oxides are common within olivine and within serpentine.	90% olivine 5% clinopyroxene 5% opaque minerals	moderate strong	546408.2	7012626.3
15LL132	dunite	adcumulate	Olivine is fine to medium grained (0.5-3 mm) and anhedral to subhedral. Grains are pervasively serpentinized. Thin 0.25 mm wide serpentine veinlets cut through sample. Clinopyroxene is fine grained (0.5 mm), anhedral, and interstitial. There is very minor fine grained, interstitial amphibole. It is difficult to tell whether amphibole is primary or secondary. Oxides are common within olivine and within serpentine.	93% olivine 5% opaque minerals 2% clinopyroxene <1% amphibole	moderate strong	546461.1	7012590.6
15LL133	dunite	adcumulate	Olivine is fine to medium grained (0.5-3 mm) and subhedral to euhedral. Grains are moderately serpentinized. Rare clinopyroxene is fine grained (0.25 mm), anhedral, and interstitial. Some CPX grains may have undergone alteration to amphibole. Oxides are common within olivine and within serpentine.	93% olivine 4% clinopyroxene 3% opaque minerals	moderate	546444.9	7012502.8
15LL134	dunite	mesocumulate	Olivine is fine to medium grained (0.5-2 mm) and subhedral to euhedral. Grains are moderately serpentinized. Rare clinopyroxene is medium to coarse grained (4-6 mm) and poikilitic. CPX has abundant orthopyroxene exsolution lamellae. Oxides are common within silicates and within serpentine.	88% olivine 7% clinopyroxene 5% opaque minerals	moderate strong	546528.1	7012384.5

136

15LL135	wehrlite	mesocumulate	Olivine is fine to medium grained (0.25-1 mm) and anhedral to subhedral. Some grains have cuspate grain boundaries. Olivine is moderately serpentinized. Clinopyroxene is fine to medium grained (0.75-2 mm), granular, and subhedral. Clinopyroxene has pervasive orthopyroxene exsolution. Opaque minerals are predominately interstitial.	65% clinopyroxene 43% olivine 2% opaque minerals	moderate strong	546491.7	7012786.7
15LL136	troctolite	orthocumulate	Olivine is fine to medium grained (0.5-1.5 mm) and anhedral to subhedral. Grains have been moderately serpentinized. Clinopyroxene is medium grained (1-3 mm), anhedral, and ranges from granular to poikilitic. CPX has inclusions of fine grained olivine and sericite and has minor orthopyroxene exsolution lamellae. Orthopyroxene is medium grained (1-3 mm), anhedral, and poikilitic. Inclusions in orthopyroxene are also olivine and sericite. Interstitial plagioclase has completely altered to sericite. No remnant plagioclase grains are visible. Opaque minerals are common within olivine and sericite.	55% olivine 20% plagioclase 10% clinopyroxene 10% orthopyroxene 5% opaque minerals	moderate	547055.0	7012094.2
15LL137	serpentinite		There a few remnant grains of olivine, clinopyroxene, and possibly sericite, but sample has been about 85% altered to serpentine and Fe oxide. Originally this was likely wehrlite.	85% alteration 15% mineral remnants	very strong	546989.5	7012170.5
15LL138	feldspathic dunite	orthocumulate	Olivine is subhedral to euhedral and fine to medium grained (0.75-3 mm). Olivine has been pervasively altered to serpentine but most of the grains are still visible. Rare clinopyroxene is interstitial, anhedral, and fine grained (<1 mm). A few grains have undergone amphibole alteration. Plagioclase has been completely altered to sericite. One 5 mm wide serpentine veinlet cuts across sample. Opaque minerals occur within olivine and sericite.	70% olivine 20% plagioclase 5% clinopyroxene 5% opaque minerals	strong	546959.1	7012188.6
15LL139	feldspathic dunite	mesocumulate	Olivine is subhedral to euhedral and fine to medium grained (0.75-3 mm). Grains are weakly to moderately altered to serpentine. Minor interstitial plagioclase has been completely altered to sericite. A few serpentinite veinlets run through sample. Euhedral spinel occurs within olivine and sericite.	83% olivine 7% plagioclase 5% clinopyroxene 5% opaque minerals	moderate	546926.4	7012225.9
15LL140	dunite	mesocumulate	Olivine has been ~60% altered to serpentine. Remnant grains in some parts of the sample are subhedral and fine to medium grained (0.75-1 mm). Interstitial sericite is visible in some of the less altered clusters of olivine. Abundant opaque minerals occur within olivine and within serpentine veinlets.	60% serpentine 31% olivine 4% plagioclase 5% opaque minerals	strong	546902.8	7012244.9
15LL141	dunite	adcumulate	Olivine has been ~40% altered to serpentine. Remnant grains in some parts of the sample are subhedral and fine to medium grained (0.75-1 mm). Interstitial sericite is visible in some of the less altered clusters of olivine. Abundant opaque minerals occur within olivine and within serpentine veinlets.	53% olivine 40% serpentine 5% opaque minerals 2% plagioclase	strong	546862.6	7012238.5

Sample	Rock type		Description	Mineralogy		Coordinates	
15LL142	dunite	adcumulate	Olivine is fine to medium grained (0.5-1.5 mm) and subhedral to euhedral. Grains have moderate to strong serpentinization. Rare clinopyroxene is medium grained (1-2 mm) and poikilitic. Clinopyroxene has pervasive exsolution lamellae. One grain of CPX may have undergone amphibole alteration. Opaque minerals occur within olivine and within serpentine veinlets.	93% olivine 4% clinopyroxene 3% opaque minerals	moderate strong	546867.3	7012362.6
15LL143	dunite	adcumulate	Olivine is medium to coarse grained (0.75-7 mm) and subhedral to euhedral. Grains have moderate to strong serpentinization. Rare clinopyroxene is fine grained (<0.75 mm), interstitial, and anhedral. Clinopyroxene has pervasive exsolution lamellae. Opaque minerals occur within olivine and within serpentine veinlets.	93% olivine 4% clinopyroxene 3% opaque minerals	moderate strong	547449.6	7012232.8
15LL144	gabbro	NC	Fine grained foliated gabbro. Plagioclase is very fine grained (10-30 microns) and anhedral. Weak twinning is visible in some grains though no primary texture remains. Grains have sutured boundaries and triple junctions. In a few clusters plagioclase has been altered to clays. Clinopyroxene is fine grained (0.25-0.75 mm) and anhedral to subhedral. A few grains are twinned. Several grains are zoned. Olivine has been completely altered to Fe oxides and clays. Oxides occur in clusters from potentially altered olivine and/or pyroxene.	48% plagioclase 40% clinopyroxene 6% altered olivine 6% oxides	strong	547706.5	7012286.8
15LL145A	leucocratic gabbro	NC	Fine grained weakly foliated gabbro. Plagioclase is fine grained (10-20 microns) and anhedral. Weak twinning is visible in some grains though no primary texture remains. Grains have sutured boundaries and triple junctions. Some clusters of plagioclase have been altered to clays. Clinopyroxene is fine grained (20-40 microns) and anhedral to subhedral. Several grains are zoned.	60% plagioclase 20% clinopyroxene 15% altered olivine 5% oxides	moderate strong	547694.2	7012322.5
15LL145B	melanocratic gabbro	NC	Fine grained foliated gabbro. Plagioclase grains have been almost completely altered to clays. Some grain boundaries are still visible. Clinopyroxene is fine grained (20-40 microns) and anhedral to subhedral. Several grains are zoned.	55% clinopyroxene 40% plagioclase 5% opaque minerals	moderate strong	547695.1	7012322.3
15LL146	feldspathic dunite	orthocumulate	Olivine is fine to medium grained (0.75-2 mm) and euhedral. Serpentinization is mostly concentrated around the grain margins and helps to outline individual grains. Interstitial plagioclase has been completely altered to sericite. Rare clinopyroxene is medium grained (2 mm) and poikilitic. Magnetite occurs within serpentinite veinlets.	80% olivine 11% plagioclase 6% clinopyroxene 3% opaque minerals	moderate strong	547946.6	7011974.8
15LL147	feldspathic dunite	mesocumulate	Olivine is pervasively serpentinized though remnant grains remain in some areas. Olivine is fine to medium grained (0.75-2 mm) and euhedral. Interstitial plagioclase has been completely altered to sericite and clays. Magnetite predominately occurs within serpentine veinlets.	60% serpentine 31% olivine 4% plagioclase 5% opaque minerals	strong	547929.9	7012028.3

15LL148	feldspathic olivine wehrlite	orthocumulate	Olivine is fine to medium grained (0.75-1.5 mm) and subhedral to euhedral. Olivine is moderately serpentinized though alteration is higher around serpentine veinlets. Clinopyroxene is fine to medium grained (0.5-1 mm), interstitial, and anhedral. Some clinopyroxene has undergone alteration to amphibole. Interstitial plagioclase has been completely altered to sericite. Oxides primarily occur within the matrix.	60% olivine 27% clinopyroxene 10% plagioclase 3% opaque minerals	moderate	547973.3	7011920.4
15LL149	wehrlite	adcumulate	Olivine is fine to medium grained (0.5-2 mm) and subhedral to euhedral. Serpentinization is very weak. Clinopyroxene is fine to medium grained (0.75-2 mm) and euhedral. CPX is granular on average, though a few grains are poikilitic and have one or two inclusions of olivine. Clinopyroxene has weak to moderate orthopyroxene exsolution lamellae. Oxides predominately occur within olivine.	65% olivine 32% clinopyroxene 3% opaque minerals	weak	547785.2	7011691.0
15LL150	wehrlite	adcumulate	Olivine is subhedral to euhedral and fine to medium grained (0.5-2 mm). Very weak serpentinization of olivine. Clinopyroxene is predominately fine grained (0.5-1 mm), granular, and euhedral. Clinopyroxene exhibits moderate exsolution lamellae. Several grains exhibit simple twins. Oxides primarily occur within olivine.	70% olivine 25% clinopyroxene 5% opaque minerals	weak	547815.6	7011673.5
15LL151	wehrlite	adcumulate	Olivine is subhedral and fine to medium grained (0.5-2.5 mm). Individual grains have undergone moderate to strong serpentinization. Clinopyroxene is fine to medium grained (0.75-2.5 mm), anhedral, and granular to poikilitic. Clinopyroxene exhibits moderate exsolution lamellae. Oxides primarily occur within olivine and serpentine.	70% olivine 25% clinopyroxene 5% opaque minerals	moderate	547846.8	7011666.7
15LL152	wehrlite	adcumulate	Olivine is subhedral to euhedral and fine to medium grained (0.5-1.5 mm). Individual grains have undergone weak serpentinization. Clinopyroxene is fine to medium grained (0.75-2.5 mm), anhedral, and granular. Clinopyroxene exhibits moderate exsolution lamellae. Oxides primarily occur within olivine and serpentine.	70% olivine 25% clinopyroxene 5% opaque minerals	weak	547855.3	7011663.7
15LL153	dunite	adcumulate	Olivine is fine to medium grained (0.5-1.5 mm) and subhedral to euhedral. Grains are moderately serpentinized. Clinopyroxene is fine grained (0.75 -1 mm), subhedral, and granular. Opaque minerals predominately occur interstitial to olivine. Spinel sometimes occurs within olivine.	93% olivine 4% clinopyroxene 3% opaque minerals	moderate	547852.6	7011630.8
15LL154	dunite	adcumulate	Olivine is fine to medium grained (0.5-2 mm) and subhedral to euhedral. Grains are moderately serpentinized. Clinopyroxene is fine to medium grained (0.75 -2 mm), subhedral, and granular. One grain is poikilitic and has inclusions of olivine. Opaque minerals predominately occur interstitial to olivine. Spinel also occurs within olivine.	90% olivine 7% clinopyroxene 3% opaque minerals	moderate	547838.9	7011607.6
15LL155	dunite	mesocumulate	Olivine is fine to medium grained (0.75-2.5 mm) and subhedral to euhedral. Grains are moderately serpentinized. Clinopyroxene is fine to coarse grained (0.75-5 mm), subhedral, and granular. One or two grains are poikilitic. Spinel occurs both within olivine and interstitial to silicates.	90% olivine 7% clinopyroxene 3% opaque minerals	moderate	547804.1	7011688.1

15LL156	dunite	adcumulate	Olivine is fine to medium grained (0.75-4 mm) and subhedral to euhedral. Grains are moderately to strongly serpentinized. Clinopyroxene is fine grained (0.5 mm), anhedral, and interstitial to olivine. Spinel occurs both within olivine and interstitial to silicates.	93% olivine 4% clinopyroxene 3% opaque minerals	moderate strong	547812.3	7011716.6
15LL157	dunite	adcumulate	Olivine is fine to coarse grained (0.75-5 mm) and subhedral to euhedral. Grains are moderately to strongly serpentinized. Clinopyroxene is fine grained (0.5 mm), anhedral, and interstitial to olivine. Opaque minerals occur both within olivine and interstitial to silicates.	93% olivine 4% clinopyroxene 3% opaque minerals	moderate strong	547845.0	7011746.6
15LL158	feldspathic dunite	orthocumulate	Olivine is fine to medium grained (0.75-1.5 mm) and subhedral to euhedral. Olivine has undergone moderate to pervasive serpentinization. Clinopyroxene is medium to coarse grained (1.5-5 mm), anhedral, and poikilitic. Clinopyroxene has pervasive exsolution lamellae. Interstitial plagioclase has been completely altered to sericite. Oxides primarily occur within the matrix.	76% olivine 10% clinopyroxene 10% plagioclase 4% opaque minerals	moderate strong	548108.0	7011733.4
15LL159	feldspathic dunite	orthocumulate	Olivine is fine to medium grained (0.75-1.5 mm) and subhedral to euhedral. Olivine has undergone moderate to pervasive serpentinization. Clinopyroxene is medium to coarse grained (1.5-12 mm), anhedral, and poikilitic. Clinopyroxene has pervasive exsolution lamellae. Interstitial plagioclase has been completely altered to sericite. Oxides primarily occur within the matrix.	78% olivine 10% clinopyroxene 8% plagioclase 4% opaque minerals	moderate strong	548006.0	7011785.0
15LL160	dunite	mesocumulate	Olivine is fine to coarse grained (0.5-5 mm) and subhedral to euhedral. Grains are moderately serpentinized. Clinopyroxene is fine to medium grained (0.5-1 mm), anhedral, and interstitial. CPX has moderate exsolution lamellae. Opaque minerals are interstitial and included within olivine.	92% olivine 5% clinopyroxene 3% opaque minerals	moderate	547875.8	7011575.7
15LL161	dunite	mesocumulate	Olivine is fine to coarse grained (0.5-5 mm) and subhedral to euhedral. Grains are moderately serpentinized. Clinopyroxene is medium to coarse grained (1.5-7 mm), anhedral, and poikilitic. CPX has moderate exsolution lamellae. Opaque minerals are interstitial and included within olivine.	90% olivine 7% clinopyroxene 3% opaque minerals	moderate	547452.0	7011694.6
15LL162	wehrlite	mesocumulate	Olivine is fine to medium grained (0.5-3 mm) and subhedral to euhedral. Grains are moderately serpentinized. Clinopyroxene is medium grained (1.5-4 mm), anhedral, and subpoikilitic. CPX has pervasive exsolution lamellae. Opaque minerals are interstitial and included within olivine. Visible sulfides (most likely pentlandite) are fine grained and disseminated.	66% olivine 30% clinopyroxene 4% opaque minerals (1% sulfide)	moderate	547433.8	7011773.6
15LL163A	clinopyroxenite	adcumulate	Medium to coarse grained (3-12 mm), anhedral to subhedral, granular clinopyroxene. Clinopyroxene grains have embayed boundaries and minor orthopyroxene exsolution lamellae. Alteration is mainly concentrated around grain boundaries. A few grains exhibit simple twins. Minor olivine is subhedral and medium grained (1 mm). Oxides are interstitial.	88% clinopyroxene 10% olivine 1% opaque minerals	weak	547979.5	7011636.3

Sample	Rock type		Description	Mineralogy	Fabric	Easting	Northing
15LL163B	wehrlite	mesocumulate	Medium to coarse grained (3-6 mm), anhedral to subhedral, granular clinopyroxene. Clinopyroxene grains have pervasive orthopyroxene exsolution lamellae. The majority of grains are amoeboidal with inclusions of olivine. Included olivine grains have strong reaction rims. Discrete olivine grains are subhedral and medium grained (1-2 mm). Oxides are predominately interstitial.	76% clinopyroxene 20% olivine 4% opaque minerals	moderate strong	547979.5	7011636.0
15LL165	schist	NC	no sample			548408.9	7011354.1
15LL166	schist	NC	no sample			548443.8	7011340.8
15LL168	dunite	adcumulate	Olivine is medium grained (1-4 mm) and subhedral to euhedral with equant, sutured grain boundaries. Olivine is weakly serpentinized. Rare clinopyroxene is fine grained (<0.5 mm), anhedral, and interstitial. Spinel is mainly interstitial but sometimes occurs as inclusions in olivine.	93% olivine 4% clinopyroxene 3% opaque minerals	weak	547494.5	7011719.4
15LL169	dunite	mesocumulate	Olivine is fine to medium grained (0.75-3 mm) and subhedral to euhedral. Olivine is weakly serpentinized. Clinopyroxene is fine to medium grained (0.25-4 mm), anhedral, and subpoikilitic. Spinel mainly occurs as inclusions in olivine.	90% olivine 7% clinopyroxene 3% opaque minerals	weak	547408.5	7011640.8
15LL170	schist	NC	no sample			547365.9	7011603.9
15LL171	dunite	mesocumulate	Olivine is fine to medium grained (1-4 mm) and subhedral to euhedral with equant, sutured grain boundaries. Olivine is weakly serpentinized. Clinopyroxene is fine to medium grained (0.25-4 mm), anhedral, and subpoikilitic. CPX has pervasive exsolution lamellae. Spinel occurs both interstitial and as inclusions in olivine.	89% olivine 7% clinopyroxene 4% opaque minerals	moderate	547362.1	7011585.5
15LL172	dunite	mesocumulate	Olivine is fine to medium grained (1-5 mm) and subhedral to euhedral. Olivine is moderately serpentinized. Rare clinopyroxene is fine to medium grained (0.5-4 mm), anhedral, and interstitial to subpoikilitic. Spinel occurs both interstitial and as inclusions in olivine.	93% olivine 4% clinopyroxene 3% opaque minerals	moderate	547287.7	7011533.1
15LL173	troctolite		no sample			547912.7	7011059.9
15LL174	troctolite	mesocumulate	Olivine is fine to medium grained (0.25-1.5 mm) and subhedral to euhedral. Grains are moderately serpentinized. Clinopyroxene is fine to medium grained (1.5-4 mm), anhedral, and poikilitic. CPX has weak exsolution lamellae. Plagioclase is medium to coarse grained (1-5 mm), anhedral, and poikilitic. Grains all exhibit polysynthetic twins. Plagioclase has patchy alteration to clays. Inclusions in both plagioclase and clinopyroxene are fine grained olivine (0.25 mm). Opaque minerals are predominately interstitial.	59% olivine 20% plagioclase 18% clinopyroxene 3% opaque minerals	moderate	548424.7	7010882.5
15LL175	granodiorite porphyry	NC	no sample			547919.3	7012576.7
15LL176	meta-andesite	NC	no sample			547891.5	7012661.6
15LL177	meta-gabbro	NC	no sample			547616.1	7012653.6
15LL178	meta-rhyolite	NC	Fine grained (10 microns) equigranular quartz and feldspar. Feldspar exhibits moderate alteration to clays.	55% quartz 45% feldspar	weak	547489.6	7012669.5

15LL179	foliated granodiorite	NC	no sample			547365.7	7012734.0
15LL180	serpentinite		no sample			547288.9	7012707.8
15LL181	wehrlite		no sample			546958.6	7012819.3
15LL182	gabbro porphyry	NC	no sample			546665.8	7012702.6
15LL184	granodiorite porphyry	NC	no sample			547748.3	7012708.0
15RN333	gabbro	NC	Sample is highly altered. Remnant clinopyroxene is anhedral and fine grained (0.25-0.75 mm) with pervasive exsolution lamellae. Feldspars have been almost fully altered to sericite and clay. Fine grained (<0.75 mm), subhedral plagioclase is still visible in a few less altered patches. Olivine is fine grained (0.25-0.75 mm), anhedral, and embayed. Oxides mainly occur as replacements on pyroxene.	55% plagioclase 31% clinopyroxene 9% olivine 5% opaque minerals	strong	547752.8	7011786.7
15RN334	gabbro	NC	no sample			547676.5	7011781.5
15RN335A	gabbro	NC	Sample is highly altered. Remnant clinopyroxene is anhedral and fine to medium grained (0.75-2 mm) with pervasive exsolution lamellae. Clinopyroxene is predominately granular but a few grains are poikilitic with inclusions of altered plagioclase. Feldspars have been almost fully altered to sericite and clay. Medium grained (1 mm), subhedral plagioclase is still visible in a few less altered areas. Olivine is fine to medium grained (0.75-1 mm), anhedral, and embayed. Oxides are mainly interstitial.	50% plagioclase 36% clinopyroxene 12% olivine 2% opaque minerals	strong	548614.9	7011411.0
15RN335B	olivine gabbro	NC	Clinopyroxene is anhedral and fine to medium grained (0.75-5 mm) with pervasive exsolution lamellae. Clinopyroxene is predominately granular but a few grains are poikilitic with inclusions of olivine. Feldspars have been fully altered to sericite and clay. Olivine is fine to medium grained (0.75-2 mm), anhedral, and embayed. Oxides are mainly interstitial but also occur as inclusions in olivine.	40% olivine 38% clinopyroxene 20% plagioclase 2% opaque minerals	moderate to strong	548614.9	7011411.0
15RN336	wehrlite	adcumulate	Olivine is fine to medium grained and ranges from 0.5 to 2 mm. Grains are anhedral to subhedral and moderately serpentinized. Clinopyroxene is granular, anhedral, and fine to medium grained (0.5 to 2 mm). All clinopyroxene has pervasive orthopyroxene exsolution lamellae. Spinels are mainly interstitial.	62% olivine 35% clinopyroxene 3% opaque minerals	moderate	547486.6	7011436.4
15RN338	wehrlite	adcumulate	Olivine is fine to medium grained and 0.5-4.5 mm. Grains are anhedral to subhedral and moderately serpentinized. Clinopyroxene is granular, anhedral, and fine to medium grained (0.5 to 2 mm). All clinopyroxene has pervasive orthopyroxene exsolution lamellae. Spinels are mainly interstitial.	72% olivine 25% clinopyroxene 3% opaque minerals	moderate	547283.2	7011463.5
15RN339	dunite	adcumulate	Olivine is medium grained (1-4 mm) and subhedral to euhedral with equant, sutured grain boundaries. Olivine is moderately to strongly serpentinized. Clinopyroxene is medium to coarse grained (1-6 mm), anhedral, and poikilitic. CPX has pervasive exsolution lamellae. Spinel occurs both interstitial and as inclusions in olivine.	90% olivine 7% clinopyroxene 3% opaque minerals	moderate to strong	547287.4	7011468.6

15RN340	dunite	adcumulate	Olivine is medium grained (1-4 mm) and subhedral to euhedral. Olivine is moderately to strongly serpentinized. Clinopyroxene is medium to coarse grained (1-6 mm), anhedral, and poikilitic. CPX has pervasive exsolution lamellae. Spinel occurs both interstitial and as inclusions in olivine.	90% olivine 7% clinopyroxene 3% opaque minerals	moderate to strong	547327.7	7011416.6
15RN341	dunite	adcumulate	Olivine is fine to medium grained (0.75-4 mm) and subhedral to euhedral with equant, sutured grain boundaries. Olivine is weakly serpentinized. Rare clinopyroxene is medium grained (2-4 mm), anhedral, and poikilitic. CPX has moderate exsolution lamellae. Spinel occurs both interstitial and as inclusions in olivine.	93% olivine 4% clinopyroxene 3% opaque minerals	weak	547253.4	7011461.6
15RN342	dunite	adcumulate	Olivine is fine to medium grained (0.75-3 mm) and subhedral to euhedral with equant, sutured grain boundaries. Olivine is weakly serpentinized. Rare clinopyroxene is fine grained (<0.75 mm), anhedral, and interstitial. CPX has moderate exsolution lamellae. Spinel occurs both interstitial and as inclusions in olivine.	93% olivine 4% clinopyroxene 3% opaque minerals	weak	547318.6	7011492.7
15RN343	wehrlite		no sample			547480.5	7011378.4
15RN344	wehrlite		no sample			547540.4	7011292.4
15RN345	dunite	adcumulate	Olivine is fine to coarse grained (0.75-7 mm) and subhedral to euhedral. Olivine is weakly serpentinized. Rare clinopyroxene is fine grained (<0.75 mm), anhedral, and interstitial. CPX has moderate exsolution lamellae. Spinel occurs both interstitial and as inclusions in olivine.	93% olivine 4% clinopyroxene 3% opaque minerals	weak	547872.7	7011109.2
15RN346	wehrlite	mesocumulate	Medium grained (1-3 mm), anhedral, granular clinopyroxene. Clinopyroxene grains have pervasive orthopyroxene exsolution lamellae. A number of grains are amoeboidal with inclusions of olivine. Included olivine grains have strong reaction rims. Discrete olivine grains are subhedral and medium grained (1-2 mm). Olivine is pervasively serpentinized. Oxides are predominately interstitial.	60% clinopyroxene 37% olivine 3% opaque minerals	moderate strong	547945.4	7011136.9
15RN347	wehrlite		no sample			548074.3	7010925.7
15RN348	clinopyroxenite		no sample			548085.5	7010877.6
15RN349	wehrlite	mesocumulate	Olivine is fine to medium grained (0.5-1.5 mm) and anhedral. Grain boundaries are mostly irregular or cuspate. One or two grains are subpoikilitic with inclusions of clinopyroxene. Olivine is moderately serpentinized. Clinopyroxene is anhedral to subhedral and fine to medium grained (0.5-2 mm). CPX has pervasive orthopyroxene exsolution lamellae. Several grains exhibit simple twins and a few grains are zoned. Plagioclase has been fully altered to clays. Spinel is mostly interstitial or included in olivine.	50% olivine 44% clinopyroxene 3% plagioclase 3% opaque minerals	moderate	548433.9	7010913.3

15RN350	olivine gabbro	mesocumulate	Clinopyroxene is anhedral and fine to medium grained (0.75-2 mm) with pervasive exsolution lamellae. A few grains exhibit simple twins. Clinopyroxene is predominately granular but a few grains are poikilitic with inclusions of altered plagioclase. Feldspars have been fully altered to sericite and clay. Olivine is fine to medium grained (0.75-2 mm), anhedral, and embayed. Oxides are mainly interstitial but also occur as inclusions in olivine.	50% plagioclase 27% clinopyroxene 21% olivine 2% opaque minerals	moderate strong	548452.8	7010883.3
15RN351	troctolite	mesocumulate	Olivine is fine to medium grained (0.25-2 mm) and anhedral to subhedral. Grains are moderately serpentinized. Clinopyroxene is medium grained (1.5-4 mm), anhedral, and poikilitic. CPX has weak exsolution lamellae. Plagioclase has been fully altered to sericite and clays. Inclusions in clinopyroxene are fine grained olivine (0.5 mm). Opaque minerals are predominately interstitial.	67% olivine 23% plagioclase 7% clinopyroxene 3% opaque minerals	moderate	548427.2	7010869.8
15RN352	olivine wehrlite		no sample			548636.9	7010878.4
15RN353	serpentinite		no sample			547772.8	7012733.5
15RN354	wehrlite		Fine grained (<10 microns), highly altered sample. Most of the sample has been altered to a fine grained mix of clays and serpentine. Remnant clinopyroxene grains are fine grained (5-30 microns) and anhedral. Interstitial oxides are abundant.	unable to identify individual minerals	very strong	547577.9	7012687.9
15RN355	serpentinite		no sample			547348.6	7012691.6
15RN356	serpentinite		no sample			547163.8	7012752.6
15RN357	serpentinite		no sample			547089.5	7012976.9
15RN358	Paleozoic volcanic rock	NC	no sample			547096.0	7012981.6
15RN359	wehrlite		no sample			546752.2	7012958.6
15RN360	serpentinite		no sample			546636.1	7012967.0

NC = not cumulate.

144